NOTA: anche questa pagina bianca fa parte del blocco di pagine della tesi

NOTA: tagliare il blocco di pagine della tesi (stampata fronte-retro) lungo le due linee qui tracciate prima di effettuare la rilegatura
La terza linea, sulla destra, indica il taglio finale che può essere fatto prima o dopo la rilegatura (io direi dopo, ma chiedete a chi fa la rilegatura).

UNIVERSITÀ
degli STUDI
di CATANIA

DEPARTMENT OF CIVIL ENGINEERING AND ARCHITECTURE
NATIONAL INTEREST PHD PROGRAM DEFENCE AGAINST NATURAL RISKS AND ECOLOGICAL TRANSITION OF BUILT ENVIRONMENT

***Marco Caragliano***

# CYCLIC BEHAVIOUR AND NUMERICAL MODELLING OF COLD-FORMED HOLLOW STRUCTURAL SECTIONS

Tutors:

Prof. Ing. Melina Bosco
Prof. Ing. Pier Paolo Rossi
Prof. Ing. Mario D'Aniello
Prof. Ing. José Miguel Castro

Ph.D. cycle XXXVIII, 2023-26

# INDEX

# Introduction

Cold-formed Hollow Structural Sections (HSS) are widely used as columns in steel moment-resisting frames due to their high strength-to-weight ratio, similar lateral stiffness along orthogonal directions, and large torsional stiffness. The growing interest in these members is reflected by numerous experimental and numerical studies aimed at: (i) characterising the stress–strain response of coupons extracted from cold-formed members; (ii) quantifying residual stresses induced by the manufacturing process; (iii) investigating the cyclic response of HSS columns under combined axial load and bending; (iv) reproducing their response through refined finite element (FE) models and assessing rotation capacity; and (v) developing simplified modelling approaches suitable for nonlinear assessment of structural systems incorporating HSS members.

Due to the manufacturing process, especially in the case of the indirect forming method for all sections and the direct method for rather narrow profiles, coupons extracted from cold-formed members are characterized by a stress-strain response with no sharply defined yield point. The cold-forming process also leads to an increase of the yield strength of steel (determined as the value corresponding to 0.2% strain offset) and to a reduction of its ductility in specimens extracted from the corner parts and the longitudinal weld of the sections.

In parallel, residual stresses represent another key feature of cold-formed HSS: bending residual stresses provide the dominant contribution, while membrane stresses are generally close to zero; tensile residual stresses develop on the outer surface and compressive residual stresses on the inner surface, with larger magnitudes typically observed toward

the middle of the plates. These characteristics influence local buckling, post-buckling degradation, and ultimately the deformation capacity of members under seismic-type loading.

A large number of laboratory testing has explored the cyclic response of HSS columns made of different steel grades and subjected to axial load ratios typically ranging from 0.0 to 0.4. The results consistently highlight the key influence of local slenderness and axial load level on deformation capacity. Symmetric loading protocol was used in almost all these laboratory tests. Asymmetric (collapse-consistent) loading protocols were used in some tests conducted by Suzuki and Lignos, which underlined that the chord rotation capacity of members subjected to collapse-consistent loading protocols is up to two-to-three times larger than that of the same members subjected to a standard symmetric cyclic loading protocol.

Refined numerical models have been developed to replicate these behaviours and to extract design-oriented metrics. Detailed FE approaches based on shell or solid elements can represent instability modes with high fidelity, but become computationally demanding when extended to large parametric studies or structural analyses. For this reason, several alternative modelling strategies have been proposed over the last decades to incorporate damage-related effects in computationally efficient frameworks. These strategies typically introduce: (i) effective section property reductions, (ii) constitutive models with distinct tensile and compressive behaviour to reproduce post-buckling response, or (iii) concentrated plasticity formulations using zero-length rotational springs with cyclic stiffness and strength deterioration at member ends. While these approaches can capture degradation, their calibration is currently mainly limited to I-shaped cross sections. Therefore, their calibration for cold-formed HSS and their extension to the combined effects of axial force and bending moment may require dedicated developments.

Despite the significant progress, most research and design-oriented proposals remain primarily focused on members subjected to axial load and uniaxial bending. In contrast, HSS columns in three-dimensional moment-resisting frames are typically subjected to biaxial bending, especially under seismic actions. Experimental evidence on biaxial response remains limited, and numerical investigations have highlighted that the

biaxial loading path may affect strength deterioration and axial shortening compared to uniaxial bending. However, consolidated proposals to estimate the rotation capacity of cold-formed HSS columns under biaxial bending and to model their cyclic response are still lacking. This gap motivates the research presented in this thesis, which aims to develop and validate modelling strategies capable of capturing local instability effects and degradation, and to provide design-oriented capacity measures under both uniaxial and biaxial bending conditions.

The thesis is organised into five chapters, which progressively move from literature background and benchmark modelling to original numerical developments and simplified modelling tools. Chapter 1 provides the state of the art on cold-formed steel box sections used as structural components, focusing on material properties, residual stresses, experimental evidence, and numerical strategies available in the literature. Chapter 2 presents the refined finite element model adopted in the thesis. More specifically, the chapter summarises the modelling approach previously proposed by Bosco et al. and its validation for uniaxial bending, and then reports the original contributions of this thesis, namely the extension and validation of the model against stub-column tests and cantilever-column tests under combined axial load and biaxial bending. Chapter 3 builds on this validated finite element model to carry out an original parametric numerical investigation on HSS columns under uniaxial and biaxial bending, considering different axial load ratios, cross-section geometries, and cantilever lengths. The results are synthesised into chord-rotation capacity domains for the Significant Damage and Near Collapse limit states, consistently with the performance-based philosophy of the second generation of Eurocode 8. Based on the evidence gathered in Chapter 3, Chapter 4 develops an original simplified OpenSees modelling strategy for uniaxial bending, based on concentrated plasticity and a zero-length rotational spring, together with calibration relationships for the model parameters. Chapter 5 further extends this research by proposing an original fibre-based OpenSees model for combined axial load and biaxial bending, employing a modified SteelRebar formulation to reproduce the strip-dependent response of box sections.

# Chapter 1
# STATE OF ART OF COLD FORMED HSS

## 1. Applications and manufacturing processes of HSS

Cold-formed Hollow Structural Sections (HSS) are an increasingly popular structural solution in civil and structural engineering. Due to their mechanical and geometric properties, they are widely used in many applications, including structural frames, bridges, transmission towers, and modular structures. Interest in HSS members lies in their high strength-to-weight ratio, excellent torsional stiffness, and good resistance to aerodynamic effects. The cold-forming process increases the yield strength due to strain hardening; however, it simultaneously reduces ductility, making the steel more vulnerable to brittle fracture. The toughness, defined as the material's ability to absorb energy before fracture, is lower than that of hot-rolled sections. Consequently, the use of cold-formed hollow sections in environments subject to dynamic loading and low temperatures requires caution.

The two most common manufacturing methods of cold-formed HSS are direct forming and continuous forming. Both processes are carried out at room temperature and exploit the ductility of steel to obtain the desired shape. However, they differ in key aspects that affect the mechanical and structural properties of the final product. In **Fig. 1** the direct-forming process includes: (i) roll-forming a coil strip directly into an open section with the desired rectangular shape; and (ii) joining the edges of the open section by welding to obtain a closed rectangular shape. Outside

dimensions up to 500 mm and thicknesses up to 40 mm can be produced [27]. In this case, cold working is concentrated in the four corner parts, while the flat parts of the final product, away from the weld, retain properties close to those of the virgin material.

The continuous-forming process (**Fig. 2**) includes: (i) roll-forming a coil strip into an open circular tube; (ii) welding the edges of the open tube to form a closed circular shape; and (iii) flattening the walls of the circular tube to obtain the desired rectangular shape. In this case, the final product experiences more general strain hardening across the cross-section, with a stronger localisation in the corner parts [1].

Manufacturing techniques directly influence the mechanical and structural properties of cold-formed hollow sections.

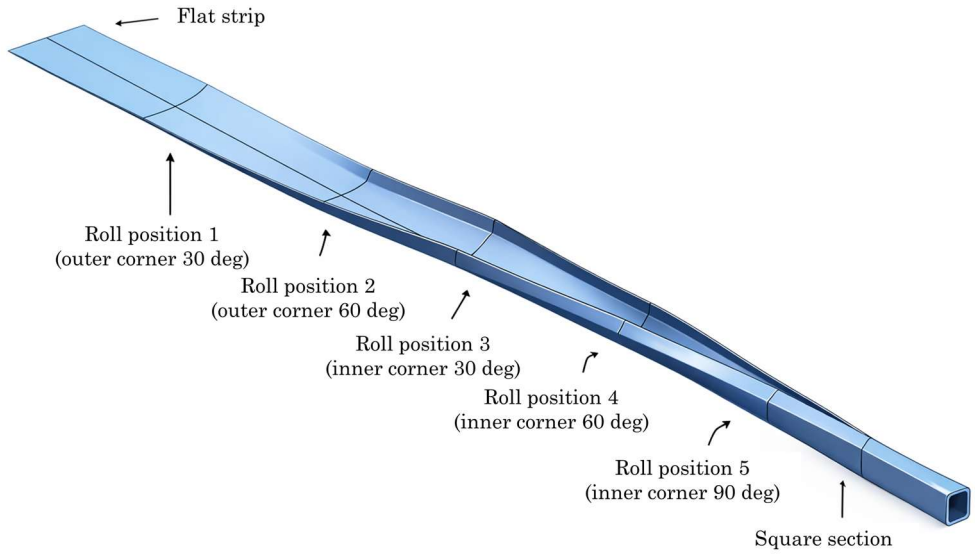


**Fig. 1** – Direct-forming process [2].

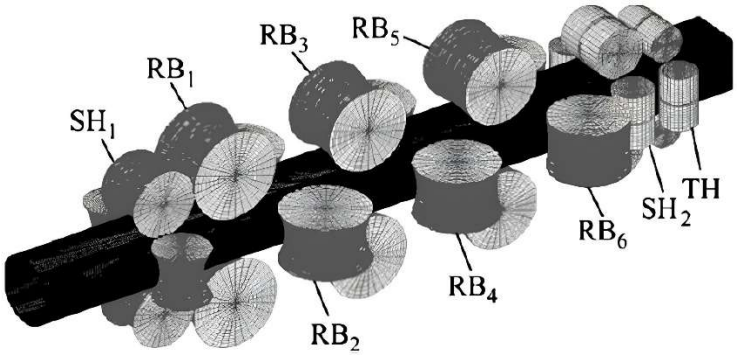


**Fig. 2** – Continuous-forming process [2].

Direct forming generates high residual stresses in the corner and weld regions, whereas the continuous process leads to a more uniform residual-stress distribution but with a greater reduction in ductility. From a practical standpoint, hollow sections produced by continuous forming are often preferred over press-formed members because they are more ductile.

HSS are employed in a wide range of structural applications due to their intrinsic properties. Their use is particularly common in lightweight and prefabricated steel construction, where weight savings and dimensional accuracy play a key role. They are particularly suitable for columns in steel moment-resisting frames owing to their ability to develop comparable stiffness and strength about the two principal axes of the cross-section (**Fig. 3**).

In addition, they are well suited for bracing systems (**Fig. 4a**) and lattice frameworks, owing to their high torsional stiffness. Another valued feature of HSS is their resistance to corrosion, especially when they are made of galvanized or coated steel. Indeed, their closed profile reduces the area exposed to atmospheric agents, limiting maintenance requirements compared to traditional open sections. This characteristic makes them particularly suitable for infrastructure built in harsh environmental conditions, such as bridges and offshore structures (**Fig. 4b**).


**Fig. 3** – Examples of applications of hollow structural sections (HSS): (a) The Shard (London), employing hollow section steel members; (b) square HSS members in a steel moment-resisting frame [3].


**Fig. 4** – (a) HSS members used in braced structures [4]; (b) Composite road bridge, Marvejols, France [5].

Despite their advantages, cold-formed hollow sections also present limitations that must be carefully considered in design. A major issue is the presence of high residual stresses, which can negatively affect material response. Moreover, reduced ductility and lower energy absorption capacity require the adoption of specific design criteria to ensure a safe and effective structural performance.

Residual stresses and the potential susceptibility to brittle fracture impose constraints on the joining techniques that can be adopted. European and American standards recommend special precautions for welding in the corner parts, where stress concentrations may compromise joint strength.

The increasing use of cold-formed hollow sections in structural engineering is motivated by their high performance in terms of strength-to-weight ratio, torsional stiffness, and dimensional accuracy. However, a critical aspect that continues to drive experimental research is the limited understanding of the cyclic behaviour of these sections, particularly with respect to strength degradation and plastic strain accumulation under cyclic loading. The lack of consolidated datasets and the limited guidance in current standards make further experimental investigation necessary to improve the understanding of their structural response and to develop more accurate predictive models. In addition, limitations in existing design codes, which often do not account for the specific characteristics of HSS, provide further motivation for continued research.

## 2. Material properties

Recent experimental work has largely focused on the mechanical characterisation of cold-formed HSS material, with particular attention devoted to the stress–strain laws in both flat and corner parts and to the effects of strain hardening during manufacturing. These effects are typically expressed in terms of increased strength and reduced deformation capacity. Experimental evidence also provides the basis for constitutive modelling, which is a central component of analytical, numerical and design-oriented approaches in structural engineering. Over the last decades, several models have been proposed to represent the nonlinear stress–strain

response of metallic materials, most of which can be traced back to the general formulation originally introduced by Ramberg and Osgood [6].

In the present work, two studies from the literature are taken as key references, namely Poursadrollah et al. [7] and Gardner and Yun [8].

Poursadrollah et al. [7] reported experimental results and finite element simulations aimed at investigating the buckling resistance of cold-formed hollow-section columns with square and rectangular cross-sections. Material stress–strain curves were obtained from coupon tests extracted from the flat and the corner parts of the cross-sections, as well as from coupons including welds. These latter coupons were elongated both in the longitudinal and transverse axes of the member. The experimental dataset was processed statistically to quantify the effects of cold-forming on strength and ductility and to calibrate the parameters of Ramberg–Osgood [6] and Giuffrè–Menegotto–Pinto [9] material models. All specimens were produced in Europe and manufactured through the continuous forming method using S275J0 and S355J0 steel plates.

To evaluate material behaviour, a total of 83 coupons were extracted from cold-formed hollow structural sections (CFHSS) and tested in tension. To avoid thermal alterations, the coupons were cut using water-jet technology. The coupons were distributed as follows: 35 taken from the flat walls of the section, 30 from the corner parts, and 18 extracted in the direction transverse to the weld. The selection of transverse coupons was limited to sections with a minimum width of 100 mm, to ensure sufficient free length for testing. As for corner-part coupons, a dedicated mechanical connector was designed to ensure proper load transfer between the testing machine and the specimen. Experimental results were processed following a standardised procedure for extracting mechanical properties. The engineering stress–strain curves were subsequently converted into true stress–strain curves by accounting for the instantaneous cross-sectional area, using Eqs. (1) and (2). These relationships are valid up to the onset of necking, where $\sigma_{eng}$ and $\sigma_{true}$ denote the engineering and true stress, and $\varepsilon_{eng}$ and $\varepsilon_{true}$ are the engineering and true strain:

$$\sigma_{true} = \sigma_{eng}\left(1 + \varepsilon_{eng}\right) \tag{1}$$

$$\varepsilon_{true} = \ln\left(1 + \varepsilon_{eng}\right) \tag{2}$$

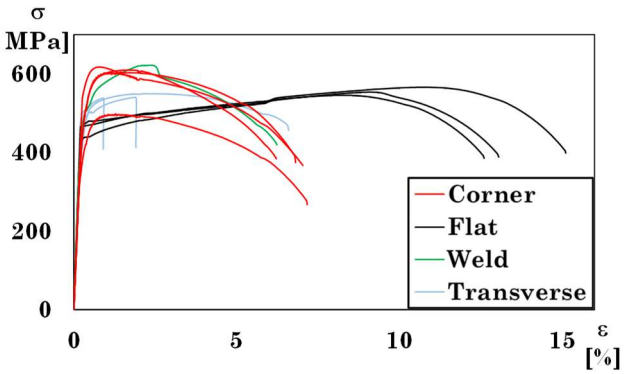


**Fig. 5** – Stress–strain curves of the coupons extracted from the S355_200×8 section [7].

As for flat part coupons, **Fig. 5** reports, as an example, the stress–strain curves of coupons extracted from the 200×8 column made of S355 steel.

The experimental analysis highlighted marked differences in mechanical properties across the cross-section. The stress–strain response exhibited a rounded shape without a clearly defined yield plateau. For this reason, a conventional yield stress was adopted, associated with a residual plastic strain equal to 0.2%. Coupons taken from the flat parts showed lower yield stress values than those extracted from the corner parts. However, they exhibited higher ductility. Corner parts displayed a larger increase in the yield strength due to strain hardening. Coupons transverse to the weld showed an intermediate strength between flat and corner parts. Moreover, the stress–strain curve in the welded region was found to be similar to that of corner parts. This indicates that the weld is not the weakest region, as necking developed outside the welded zone.

**Table 1** lists the sections from which coupons were extracted and compares the measured yield and ultimate strengths of the flat parts ($f_{yf}$, $f_{uf}$) and corner parts ($f_{yc}$, $f_{uc}$) with the nominal values of the virgin material ($f^*_{y,nom}$, $f^*_{u,nom}$). It is noted that, for both flat and corner parts, the values reported in the table represent the mean of the corresponding coupon results (flat or corner) taken from that same section, rather than a global average across different sections. On average, the measured yield strength in the corner parts was approximately 20% higher than that in

the flat parts. In addition, the strength of the flat parts was, on average, about 70% higher than the nominal value for grade S275 and about 40% higher for grade S355. A comparison in terms of average ductility based on the strain ratio $\varepsilon_u/\varepsilon_y$ is provided in **Fig. 6**.

Flat parts exhibit higher ductility than corner parts, with an average increase by a factor of 4.8. This trend is consistent with the higher degree of the plastic strain hardening experienced by corner parts during cold forming.

**Table 1** – Strength values of the tested specimens.

| Specimen | $f^*_{y,nom}$ (MPa) | $f^*_{u,nom}$ (MPa) | $f_{yf,med}$ (MPa) | $f_{yc,med}$ (MPa) | $f_{uf,med}$ (MPa) | $f_{uc,med}$ (MPa) |
|---|---|---|---|---|---|---|
| S275_50x6 | 275 | 430 | 471.0 | 471.3 | 503.7 | 492 |
| S355_50x6 | 355 | 510 | 481.9 | 524.7 | 525.2 | 565.2 |
| S275_100x8 | 275 | 430 | 454.1 | 505.0 | 509.3 | 553.4 |
| S355_100x8 | 355 | 510 | 453.4 | 542.2 | 532 | 554.8 |
| S355_200x8 | 355 | 510 | 463.8 | 536.1 | 554.9 | 582.5 |
| S275_60x40x6 | 275 | 430 | 470.6 | 510.6 | 501.2 | 542.6 |
| S355_70x50x6 | 355 | 510 | 429.7 | 477.5 | 518.5 | 557.5 |
| S355_200x100x12.5 | 355 | 510 | 535.0 | 523.0 | 601.6 | 616.1 |
| S355_220x140x8 | 355 | 510 | 445.6 | 521.9 | 598.1 | 597.7 |
| S275_200x120x12 | 275 | 430 | 363.2 | 400.3 | 485.5 | 503.1 |

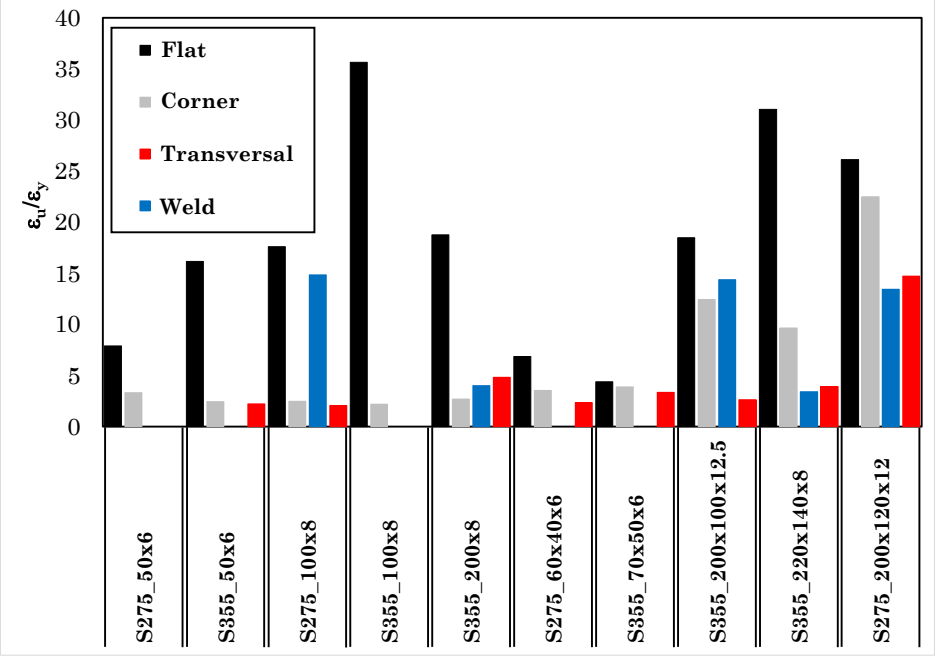


**Fig. 6** – Ductility of the extracted coupons.

Unlike Poursadrollah et al. [7], whose work relies on an extensive experimental campaign, the study by Gardner and Yun [8] is based on a broad review and processing of data available in the literature. Their objective was to develop a predictive model using a database of 729 tensile tests on cold-formed steel coupons, including 581 tests on specimens extracted from flat parts and 148 from corner parts.

The collected data span a wide range of steel grades, manufacturing methods, and cross-section geometries. The section types considered include square (SHS), rectangular (RHS), elliptical (EHS), semi-oval (SOHS), circular (CHS), polygonal hollow sections (PHS), as well as channels (CNS), box/cassette sections (CSS), angles, and Z- and C-sections. The investigated steels cover nominal yield strengths ranging from 235 N/mm² to 1100 N/mm². Ultimate strain values were available for 598 tests, as the remaining studies did not report this quantity explicitly. In addition, 356 complete stress–strain curves were analysed, which were essential to derive predictive equations for the strain-hardening exponents $n$ and $m$ within the two-stage Ramberg–Osgood framework [6] as

adopted by Mirambell and Real [1] for cold-formed steels. Out of the experimental campaigns considered by Gardner and Yun [8], those dealing with sections produced with European steels are summarised in **Table 2**. For each campaign, the steel grade, a label identifying the cross-section geometry, and the number of tested sections is reported, distinguishing datasets used to determine strength and ultimate strain parameters from those used to characterise the constitutive relationship.

**Table 2** – Tested specimen using European steels.

| Study | Steel | Parameters $\sigma_y$, $\sigma_u$ and $\varepsilon_u$ | Full σ-ε curves |
|---|---|---|---|
| Afshan et al. [10] | S355 | 12 (SHS/RHS) | 8 (SHS/RHS) |
| Gardner et al. [11] | S235 | 10 (SHS/RHS) | 10 (SHS/RHS) |
| Kesti [12] | S350 | 2 (CNS) | - |
| Kaitila [13] | S350 | 32 (CSS) | 32 (CSS) |
| Kettler [14] | S275/S355 | 24 (SHS/RHS) | 24 (SHS/RHS) |
| Kyvelou et al. [15] | S450 | 6 (C-section) | 6 (C-section) |
| Kyvelou et al. [16] | S450 | 9 (C-section) | 9 (C-section) |
| Li and Young [17] | S700/S900 | 3 (SHS/RHS) | - |
| Li and Young [18] | S700/S900 | 11 (SHS/RHS) | - |
| Ma [19]; Ma et al. [20] | S700/S900/S1100 | 22 (SHS/RHS/CHS) | 22 (SHS/RHS/CHS) |
| McCann et al. [21] | S355 | 3 (SHS/RHS/CHS) | - |
| Nseir [22] | S355 | 17 (SHS/RHS/CHS) | 16 (SHS/RHS/CHS) |
| Schillo et al. [23] | S500/S700 | 34 (SHS/RHS) | 19 (SHS/RHS) |
| Salmi et al. [24] | S355/S460 | 215 (SHS/RHS) | 112 (SHS/RHS) |
| Tran et al. [25] | S650 | 18 (CHS/PHS) | - |

The analysis of the collected stress–strain curves enabled the extraction of key material parameters. Young's modulus $E$ was defined as the slope of the initial linear portion of the response. To reduce experimental scatter, Gardner and Yun recommended estimating $E$ over a stress range between $0.2\sigma_y$ and $0.4\sigma_y$. The mean value obtained from the database was

203'000 N/mm², which is close to the value recommended by AISI S100-2007 [32], but slightly lower than the 210'000 N/mm² adopted in EN 1993-1-1. The conventional yield stress $\sigma_y$ was defined consistently with Poursadrollah et al. [7], as the intersection between the measured stress–strain curve and a line offset from the origin by the specified plastic strain while maintaining the same slope $E$. An empirical equation was proposed to estimate the ultimate stress $\sigma_u$ of the flat parts from the yield stress $\sigma_y$ (Eq. (3)), accounting for the reduction of the ratio $\frac{\sigma_u}{\sigma_y}$ with the increase of the yield strength.

$$\frac{\sigma_u}{\sigma_y} = 1 + \left(\frac{130}{\sigma_y}\right)^{1.4} \tag{3}$$

**Fig. 7** plots the experimental yield and ultimate stresses ($\sigma_y$ and $\sigma_u$) from literature HSS tests (markers) and the corresponding ultimate stress predicted by Eq. (3) from the ultimate stress $\sigma_u$ (dashed line).

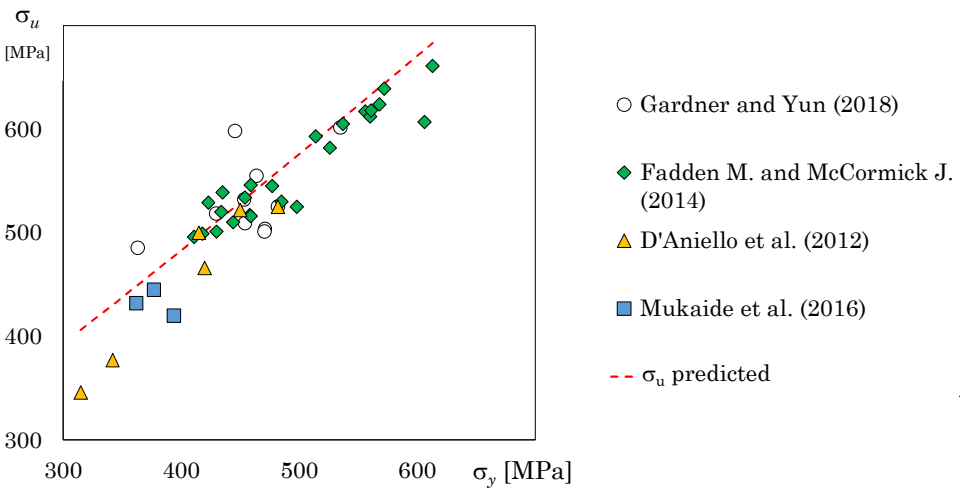


**Fig. 7** – Comparison of the ultimate stress $\sigma_u$ predicted by Gardner and Yun [8] with $\sigma_u$ from different experimental results.

Overall, among the two reviewed contributions, the study by Poursadrollah et al. [7] is more closely aligned with the modelling performed in the present work, as it is based on experimental data obtained

exclusively from steels produced according to European standards. In contrast, Gardner and Yun [8] relied on literature data and considered a broader range of steel grades manufactured under different standards.

## 3. Geometric and mechanical imperfections in HSS

The manufacturing process of cold-formed steel hollow structural sections leads to the development of two main categories of imperfections, namely mechanical and geometric. Mechanical imperfections primarily refer to non-uniform material properties and residual stresses introduced by plastic straining during cold forming and by welding operations. Geometric imperfections, on the other hand, include deviations from the nominal shape such as out-of-straightness, local plate waviness, and thickness or corner-radius variations, which may significantly affect the onset of local instability and the overall structural response.

### 3.1. Mechanical imperfections

The variation of mechanical properties in cold-formed profiles is primarily attributable to strain hardening caused by plastic deformations induced during the cold forming process. This phenomenon may increase the yield strength of the material by up to 50%, with a more pronounced effect in the most highly strained regions. This trend was already highlighted in the previous section.

Residual stresses are self-equilibrated internal stresses that develop as a consequence of industrial manufacturing processes, including thermal processes (cooling, welding, cutting) and mechanical processes (cold rolling, straightening). In cold-formed profiles, rolling chiefly induces residual stresses that vary through the thickness of the material [26].

A major contribution to the characterisation of residual stresses in cold-formed profiles was provided by Somodi B. and Kövesdi B. [2], who experimentally measured residual stresses and proposed analytical relationships for their estimation. According to these researchers, the effect of residual stresses on high-strength steel members is less severe than in mild-steel structures. Nevertheless, residual stresses significantly influence the global buckling behaviour of steel members. By reviewing the

available literature, Somodi and Kövesdi also observed that residual-stress distributions depend on the manufacturing method. However, for both direct and continuous forming methods, tensile residual stresses generally develop on the outer surface, whereas compressive residual stresses are found on the inner surface. Overall, the residual-stress field can be decomposed into three distinct components: (i) membrane stresses, (ii) bending stresses, and (iii) layering stresses, i.e., the stress distribution through the thickness. For these reasons, the experimental campaign was carried out on 15 square hollow-section specimens, supplied by three different manufacturers with five steel grades (S420, S460, S500, S700, S960). All specimens were manufactured through the continuous-forming process. Nine cross-sections were investigated to evaluate the influence of geometry and local plate slenderness $b/t$ of the flat parts on the residual-stress distribution. The section width $b$ ranged from 100 mm to 250 mm, while the thickness $t$ varied between 3 mm and 8 mm. The local slenderness ranged from 13.75 to 60.5 and was defined as the ratio between the clear width, i.e., the total width $b$ minus twice the external corner radius $r$, and the thickness $t$. The length of each profile was equal to four times the cross-section width.

Residual stresses were measured using the sectioning method, which was considered the most reliable and cost-effective among those available in the literature. Strain gauges were applied on the specimen surfaces and protected with a waterproof film. The gauges were arranged along the cross-section of each profile at a minimum distance of $2b$ from the member end, with a number that varied depending on the section width and corner radius. In total, measurements were taken at 386 locations, enabling an accurate mapping of residual stresses. The sectioning procedure consists of two steps. First, a transverse cut is performed at a distance of 2–3 mm from the gauges. Second, longitudinal cuts are executed on both sides of each gauge at approximately 1 mm distance. During cutting, the released strain is recorded by gauges with a sampling frequency of 0.5 Hz. The final strain values are then multiplied by the elastic modulus of steel ($E$=210 GPa) to obtain the residual stresses. The resulting values correspond to residual stresses on the outer or inner surface, depending on the gauge position. Conversely, membrane residual stresses,

i.e., stresses at the mid-thickness of the plate, are evaluated as the average of the values measured by gauges on opposite surfaces.

The experimental campaign led to the following main observations. Tensile residual stresses develop on the outer surface, whereas compressive residual stresses develop on the inner surface. Membrane stresses are nearly zero and can therefore be neglected in comparison with bending residual stresses. Residual stresses in the corner parts are significantly lower than those measured at the centre of the flat parts. At the centre of the plates, residual stresses are slightly lower than those at the plate edges, and the magnitude of this difference depends on the $b/t$ ratio of the cross-section. In the vicinity of the weld, residual stresses decrease.

Laser interferometry, also referred to as the "Laser-Falconeye" method, was employed to assess the accuracy of the sectioning technique and investigate the through-thickness distribution of residual stresses. The measurements indicated that the through-thickness distribution is not strictly linear, although it can be approximated reasonably well by a linear trend

Based on the experimental evidence and the literature review, the researchers proposed relationships to estimate residual stresses [2]. The model assumes a constant residual-stress distribution along the cross-section, with a reduced magnitude in the corner parts equal to 55% of the value of the flat parts. The resulting pattern is shown in **Fig. 8**.

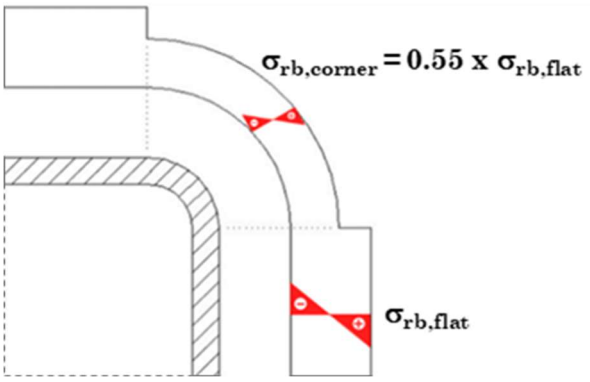


**Fig. 8** – Residual stresses of the proposed model.

The mean bending residual stresses can be estimated using the following expressions [2], proposed for: (4) flat parts made of high-strength steel (S500–S960), (5) flat parts made of normal-strength steel (S235–S460), and (6) corner parts:

$$\sigma_{rb,flat,HSS} = \pm\left(1.28 - \frac{\sigma_y}{1270MPA}\right)\sigma_y \quad (4)$$

$$\sigma_{rb,flat,NSS} = \pm\left(0.8\sigma_y - 67MPa\right) \quad (5)$$

$$\sigma_{rb,corner} = \pm 0.55\sigma_{rb,flat} \quad (6)$$

The model discussed in this section has the following limitations: (i) it is applicable only to sections produced through the continuous-forming process; (ii) it is preferable for square HSS made of steel grades from S500 to S960 (for normal-strength steels it may overestimate residual stresses); (iii) it is suggested for sections with thickness between 4 mm and 7 mm and a $b/t$ ratio between 18 and 38.

### 3.2. Geometric imperfections

Geometric imperfections can be classified into two main categories: transverse and longitudinal imperfections. The former affects the cross-section geometry, whereas the latter refer to deviations of the member longitudinal axis from the theoretically straight configuration.

Regarding transverse imperfections, rolled profiles may exhibit thickness variations due to the progressive wear of the rolls, which can lead to irregularities in the dimensions of the different parts of the cross-section. An additional source of transverse imperfection is the lack of perfect orthogonality between the plates forming the section. Longitudinal geometric imperfections mainly appear as out-of-straightness, i.e., deviations of the member axis from its ideal rectilinear position. These irregularities arise from manufacturing processes and may be further exacerbated by erection procedures on site [26]. EN 10219 [27] specifies the technical delivery conditions for cold-formed hollow sections with circular, square and rectangular cross-sections. Tolerances prescribed for square and rectangular hollow sections are summarised in **Table 3** and illustrated in **Fig. 9**.

**Table 3** – EN 10219 [27] tolerances.

| Characteristic | Tolerance |
|---|---|
| External dimensions ($b$ and $h$) | If $h$, $b$ < 100 mm → 1% with a minimum of ±0.5 mm<br>if 100 < $h$, $b$ < 200 mm → 0.8%<br>if $h$, $b$ > 200 mm → 0.6% |
| Thickness ($t$) | If $t$ < 5 mm → ±10%<br>if $t$ > 5 mm → ±0.50 mm |
| Concavity / Convexity | $X_1$ and $X_2$ = 0.8%($h$,$b$),<br>with a minimum of 0.5 mm over the side length |
| Face squareness | θ = 90° ±1° |
| Corner radius profile | If $t$ < 6 mm → $r$ = 1.6$t$ to 2.4$t$<br>If 6 < $t$ < 10 mm → $r$ = 2.0$t$ to 3.0$t$<br>If $t$ > 10 mm → $r$ = 2.4$t$ to 3.6$t$ |
| Twist / warping | $v$ = 2mm plus 0.5 mm per metre of length |
| Straightness | $e$ = 0.15% of the total length |
| Mass ($M$) | ±6% per individual profile |

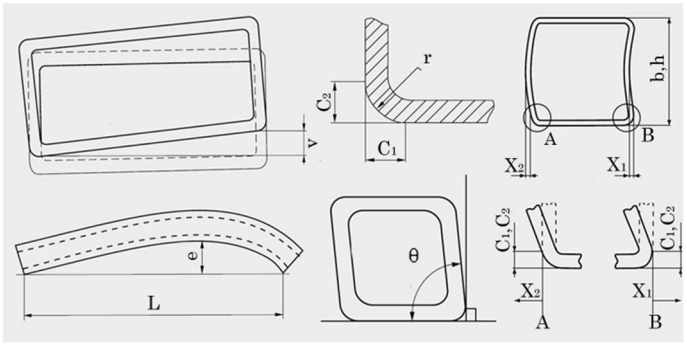


**Fig. 9** – Dimensional and geometrical tolerances according to EN 10219 [27].

Toffolon [28] conducted an extensive measurement campaign on local geometric imperfections in cold-formed hollow sections. The aim was to characterise the as-built geometry of the profiles, since imperfections can markedly influence the structural response by affecting local buckling, plastic behaviour, and ultimate capacity. Prior to scanning, the specimens were thoroughly cleaned to remove surface contaminants that could compromise the measurements. The external surface geometry was then acquired using a Zeiss 3D laser scanner, producing a high-resolution

point cloud of each section. The main outcome of the study is that the highest imperfection amplitudes were consistently observed near the specimen ends, which was attributed to the cutting or welding operations used during fabrication. More generally, larger imperfections tend to concentrate in the corner parts and at the mid-width of the flat parts. For completeness, mean values and standard deviations for selected sections are reported in **Table 4**.

Overall, the geometric imperfections were found to be smaller than the tolerance limits prescribed by EN 10219.

**Table 4** – Concavity/convexity ($X_1$ and $X_2$) measured by Toffolon [28] for SHS and RHS sections.

| Specimen | Mean value [mm] | Standard deviation [mm] |
|---|---|---|
| SHS 140X140X4 | 0.180 | 0.164 |
| SHS 200X200X5 | 0.199 | 0.156 |
| SHS 200X200X8 | 0.432 | 0.433 |
| SHS 200X200X4 | 0.301 | 0.247 |
| SHS 200X200X5 | 0.186 | 0.151 |
| RHS 300X150X6 | 0.273 | 0.294 |
| RHS 300X150X8 | 0.663 | 0.585 |

## 4. Experimental studies on members

Following material characterisation, research efforts reported in the literature have increasingly shifted toward the global response of cold-formed hollow structural members [28]-[35]. Early experimental programmes on cold-formed box-section members primarily addressed stability under monotonic loading [36]-[38]. Subsequent studies progressively extended this scope to include cyclic axial compression, flexural response, and beam–column behaviour under combined axial load and bending [29]-[33]. More recently, experimental investigations have also considered members subjected to biaxial bending in the presence of axial

load, i.e., combined compression and bending about the principal axes [34]-[35].

Cyclic axial compression tests have been mainly aimed at quantifying the deformation capacity of members employed as bracing elements [39]-[41]. For this reason, such tests are not discussed within the present thesis. which focuses on members governed by the combined effects of compression and bending.

### 4.1. Stub column tests

An extensive experimental programme of stub column tests was carried out by Toffolon [28] with the aim of developing dedicated design rules for the verification of slender hollow sections made of mild and high-strength steel. The experimental campaign was performed at the laboratory of the Universität der Bundeswehr München and involved cold-formed square and rectangular hollow sections (SHS and RHS), stiffened hollow sections (SHS-S, SHS-T), and hot-rolled hexagonal sections (HEX) (**Fig. 10**). Two steel grades (S355 and S500) and twelve cross-section geometries were investigated so as to cover all four cross-section slenderness classes defined in Eurocode 3.

The experimental investigation included two main configurations: (i) stub column tests under nominally pure axial compression and (ii) short beam–column tests, in which the load was applied with different eccentricities to reproduce combined compression and bending. All the tests were conducted under displacement control. Target axial displacements ranged between 10 mm and 20 mm for the pure compression tests and between 10 mm and 60 mm for the combined compression–bending tests. Loading was applied at a constant, low rate between 0.01 mm/s and 0.06 mm/s in order to reproduce quasi-static conditions.

Surface strains and rotations were monitored through a digital image correlation (DIC) system.

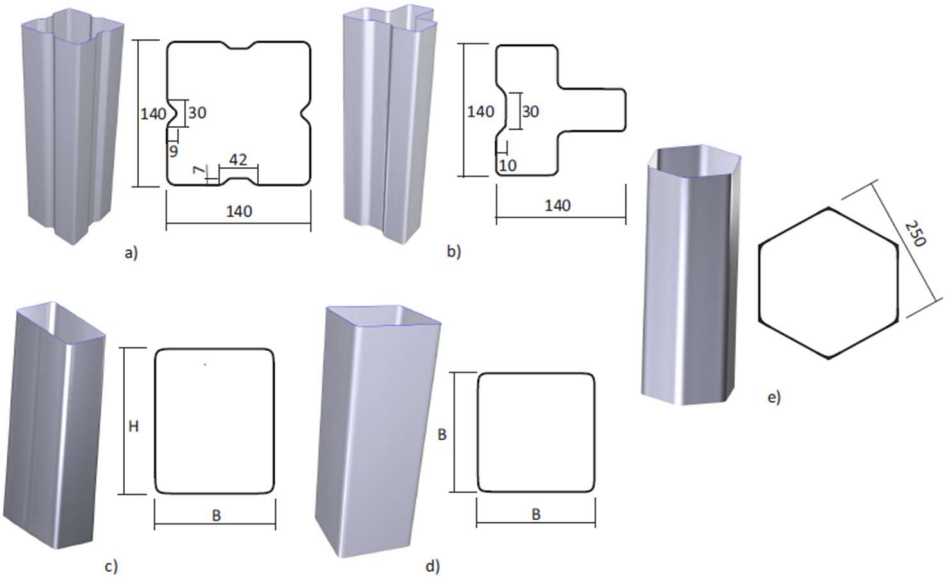


**Fig. 10** – Cross-sections tested [28]: a) SHS-S; b) SHS-T; c) RHS; d) SHS; e) HEX.

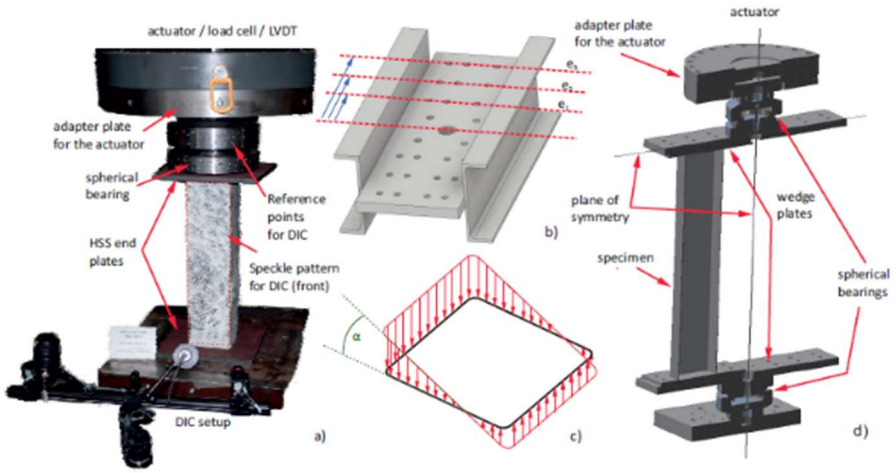


**Fig. 11** – Stub column test setup and loading conditions [28]: (a) stub column test configuration; (b) eccentricity levels; (c) stress field induced in the eccentric compression tests; (d) layout of the eccentric compression tests.

Overall, the experimental programme comprised twelve tensile coupon tests, twelve stub column tests, thirty-six short beam–column tests, and geometric imperfection measurements for each specimen. Tests were grouped into five categories based on loading conditions and specimen length. In the first four categories, local buckling was investigated by progressively increasing the load eccentricity (T1 to T4, **Fig. 11**). Category T1 consisted of pure compression tests. Category T2 featured a small eccentricity at the top end, linearly reducing to zero at the bottom end, thus producing a response still dominated by compression. Category T3 adopted a moderate eccentricity representative of combined axial force and bending moment interaction. Category T4 involved a large eccentricity leading to a condition with virtually no compression, closely resembling major axis bending. Specimens in categories T1–T4 had a length of 800 mm. In addition, category T5 included seven tests designed to explore the interaction between local and global buckling. The loading configuration was equivalent to T3, but the specimen length was increased to 2000 mm.

All tested specimens exhibited local buckling phenomena. As an example, the response of specimen SHS_200×8_S355 is reported in **Fig. 12**. **Table 5** lists the SHS and RHS cross-sections investigated and reports the ultimate loads $N_u$ associated with the onset of local buckling.

In the present thesis, the results from the stub column tests have been used for the validation of a numerical model made on OpenSees. They are discussed in Chapter 5.

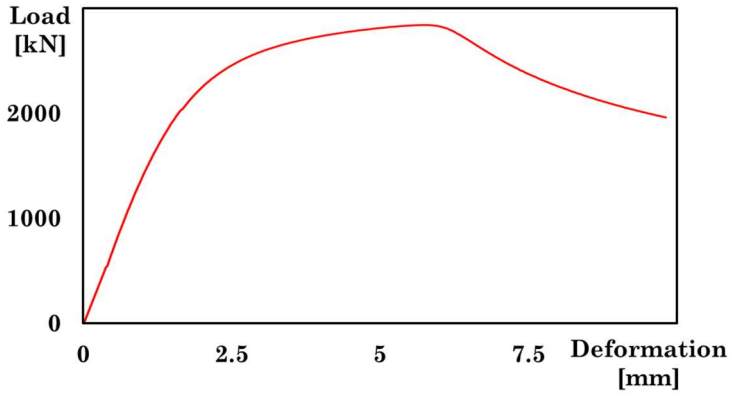


**Fig. 12** – Stub column test response for SHS_200×8_S355 [28].

**Table 5** – Stub column test results for SHS and RHS sections in terms of ultimate load [28].

| Specimen | Steel grade | $N_u$ [kN] |
|---|---|---|
| SHS 140X140X4 | S355 | 861.3 |
| SHS 200X200X5 | S355 | 1227.9 |
| SHS 200X200X8 | S355 | 2917.9 |
| SHS 200X200X4 | S500 | 1111.2 |
| SHS 200X200X5 | S500 | 1736.1 |
| RHS 300X150X6 | S355 | 1482 |
| RHS 300X150X8 | S355 | 2806.8 |

## 4.2. Uniaxial bending test

Current code provisions [42] for evaluating the cyclic rotation capacity of beam–column members are not specifically designed to cold-formed box sections. Furthermore, the rotation capacity of HSS is expected to differ from that of wide-flange members due to a different yield-line pattern and the distinct evolution of local buckling phenomena. Consequently, investigating the cyclic behaviour of cold-formed HSS is essential to clarify key aspects such as the location and extent of the plastic hinge region, as well as the cyclic degradation of strength under seismic-type loading. This research will also contribute to the development of more reliable modelling approaches and appropriate design criteria.

The following section summarises the most recent and relevant findings obtained from experimental programmes carried out using different cyclic loading protocols.

### 4.2.1. D'Aniello et al. (2012)

The study by D'Aniello et al. [30] is relevant to seismic and plastic design of steel structures, as it provides improved criteria for cross-section classification and structural response prediction. The main objective was to calibrate design-oriented relationships for prediction of rotation capacity and flexural overstrength of steel beams. To this end, the ultimate behaviour of HSS was investigated under non-uniform bending.

Two main cross-section typologies were examined: (i) hot-rolled I- and H-sections, and (ii) cold-formed HSS with rectangular and square shape (RHS and SHS). Hot-rolled open sections are generally more prone to lateral–torsional instability and less prone to local buckling than hollow sections. In particular, local buckling may significantly limit the rotation capacity of HSS.

The experimental programme comprised a total of 18 bending tests, including 9 monotonic and 9 cyclic tests. Specimens were selected to investigate the influence of local slenderness of cross-section plates on flexural performance. **Table 6** reports the main geometric properties of the tested members, together with the yield and ultimate strengths of the steels of the flat parts. In particular, the global slenderness $L/b$ and the local plate slenderness ratios $c/t_f$ and $b/t_w$ were provided.

All tests were carried out on cantilever beam specimens, loaded at the free end through a hydraulic actuator. Lateral bracing was also provided so that lateral–torsional instability so prevented and failure was governed by local buckling phenomena. The clear length of the specimens was $L$ = 1875 mm. A set of displacement transducers (LVDTs) and inclinometers was used to measure deformations and rotations in the region where plastic hinges were expected to develop (**Fig. 13**).

**Table 6** – Summary of the properties of the tested HSS sections [30].

| Specimen | $L/b$ [-] | $c/t_f$ [-] | $b/t_w$ [-] | $\sigma_y$ [MPa] | $\sigma_u$ [MPa] |
|---|---|---|---|---|---|
| RHS 150x100x5 | 26.670 | 18.51 | 35.50 | 342 | 377 |
| RHS 160x80x4 | 25.00 | 19.75 | 30.00 | 315 | 346 |
| RHS 250x100x10 | 16.00 | 10.00 | 23.00 | 415 | 500 |
| SHS 160x160x6.3 | 25.00 | 25.64 | 23.40 | 420 | 466 |
| SHS 200x200x10 | 20.00 | 20.4 | 18.00 | 450 | 522 |
| SHS 250x250x8 | 16.00 | 31.25 | 29.25 | 482 | 525 |

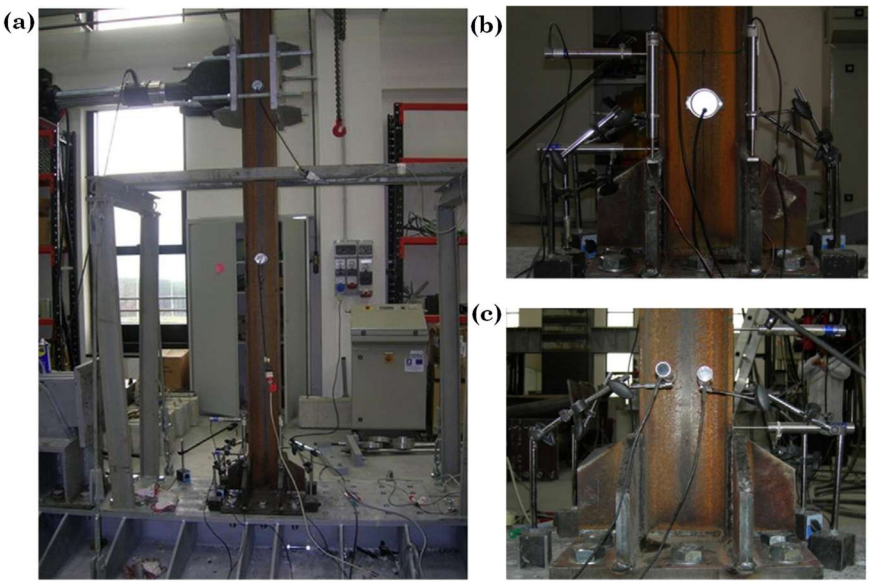


**Fig. 13** – Test setup and instrumentation: (a) test configuration; (b,c) transducer locations [30].

Cyclic tests followed the loading protocol prescribed by AISC (2005), which applies progressively increasing deformation amplitudes and repeats a fixed number of cycles at each displacement level. In particular the displacement level is expressed in terms of chord rotation, which is defined as the ratio of lateral displacement at the tip of a cantilever element to the shear length of the member. For chord rotations exceeding 0.04 rad, the protocol continued with increasing amplitudes (+0.01 rad per step) up to failure. This procedure allowed the researchers to evaluate low-cycle fatigue effects and the progressive degradation of rotation capacity. Monotonic tests were performed under displacement control up to failure of the member. The flexural response of the six HSS specimens is shown in **Fig. 14** and **15** in terms of bending moment and chord rotation.

The cyclic results highlight that rotation capacity and overstrength under cyclic loading are lower than those developed under monotonic loading; in particular, the cyclic rotation capacity may be approximately 60–70% lower than the monotonic one. Cyclic degradation was more pronounced for thin-walled members. Failure was mainly governed by local

buckling of the compressed plates, with no clear evidence of torsional instability.

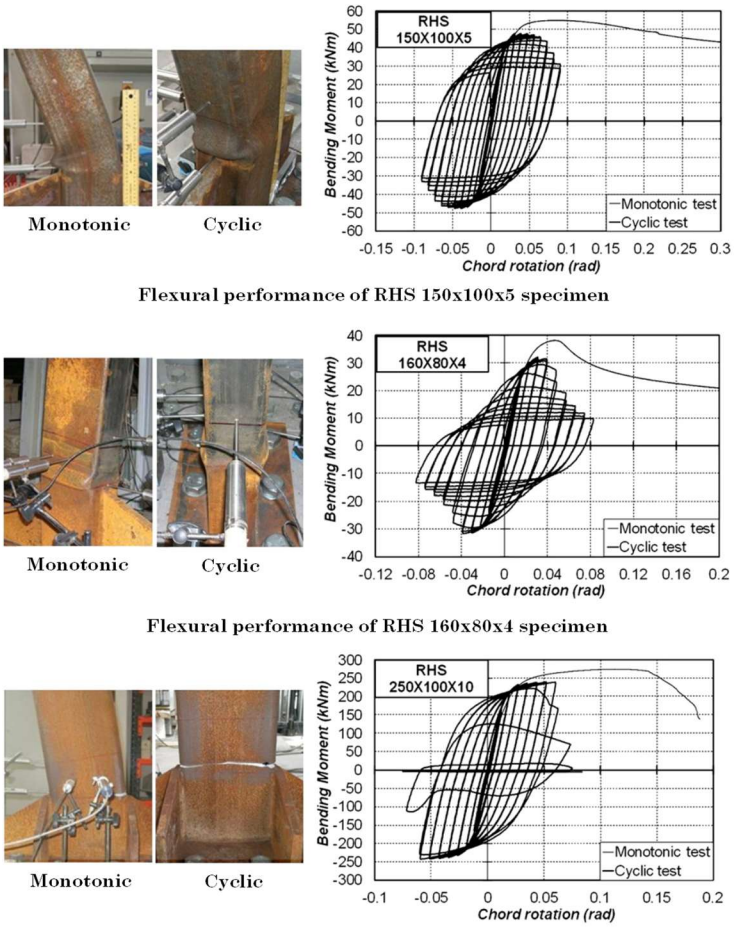


**Fig. 14** – RHS experimental test results [30].

Web instability was amplified by the limited restraint provided by slender flanges. During cyclic loading, progressive crack formation was observed in the transition region between flange and web, attributed to repeated load reversals. The observed collapse mechanisms were characterised by an "elephant-foot" pattern, i.e., a plastic bulging of the compressed wall near the base of the specimen, which accelerated the loss of

the load-carrying capacity and became more evident with the increase of local slenderness. Energy dissipation was also investigated, showing that hollow sections may experience a rapid drop of strength after the first plastic cycle due to progressive localisation of plastic deformations. The experimental evidence indicated that current code criteria may be non-conservative in some cases. On the basis of the experimental database and existing literature, the researchers proposed revised empirical expressions to predict rotation capacity and flexural overstrength under both monotonic and cyclic loading, and validated these formulations against test results.

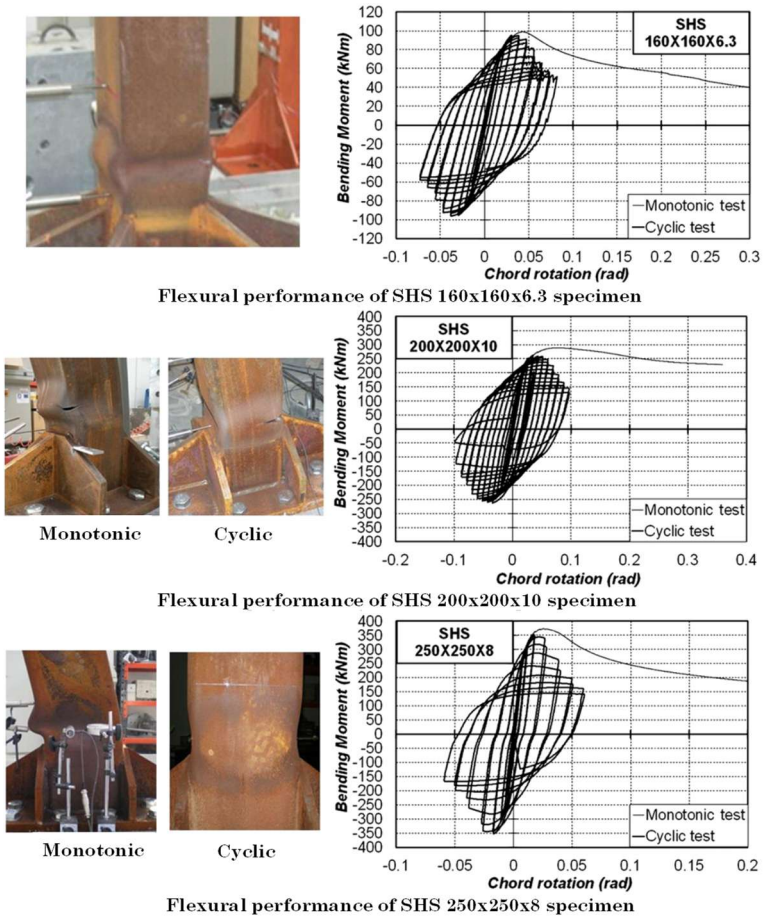


**Fig. 15** – SHS experimental test results [30].

4.2.2. Fadden M. and McCormick J. (2012)

To investigate the flexural behaviour of HSS members under cyclic loading, Fadden and McCormick [31] considered 11 standard American HSS sections manufactured from ASTM A500 Grade B steel. The selected specimens covered a broad range of width-to-thickness and depth-to-thickness ratios, with $b/t$ varying from 8.46 to 31.3 and $h/t$ from 19.9 to 48.5 (**Table 7**). The experimental campaign examined the effects of cyclic loading on strength degradation, rotation capacity, secant stiffness, and energy dissipation up to relatively high rotation demands.

Tests were performed on vertical cantilever specimens, fixed at one end and free at the other. All members had the same length, equal to 1537 mm. To ensure a predominantly flexural response, the load was applied so as to avoid axial forces. In addition, local reinforcement plates were provided to shift plastic deformations away from the clamped region (**Fig. 16**). Displacements were recorded through an infrared optical tracking system, while strain gauges were installed on the flanges at different distances from the support to monitor the progression of yielding along the member length.

**Table 7** – Summary of the properties of the tested HSS sections [31].

| Specimen | $b/t$ [-] | $h/t$ [-] | $\sigma_{y,flat}$ [MPa] | $\sigma_{u,flat}$ [MPa] | $\sigma_{y,corner}$ [MPa] | $\sigma_{u,corner}$ [MPa] |
|---|---|---|---|---|---|---|
| HSS 203.2 x 101.6 x 6.4 | 14.2 | 31.3 | 453.8 | 489.6 | - | - |
| HSS 203.2 x 101.6 x 9.5 | 8.46 | 19.9 | 430.0 | 487.5 | - | - |
| HSS 203.2 x 152.4 x 6.4 | 22.8 | 31.3 | 381.8 | 469.6 | - | - |
| HSS 203.2 x 152.4 x 9.5 | 14.2 | 19.9 | 417.8 | 499.1 | 513.7 | 592.5 |
| HSS 203.2 x 203.2 x 6.4 | 31.3 | 31.3 | 423.3 | 529.1 | 555.9 | 617.0 |
| HSS 203.2 x 203.2 x 9.5 | 19.9 | 19.9 | 425.2 | 481.9 | - | - |
| HSS 254.0 x 101.6 x 6.4 | 14.2 | 39.9 | 434.0 | 505.0 | - | - |
| HSS 254.0 x 152.4 x 6.4 | 22.8 | 39.9 | 379.6 | 457.3 | - | - |
| HSS 254.0 x 203.2 x 6.4 | 31.3 | 39.9 | 406.7 | 495.5 | - | - |
| HSS 304.8 x 101.6 x 6.4 | 14.2 | 48.5 | 391.3 | 469.4 | - | - |
| HSS 304.8 x 152.4 x 6.4 | 22.8 | 48.5 | 422.9 | 491.1 | - | - |

The loading history consisted of cycles with increasing target displacements, intended to emulate a "far-field" earthquake demand.

**Fig. 17** reports the quasi-static displacement-controlled protocol. For each specimen, the chord rotation was computed as the lateral displacement divided by the shear span length, and the maximum imposed rotation was 0.08 rad. In practice, none of the specimens reached the target value: several attained rotations of about 0.07 rad, and all specimens achieved at least 0.05 rad.

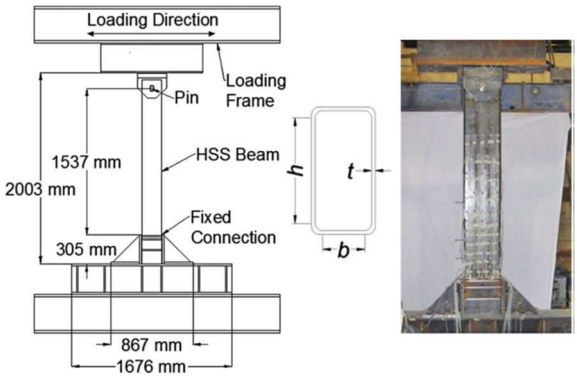


**Fig. 16** – HSS test setup [31]: schematic view and photograph.

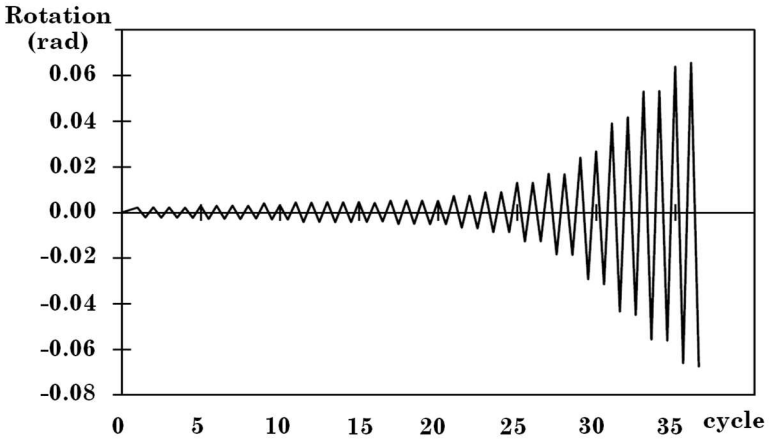


**Fig. 17** – Loading protocol used for the experimental tests.

Among the tested sections, HSS 203.2×203.2×9.5 developed the highest flexural capacity, i.e. 225 kNm, whereas HSS 203.2×101.6×6.4 exhibited the lowest, i.e. 87 kNm. The 9.5 mm-thick specimens showed higher flexural overstrength $s$ (defined as the ratio between the maximum moment and the plastic moment) and reached their peak strength at larger chord rotations than 6.4 mm-thick specimens. Reported overstrength values ranged from 0.90 to 1.28. Sections exhibiting $s < 1.0$ experienced local buckling before the plastic bending moment could be fully developed.

As illustrated in **Fig. 18**, subfigures (a), (c), and (e) present the cyclic responses—expressed in terms of normalised bending moment and chord rotation—for three representative specimens, while subfigures (b), (d), and (f) show the plastic hinge region at the base after testing. The observed cyclic behaviour varied markedly across specimens. For example, HSS 203.2×152.4×9.5 exhibited full hysteresis loops with limited degradation, whereas the 6.4 mm-thick specimens showed a noticeable reduction in flexural strength at higher rotation levels due to local buckling and progressive deterioration.

All HSS specimens displayed a stable hysteretic response during the initial cycles. The largest percentage drop in bending moment typically occurred between the first and the second cycle after reaching the maximum moment, particularly for sections with higher $b/t$ and $h/t$. This reduction remained below 5% for all 9.5 mm-thick specimens, while for HSS 254×203.2×6.4 it ranged between 10% and 15%, and for HSS 304.8×152.4×6.4 strength losses up to 19% were observed. Based on these results, the researchers suggested that $b/t < 25$ and $h/t < 40$ should be required to ensure at least 90% of the maximum bending moment at a chord rotation of 0.04 rad. In all cases, secant stiffness decreased as rotation demand increased, with the three 9.5 mm-thick specimens showing the most stable overall behaviour.

In conclusion, box-section members exhibited a strong capacity to dissipate energy through stable hysteresis, provided that width-to-thickness and depth-to-thickness ratios were adequately limited to mitigate the onset and progression of local buckling.

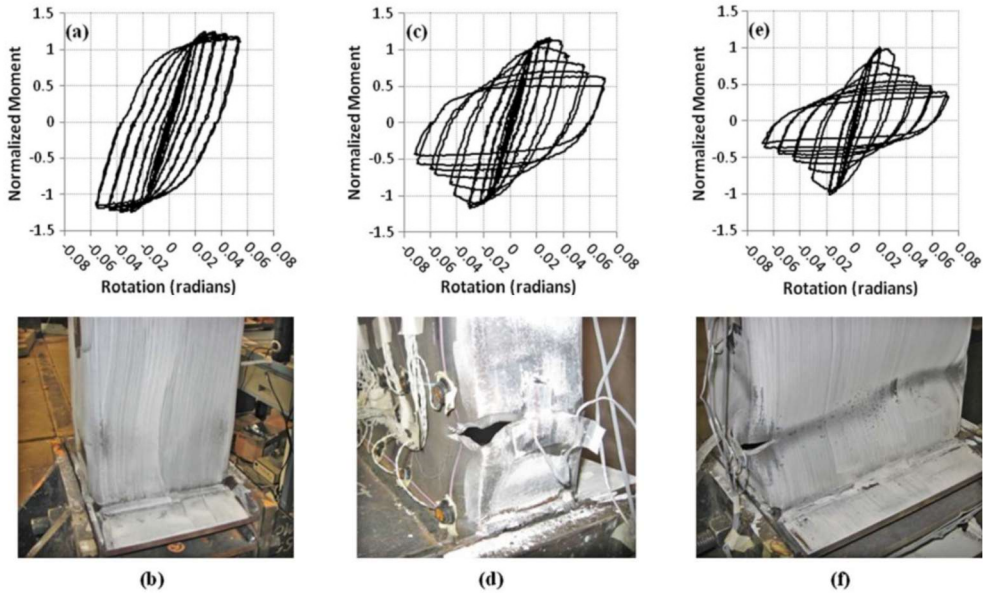


**Fig. 18** – Normalized moment–rotation hysteresis curves and test photographs for HSS specimens [31]: (a,b) HSS 203.2 × 152.4 × 9.5 mm; (c,d) HSS 254 × 101.6 × 6.4 mm; (e,f) HSS 304.8 × 152.4 × 6.4 mm.

4.2.3. Bai Y. et al. (2015)

In steel buildings, local buckling of structural members can play a decisive role in the progression toward collapse. Local buckling in HSS columns leads to a reduction in member stiffness and strength, thereby undermining load-carrying capacity. After buckling occurs, a progressive axial shortening of the column may develop, which can increase the axial demand and further accelerate structural deterioration.

Bai et al. [32] carried out an experimental programme on HSS columns subjected to cyclic lateral loading under constant axial force. The primary goal was to investigate the post-buckling behaviour, focusing on strength and stiffness degradation and, in particular, on the axial shortening that develops after plastic deformation and subsequent local buckling.

The tested members were square HSS columns with outer width $b$ = 200 mm and a height of approximately 1200 mm. To examine the influence of local slenderness, three wall thicknesses were selected: $t$ = 6, 9, and 12 mm, corresponding to $b/t$ ratios of 33, 22, and 17, respectively.

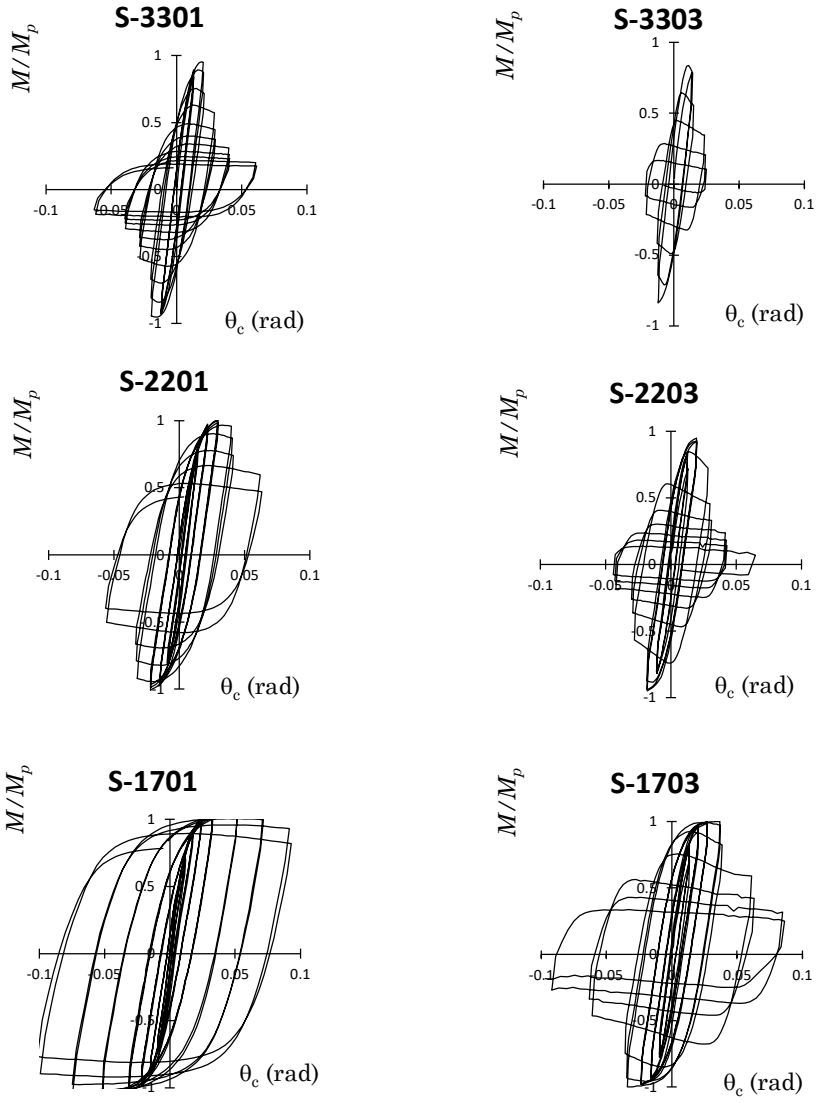


**Fig. 19** – Normalized moment–rotation response [32].

A symmetric, displacement-controlled cyclic protocol with increasing amplitude was adopted, pushing the specimens to large deformation levels, up to 8–10 times the yield rotation. To assess the influence of axial load on the lateral resistance, two constant axial load ratios were applied, namely $N/N_{pl} = 0.1$ and 0.3.

The bending moment–rotation responses show a progressive loss of load-carrying capacity after the onset of local buckling (**Fig. 19**). The initial strength deterioration occurred at a rotation of about 0.04 rad for both axial load levels. Strength degradation was more pronounced for specimens with $N/N_{pl} = 0.3$, confirming that higher axial load accelerates loss of resistance. Specimen S1703 reached structural collapse at a rotation of 0.06 rad, losing its ability to sustain the acting axial force.

Axial shortening after local buckling was also examined. After buckling initiation, the deformed steel plates at the member ends may come into contact, triggering an acceleration of axial shortening (**Fig. 20**). **Fig. 21** presents the bending moment–axial shortening response for the specimen with $b/t = 33$, highlighting a marked increase in axial contraction following the onset of local buckling. In this case, an axial load ratio of 0.3 further accelerated resistance degradation.

**Fig. 20** – Local buckling at the fixed-end section [32].

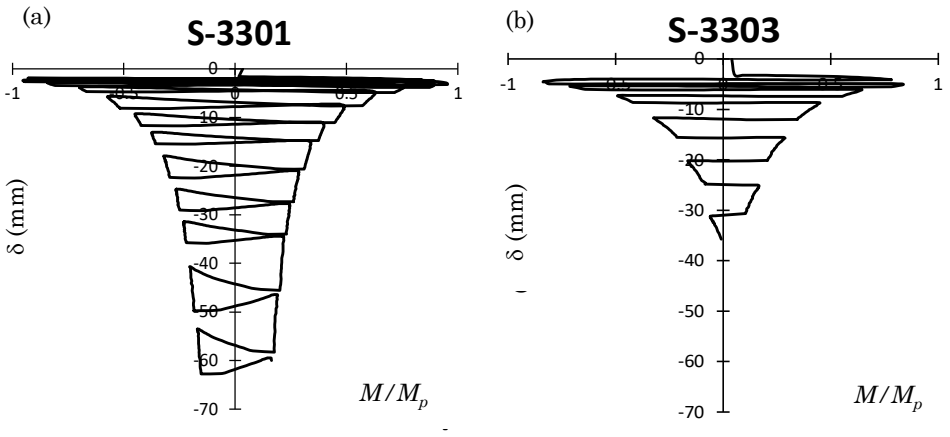


**Fig. 21** – Normalized moment–axial shortening response with different values of axial load ratio [32]: (a) $N/N_{pl} = 0.1$; (b) $N/N_{pl} = 0.3$.

The experimental results confirm that higher axial load ratios lead to faster strength deterioration after local buckling. The observations also underline the strong influence of local slenderness: columns with $b/t = 33$ experienced a more rapid and severe degradation, accompanied by substantial axial shortening. Plastic deformations concentrated near the member ends, and for specimens under higher axial load, the interaction between deformed plates contributed to an accelerated collapse mechanism.

4.2.4. Suzuky Y. e Lignos D.G. (2021)

Most studies available in the literature rely on quasi-static tests with symmetric loading protocols. These protocols may not faithfully reproduce the actual collapse conditions of steel structures during seismic events, with the potential consequence of underestimating deformation capacity. The experimental programme by Suzuki and Lignos [33] investigates the behaviour of steel columns subjected to cyclic demands representative of earthquakes, with specific attention to loading histories consistent with seismic hazard.

A total of 21 tests were carried out on steel columns with wide-flange and hollow cross-sections. The specimens were fabricated according to

North American and Japanese standards, using A992 Grade 50 steel with nominal yield strength $f_y$ = 345 MPa for wide-flange members, and ASTM A500 Grade B steel with $f_y$ = 315 MPa for HSS members.

The tested HSS columns had cross-sections 254x9.5 mm and 305x16 mm, corresponding to $b/t$ ratios of 27 and 19, respectively. Nine loading tests were performed using different loading protocols. Both constant and variable axial load conditions were considered to simulate the behaviour of columns in moment-resisting frames. The columns were tested in a cantilever configuration. The base was anchored to a 76 mm thick steel plate connected to the laboratory floor through twelve ASTM A490 high-strength bolts, ensuring rigid boundary conditions (**Fig. 22**). The top end was connected to a loading plate.

Damage evolution and structural response were monitored through extensive instrumentation. Local strains and the development of local buckling were captured using 27 strain gauges distributed over three levels along the column. Displacement transducers (LVDTs) were used to measure axial shortening and lateral drift, while inclinometers and LED tracking were employed to monitor local instabilities and out-of-plane displacements (**Fig. 23**). The acquired data enabled a direct correlation between the progression of instability and the global response, and allowed quantification of stiffness and strength degradation as a function of the loading history.

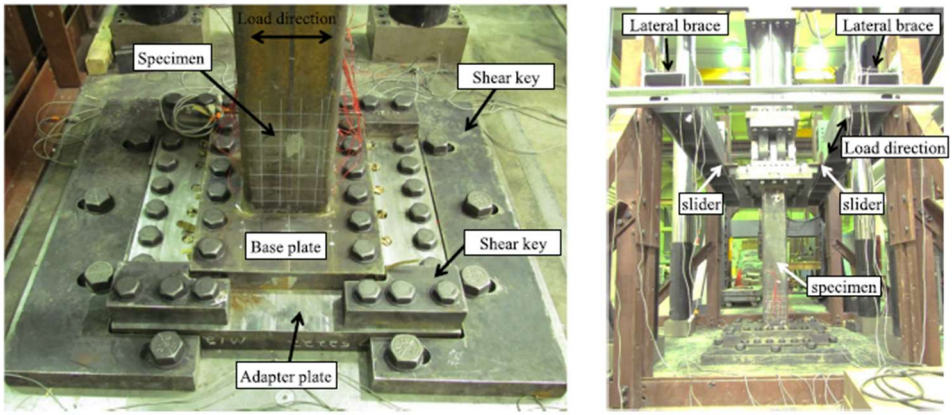


**Fig. 22** – Anchorage plate and test setup [33].

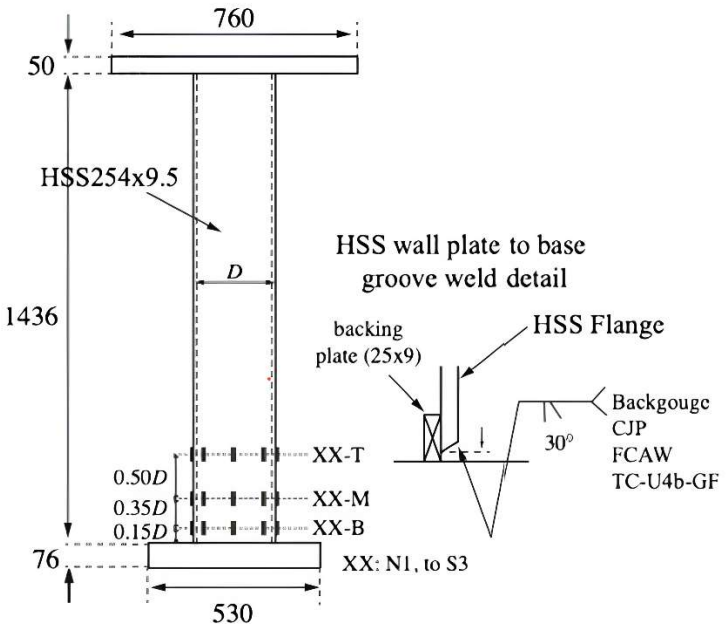


**Fig. 23** – Test specimen details and strain-gauge layout [33].

The specimens were subjected to one monotonic protocol and three cyclic protocols: (i) a standard symmetric cyclic protocol (SAC 2000), characterised by progressively increasing displacement amplitudes; (ii) a near-fault-consistent protocol, representative of earthquakes dominated by pulse-type demands; and (iii) a long-duration-consistent protocol, associated with higher cumulative energy dissipation prior to collapse. The axial load was applied with either a constant value $N/N_{pl} = -0.30$, representative of the axial load ratio in interior columns, or with a variable axial load ratio $N/N_{pl}$ ranging between 0.20 and −0.50, representative of exterior columns.

The experimental investigation of the HSS specimens provided several key insights into their seismic-response characteristics up to collapse. For the HSS 254x9.5 mm section ($b/t = 27$), the dominant instability mode was first-mode local buckling, which led to a rapid loss of strength. Collapse was associated with a sudden failure mechanism, including fracture at stress concentration regions located at the section

corners. For the HSS 305x16 mm section ($b/t$ = 19), local buckling developed more gradually, with the formation of so-called elephant-foot buckling. This response provided a greater energy dissipation capacity prior to strength loss, with a more progressive damage evolution and without immediate fracture.

Axial load significantly influenced the response. Under constant axial compression, columns exhibited larger axial shortening, with more pronounced effects in the slenderer sections. Under variable axial load, the presence of tensile axial force components during load reversals temporarily stabilised the local buckling response, delaying the loss of capacity and increasing the rotation capacity.

**Fig. 24** reports the bending moment–rotation relationships for the HSS columns, comparing symmetric cyclic loading, near-fault-consistent collapse protocols, and long-duration protocols. HSS columns subjected to the near-fault protocol (left figure) developed a markedly higher rotation capacity, with collapse rotations up to 2.5 times those measured under the symmetric cyclic protocol, while the peak strength remained broadly comparable. Strength deterioration was more gradual under near-fault loading, whereas the symmetric cyclic protocol produced a faster loss of load-carrying capacity and a greater reduction in the peak bending moment. The near-fault tests also showed a delayed onset of local buckling, indicating that the loading history affects not only the rotation capacity but also damage progression.

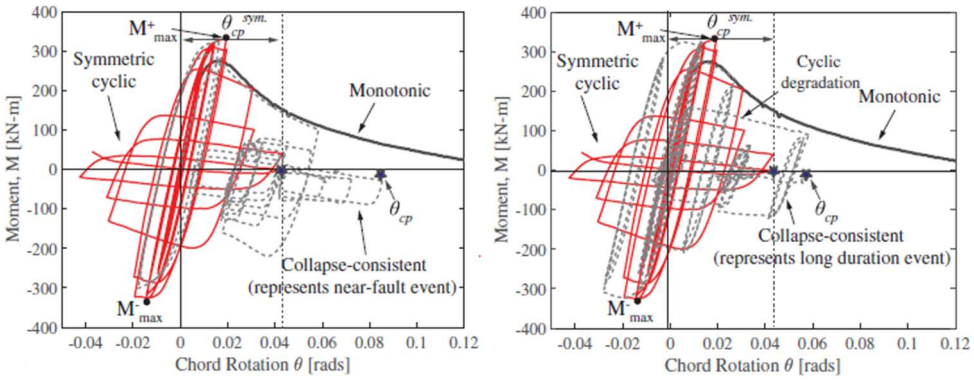


**Fig. 24** – Moment–rotation curves for different loading protocols [33].

Columns tested under long-duration protocols (dashed grey line in the right figure) exhibited a rotation capacity slightly higher than that obtained with the symmetric cyclic protocol. However, the corresponding strength deterioration was significantly more gradual, suggesting that collapse under long-duration earthquakes is driven primarily by the progressive accumulation of plastic damage rather than by a sudden loss of resistance. In addition, the long-duration protocol promoted a more distributed damage development along the column height, whereas under symmetric cyclic loading damage tended to localise early and rapidly around the local-buckling region.

The comparison suggests that standard symmetric cyclic protocols may underestimate column deformation capacity under realistic seismic demands. In addition, near-fault-type loading histories allowed HSS columns to reach substantially larger rotations prior to collapse, indicating that current acceptance criteria may be conservative for such events. These observations are relevant for improving seismic design practice and for refining code-based acceptance criteria for HSS columns by accounting for the earthquake characteristics.

### 4.3. Biaxial bending test

In seismic-resistant moment frames, column demands are rarely confined to a single bending plane. Floor diaphragms and the simultaneous action of horizontal components can induce axial forces combined with biaxial bending, so the critical response may develop along an inclined bending direction rather than a principal axis. For cold-formed HSS members, this loading condition can alter the spread of inelasticity and the progression of local buckling compared with uniaxial bending. The following experimental studies thus focus on beam–column behaviour under biaxial bending, providing evidence that supports a more representative assessment of strength degradation and deformation capacity under earthquake-type actions.

4.3.1. Ishida T. et al. (2012)

Ishida et al. [34] investigated the biaxial bending response of square hollow section (SHS) steel columns. The experimental programme aimed to quantify the influence of cyclic biaxial loading on the structural response, with particular emphasis on the role of the horizontal loading direction in strength deterioration.

The specimens were SHS columns 200 × 9 mm made of BCR295 steel, with a width-to-thickness ratio of 22.2 and a total length of 1734 mm. Steel end plates were welded at both ends to ensure an adequate connection to the loading system. The test setup comprised one horizontal actuator and two vertical actuators, allowing the simultaneous application of a constant axial load and biaxial bending. To generate biaxial bending moments, the loading frame was laterally restrained so as to reproduce realistic loading conditions representative of seismic actions (**Fig. 25**).

The horizontal cyclic loading history was imposed under displacement control, targeting representative demand for columns subjected to biaxial bending under constant axial force. The loading sequence was defined in terms of the parameter $\theta_{pc0}$ and consisted of progressively increasing amplitudes equal to $2\theta_{pc0}$, where $\theta_{pc0}$ denotes the elastic rotation associated with the plastic bending moment $M_{pc0}$ under pure bending.

The key variable was the angle of application of the horizontal load. Four directions were considered: 0, 15, 30, and 45 degrees with respect to the principal axis of the column cross-section. In addition, for each loading direction, two axial load ratios were examined, namely 0.2 and 0.4. The tested configurations are summarised in **Fig. 26**.

The experimental results indicate that the response of RHS columns under biaxial bending is strongly affected by both the horizontal loading direction and the axial load ratio. **Fig. 27** presents the bending moment–rotation curves for each specimen, normalised by the plastic bending moment $M_{pc0}$ and the corresponding plastic rotation $\theta_{pc0}$.

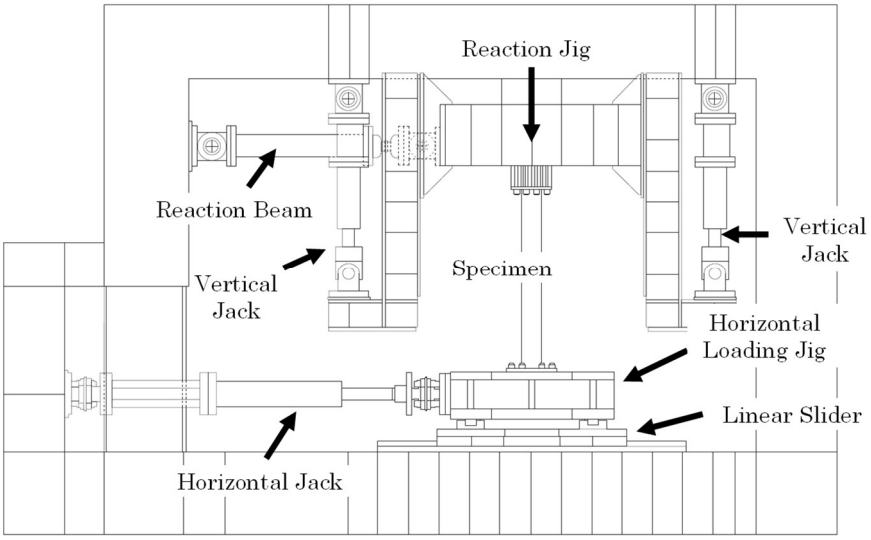


**Fig. 25** – Experimental test configuration [34].

| **Specimen Name** | **C00_0.2** | **C00_0.4** | **C15_0.2** | **C15_0.4** |
|---|---|---|---|---|
| **Axial Force Ratio** | **0.2** | **0.4** | **0.2** | **0.4** |
| **Material No.** | **(1)** | **(1)** | **(2)** | **(2)** |
| **Loading Direction** | 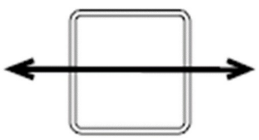 **0 [Deg]** | | 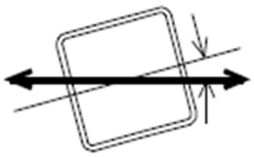 **15 [Deg]** | |
| **Specimen Name** | **C00_0.2** | **C00_0.4** | **C15_0.2** | **C15_0.4** |
| **Axial Force Ratio** | **0.2** | **0.4** | **0.2** | **0.4** |
| **Material No.** | **(1)** | **(1)** | **(2)** | **(2)** |
| **Loading Direction** | 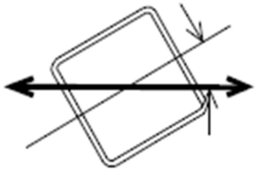 **30 [Deg]** | | 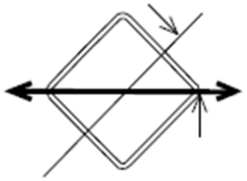 **45 [Deg]** | |

**Fig. 26** – Specimens tested [34].

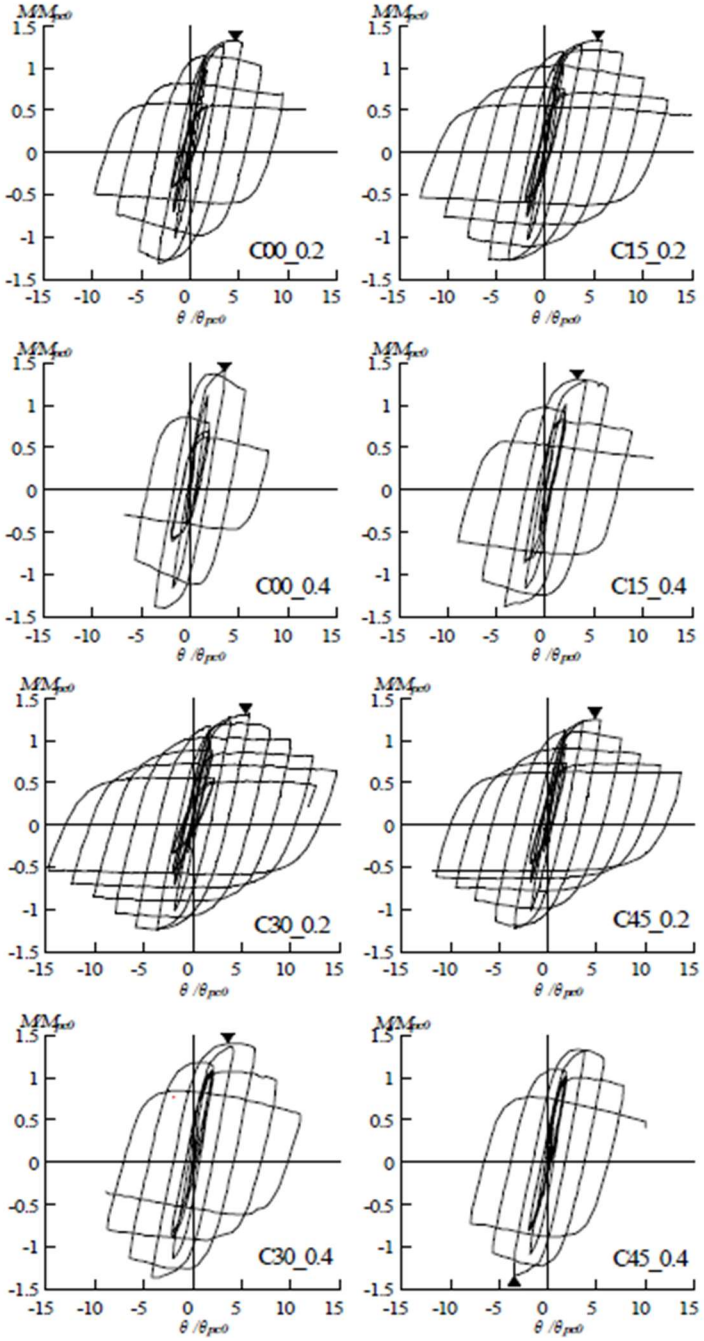


**Fig. 27** – Section responses in terms of moment–rotation [34].

For all specimens, the peak strength was governed by local buckling. Columns loaded along a principal axis (0 degrees) exhibited a faster strength deterioration than those loaded along inclined directions. Specimens subjected to inclined loading showed a higher post-buckling strength, suggesting that the corner parts help restrain the propagation of local buckling. Overall, the loading direction was found to influence both the development of local buckling and the energy dissipation capacity.

**Fig. 28** reports the responses in terms of vertical displacement and normalised cumulative chord rotation. Vertical displacements increased as a consequence of progressively localised plastic deformations developing in the flat parts of the cross-section after local buckling. Columns loaded along a principal axis experienced substantially larger vertical displacements than those loaded along inclined directions. This behaviour was attributed to the more rapid development of local plastic deformations under principal-axis loading, whereas, under diagonal loading, the corner parts contributed to limiting local buckling propagation, thereby reducing the associated vertical deformation.

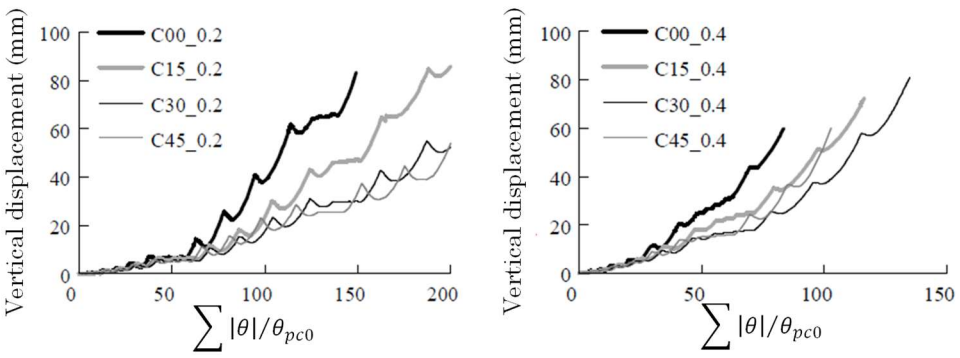


**Fig. 28** – Vertical displacement–cumulative strain relationship [34].

### 4.3.2. Mukaide et al. (2016)

Hollow structural section columns are widely used in steel construction in Japan. For this reason, Mukaide et al. [35] performed an experimental campaign to investigate the strength deterioration of box-section columns

subjected to severe deformation demands, explicitly accounting for differences associated with manufacturing methods.

Nine rectangular hollow-section configurations were tested under pure bending, combined axial load and bending, and biaxial bending, for a total of 25 specimens. Three different steels were employed depending on the fabrication method: BCR295 for roll-formed (cold-rolled) sections, SN490B for welded built-up sections, and a steel equivalent to BCP325 for press-formed (cold-pressed) sections obtained by cold-pressing SN490B plates with an inside corner radius equal to $3.5t$. All columns had a square hollow cross-section with an outer width $b$ = 300 mm and a length $L$ = 1640 mm ($L/b$ = 5.5). Local slenderness was varied by adopting three width-to-thickness ratios, i.e. $b/t$ = 19, 25, and 33.

To characterise the mechanical properties of the materials used in the columns, tensile coupon tests were carried out on specimens extracted from both the flat parts and the corner parts of the cross-section. These tests highlighted variations in yield strength depending on the manufacturing method. As an example, the ratio between $f_u/f_y$ varied between 1.05 and 1.2 for the specimens realized with the continuous forming method, and between 1.35 and 1.6 for the specimens realized with the direct forming method.

Differences among the materials were also associated with residual stresses induced by fabrication processes. Initial geometric imperfections were measured as well, given their potential influence on the onset and development of local buckling.

The experimental set-up consisted of a vertical cantilever configuration. Axial force and bending moments were applied simultaneously through hydraulic jacks. A constant axial load normalised with respect to the plastic axial resistance $N_{pl}$ was applied, with $n = N/N_{pl}$ = 0 or 0.25. For some specimens, the load was applied with a 45° inclination, i.e., along the diagonal of the cross-section. Both symmetric and asymmetric cyclic loading protocols were employed to represent progressive-collapse-type scenarios (**Fig. 29**). In addition, monotonic tests with increasing demand were conducted up to failure.

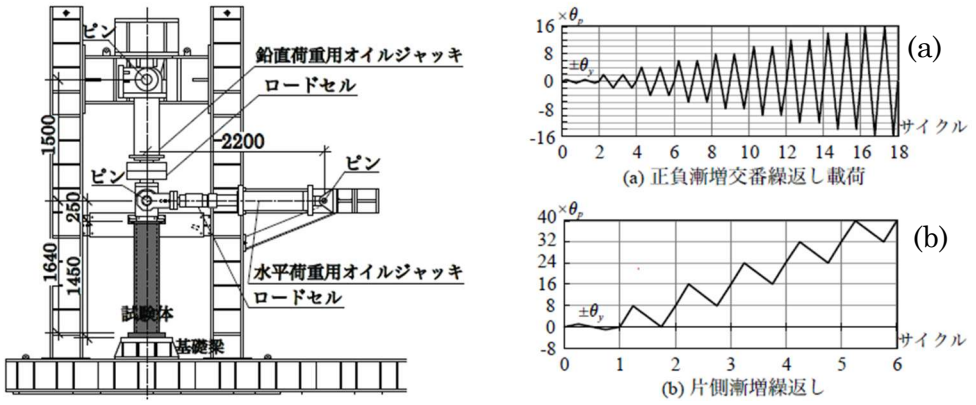


**Fig. 29** – Test configuration and loading protocols [35]: (a) symmetric loading protocol; (b) asymmetric loading protocol.

The experimental responses are presented in the figures in terms of bending moment versus rotation. In the plots, the letter P identifies press-formed sections, R roll-formed sections, and B welded built-up sections. The specimen designation also includes the selected $b/t$ ratio, the axial load level, and the loading direction. For example, specimen P1925-45 corresponds to a press-formed section with $b/t$ = 19, subjected to $n$ = 0.25, with loading applied at 45°.

Under monotonic loading (**Fig. 30**), all specimens, except P1925-45, exhibited a strength reduction associated with local buckling. Columns with $b/t$ = 19 developed an increase in resistance, accompanied by significant plastic deformation, before local buckling developed. In contrast, for $b/t$ = 25 and 33, local buckling occurred before the section could develop noticeable overstrength, resulting in a more pronounced and premature loss of resistance. The presence of axial load reduced the bending resistance and accelerated degradation. Overall, the comparison highlights a clear influence of the fabrication method on the observed behaviour.

Applying the load at 45° resulted in a slightly higher maximum bending moment than tests loaded at 0°. Local buckling developed at larger deformation levels, which was attributed to a more uniform distribution of demand among the section walls.

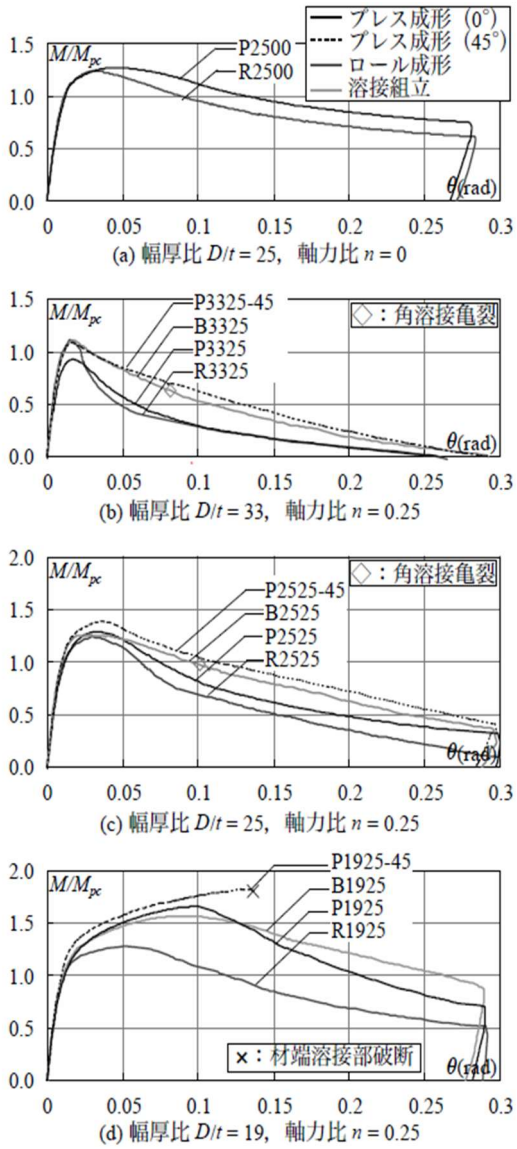


**Fig. 30** – Experimental bending moment–rotation responses under monotonic loading [35].

For symmetric cyclic loading, local buckling was identified as the dominant mechanism governing strength deterioration, with the rate of degradation strongly influenced by local slenderness. Two distinct trends were observed: at $n$ = 0, resistance decreased progressively with

increasing cycles; in contrast, with axial load ($n$ = 0.25) the response exhibited a much more rapid drop between successive cycles, particularly as local slenderness increased (**Fig. 31**). The reported collapse modes included fracture at welded joints and plastic collapse in the roll-formed and press-formed sections (**Fig. 32**).

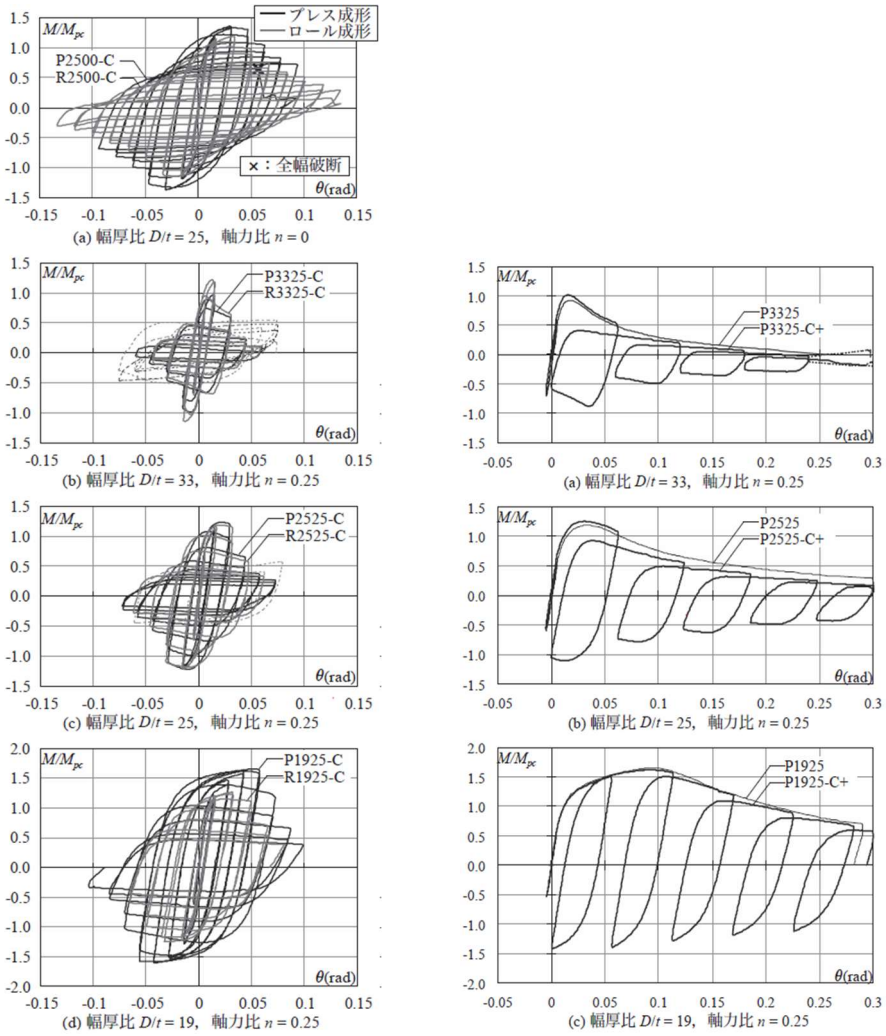


**Fig. 31** – Experimental bending moment–rotation responses under cyclic loading [35]: symmetric protocol (right) and asymmetric protocol (left).

Responses under asymmetric cyclic loading showed that specimens with $b/t$ = 33 experienced a rapid cycle-by-cycle loss of resistance up to failure. Specimens with $b/t$ = 25 showed a more stable response prior to the final strength drop. Press-formed columns with $b/t$ = 19 exhibited a highly variable cyclic response, including a possible partial recovery of strength before final collapse.

The initial resistance was higher in press-formed specimens than in roll-formed columns. Press-formed specimens also developed larger plastic deformations before local buckling and exhibited a more stable cyclic response. Nevertheless, for higher $b/t$ ratios, strength deterioration remained significant regardless of the fabrication method.

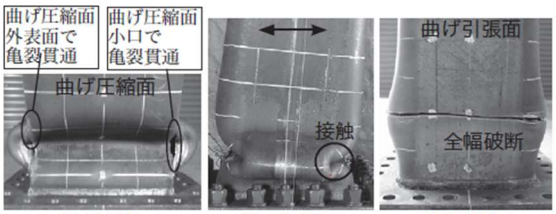


**Fig. 32** – Failure modes for the different cross-sections [35].

## 5. Numerical model proposed in literature

Over the last decades, several numerical strategies have been developed to incorporate damage-related effects in steel members, each characterised by specific advantages and limitations. Finite element (FE) approaches can reproduce instability modes with high fidelity, typically through shell-element modelling [43]-[45]. However, these models become computationally demanding when applied to large-scale structural analyses.

More computationally efficient modelling frameworks rely on one-dimensional members with fibre-discretised sections, in which the degradation in strength and stiffness is captured either by reducing the effective cross-sectional area or by adopting constitutive material models that distinguish between tensile and compressive response. In addition,

concentrated plasticity formulations based on spring models are available to represent post-buckling behaviour. Although these models can capture stiffness and strength deterioration, they do not explicitly represent the evolution of deformation along the member.

Three distinct modelling methods are identified in the literature.

The first modelling approach [46] suggests diminishing the effective area of the cross-section by utilizing beam elements with finite length ending hinges. In this method, I-shaped cross-sections are discretized into fibres, and a fatigue material is applied to the base steel material. To replicate the progressive reduction in cross-sectional stiffness and strength resulting from flange buckling, failure of the single fibre is identified through the Coffin and Manson [47], [48] model. The strain value at which a single cycle leads to failure varies linearly across the width of the flange. Specifically, a minimum value $\varepsilon_{0,min}$ is assigned to the fibres located at the flange tips, while a maximum value ($\varepsilon_{0,min} + \Delta_{\varepsilon 0}$) is assigned to the fibres situated at the web-to-flange intersection. Predictive equations for $\varepsilon_{0,min}$ and ($\varepsilon_{0,min} + \Delta_{\varepsilon 0}$) have been introduced through calibration against results of laboratory experiments conducted on I-shaped elements [49]-[54].

The second strategy [55], [56] examines material models with different behaviour in tension and compression. The constitutive law [56] that models the monotonic response under compression assumes the presence of elastic, post-yield, and post-buckling regions. The ratios of capping to yield stress, capping to yield strain, post-capping stiffness to elastic modulus, and post-capping to capping stress are determined through regression analysis. The values of the aforementioned parameters are updated throughout the cyclic response in accordance with the inelastic damage mechanism.

The third strategy (referred to as the modified Ibarra-Krawinkler model) involves the incorporation of zero-length rotational springs with cyclic flexural stiffness and strength degradation at the beam element ends, as initially suggested by Ibarra et al. [57] and later modified by Lignos and Krawinkler [58]. This model is commonly employed in most research studies focusing on the response of steel moment resisting frames [59], [60]. The model was initially calibrated using the results of

beam with W-cross-section [61] and later extended to simulate the cyclic behaviour of columns [62]. This approach has also been utilized to predict the cyclic behaviour of square hollow steel columns [63]. However, the available equations were formulated specifically to estimate only the deformation-related parameters of the adapted Ibarra–Krawinkler model.

## 6. Motivation and objectives of the research.

The growing interest in cold-formed HSS among engineers, steel producers, and researchers motivates the investigation of their suitability in seismic applications. Although columns in moment-resisting frames are generally intended to remain essentially non-dissipative under capacity-design principles, the evaluation of their deformation capacity and cyclic response is still relevant. This is particularly true for column bases, which may act as dissipative regions, and for members subjected to axial load levels within the range for which Eurocode-based seismic design still admits ductile flexural behaviour [42]. An accurate estimate of the deformation capacity and numerical representation of their cyclic response is therefore essential, particularly to capture cumulative damage mechanisms associated with plastic local buckling.

Despite the widespread use of cold-formed HSS, current code provisions remain limited and are not fully tailored to their specific cyclic response. In the current Eurocodes, for instance, rotation-capacity limits are largely aligned with those adopted for I- and H-shaped members, and they are typically provided only for axial load ratios up to 0.3, with rotation demands assumed to be essentially independent of the axial load ratio within this range. The forthcoming version of Eurocode 8 introduces specific provisions for HSS columns, but the proposed limits depend primarily on the axial load ratio (up to 0.5) and on the depth-to-thickness ratio ($b/t$).

However, Eurocodes' provisions concern columns subjected solely to uniaxial bending, ignoring the influence of biaxial bending on the chord rotation capacity. Moreover, previous studies indicate that the cyclic response of HSS members may be strongly influenced by additional

geometric and mechanical parameters, suggesting that a broader and more detailed framework is needed for both assessment and design.

The manufacturing method is an additional aspect that affects the response of cold-formed HSS and should be explicitly considered in research and modelling.

Within this context, the present research focuses on HSS members used as beams and columns in moment-resisting frames. In this project, the HSS members are produced through a direct forming process, in which a steel strip is roll-formed into an open rectangular shape and then closed by welding. Compared with hot-rolled products, this process typically leads to higher strength and hardness, while also introducing residual stresses in both corner parts and flat parts of the section.

Regarding these members, engineers must be able to estimate overstrength and rotation capacity, particularly under combined axial load, and reliably simulate cyclic response under biaxial bending. To address these needs, the work develops a set of practical tools aimed at combining accuracy with usability in engineering practice. Specifically, it provides: (i) a finite element model of a cantilever configuration, developed to reproduce the cyclic response of columns under axial load and biaxial bending and validated against results of laboratory tests; (ii) a database of cyclic responses determined by parametric analyses on columns and beams subjected to uniaxial and biaxial bending, generated using the finite element model; (iii) chord rotation domains to estimate the rotation capacity of HSS members under biaxial bending and axial load ratio not exceeding 0.5, proposed as an alternative to the provisions in the forthcoming Eurocode 8 at both the Near Collapse (NC) and Significant Damage (SD) limit states; and (iv) two simplified numerical models implemented in OpenSees and validated against the numerical database and available laboratory tests.

The two simplified models are designed to cover complementary needs. The first targets HSS members under uniaxial bending and relies on zero-length rotational springs to provide a computationally efficient representation of cyclic behaviour. The second is intended to simulate the combined effects of axial load and biaxial bending through a distributed-plasticity formulation with a fibre-based section. Taken together, these

outputs aim to support a more accurate and practical evaluation of the seismic performance of steel buildings employing cold-formed HSS members, bridging the gap between detailed finite element simulations and tools suitable for routine engineering use.

# Chapter 2
# FINITE ELEMENT MODEL IN ABAQUS

Chapter 2 presents the finite element model adopted in this thesis, clearly distinguishing between the reference modelling framework taken from the literature and the additional validation work carried out in the present study. Section 1 summarises the Abaqus model originally developed by Bosco et al. [44], including its general modelling strategy, the material properties assigned to the flat and corner regions of the cross-section, and the mesh sensitivity analysis performed to define an appropriate discretisation. The following sections report original validation studies performed as part of this thesis. In particular, Section 2 validates the model against the stub-column tests by Toffolon [28]. Section 3 presents an additional validation under uniaxial bending with reference to the experimental tests by Fadden and McCormick ([31], [45]). Finally, Section 4 investigates the influence of geometric imperfections and validates the model under biaxial bending against the tests by Ishida et al. [34].

## 1. General features of the FE model

With the aim of carrying out a campaign of parametric analyses on columns and beams subjected to axial load and biaxial bending, a finite element model was developed in Abaqus. The model is based on the work of Bosco et al. [44] and uses a cantilever configuration, which is adopted for all analysed members.

To reduce the computational effort, the numerical model is divided into two parts (see **Fig. 33**). The first part, hereafter referred to as the plastic region, is modelled with 3D solid elements and extends from the fully restrained end of the member to a distance equal to twice the section depth. Based on a sensitivity analysis, second-order (quadratic) reduced-integration hexahedral elements (C3D20R) were selected. The second part, referred to as the elastic region, is modelled using elastic quadratic beam elements (B32). The cross-sectional properties (e.g., area and second moments of area) are consistent with those adopted for the plastic region. Likewise, the Young's modulus and Poisson's ratio are taken equal to those used in the plastic region. The maximum finite element size in this region is 50 mm.

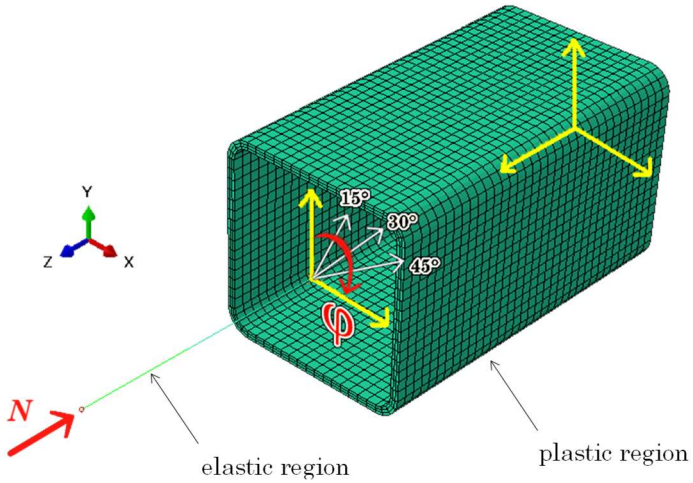


**Fig. 33** – Numerical model used.

The elastic region is connected to the plastic region through a beam-type multi-point constraint (MPC). Its free end is used to apply the loading protocol and the axial force. When the cantilever is not subjected to biaxial bending, the displacement along the x-direction of the tip of the cantilever is restrained to prevent out-of-plane displacements.

### 1.1. Cross-section and material properties

The cross-section of the plastic region consists of flat and corner parts. To reproduce the effects of the cold-forming process, different material properties are assigned to the flat and corner parts. For both parts, the material behaviour is modelled using a combined isotropic–kinematic hardening law and neglecting strain-rate effects.

Isotropic hardening can be considered by increasing the size of the yield surface $\sigma^0$ according to the following equation.

$$\sigma^0 = \sigma|_0 + Q_\infty \left(1 - e^{-b\bar{\varepsilon}^{pl}}\right) \tag{7}$$

In this equation, $\sigma|_0$ represents the yield stress at zero plastic strain, $Q_\infty$ is the maximum change in the size of the yield surface, $b$ represents the rate at which the size of the yield surface changes, and $\bar{\varepsilon}^{pl}$ is the equivalent plastic strain.

The kinematic hardening translates the yield surface by adding $N$ kinematic hardening components $\alpha_k$ (back-stress) based on Eq. (8).

$$\alpha = \sum_{k=1}^{N} \alpha_k \tag{8}$$

where $\alpha = \sigma - \sigma^0$.

The evolution law of each kinematic hardening component is defined as shown in the following equation.

$$\dot{\alpha}_k = C_k \frac{1}{\sigma^0}(\sigma - \alpha)\dot{\bar{\varepsilon}}^{pl} - \gamma_k \alpha_k \dot{\bar{\varepsilon}}^{pl} \tag{9}$$

where $\dot{\bar{\varepsilon}}^{pl}$ is the equivalent plastic strain rate, while $C_k$ and $\gamma_k$ are parameters that need to be determined.

The isotropic hardening has a minor impact in cold-formed members [64], [65] and so it is disregarded in the numerical model by setting $Q_\infty$ equal to 0.

The kinematic hardening is modelled considering two back-stresses. If the experimental stress-strain curves for flat and corner parts of the specimens to be modelled are available, the following procedure is used to calibrate the coefficients $C_k$ and $\gamma_k$. First, the experimental engineering stress-engineering strain curve is transformed into a true stress-true strain curve. Second, the translation of the yield surface in the stress space is determined by Eq. (10).

$$\alpha = \sigma - \sigma^0 \tag{10}$$

The values of α are obtained by integration of the back-stress evolution laws over a half cycle as follows:

$$\alpha_k = \sum_{k=1}^{N} \frac{C_k}{\gamma_k}\left(1 - e^{-\gamma_k \varepsilon^{-pl}}\right) \tag{11}$$

Finally, values of the coefficients $C_k$ and $\gamma_k$ are determined by minimizing the differences between the values of α that are experimentally obtained and those predicted by the material model.

If specific data on the experimental stress-strain curves are not available, values of the coefficients $C_k$ and $\gamma_k$ calibrated by in literature can be used instead [56].

Residual stresses are included in the finite element model following the methodology proposed by Somodi and Kövesdi [2]. According to these researchers, bending residual stresses provide the dominant contribution to the overall response; therefore, only this type of residual stresses is considered. These stresses are assigned to the cross-section of cold-formed HSS with a linear distribution across the plate thickness. The intensity of these stresses is given by the following equations:

$$\sigma_{rb,flat} = \pm(0.8\sigma|_0 - 67\text{MPa}) \tag{12}$$

$$\sigma_{rb,corner} = \pm 0.55\sigma_{rb,flat} \tag{13}$$

Geometric imperfections have been taken into account in the plastic region to simulate the occurrence of local buckling phenomena (**Fig. 34**). The geometric imperfections are defined as a linear combination of the first two buckling modes obtained under a unit transverse load applied at the cantilever free end.

The material properties adopted for cold-formed HSS reflect the strong non-uniformity induced by manufacturing, with corner parts typically exhibiting higher strength but reduced ductility compared to the flat walls. In the study by Bosco et al. [44], results of tensile tests performed by [7] on a cold-formed square hollow section 200 × 200 × 8 made of S355 JR are used. Coupon geometry followed BS EN ISO 6892-1, and water-jet cutting was used to limit thermal alterations (see **Fig. 35a**).

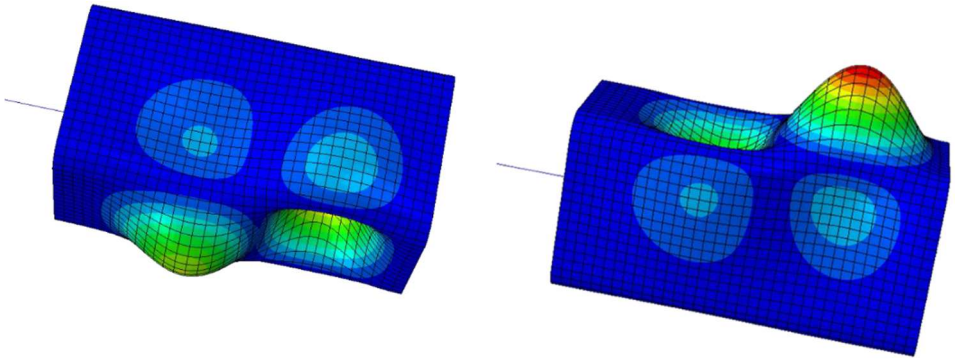

**Fig. 34** – First two buckling modes of the buckling analysis.

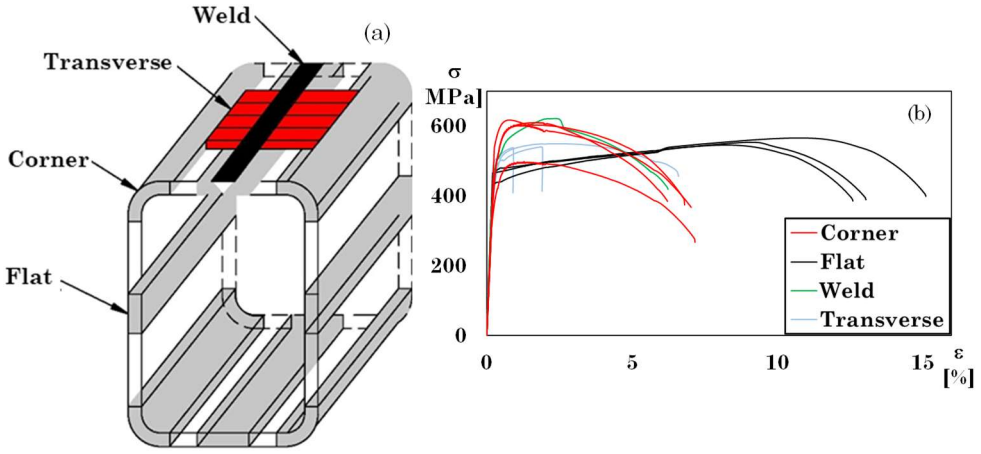


**Fig. 35** – Characterization of materials [7]: (a) location of coupon tests; (b) true stress – true strain curves.

The resulting stress–strain curves are shown in **Fig. 35b** and highlight (i) a marked differentiation between corner and flat parts and (ii) an appreciable influence of the weld when comparing the flat-wall responses.

For modelling purposes, Bosco et al. defined the yield strength as the strength at the end of the linear response of the experimental stress-strain curve (rather than the conventional 0.2% offset), leading to $\sigma|_0$ values of 467.4 MPa for flat parts and 402.9 MPa for corner parts. The

adopted value of the yield strength in the corner part is the smaller of the above two values even though its conventionally determined yield strength is the greater. This datum is not contradictory, but reflects the way the material response curve has been modelled. Two back-stresses are used to reproduce the non-linear part of the stress-strain curve. The values of $C_k$ and $\gamma_k$ are given in **Table 8**. The values of the residual stresses are reported in the same table and, as aforementioned, are assigned to the cross-section of the plastic region linearly across the thickness of the plates, as illustrated in **Fig. 36**.

**Table 8** – Properties of the material model for flat and corner parts

| Material | $\sigma\|_0$ [MPa] | $C_1$ [MPa] | $\gamma_1$ [-] | $C_2$ [MPa] | $\gamma_2$ [-] | $\sigma_r$ [MPa] |
|---|---|---|---|---|---|---|
| Flat | 467.4 | 129912 | 17667.9 | 1359.3 | 15.9 | ±366.92 |
| Corner | 402.9 | 180605 | 930.9 | 6.4 | 499.3 | ±168.81 |

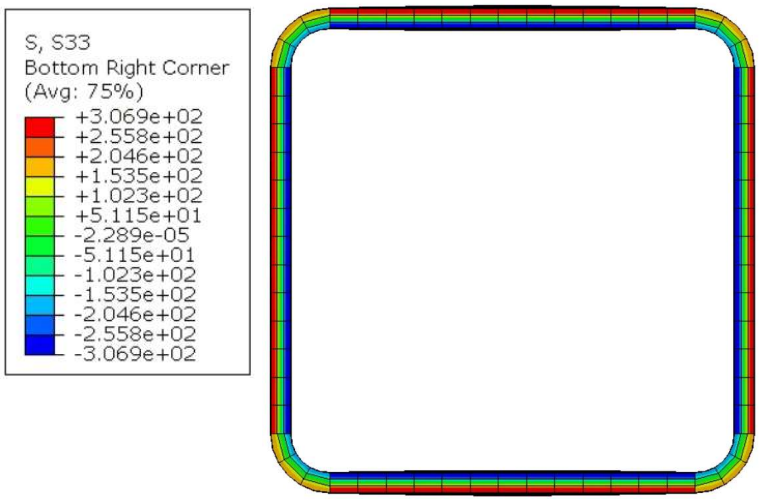


**Fig. 36** – Residual stresses assigned to the cross-section.

### 1.2. Sensitivity analysis from Bosco et al. (2021)

To define a mesh that is both accurate and computationally efficient, Bosco et al. [44] carried out a sensitivity analysis on the specimen HSS 254 × 203 × 6.4 experimentally tested in [31] ( $b$ = 203 mm, $h$ = 254 mm, $t$ = 6.4). They first discretized the plastic region using first-order (linear) hexahedral elements with element sizes of approximately 40, 30, 20, 10, and 5 mm, and then repeated the analysis using second-order (quadratic) hexahedral elements (C3D20R) with the same target sizes; in all cases, three elements were used through the plate thickness. Under a unit transverse load applied at the cantilever free end, an eigenvalue buckling analysis showed that the predicted first buckling load is strongly mesh-dependent when linear elements are employed, whereas it is only marginally affected by the element size when quadratic elements are adopted (**Fig. 37**).

The researchers further extended the sensitivity study to the nonlinear cyclic response by imposing the experimental displacement protocol reported in [31] and tracking the cumulative dissipated energy over the loading history. They observed that, with linear elements, the dissipated energy increases markedly as the mesh is coarsened because local buckling does not develop within the plastic hinge for element sizes not smaller than 20 mm, and therefore no stiffness/strength degradation is captured (**Fig. 38**).

Conversely, with quadratic elements the dissipated energy is only slightly influenced by mesh refinement: reducing the element size from 20 mm to 5 mm resulted in a 2.35% reduction in dissipated energy, at the expense of a significant increase in computational time (**Fig. 39**).

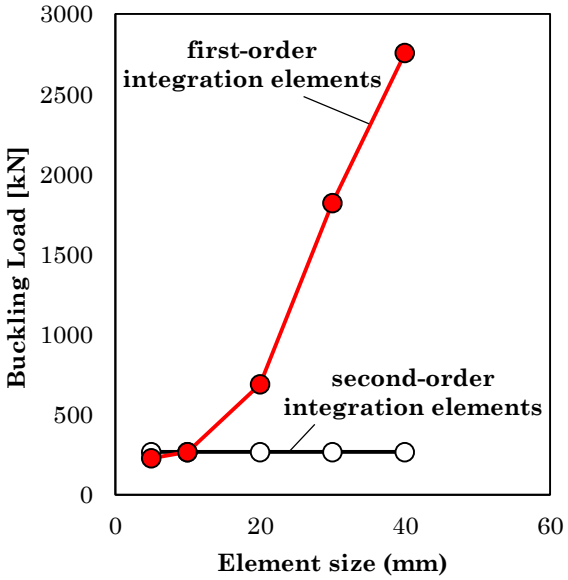


**Fig. 37** – Influence of the element-size on the buckling load [44].

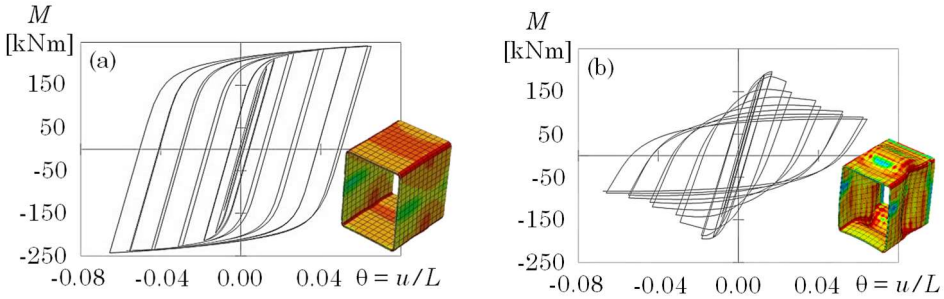


**Fig. 38** – Local buckling within the plastic hinge at the end of the loading protocol for different element types (element size = 20 mm): (a) first-order integration elements; (b) second-order integration elements.

Based on this trade-off between accuracy and computational burden, the researchers recommended the use of C3D20R elements with an element size of about 20 mm, which is the discretization adopted in this thesis for the plastic region.

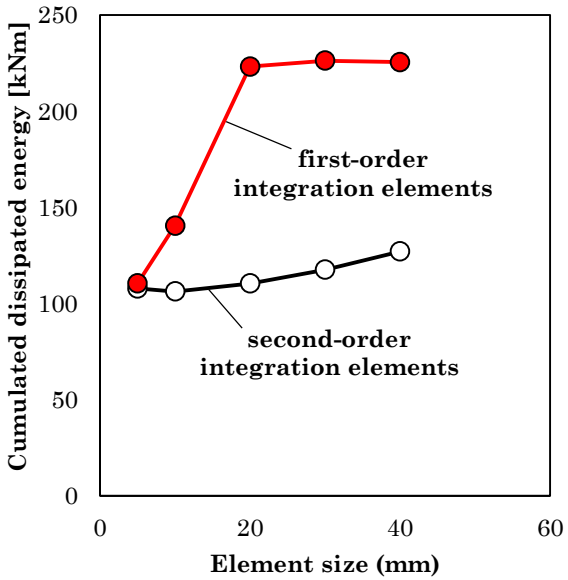


**Fig. 39** – Influence of the element-size on cumulated dissipated energy.

## 2. Validation of the finite element model with stub column test

This section presents the validation of the finite element (FE) model against the experimental force–shortening responses from the stub column tests reported by Toffolon [28]. The objective is to verify that the modelling assumptions adopted in the previous chapter can reproduce the experimental response with satisfactory accuracy.

It is worth noting that, for the purpose of stub column simulations, the FE model used in the validation includes only the solid part of the member, corresponding to the plastic region defined in the previous section. The additional beam segment (elastic region) adopted in bending

simulations is not included here, because in stub column tests the inelastic response is expected to develop in the mid-height portion of the specimen and cannot be represented by an elastic extension.

All simulations described in this section are performed using the material model described in the previous section and already implemented in the FE framework for the definition of the steel response in both flat and corner parts. Accordingly, the present validation is not aimed at comparing alternative material formulations, but rather at assessing the extent to which geometric imperfections and other modelling details affect the ability of the model to reproduce the experimental curves.

**Fig. 40** compares the experimental response (red curve) of specimen SHS 140x140x4 and specimen SHS 200x200x8 with numerical predictions obtained by assuming five different values of the maximum geometric imperfection amplitude: (i) 0.64% of $b_f$, according to the requirement reported in Annex C of Eurocode 3, Part 1–5 [67], i.e., 80% of the manufacturing geometric tolerance, which is equal to 0.8% of the cross-section width [69]; (ii) 0.40% of $b_f$; (iii) 0.20% of $b_f$; (iv) 0.1% of $b_f$; (v) 0.05% of $b_f$, based on the measurements reported by Toffolon [28].

The results indicate that the imperfection amplitude suggested by Eurocode 3, albeit conservative, leads to an excessively pronounced strength degradation and thus penalises the numerical response. Conversely, an imperfection amplitude equal to 0.05% appears overly optimistic and results in an overestimation of the mechanical response. Overall, an imperfection amplitude equal to 0.10% and 0.20% of $b_f$ provides the closest agreement with the experimental curve and was thus adopted in the validation study.

In all numerical simulations, the initial stiffness was found to be higher than that measured experimentally. This discrepancy suggests that, during the laboratory tests, some slip may have occurred within the test setup. To account for this effect, an axial spring was introduced in the FE model along the vertical direction to reproduce the axial deformability of the experimental apparatus. The spring stiffness was determined through the following relationship:

$$k_{\exp} = \frac{1}{\left(\frac{1}{k_{FEM}} + \frac{1}{k_{spring}}\right)} \tag{14}$$

where $k_{exp}$ is the stiffness associated with the elastic branch of the experimental curve and $k_{FEM}$ is the axial stiffness obtained from the numerical model without the spring. The spring stiffness $k_{spring}$ was computed by enforcing the above identity through the Excel solver, so as to minimise the mismatch between the left- and right-hand sides of Eq. (14).

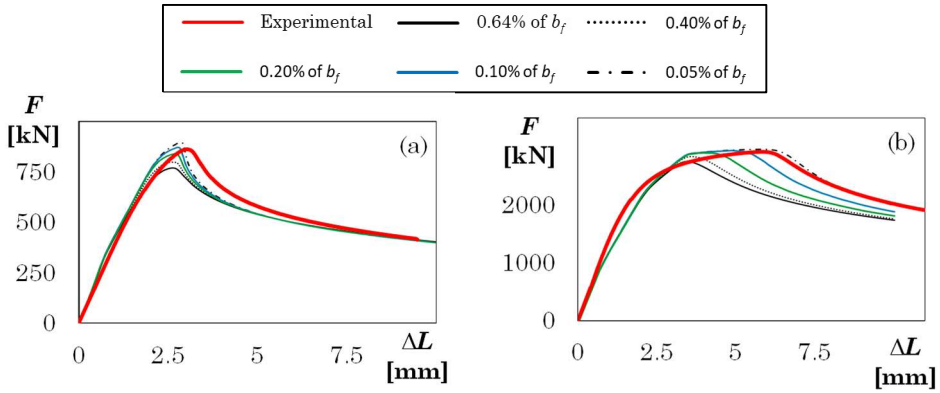


**Fig. 40** – Comparison of the influence of geometric imperfections: (a) specimen SHS 140x140x4; (b) specimen SHS 200x200x8.

In Abaqus the fully restrained end of the plastic region was modified to permit the displacement along the z-axis, while a spring along the same axis was implemented with a stiffness equal to $k_{spring}$. **Fig. 41a** compares the numerical response obtained with the spring and without the spring for specimen SHS 140x4. The remaining plots in the same figure (**Fig. 41b–d**) show that both imperfection amplitudes (0.1% and 0.2%) allow a satisfactory match, with minor differences depending on the local slenderness of the investigated sections.

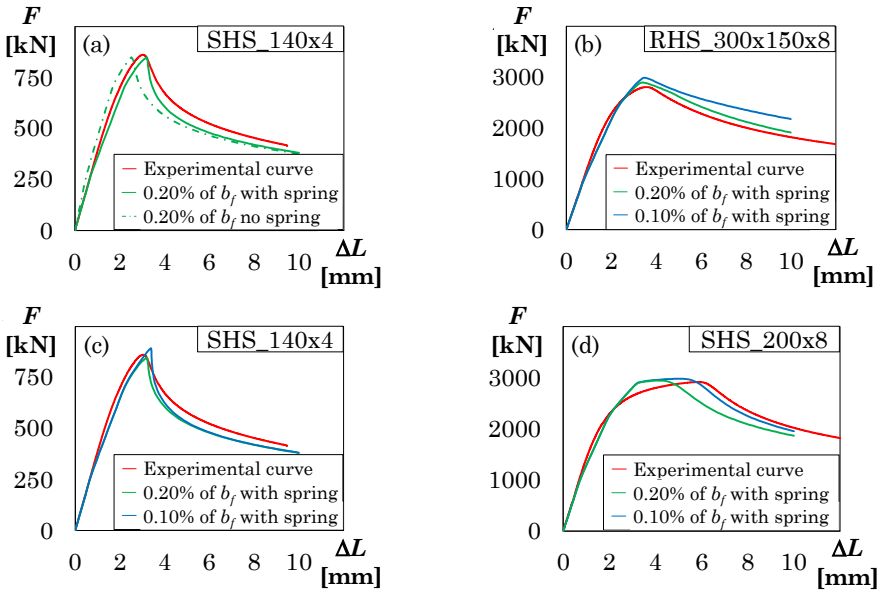


**Fig. 41** – Numerical and experimental comparisons for SHS 140x140×4: (a) numerical response with spring (M) versus without spring (SM); (b–d) numerical-to-experimental comparison for different geometric imperfection amplitudes.

To quantify these differences, the dissipated energy was computed as the area enclosed by the force–shortening curve, for both experimental and numerical responses, using the trapezoidal rule. The area associated with each interval between consecutive points is evaluated as:

$$A_i = \frac{\left(x_{i+1} - x_i\right) \bullet \left(y_{i+1} + y_i\right)}{2} \tag{15}$$

where $x_i$ is the shortening and $y_i$ is the corresponding force. The total energy is obtained by summing $A_i$ over the full response history.

In addition, the relative percentage error with respect to the ultimate load and the dissipated energy was evaluated as:

$$Error_{\%} = \frac{x_{\exp} - x_{FEM}}{x_{exp}} \bullet 100 \tag{16}$$

where x denotes, in turn, either the ultimate load or the dissipated energy. The results are summarised in **Table 9** (ultimate load) and **Table 10** (dissipated energy). Overall, the errors are generally limited. A

slightly improved performance of the 0.1% imperfection is observed for stockier sections, whereas 0.2% tends to provide a better match for more slender sections. Since these differences are modest, and adopting a conservative standpoint consistent with international literature [65], an imperfection amplitude of 0.2% was selected for the numerical study that will be discussed in a further chapter.

**Table 9** – Comparison between experimental and numerical ultimate load for different imperfection amplitudes.

| Specimen | Imp. [%] | $N_{u,exp}$ [kN] | $N_{u,FEM}$ [kN] | error [%] |
|---|---|---|---|---|
| SHS 140x140x4 | 0.1 | 5097.2 | 4787.9 | -6.07% |
| | 0.1 | 861.3 | 893.1 | 3.69% |
| SHS 200x200x8 | 0.2 | 23237.3 | 848.1 | -1.53% |
| | 0.1 | 2916.7 | 2981.3 | 2.21% |
| RHS 300x150x8 | 0.2 | 20890.9 | 2945.3 | 0.98% |
| | 0.1 | 2806.9 | 2988.1 | 6.46% |

**Table 10** – Comparison between experimental and numerical dissipated energy for different imperfection amplitudes.

| Specimen | Imp. [%] | $E_{exp}$ [mJ] | $E_{FEM}$ [mJ] | error [%] |
|---|---|---|---|---|
| SHS 140x140x4 | 0.1 | 5097.2 | 4787.9 | -6.07% |
| | 0.2 | | 4770.63 | -6.41% |
| SHS 200x200x8 | 0.1 | 23237.3 | 23042.8 | -0.84% |
| | 0.2 | | 21958.3 | -5.50% |
| RHS 300x150x8 | 0.1 | 20890.9 | 22662.1 | 8.48% |
| | 0.2 | | 21457.3 | 2.71% |

## 3. Validation of the finite element model under uniaxial bending

The validation against the experimental results of Fadden and McCormick [31] was carried out on both rectangular and square hollow cross-sections, characterized by different depth-to-thickness ratios of the flat parts, and subjected to uniaxial bending. Specifically, specimens 254×203×6.4, 254×102×6.4, 203×203×6.4, and 203×152×9.5 were considered. All specimens were cantilever members with a length equal to 1537 mm and were fabricated from A500 grade B steel. The stress-strain curves of the steel were derived by Fadden and McCormick from coupon tests performed on both flat and corner regions of the sections [45]. The calibrated parameters of the constitutive model are reported in **Table 11**, while the target and predicted engineering stress-strain curves are shown in **Fig. 42a**.

**Table 11** – Parameters of the material model for flat and corner parts to replicate stress-strain curves provided by Fadden and McCormick [45].

| Material | $E$ [MPa] | $\sigma_0$ [MPa] | $C_1$ [MPa] | $\gamma_1$ [-] | $C_2$ [MPa] | $\gamma_2$ [-] | $C_3$ [MPa] | $\gamma_3$ [-] | $\sigma_{rb}$ [MPa] |
|---|---|---|---|---|---|---|---|---|---|
| Flat | 181000 | 412.0 | 2426.3 | 17.50 | 15453.1 | 809.5 | 0.0 | - | ± 262.60 |
| Corner | 193000 | 519.0 | 23251.9 | 814.10 | 9769.40 | 202.70 | 7.70 | 1.40 | ± 144.43 |

The loading protocol consisted of progressively increasing cyclic end displacements, defined as the product of the cantilever length and the chord rotation provided in AISC 341-16 [75] (see **Fig. 42b**).

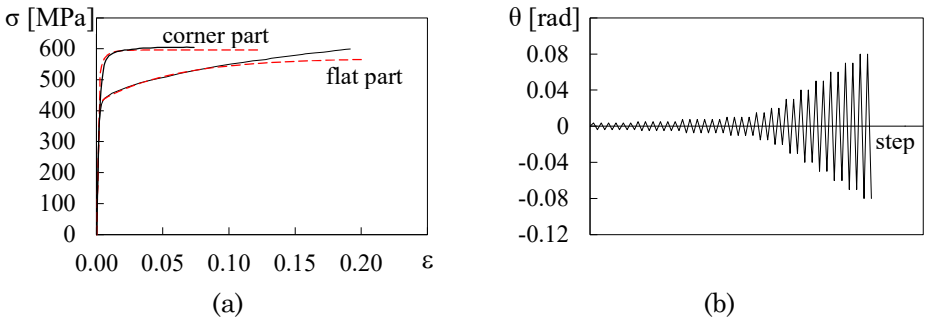


**Fig. 42** – (a) Comparison between true stress-strain curves provided by the material model (dashed red curve) and the coupon tests (black continuous line) and (b) loading protocol provided in [45]

The accuracy of the numerical model has been assessed by comparing target and predicted responses in terms of bending moment versus chord rotation (**Fig. 43**). The numerical results corresponding to the two selected amplitudes of geometric imperfections are represented by dashed lines (green and red), whereas the experimental response is shown by a solid black line.

In all the cases, the assumed imperfection amplitude has a limited influence on the global cyclic response, with only minor differences between the numerical predictions obtained from the two imperfection amplitudes. Overall, excellent agreement was observed between experimental and numerical responses for all the investigated specimens. In particular, specimen 203×152×9.5 characterised by the lowest depth-to-thickness ratio, did not exhibit any strength degradation up to the maximum imposed lateral displacement, which was limited by the test setup. This agreement confirms the ability of the FE model to accurately capture the strength and stiffness degradation associated with local buckling, which precedes corner fracture.

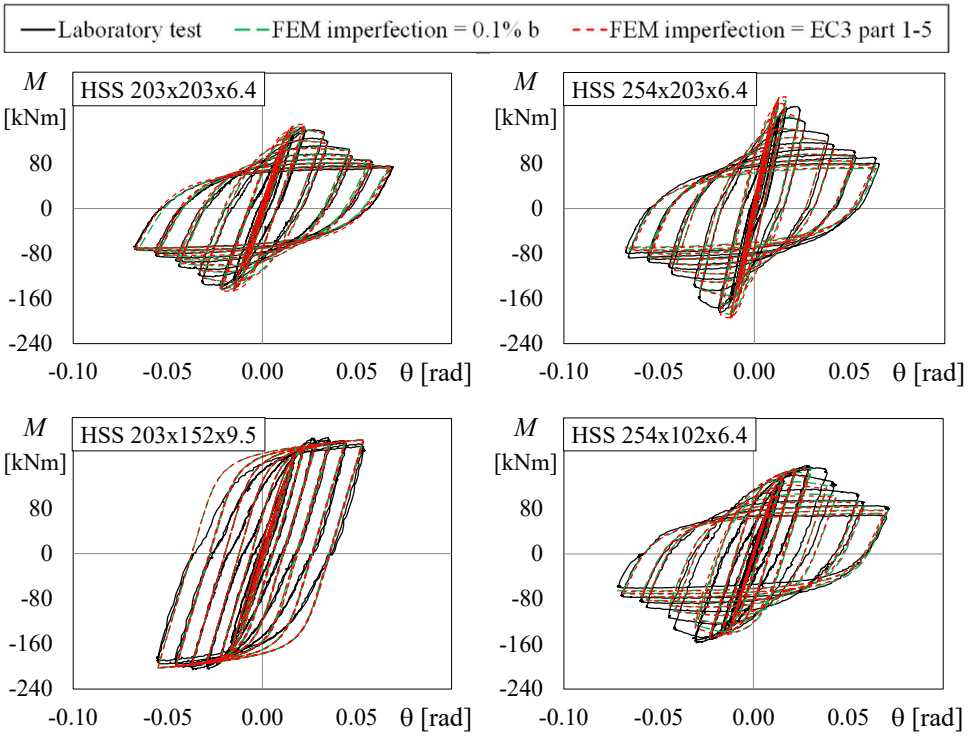


**Fig. 43** – Comparison between the bending moment-chord rotation response obtained from numerical models and laboratory tests carried out in [31]

## 4. Validation of the finite element model under biaxial bending and influence of geometric imperfections

In the present thesis, the experimental campaign by Ishida et al. [34] was adopted as a benchmark (see Chapter 1 for the full description of the test setup and loading programme) for the validation of the finite element model under biaxial bending. The model was calibrated and assessed against eight quasi-static cyclic tests performed on two cold-formed hollow columns made of BCR295 steel, with net length *L'* equal to 1734 mm and cross-section 200x9 mm, including an external corner radius of 22.5 mm. The mechanical properties of the steel were determined by

Ishida et al. [34] by means of coupon tests extracted from the flat parts of the section. The yield strength, the ultimate strength and the elongation at fracture were equal to 443 MPa, 483 MPa and 16% for specimen #1, and equal to 375 MPa, 427 MPa and 27% for specimen #2, respectively. No information, however, was reported regarding the mechanical properties of the corner parts of the sections, which are expected to exhibit higher strength and lower ductility due to the cold-forming process.

Both ends of the column were clamped to the reaction jig and the horizontal loading jig. An axial force corresponding to an axial load ratio equal to 0.2 or 0.4 was applied by vertical jacks at the top of the specimen. Lateral displacements were applied to the bottom end of the member by means of a horizontal jack. In particular, the two specimens were subjected to symmetric cyclic displacement loading histories. In specimen #1, the displacements were applied along horizontal directions inclined at angles $\phi$ equal to 0° and 45° with respect to the principal axis of inertia of the column cross-section; in specimen #2, instead, the loading directions were inclined at angles $\phi$ equal to 15° and 30° with respect to the principal axes of inertia of the column cross-section.

The loading protocol (**Fig. 44a**) was defined in terms of multiples of the elastic column chord rotation $\theta_{p0}$ corresponding to the full plastic bending moment $M_{p0}$, which was calculated by taking into account the interaction with the axial force in the column. Both the chord rotation $\theta_{p0}$ and the full plastic bending moment $M_{p0}$ are reported in **Fig. 44b**.

As the rotations of both ends of the selected laboratory specimen are virtually fully restrained, the numerical model represents half of the length of the specimen. To simulate the deformability of the test setup, two flexural springs, associated with the rotations about the $x$- and $y$-axes, have been introduced at the only one fixed end of the numerical model.

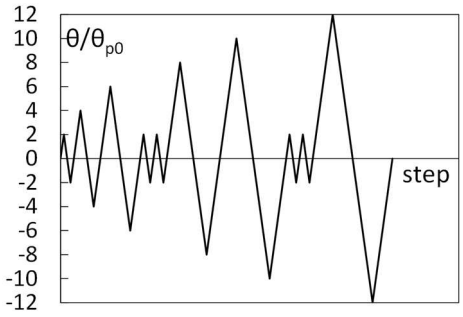


(a)

| Specimen | Axial Load ratio (ν) | Angle of displacement (φ) | $M_{P0}$ [kNm] | $\theta_{P0}$ [rad] |
|---|---|---|---|---|
| # 1 | 0.20 | 0°, 45° | 196.0 | 0.0079 |
| # 1 | 0.40 | 0°, 45° | 167.0 | 0.0068 |
| # 2 | 0.20 | 15°, 30° | 165.0 | 0.0067 |
| # 2 | 0.40 | 15°, 30° | 137.0 | 0.0055 |

(b)

**Fig. 44** – Loading protocol and key reference parameters from study [34]: (a) loading protocol; (b) values of the axial load $N$, elastic column chord rotation, $\theta_{p0}$, and the column full plastic moment under axial force, $M_{p0}$.

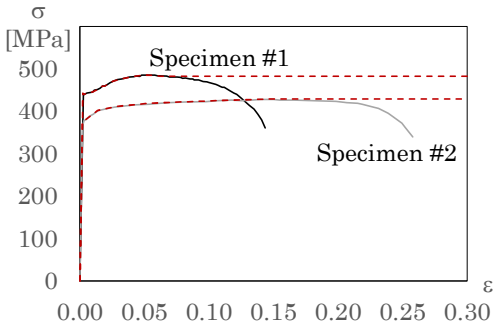


**Fig. 45** – Comparison between engineering stress-strain curves provided by the material model (dashed red curve) and the coupon tests (black continuous line)

Based on the results of the coupon tests conducted by Ishida et al. [34], the yield stress at zero plastic strain $\sigma|_0$ of the steel material model has been set equal to 443 MPa for specimen #1 and equal to 375 MPa for

specimen #2. In any case, the elastic modulus of steel $E_s$ is set equal to 200000 MPa. The back-stresses considered for the flat parts of the section are two. Coefficients $C_k$ and $\gamma_k$ have been calibrated so as to match the stress-strain curve provided in [34] and are reported in **Table 12**. The comparison between the target and predicted engineering stress-strain curves is shown in **Fig. 45**. Good agreement is observed up to the ultimate stress. Beyond this point, the experimental curves show a marked softening, while the predicted curves remain constant. This discrepancy is expected, since the adopted back-stress formulation does not account for the post-peak degradation of the material.

Table 12 – Material properties

| Specimen | $E_s$ [MPa] | $\sigma\|_0$ [MPa] | $C_1$ [MPa] | $\gamma_1$ [-] | $C_2$ [MPa] | $\gamma_1$ [-] |
|---|---|---|---|---|---|---|
| #1 | 200000 | 443 | 1952.2 | 17.32 | 15.41 | 88074 |
| #2 | 200000 | 375 | 3547.9 | 104.3 | 647.9 | 1.0 |

Since no coupon tests were performed on the corner parts of the section their mechanical properties have been determined based on experimental studies on BCR295 HSS members characterised by thickness and corner radius equal to those of the specimen under investigation [35]. For these specimens, comparable strain-hardening effects in the corner parts, including increased strength and reduced ductility, are expected. Accordingly, the yield strength of the corner parts has been set equal to 1.31 times the yield strength of the flat parts. In addition, a single back stress has been used for the corner parts. Namely, coefficients $C_1$ and $\gamma_1$ have been set equal to 1087 MPa and 14.0, as suggested in [65] for BCR295 steel grade.

To assess the influence of geometric imperfections on the cyclic response of the member, two values of the maximum imperfection have been selected. The first value corresponds to 0.1% of the cross-sectional size and represents the lower bound of the geometric imperfections measured in [28] using a 3D laser scanning technique. A similar level of local imperfection was also recommended by Suzuki [65] for cross-sections made of BCR295 steel grade with a height-to-thickness ratio greater than 20. The second value of the maximum geometric imperfection

corresponds to the requirement reported in Annex C of Eurocode 3, Part 1–5 [67], i.e., 80% of the manufacturing geometric tolerance, which is equal to 0.8% of the cross-section width [69].

Since the numerical model replicates only half of the specimen, the loading displacement history applied at the free end of the specimen is equal to $L/2$ times the chord rotation $\theta$, and is inclined at an angle $\phi$ with respect to the $y$-axis as shown in **Fig. 33**. In the absence of direct knowledge of the value of $L$, this has been derived by equating the chord rotation corresponding to the full plastic bending resistance $M_{p0}$ to the value of $\theta_{p0}$ provided by Ishida and reported in **Fig. 44**. The so obtained value of $L$ is 1900 mm.

The accuracy of the numerical model has been assessed by comparison of targeted and predicted responses. The first response parameter investigated is the bending moment acting at the bottom end of the specimen tested by Ishida et al. [34], while the second is the axial shortening. Due to the cantilever configuration of the numerical model, the bending moment described above is compared with that at the base of the model, while the axial shortening is compared with twice the axial shortening observed in the numerical model.

With reference to the first response parameter investigated, i.e., the bending moment, it is plotted as a function of the chord rotation. In addition, it is normalized by $M_{P0,}$ whereas the chord rotation is normalized by $\theta_{P0}$. In keeping with the approach followed in the laboratory tests, reactions $F_x$ and $F_y$ have been recorded at the reference point of the plastic region, whereas displacements $u_x$ and $u_y$ have been recorded at the tip of the elastic region. The displacement $u$ along the assigned loading direction and the force $F$ along the same direction are calculated as

$$u = u_x \sin\varphi + u_y \cos\varphi \tag{17}$$

$$F = F_x \sin\varphi + F_y \cos\varphi \tag{18}$$

Hence, the bending moment $M$ (acting in the vertical plane that is parallel to the displacement loading direction) is calculated as

$$M = F\frac{L}{2} + N\,u \tag{19}$$

where $N$ is the external axial force.

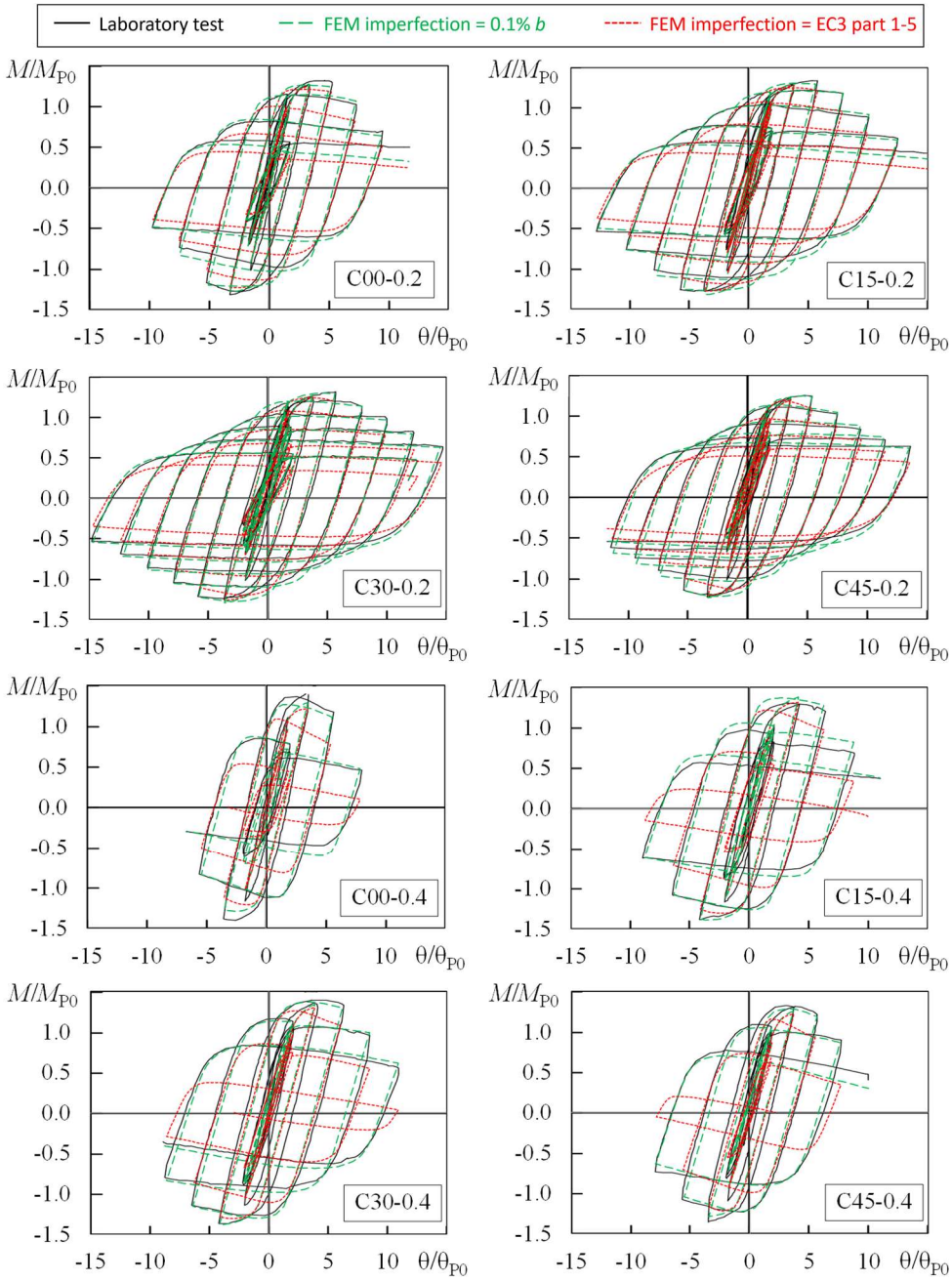


**Fig. 46** – Comparison between the normalized bending moment-chord rotation response obtained from numerical models and laboratory tests.

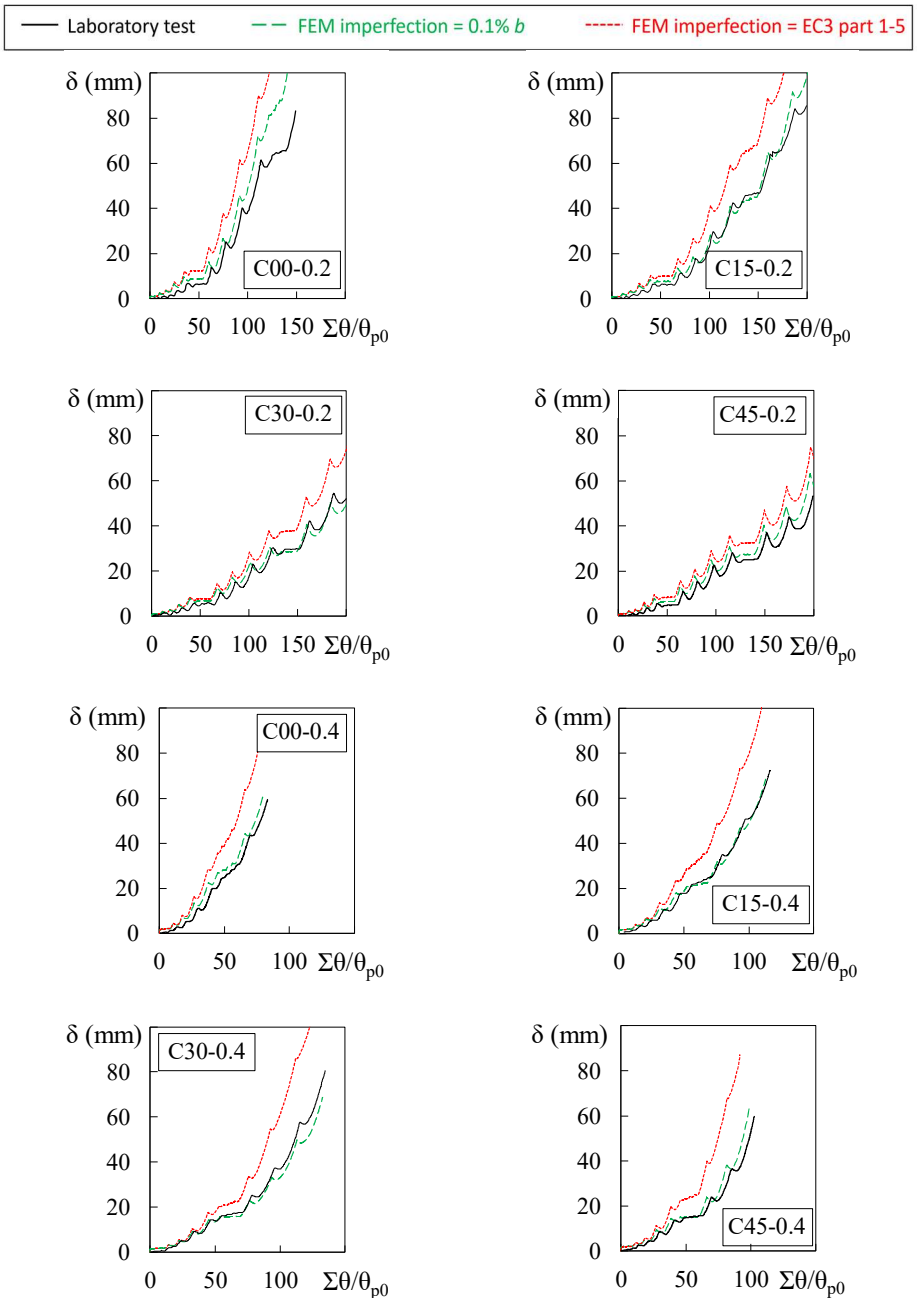


**Fig. 47** – Comparison between the axial shortening-cumulated normalized chord rotation response obtained from numerical models and laboratory tests.

With reference to the second response considered, it is plotted as a function of the cumulated chord rotation of the member, again normalized by $\theta_{P0}$. The targeted and predicted responses described above are shown in **Fig. 46-47**.

In particular, the numerical responses corresponding to the two selected values of the geometric imperfections are shown by dashed lines (green or red), whereas a solid (black) line. In contrast to the results presented in the previous subsection, the presence of axial force induces a marked dependence of the predicted cyclic response on the amplitude of the assumed geometric imperfection. Indeed, **Fig. 46**, which refers to the bending moments, shows that despite the uncertainties in the material properties of the corner parts, the numerical model with a geometric imperfection equal to 0.1% of the cross-sectional side accurately reproduces the experimental response. The model with a maximum imperfection according to Annex C of Eurocode 3 part 1–5 [67], instead, exhibits a higher rate of degradation, especially in the cases with an axial load ratio of 0.4. The analysis of the axial shortening of the specimens (**Fig. 47**) confirms the aforementioned observations and shows that the experimental response is generally bounded by the numerical predictions obtained using a geometric imperfection equal to 0.1% of the cross-sectional side and that defined according to EC3 Part 1-5.

Although the model with the smallest imperfection yields the most accurate results, the models with larger imperfections may better represent real members due to the manufacturing geometric tolerances specified in UNI-EN-10219-2 [69]. Hence, to provide a conservative estimate of the rotation capacity, the numerical analyses discussed in the following sections have been carried out considering the value of the maximum imperfection reported in UNI-EN-10219-2 [69].

# Chapter 3

# FORMULATION OF CHORD ROTATION CAPACITY DOMAIN

## 1. Parametric analyses on HSS members of European S355 Steel grade

Parametric analyses have been carried out on cantilever specimens with square or rectangular HSS. All members are made of European S355 steel grade. The yield stress at zero plastic strain $\sigma_0$ and the values of the parameters $C_k$ and $\gamma_k$ used to compute the back-stresses of the flat and corner parts are those calibrated in [44] to match the stress-strain curves obtained by coupon tests provided in [7] and are reported in **Table 8**. The specimens considered for the parametric analyses differ in the size of the cross-sections, the local slenderness of the flat parts, the shear length, and the axial load ratio. In total, 252 specimens are numerically investigated. Specifically, 6 square cross-sections (300x300x10, 350x350x14.2, 350x350x16, 400x400x14.2, 400x400x16 and 400x400x20) and 6 rectangular cross-sections (150x300x14.2, 150x350x8, 150x350x14.2, 150x350x16, 200x500x16, and 250x450x10) are selected. Three values of the cantilever length used in the numerical model, hereafter referred to as the shear span length are considered (1.50 m, 2.25 m, and 3.00 m), and 7 values of axial load (ranging from –0.1 to 0.5 $N_{pl}$ in steps of 0.1 $N_{pl}$) are applied to the tip of the member.

Regarding the shear span length, the above values are chosen to represent the segment of a first order column between the contraflexure

point and the column base, accounting of different interstorey heights or different base connection stiffnesses.

Regarding the axial load ratio, it should be noted that the buckling resistance of each specimen was preliminarily computed and compared with the axial load required to achieve the prescribed axial load ratio. Cases in which the buckling resistance was lower than the required axial load were excluded from the parametric investigation. For a shear span length equal to 2.25m, this condition occurred for specimens S150×300×14.2, S150×350×8, S150×350×14.2, and S150×350×16.0 with v = 0.5. For a shear span length equal to 3000 mm, the same condition occurred for specimens S150×300×14.2, S150×350×8, S150×350×14.2, and S150×350×16.0 with v ranging from 0.3 to 0.5, for specimen S200×500×16.0 with v = 0.4 and 0.5, and for specimen S250×450×10.0 with v = 0.5.

In addition to the commonly considered members subjected to compressive axial forces, members subjected to low levels of tensile forces (–0.1 $N_{pl}$) have been investigated. These cases have been added because during seismic events, low tensile axial forces can arise in corner columns due to the shear forces acting at the ends of the beams.

The numerical model described in the previous section has been used to simulate the cyclic response of the specimens under the loading protocol given in AISC 341 [75] for the qualification of beam-to-column connections. The lateral displacements are applied at the tip of the specimen along directions that are inclined at angles φ with respect to the *y*-axis equal to 0°, 15°, 30°, 45°, 60°, 75°, or 90°. In the case of rectangular cross-sections, the *y*-axis is the major principal axis of inertia of the cross-section.

To prevent lateral buckling phenomena, a maximum axial load ratio was assigned to each specimen. **Table 13** presents a summary of all the specimens considered in the parametric study, together with the main geometric parameters of the cross-sections, for a total of 1,272 analysed cases. The local slenderness values, evaluated with reference to the net flat-part dimensions, cover a wide range of cross-section configurations. In particular, $h_f/t$ varies between 14.0 and 40.0, while $b_f/t$ ranges from 3.4 to 25.0. Considering the maximum slenderness between the two flat

parts, the analysed sections range from relatively stocky configurations, with a governing slenderness equal to 14.0, to highly slender configurations, with a governing slenderness equal to 40.0.

**Table 14** and **Table 15** present the classification of the cross-sections considered in the parametric analyses for each axial load ratio, according to the current and the forthcoming version of Eurocode, respectively.

**Table 13** – Main parameters of the specimens considered for the parametric analyses.

| Cross-section | $L_v$ [m] | | | $r_e$ [mm] | $A$ [cm²] | $b_f$ [mm] | $h_f$ [mm] | $h_f/t$ [-] | $b_f/t$ [-] |
|---|---|---|---|---|---|---|---|---|---|
| | 1.50 | 2.25 | 3.00 | | | | | | |
| | $\nu_{max}$ | $\nu_{max}$ | $\nu_{max}$ | | | | | | |
| HSS350x150x8.0 | 0.5 | 0.4 | 0.3 | 20.0 | 75.2 | 310.0 | 110.0 | 38.7 | 13.7 |
| HSS450x250x10.0 | 0.5 | 0.5 | 0.5 | 25.0 | 132.6 | 400.0 | 200.0 | 40.0 | 20.0 |
| HSS300x300x10.0 | 0.5 | 0.5 | 0.5 | 25.0 | 112.6 | 250.0 | 250.0 | 25.0 | 25.0 |
| HSS400x400x20.0 | 0.5 | 0.5 | 0.5 | 60.0 | 286.8 | 280.0 | 280.0 | 14.0 | 14.0 |
| HSS350x350x14.2 | 0.5 | 0.5 | 0.5 | 42.6 | 182.1 | 264.8 | 264.8 | 18.6 | 18.6 |
| HSS400x400x14.2 | 0.5 | 0.5 | 0.5 | 42.6 | 210.5 | 314.8 | 314.8 | 22.2 | 22.2 |
| HSS350x350x16.0 | 0.5 | 0.5 | 0.5 | 48.0 | 202.8 | 254.0 | 254.0 | 15.9 | 15.9 |
| HSS400x400x16.0 | 0.5 | 0.5 | 0.5 | 48.0 | 234.8 | 304.0 | 304.0 | 19.0 | 19.0 |
| HSS350x150x14.2 | 0.5 | 0.4 | 0.2 | 43.7 | 125.0 | 262.5 | 62.5 | 18.5 | 4.4 |
| HSS300x150x14.2 | 0.5 | 0.4 | 0.2 | 42.9 | 111.0 | 214.1 | 64.1 | 15.1 | 4.5 |
| HSS350x150x16.0 | 0.5 | 0.4 | 0.2 | 48.1 | 138.8 | 253.8 | 53.8 | 15.9 | 3.4 |
| HSS500x200x16.0 | 0.5 | 0.5 | 0.4 | 48.0 | 202.8 | 404.0 | 104.0 | 25.2 | 6.5 |

**Table 14** – Classification of the considered cross-section for each axial load ratio according to the current version of Eurocode.

| | **Classification of cross-section – current Eurocode** | | | | | | |
|---|---|---|---|---|---|---|---|
| **Cross-section** | **ν= - 0.1** | **ν = 0.0** | **ν = 0.1** | **ν = 0.2** | **ν = 0.3** | **ν = 0.4** | **ν = 0.5** |
| HSS350x150x8.0 | 3 | 3 | 3 | 3 | 3 | 3 | 3 |
| HSS450x250x10.0 | 3 | 3 | 3 | 3 | 3 | 3 | 3 |
| HSS300x300x10.0 | 2 | 2 | 2 | 2 | 2 | 2 | 3 |
| HSS400x400x20.0 | 1 | 1 | 1 | 1 | 1 | 1 | 1 |
| HSS350x350x14.2 | 1 | 1 | 1 | 1 | 1 | 1 | 1 |
| HSS400x400x14.2 | 1 | 1 | 1 | 1 | 1 | 1 | 1 |
| HSS350x350x16.0 | 1 | 1 | 1 | 1 | 1 | 1 | 1 |
| HSS400x400x16.0 | 1 | 1 | 1 | 1 | 1 | 1 | 1 |
| HSS350x150x14.2 | 1 | 1 | 1 | 1 | 1 | 1 | 1 |
| HSS300x150x14.2 | 1 | 1 | 1 | 1 | 1 | 1 | 1 |
| HSS350x150x16.0 | 1 | 1 | 1 | 1 | 1 | 1 | 1 |
| HSS500x200x16.0 | 2 | 2 | 2 | 3 | 3 | 3 | 3 |

**Table 15** – Classification of the considered cross-section for each axial load ratio according to the upcoming version of Eurocode.

| | **Classification of cross-section – new Eurocode** | | | | | | |
|---|---|---|---|---|---|---|---|
| **Cross-section** | **ν=- 0.1** | **ν = 0.0** | **ν = 0.1** | **ν = 0.2** | **ν = 0.3** | **ν = 0.4** | **ν = 0.5** |
| HSS350x150x8.0 | 3 | 3 | 3 | 3 | 3 | 3 | 3 |
| HSS450x250x10.0 | 3 | 3 | 3 | 3 | 3 | 3 | 3 |
| HSS300x300x10.0 | 3 | 3 | 3 | 3 | 3 | 3 | 3 |
| HSS400x400x20.0 | 1 | 1 | 1 | 1 | 1 | 1 | 1 |
| HSS350x350x14.2 | 1 | 1 | 1 | 1 | 1 | 1 | 1 |
| HSS400x400x14.2 | 2 | 2 | 2 | 2 | 2 | 2 | 3 |
| HSS350x350x16.0 | 1 | 1 | 1 | 1 | 1 | 1 | 1 |
| HSS400x400x16.0 | 1 | 1 | 1 | 1 | 1 | 1 | 1 |
| HSS350x150x14.2 | 1 | 1 | 1 | 1 | 1 | 1 | 1 |
| HSS300x150x14.2 | 1 | 1 | 1 | 1 | 1 | 1 | 1 |
| HSS350x150x16.0 | 1 | 1 | 1 | 1 | 1 | 1 | 1 |
| HSS500x200x16.0 | 3 | 3 | 3 | 3 | 3 | 3 | 3 |

**Table 16** and **Table 17** show the cross-section requirements for HSS according respectively to the current and the forthcoming version of Eurocode.

**Table 16** – Cross-section requirements for internal compression parts: current Eurocode 3 [67].

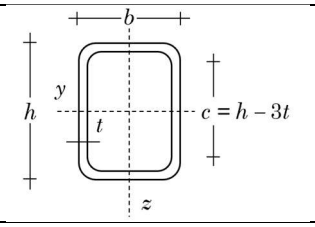


| EC3 2005 | | | |
|---|---|---|---|
| Class | Part subject to bending | Part subject to compression | Part subject to bending and compression |
| Stress distribution in parts** | 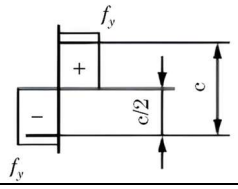 | 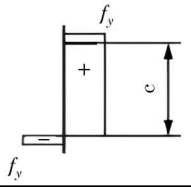 | 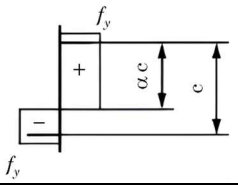 |
| 1 | $c/t \le 72\,\varepsilon$ | $c/t \le 33\,\varepsilon$ | $when\ \alpha > 0.5 : c/t \le \frac{396\varepsilon}{13\alpha - 1}$<br>$when\ \alpha \le 0.5 : c/t \le \frac{36\varepsilon}{\alpha}$ |
| 2 | $c/t \le 83\,\varepsilon$ | $c/t \le 38\,\varepsilon$ | $when\ \alpha > 0.5 : c/t \le \frac{456\varepsilon}{13\alpha - 1}$<br>$when\ \alpha_c \le 0.5 : c/t \le \frac{41.5\varepsilon}{\alpha_c}$ |
| Stress distribution in parts** | 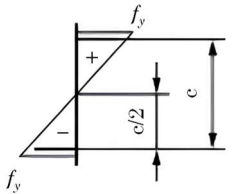 | 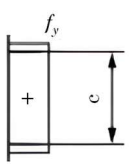 | 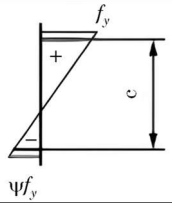 |
| 3 | $c/t \le 124\,\varepsilon$ | $c/t \le 42\,\varepsilon$ | $when\ \psi > -1 : c/t \le \frac{42\varepsilon}{0.67 + 0.33\psi}$<br>$when\ \psi \le -1^{*} : c/t \le 62\varepsilon(1 - \psi)\sqrt{(-\psi)}$ |
| $\varepsilon = \sqrt{235/f_y}$ | | | |

*) $\psi \le -1$ applies where either the compression stress $\sigma \le f_y$ or the tensile strain $\varepsilon_y > f_y/E$

**) The compression is positive

**Table 17** – Cross-section requirements for internal compression parts: New Eurocode 3 [68].

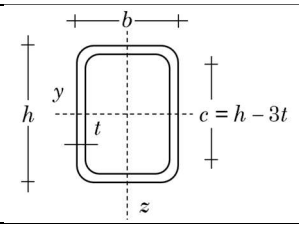


| EC3 2025 | | | |
|---|---|---|---|
| Class | Part subject to bending | Part subject to compression | Part subject to bending and compression |
| Stress distribution in parts** | 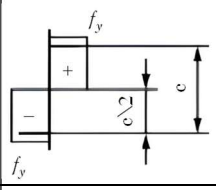 | 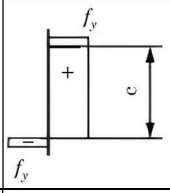 | 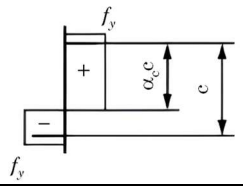 |
| 1 | $c/t \le 72\,\varepsilon$ | $c/t \le 28\,\varepsilon$ | $when\ \alpha_c > 0.5 : c/t \le \frac{126\varepsilon}{5.5\alpha_c - 1}$<br>$when\ \alpha_c \le 0.5 : c/t \le \frac{36\varepsilon}{\alpha_c}$ |
| 2 | $c/t \le 83\,\varepsilon$ | $c/t \le 34\,\varepsilon$ | $when\ \alpha_c > 0.5 : c/t \le \frac{188\varepsilon}{6.53\alpha_c - 1}$<br>$when\ \alpha_c \le 0.5 : c/t \le \frac{41.5\varepsilon}{\alpha_c}$ |
| Stress distribution in parts** | 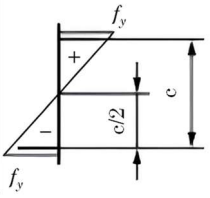 | 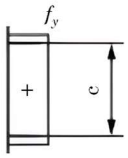 | 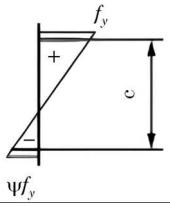 |
| 3 | $c/t \le 121\,\varepsilon$ | $c/t \le 38\,\varepsilon$ | $when\ \psi > -1 : c/t \le \frac{38\varepsilon}{0.608 + 0.343\psi + 0.049\psi^2}$<br>$when\ \psi \le -1^* : c/t \le 60.5\varepsilon(1 - \psi)$ |

$\alpha_c = 0.5\left(1 + \frac{N_{Ed}}{c\, t_w\, f_y}\right)$ Where $N_{Ed}$ is the design axial force taken as positive for compression and negative for tension

*) $\psi \le -1$ and a compression stress of $\sigma_{com,Ed} = f_y$ applies where the tensile strain $\varepsilon_t > f_y/E$

**) The compression is positive

## 2. Methodology

Following an approach that is commonly adopted in experimental tests [70], the direction of the transverse displacements applied at the tip of the specimen remains constant during the single numerical test. Consequently, the two components $u_x$ and $u_y$ of the displacement $u$ of the tip of the cantilever are proportional to each other during the entire imposed loading history. However, the two components of the bending moment (i.e., $M_x$ and $M_y$) do not vary proportionally. Hence, two approaches can be used to analyse and plot the cyclic response of the specimens. The first approach, followed by Ishida et al. [34], consists of plotting both the displacement and the bending moment in the vertical plane inclined at the angle φ (see equations 17-19). According to second approach, the resultant bending moment is directly evaluated and plotted. In the present study, the latter approach has been preferred, since both the displacement loading direction and the angle ß of the resultant bending moment vector may change during seismic events. To ensure a unique and consistent evaluation of the orientation of the resultant bending moment vector, the direct use of the inverse tangent function, ß=arctan ($M_y/M_x$) is inadequate, as it cannot distinguish between vectors belonging to different quadrants and yields identical values for directions separated by π. Moreover, the expression becomes undefined for $M_x$=0, leading to numerical singularities. To overcome these limitations, a piecewise formulation is introduced, in which the angle ß is calculated at each instant of time by explicitly accounting for the signs of $M_x$ and $M_y$, as illustrated in **Fig. 48**. This approach allows the angle to be uniquely determined over the full interval (-π, π], thereby ensuring correct quadrant identification and proper treatment of degenerate cases.

The magnitude of the resultant bending moment vector is

$$M = |M_x| \cdot \cos\beta + |M_y| \cdot \sin\beta \tag{20}$$

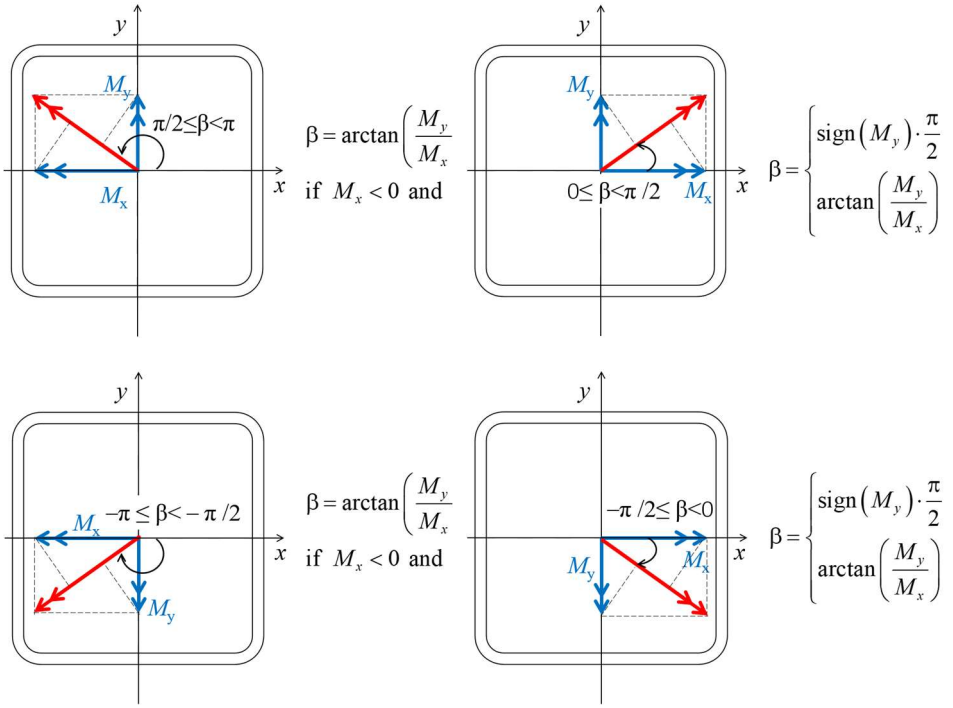


**Fig. 48** – Definition of the angle of inclination of the resulting bending moment

Once the cyclic response predicted by the numerical model has been determined, the bending moment is normalized to the maximum bending moment $M_{max,}$ and the normalized curve is used to evaluate the envelope curve corresponding to the first cycle and the chord rotations $\theta_{80\%}$ and $\theta_{50\%}$ at the achievement of a residual normalized bending moment equal to 0.80 and 0.50. The values of the response parameters corresponding to a residual normalized bending moment equal to 0.80 and 0.50 are assumed to represent the chord rotation capacity at Significant Damage (SD) and Near Collapse (NC) limit states, respectively. As an example, **Fig. 49** shows the normalized cyclic response (grey lines) of a specimen with a 400x400x16 mm cross-section, a shear span length of 1.50 m, and an axial force equal to 0.2 $N_{pl}$. The figure refers to loading directions at angles of 15° and 30° and also shows the first-cycle envelope curves (red lines) as well as the chord rotations $\theta_{80\%}$ and $\theta_{50\%}$.

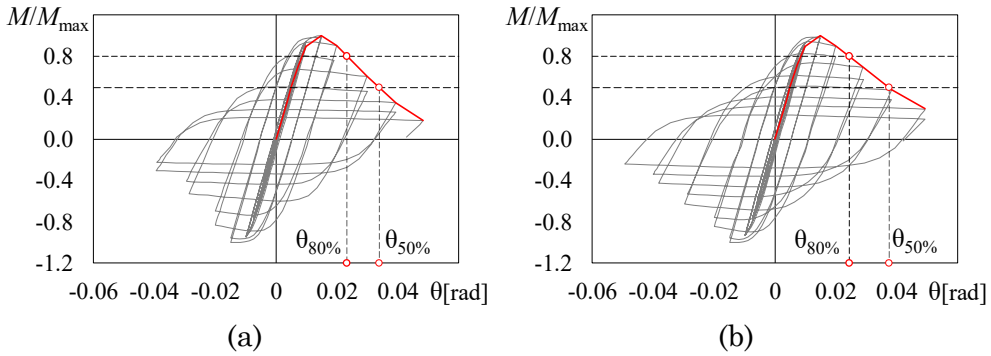


**Fig. 49** – Chord rotations corresponding to a residual normalized bending moment equal to 0.80 and 0.50 based on the first-cycle envelope curve (specimen 400x400x16, $L_v$ = 1.5 m, v=0.2): (a) φ = 15°, (b) φ = 30°

The chord rotation capacities corresponding to the achievement of the SD and NC limit states are decomposed in their projections along the *x*- and *y*-axes by means of the following relations

$$\theta_x = \theta_{\%} \cos \varphi \tag{21a}$$

$$\theta_y = \theta_{\%} \sin \varphi \tag{21b}$$

Then, $\theta_x$ and $\theta_y$ are plotted to identify trends associated with variations in the main geometric and mechanical properties of the cross-section, as well as with the increase of the external axial load. **Figs. 50a** and **b** show the components of the rotation capacities of the above exemplary specimen at the SD and NC limit states. In particular, symbols of different colours and shapes identify chord rotations corresponding to different values of the axial load ratio v. The figures clearly illustrate the detrimental effect of increasing axial load ratios on chord rotation capacity, with a more significant reduction observed for $\theta_{50\%}$. It should be noted that the values of the chord rotation capacity $\theta_{50\%}$ achieved in columns subjected to tensile axial loads or to null values of the axial loads are very high. Such values are not compatible with the stability of buildings. In addition, in laboratory tests involving very compact cross-sections, such rotations are not reached, as the applied loading protocol is generally interrupted due to limitations of the test setup.

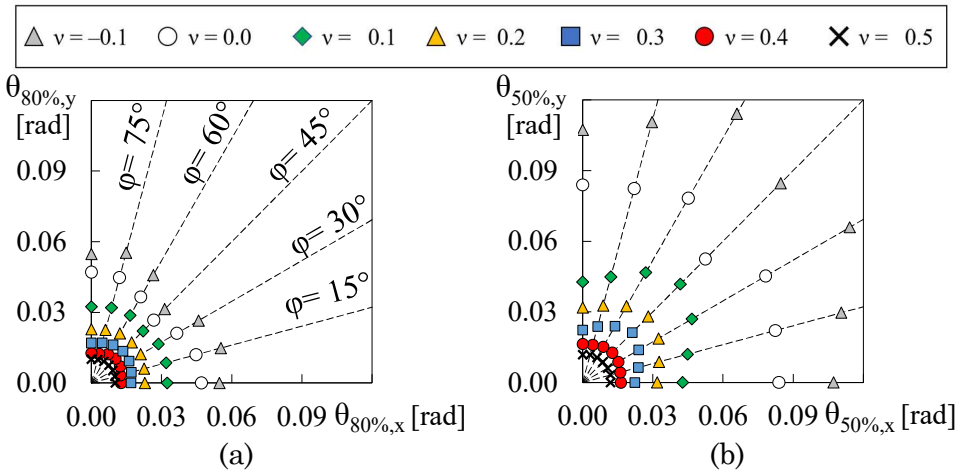


**Fig. 50** – Chord rotation domain (specimen 400×400×16, $L_v$ = 1.5 m): (a) SD and (b) NC limit state

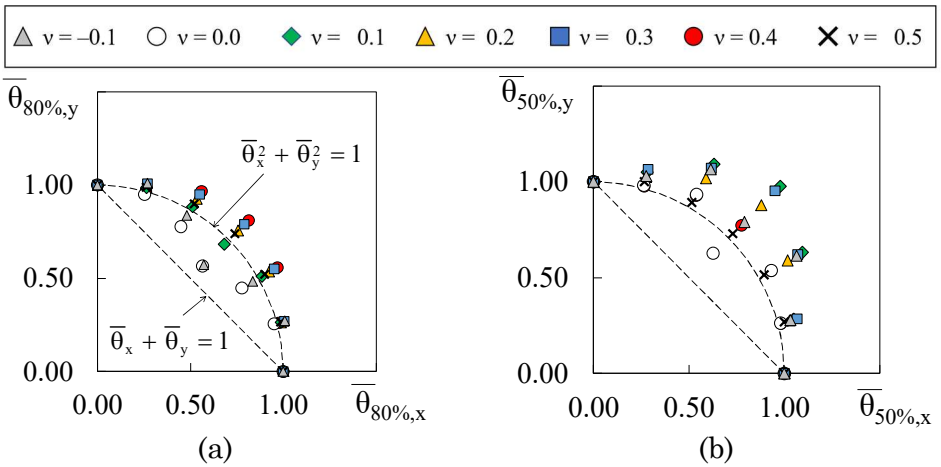


**Fig. 51** – Normalized chord rotation domain (specimen 400×400×16, $L_v$ = 1.5 m): (a) SD and (b) NC limit state

Finally, to assess the influence of the direction of the resultant displacement vector on the chord rotation capacity, the components of the chord rotation capacities are normalized to the values obtained under uniaxial bending, i.e., φ = 0° (see **Fig. 51** as an example), named as $\overline{\theta}_{80\%}$ and $\overline{\theta}_{50\%}$. Referring to this figure, dashed lines are used to represent the

curve corresponding to a chord rotation capacity magnitude that remains constant regardless of the direction of the applied displacement (i.e. $\overline{\theta}_x^2 + \overline{\theta}_y^2 = 1$) and the curve corresponding to an assigned reduction in the chord rotation capacity due to biaxial bending, described by a linear interaction domain (i.e. $\overline{\theta}_x + \overline{\theta}_y = 1$). The figure shows that, especially with reference to $\theta_{50\%}$ and columns with an axial load ratio in the range from 0.1 to 0.4, the chord rotation capacity under biaxial bending is larger than that under uniaxial bending (i.e., the dots identifying the chord rotation capacity are outside the region of the plot bounded by the curve given by the equation $\overline{\theta}_x^2 + \overline{\theta}_y^2 = 1$). This behaviour is attributed to the restraining effect exerted by the corner parts of the section, which inhibit the development of local buckling in the flat areas, and is consistent with the results of laboratory tests carried out by Ishida et al. [34]. The beneficial effect of the biaxial bending on the chord rotation capacity is not observed in the specimens subjected to low tensile ($F = -0.1\ N_{pl}$) or zero external axial forces and lateral displacements applied at an angle $\varphi = 45°$. The reasons underlying this behaviour are discussed in the Section 4, where the evolution of the plastic hinge and the associated local buckling modes are illustrated.

## 3. Trends on the finite element model responses

### 3.1. Trends in the chord rotation capacity under biaxial bending

The trends previously observed for the exemplary section are confirmed by the analysis of the cyclic response of all square-shaped HSS. Based on these trends, a normalized chord rotation capacity domain has been formulated as

$$\overline{\theta}_x^m + \overline{\theta}_y^m = 1 \tag{22}$$

where $m$ is a parameter that accounts for the reduction (values of $m$ smaller than 2.0) or the increase (values of $m$ greater than 2.0) in rotation capacity under biaxial-bending conditions. The interaction curves

corresponding to different values of the exponent $m$ (ranging from 1.0 to 10) are shown as red dashed lines in **Figs. 52-53,** with reference to square columns with varying axial load ratios.

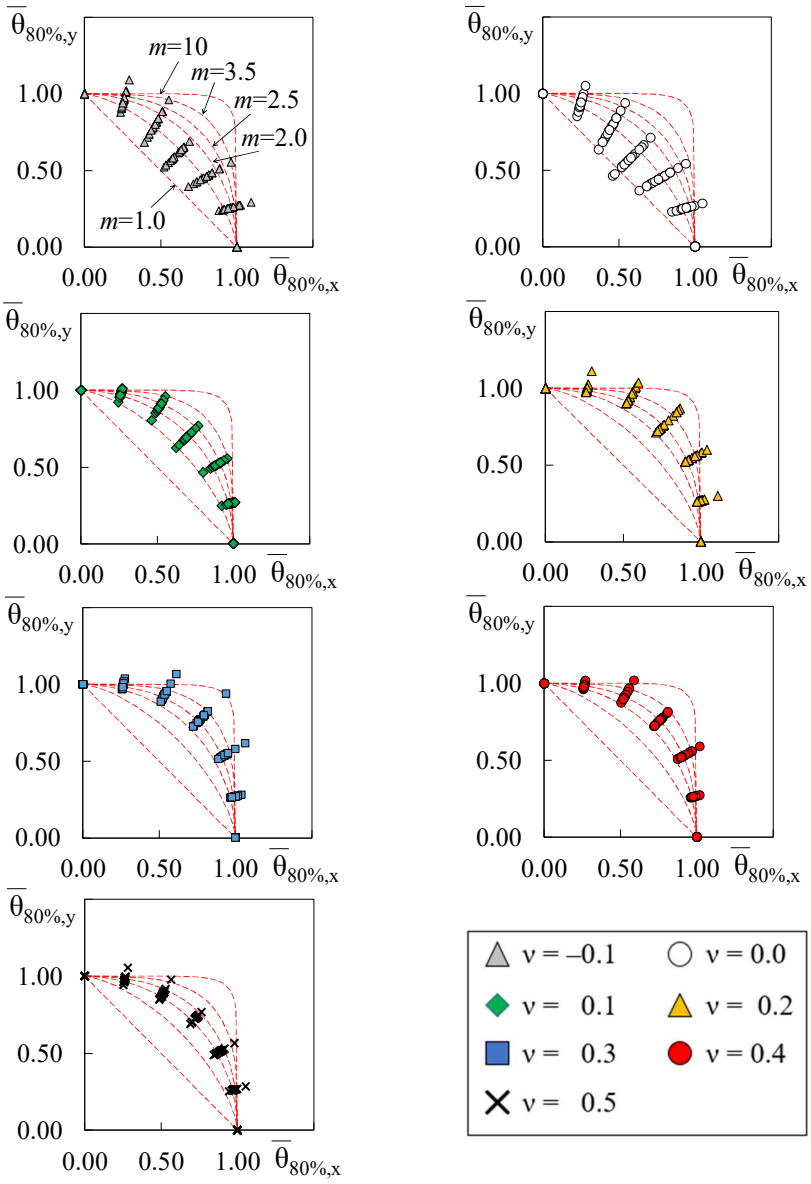


**Fig. 52** – Trends of the normalized chord rotation capacity under biaxial bending at the SD limit state: square HSS.

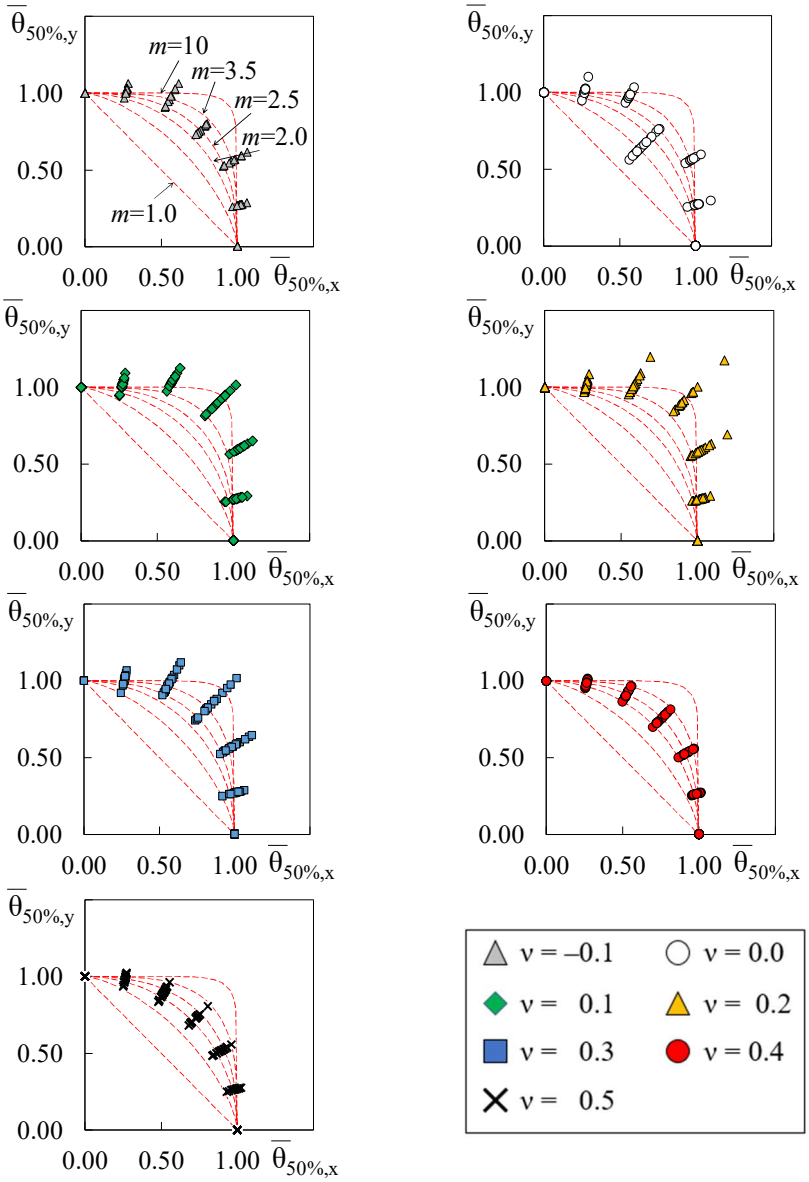


**Fig. 53** – Trends of the normalized chord rotation capacity under biaxial bending at the NC limit state: square HSS.

**Fig. 52** shows that, when referring to the chord rotation capacity at the SD limit state of columns under biaxial bending, exponent *m* should be expressed as a function of the axial load ratio. In particular, higher values of *m* should be used for intermediate axial load ratios (i.e., v between 0.2 and 0.4).

Further, the comparison of **Figs. 52-53** suggests that the same domain could be used with regard to SD and NC limit states. However, for this latter limit state, values of the exponent *m* higher than those required at the SD limit state should be used.

Regarding the specimens with rectangular-shaped HSS, the projections along the x- and y-axes of the normalized rotation capacities obtained at the SD and NC limit state are plotted in **Figs. 54-55**. it is important to note that the chord rotation capacities obtained from FE analyses at $\varphi = 0°$ and $\varphi = 90°$ are not identical. Specifically, for low values of the axial load ratio (v = 0.0, 0.1, or 0.2), the chord rotation capacities obtained at the SD limit state for $\varphi = 90°$ are either smaller or larger than those obtained for $\varphi = 0°$, depending on the size of the cross-section. This is evident in **Fig. 54,** where, for members with v = 0.0, 0.1 or 0.2, values of $\overline{\theta}_{80\%,y}$ either larger or smaller than 1.0 are obtained when $\overline{\theta}_{80\%,x}$ is equal to 0.0. In the case of specimens subjected to higher axial loads, instead, the chord rotation capacities corresponding to the achievement of the NC limit state for $\varphi = 90°$ are generally close to or larger than those obtained for $\varphi = 0°$.

Under biaxial bending, if the angle $\varphi$ is in the range from 0° to 30°, the chord rotation capacity is similar to that obtained under uniaxial bending about the major principal axis of inertia of the cross-section. Instead, a large increase in the chord rotation capacity is evident when the direction of the lateral displacements is inclined at an angle $\varphi$ in the range from 60° to 75°. The development of the plastic hinge and the local buckling modes for an illustrative rectangular cross-section are discussed in the section 4. Unlike the case of square-shaped HSS, the beneficial effect of biaxial bending on the chord rotation capacity is also observed in specimens subjected to a null value of the axial load ratio and to lateral displacements inclined at an angle $\varphi = 45°$.

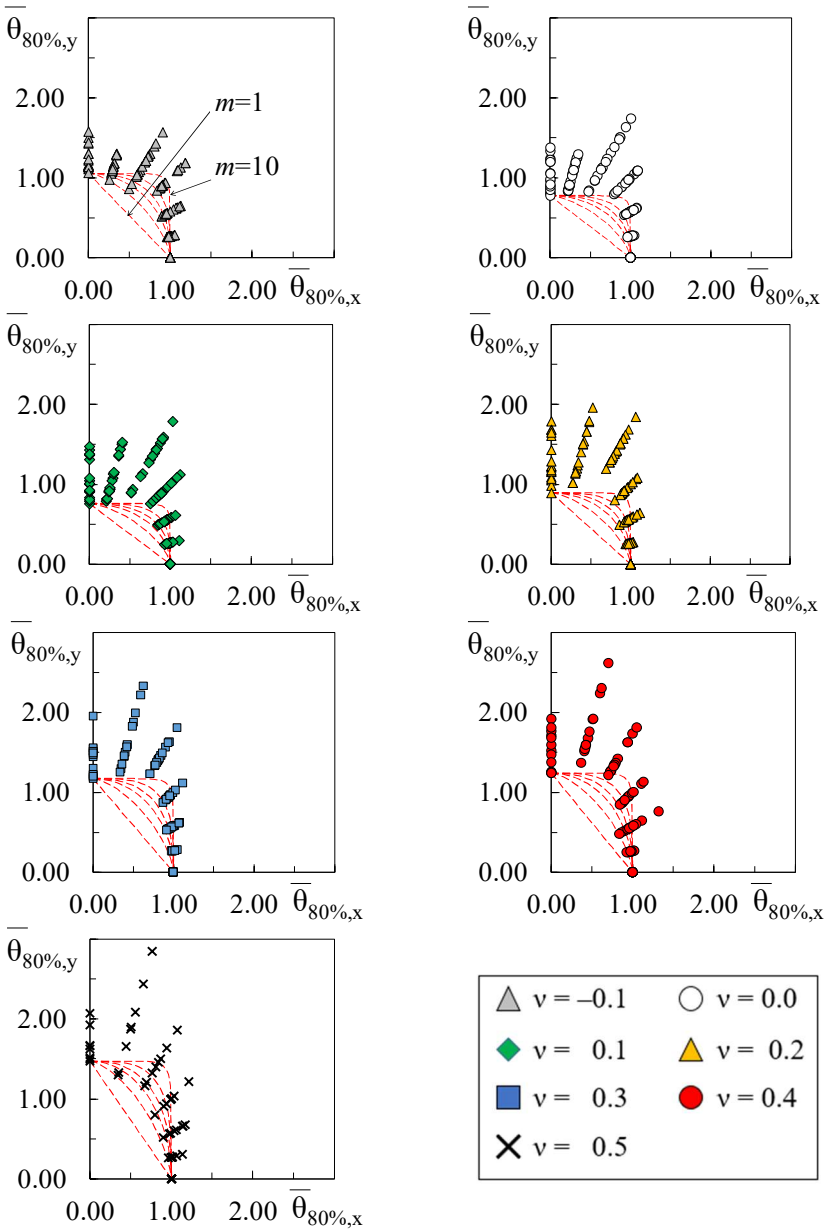


**Fig. 54** – Trends of the normalized chord rotation capacity under biaxial bending at the SD limit state: rectangular HSS

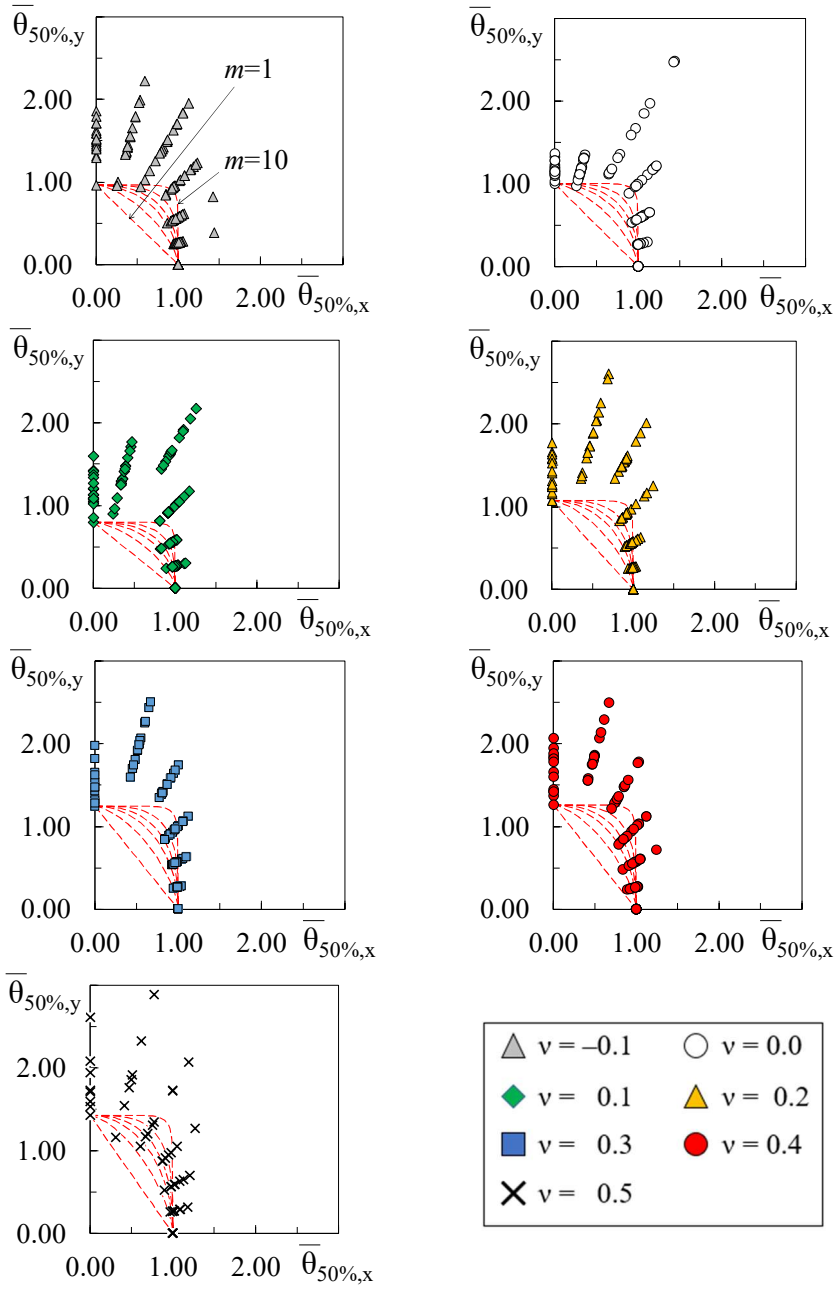


**Fig. 55** – Trends of the normalized chord rotation capacity under biaxial bending at the NC limit state: rectangular HSS

Based on these results, the proposed equation of the chord rotation capacity domain can be generalized as follows:

$$\overline{\theta}_x^m + \overline{\theta}_y^m \Big/ \eta^m = 1 \tag{23}$$

where $\eta = \theta_{90°}/\theta_{0°}$

In Eq. (23), the parameter η is introduced to account for the different chord rotation capacities of specimens with rectangular cross-sections under uniaxial bending about the minor or major principal axis of inertia of the cross-section (φ = 90° or 0°, respectively). The proposed domain is plotted in **Figs. 54-55** by red dashed lines for values of *m* ranging from 1.0 to 10. It should be noted that the parameter η depends on the geometric and mechanical properties of the cross-section. Hence, a different domain should be plotted for each considered cross-section. However, for the sake of simplicity, a single curve, referring to the cross-section characterized by the smallest value of η, has been plotted.

The comparison between the normalized chord rotation values obtained from the numerical analyses and those predicted by Eq. (22) suggests that the exponent *m* should generally be larger than that used for square cross-sections. Hence, to derive a generalized expression of the interaction domain, this exponent should be formulated as a function of both the axial load ratio and the depth-to-width ratio of the cross section.

### 3.2. Trends in the chord rotation capacity under uniaxial bending

Since the chord rotation capacity domains examined in the previous section are expressed in normalized terms with respect to the capacity under uniaxial bending, it is necessary to develop predictive equations for this reference condition. In the recent past, predictive equations of the chord rotation capacity under uniaxial bending have been proposed [44]. However, these equations cannot be applied to the present framework for three main reasons: (1) in accordance with the approach adopted in the second generation of Eurocode 8, the rotation capacities at the SD and NC limit states are defined here with reference to a residual bending capacity equal to 80% and 50% of the maximum bending moment, respectively—whereas in the equations proposed in literature, the reference

value was the plastic flexural resistance; (2) the specimens in this study are subjected to axial load ratios ranging from –0.1 to 0.5, compared to a narrower range (0.0 to 0.3) considered in the previous work; and (3) in the case of rectangular cross sections, both the chord rotation capacities under uniaxial bending about the major and minor principal axes of inertia must to be considered.

To identify predictive parameters for the chord rotation capacity at the SD and NC limit states, the logarithms of the chord rotations, $\theta_{80\%}$ and $\theta_{50\%}$, obtained from FE analyses with displacement directions at 0° or 90°, are first plotted as a function of geometric and mechanical parameters that are expected to affect the cyclic response of HSS members. To enhance the validity of the proposed equations, chord rotation capacities reported in the literature from laboratory tests (i.e. Kurata et al. [29], Fadden and McCormick [31], D'Aniello et al. [30], Mukaide et al. [35], and Suzuki and Lignos [33]) on HSS with different steel grades are also included in the investigation.

The geometric and mechanical parameters considered in the present investigation are in particular, the flange slenderness $\lambda_f$ and the web slenderness $\lambda_w$ are considered as predictors as they are strongly related to local buckling phenomena, which govern strength and stiffness degradation. These parameters are also commonly used in design codes to distinguish between compact and slender cross-sections. They are calculated as $\lambda_f = b_f/t\sqrt{f_y/E}$ and $\lambda_w = h_w/t\sqrt{f_y/E}$, where $t$ is the wall thickness, while $h_w$ and $b_f$ are obtained from the cross-sectional depth $h$ and width $b$, respectively, by subtracting twice the exterior corner $r_e$. The depth-to-width ratio $h_w/b_f$ is introduced to account for the different behaviour observed in square and rectangular cross-sections. To describe the portion of the member involved in plastic dissipation, attention is also focused on the half-wavelength of the buckled flange $L_m$, which is calculated as $L_m = 1.2\,b_f\left(h/b_f\right)^{0.25}$ [30], and on the slope of the bending moment diagram. Since the plastic bending moment is fixed, the slope of the bending moment diagram is captured by the shear span length $L_v$. To make use of normalized parameters, the shear span length is normalized to either the

depth ($L_v/h_w$), the width ($L_v/b_f$), or to the half-wavelength of the buckled flange ($L_m/L_v$). Finally, the axial load ratio ν is considered because it is used is in the current Eurocode 8 to distinguish between ductile (specimens with $\nu \leq 0.30$) and fragile (specimens with $\nu > 0.30$) members.

It should be noted that, in the definition of all the aforementioned parameters, the depth of the cross-section is taken as parallel to the displacement loading direction.

The linear relationship between each parameter and the logarithms of chord rotation capacity at the SD and NC limit states is evaluated using the coefficient of determination ($R^2$), derived from the Pearson product-moment correlation. As an example, **Fig. 56a** shows the logarithms of the chord rotations $\theta_{80\%}$ as a function of the axial load ratio in the range from -0.1 to 0.5. In particular, coloured symbols pinpoint results of numerical analyses, whereas black symbols pinpoint results from laboratory tests. The figure demonstrates good agreement between FE and laboratory results and confirms the strong influence of the axial load ratio on the chord rotation capacity. On the other hand, **Figs. 56b-f** present the logarithms of the chord rotation capacity $\theta_{80\%}$ as a function of some of the other above-mentioned parameters, considering only two values of the axial load ratios (i.e., $\nu = 0$ or 0.3). For each value of the axial load ratio, trend lines and coefficients of determination are also reported. Among the considered axial load ratios, the slenderness of the web $\lambda_w$ is the parameter that mostly affects the chord rotation capacity, with coefficients of determination equal to 0.47 or 0.59 for $\nu = 0$ and 0.3, respectively. The slenderness of the flange $\lambda_f$ primarily influences the chord rotation capacity in specimens with a zero axial load ratio, whereas an opposite trend is recorded for the parameter $L_v/h_w$. The ratio $L_m/L_v$ has a moderate influence on the chord rotation capacity, regardless of the axial load ratio. Finally, the coefficients of determination calculated with reference to the parameter $h_w/b_f$ are close to 0.0.

These trends are confirmed by the analysis of the coefficients of determination calculated for all the examined parameters concerning HSS members at the SD and NC limit states (see **Fig. 57)**. With specific regard to the NC limit state, the values of $R^2$ obtained for members subjected to

tensile axial loads are not reported here. Indeed, as already mentioned, the chord rotation capacities achieved for such columns are not considered compatible with the stability of columns belonging to buildings. In addition, there are no laboratory tests available in the literature that can validate the results of numerical results in the case of members subjected to the combined effect of tensile force and bending moments. Therefore, these values are not considered for the calibration of the predictive equations.

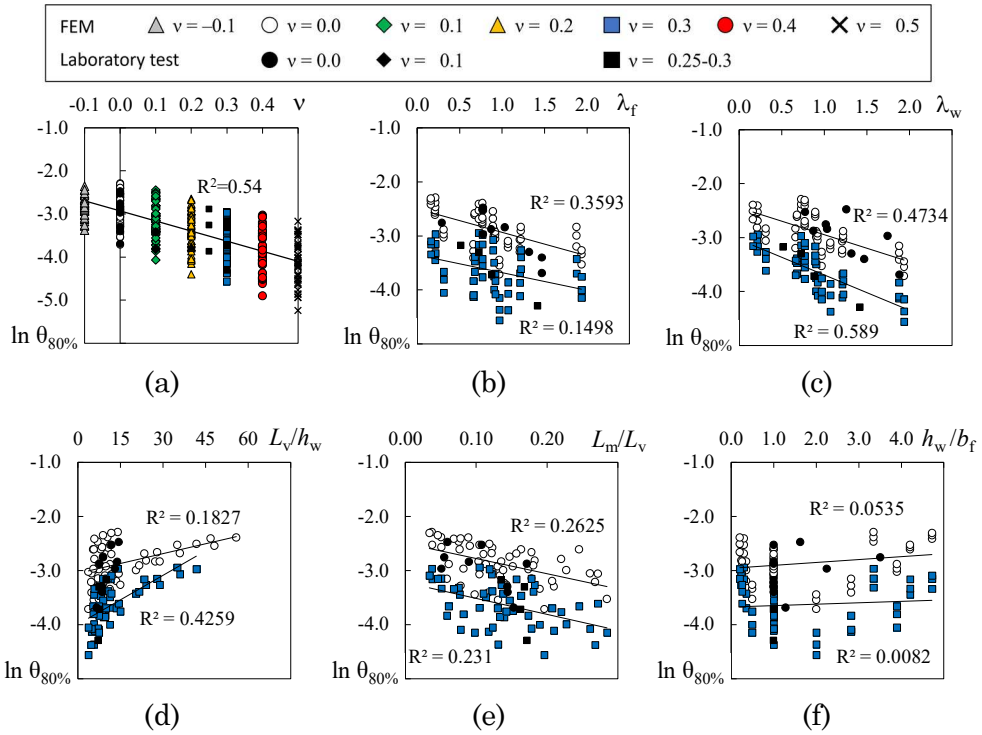


**Fig. 56** – Natural logarithm of the chord rotation at the SD limit state as a function of (a) ν, (b) $\lambda_f$ , (c) $\lambda_w$, (d) $L_v/h_w$, (e) $L_m/L_v$, (f) $h_w/b_f$. ($\theta_{80}$ expressed in rad).

The trends shown in **Fig. 57** clearly show that the ratio $h_w/b_f$ is not linearly related to the logarithms of the chord rotation capacity. However, it is believed that the above ratio should have an influence on the chord rotation capacity of members. Indeed, the ratio $h_w/b_f$ affects the relative

stiffness between the web and the flange. In particular, the flexural stiffness provided by the web–corners assembly at the ends of the flange plates increases as the ratio $h_w/b_f$ decreases, thus modifying the flange slenderness. Similarly, the flexural stiffness provided by the flange–corners assembly at the ends of the web plates decreases as the ratio $h_w/b_f$ decreases, thus modifying the web slenderness. To confirm this idea, the coefficient of determination between the slenderness of the flange $\lambda_f$ and the chord rotation capacity of HSS members at the SD and NC limit states is calculated again, considering only square cross-sections. Values referring to the web slenderness are not reported because, for square cross-sections, the two values of slenderness are equal. The comparison of the $R^2$ values reported in **Figs. 57 and 58** shows that the correlation between the slenderness of the flange $\lambda_f$ (and hence that of the web) with the logarithms of the chord rotation capacity is different for specimens characterized by different values of the ratio $h_w/b_f$.

Based on the observed trends, two formulations are preliminarily selected to predict the chord rotation capacity at the SD and NC limit states under uniaxial bending, i.e.

$$\theta_{pred}\left(\varphi = 0°, \varphi = 90°\right) = C_0 \cdot \lambda_f^{C_f\left(h_w/b_f\right)} \cdot \lambda_w^{C_w\left(h_w/b_f\right)} \cdot \left(L_m/L_V\right)^{C_L} \cdot \left(1-\nu\right)^{C_\nu} \cdot \varepsilon \tag{24}$$

$$\theta_{pred}\left(\varphi = 0°, \varphi = 90°\right) = C_0\left(\nu\right) \cdot \lambda_f^{C_f\left(h_w/b_f,\nu\right)} \cdot \lambda_w^{C_w\left(h_w/b_f,\nu\right)} \cdot \left(L_m/L_V\right)^{C_{L(\nu)}} \cdot \varepsilon \tag{25}$$

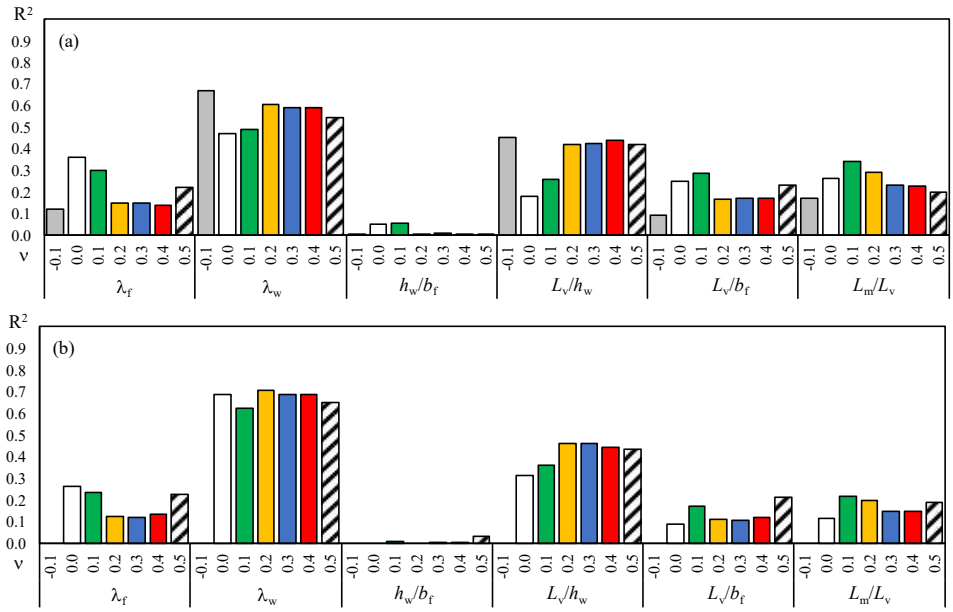


**Fig. 57** – Coefficient of determination related to different parameters and the logarithms of the chord rotation capacity at the (a) SD and (b) NC limit states.

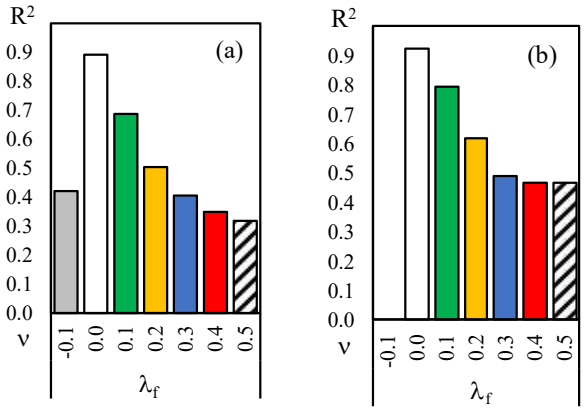


**Fig. 58** – Coefficient of determination related to the flange slenderness and the logarithms of the chord rotation capacity at the (a) SD and (b) NC limit states: square cross-sections

In the previous equations, the flange and web slenderness $\lambda_f$ and $\lambda_w$, and the ratio $L_m/L_v$ are considered predictors. The terms $C_0$, $C_f$, $C_w$, $C_L$, and $C_v$ are regression coefficients, while $\varepsilon$ represents the residuals. The regression coefficients related to the web and flange slenderness, i.e., $C_f$ and $C_w$, are assumed to be functions of the $h_w/b_f$ ratio. The two equations incorporate the effect of the axial load ratio in different ways. Specifically, in Eq. (24) the term (1-v) is used as a predictor, whereas in Eq. (25) the regression coefficients are expressed as a function of the axial load ratio v. In both equations, the shear span-to-depth ratio $L_v/h_w$ has been excluded as a predictor due to collinearity issues.

## 4. Evolution of the plastic hinge

To explain the differences in rotation capacity observed under uniaxial and biaxial bending, the cross-section 400×400×20 and the 350×150×14.2 are considered as an illustrative case of square and rectangular cross-sections, respectively.

For the square cross-section, two displacement angles (i.e., $\varphi = 0°$ and $\varphi = 45°$) are examined. **Figs. 59a** and **59b** show the chord rotation capacities $\theta_{80\%}$ and $\theta_{50\%}$, respectively, for increasing values of the axial load ratio. In each figure, two curves are plotted, each corresponding to one of the considered displacement angles. The figures show that, for $\varphi = 0°$, the rotation capacity $\theta_{80\%}$ significantly decreases with the increase of the axial load ratio, whereas this reduction is less pronounced for $\varphi = 45°$. Owing to these different trends, in the absence of axial load the rotation capacity corresponding to $\varphi = 45°$ is lower than that corresponding to $\varphi = 0°$. Conversely, for an axial load ratio equal to $v = 0.3$, the rotation capacity associated with $\varphi = 45°$ becomes slightly greater than that corresponding to $\varphi = 0°$.

To explain these different trends, the development of the plastic hinge and, in particular, the local buckling modes are illustrated for increasing values of the chord rotation in members with axial load ratios equal to 0 and 0.3.

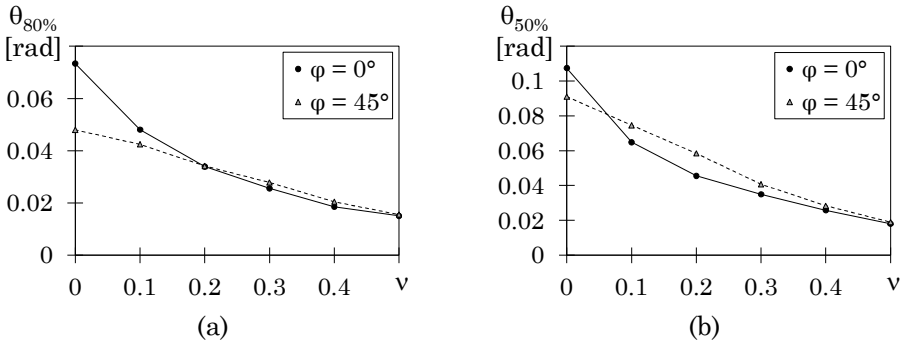


**Fig. 59** – Values of the chord rotation capacities (a) $\theta_{80\%}$ and (b) $\theta_{50\%}$ for increasing axial load ratios (cross-section 400x400x20 with $L_v$ = 2.25 m)

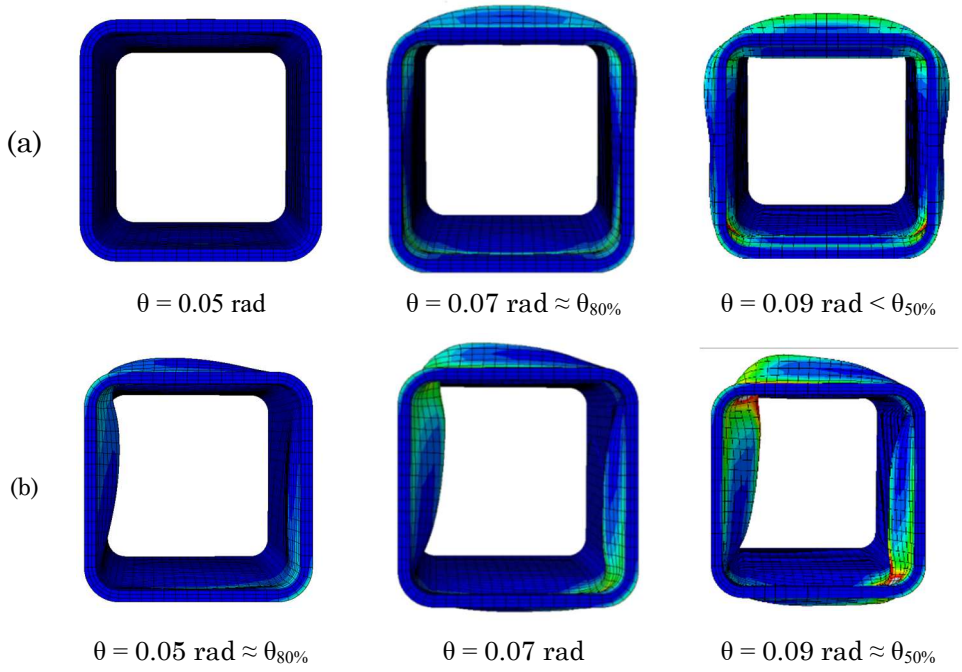


**Fig. 60** – Plastic hinge development for specimen 400×400×20 with ν = 0 subjected to loading protocols with different displacement angles: (a) φ=0°; (b) φ=45°.

In the following explanation, the cross-section sides that are partially in compression and intersected by the neutral axis are named webs. This clarification is necessary as, in biaxial bending, the inclination of the neutral axis is variable and, thus, flanges and webs are not univocally identified. In general, the strength degradation appears to be primarily related to web buckling.

For $\nu = 0$ and $\varphi = 0°$ (**Fig. 60a**), no appreciable local buckling occurs up to a chord rotation of 0.05 rad. At larger rotations, local buckling of the flanges develops, while the webs retain their strength and stiffness. Indeed, at flange buckling, the neutral axis is parallel to the flanges, and only half of each web is subjected to compressive axial stresses. Web buckling becomes appreciable at a chord rotation of 0.07 rad, i.e., at a rotation close to that identified as $\theta_{80\%}$. At a chord rotation of 0.10 rad, i.e., corresponding approximately to $\theta_{50\%}$, the strength degradation becomes significant. This loss of strength is induced by combined buckling of flanges and webs, which also causes rotation of the four corner regions.

Conversely, when the same cross-section is subjected to loading protocols with a displacement angle $\varphi = 45°$ **Fig. 60b**), the neutral axis orientation causes flange and web buckling to occur simultaneously at a chord rotation of approximately 0.04 rad. This leads to rapid strength degradation, thereby explaining the lower rotation capacity observed at the SD limit state for specimens subjected to zero axial load ratio.

For $\nu = 0.3$, the portion of the webs subjected to compressive axial stresses becomes significant also in the case of $\varphi = 0°$ (**Fig. 61a**). Consequently, buckling of both webs and flanges occurs at chord rotations similar to those observed for $\varphi = 45°$. However, in the latter case, buckling of flanges and webs is less pronounced and no longer symmetric with respect to the horizontal and vertical axes of the cross-section, since two of the four corners retain their restraining effect (**Fig. 61b**).

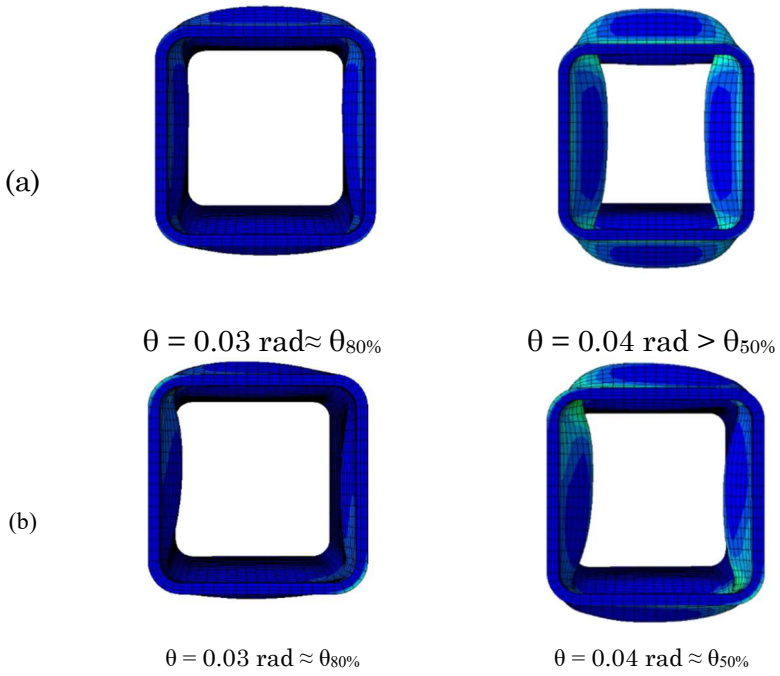


**Fig. 61** – Plastic hinge development for specimen 400×400×20 with ν = 0.3 subjected to loading protocols with different displacement angles: (a) φ=0°; (b) φ=45°.

With regard to the rectangular cross-sections, instead, the largest increase in rotation capacity occurs, irrespective of the axial load ratio, for displacement angles in the range from 60° to 75°. Accordingly, the cases with φ = 0° (**Fig. 62a**) and φ = 75° (**Fig. 62b**), with ν=0.3, are taken herein as representative cases.

In the case of φ = 0°, no local buckling occurs up to a chord rotation equal to 0.02 rad. At a chord rotation of 0.03 rad (approximately corresponding to $\theta_{80\%}$) web buckling occurs before local buckling of the flanges becomes appreciable. This behaviour is due to the low slenderness ratio of the flanges, while half of the web is in compression. Web buckling induces rotation of the corner parts and subsequently triggers flange buckling (θ = 0.04 rad ≈ $\theta_{50\%}$). In the case of φ = 75°, by contrast, the flanges

exhibit a larger slenderness ratio than the web, which therefore retains its stiffness.

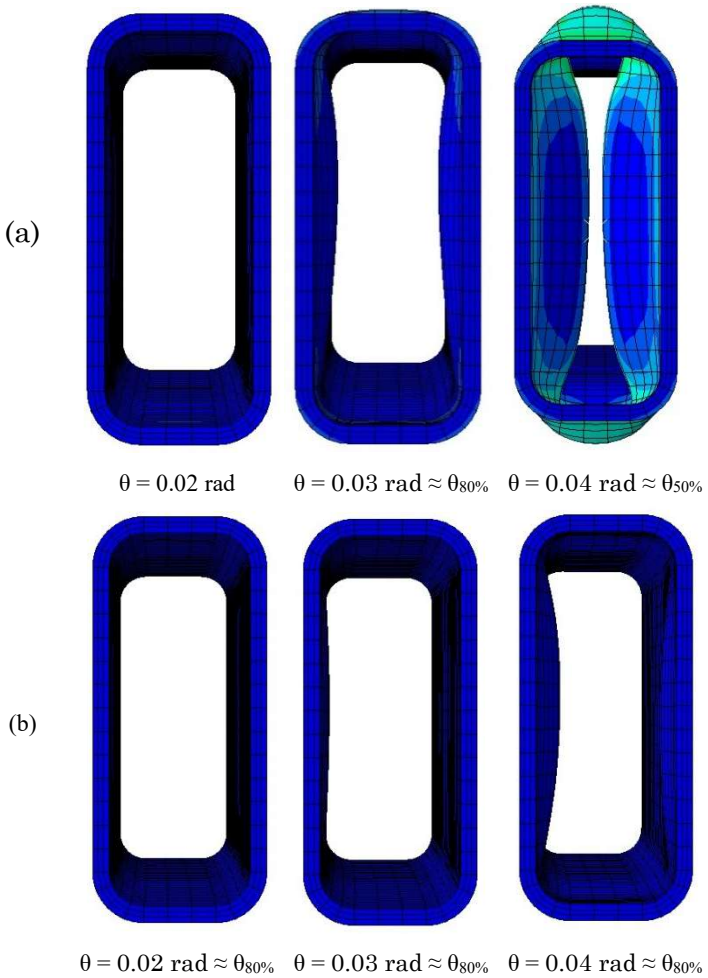


**Fig. 62** – Plastic hinge development for specimen 350×150×14.2 with ν = 0.3 subjected to loading protocols with different displacement angles: (a) φ=0°; (b) φ=75°.

## 5. Formulation of the chord rotation capacity under biaxial bending

To predict the chord rotation capacity under biaxial bending, the normalized chord rotation capacities ($\theta_x$ and $\theta_y$) are first expressed as:

$$\overline{\theta}_x = \frac{\theta \cos\varphi}{\theta_{\text{pred}}\left(\varphi = 0°\right)} \tag{26a}$$

$$\frac{\overline{\theta}_y}{\eta} = \frac{\theta \sin\varphi}{\theta_{\text{pred}}\left(\varphi = 0°\right)} \cdot \frac{\theta_{\text{pred}}\left(\varphi = 0°\right)}{\theta_{\text{pred}}\left(\varphi = 90°\right)} \tag{26b}$$

where $\varphi$ is the angle of the displacement loading direction. Still in the same equations, $\theta_{\text{pred}}$ ($\varphi$ = 0°) and $\theta_{\text{pred}}$ ($\varphi$ = 90°) are the chord rotation capacities corresponding to angles of the displacement loading direction equal to 0° or 90°, respectively. These latter chord rotation capacities are formulated by either Eq. 24 or Eq. 25.

Then, Eqs. 26a and 26b are substituted into Eq. (23), and the chord rotation capacity under biaxial bending is obtained as:

$$\theta_{\text{pred}}\left(\varphi\right) = \frac{\theta_{\text{pred}}\left(\varphi = 0°\right) \cdot}{\sqrt[m]{\left(\cos\varphi\right)^m + \left(\sin\varphi/\eta\right)^m}} \tag{27}$$

To determine the values of the regression coefficients needed for the prediction of the chord rotation capacity under biaxial bending, a regression analysis is conducted on the log-transformed data, and the least-squares method is used. In particular, the regression analysis has been performed with reference to both the SD and NC limit states, following either of the two proposed alternative formulations of the uniaxial chord rotation capacity (i.e., Eq. 24 or Eq. 25).

It should be noted that an additional constraint has been considered within the optimization problem to obtain normally-distributed logarithms of the residuals. To enforce this latter constraint, the Jarque-Bera [71] test has been performed on the logarithms of the residuals, and a p-value not less than 0.30 has been required.

The optimal regression coefficients ($C_0$, $C_f$. $C_w$, $C_L$, $C_v$, and $m$) are reported in **Tables 18-21**.

**Table 18 –** Proposed regression coefficients at the SD limit state, if the chord rotation capacity under uniaxial bending is calculated by Eq. (24)

| Regression coefficient | Proposed expression |
|---|---|
| $C_0$ | 0.022 |
| $C_f$ | $0.047\,h_w/b_f - 0.16$ |
| $C_w$ | $-0.16\,h_w/b_f - 0.383$ |
| $C_L$ | −0.354 |
| $C_V$ | 1.734 |
| m | $\left(9.12\,\nu^2 - 6.0\nu + 2.84\right)\left(0.753\,h_w/b_f + 0.247\right)$ *if* $\nu \geq 0$<br>$2.84\left(0.753\,h_w/b_f + 0.247\right)$ *if* $-0.1 \leq \nu < 0$ |

**Table 19 –** Proposed regression coefficients at the SD limit state, if the chord rotation capacity under uniaxial bending is calculated by Eq. (25)

| Regression coefficient | Proposed expression |
|---|---|
| $C_0$ | $\exp\left(-4.24\nu - 3.53\right)$ |
| $C_f$ | $\max\left(-0.708\,\nu + 0.015, 0.036\right)h_w/b_f + 0.608\,\nu - 0.221$ |
| $C_w$ | $\left(0.10\,\nu - 0.176\right)h_w/b_f - 0.833\,\nu - 0.250$ |
| $C_L$ | $-0.903\nu - 0.246$ |
| m | $\left(-22.8\,\nu^2 + 13.9\nu + 1.496\right)\left(1.485\,h_w/b_f - 0.485\right)$ *if* $\nu \geq 0$<br>$1.496\left(1.485\,h_w/b_f - 0.485\right)$ *if* $-0.1 \leq \nu < 0$ |

**Table 20 –** Proposed regression coefficients to be used at the NC limit state, if the chord rotation capacity under uniaxial bending is calculated by Eq. (24)

| Regression coefficient | Proposed expression |
|---|---|
| $C_0$ | 0.042 |
| $C_f$ | $0.045\,h_w/b_f - 0.17$ |
| $C_w$ | $-0.164\,h_w/b_f - 0.446$ |
| $C_L$ | −0.255 |
| $C_V$ | 2.260 |
| m | $\left(42\nu^2 - 19.8\nu + 4.07\right)\left(6\,h_w/b_f - 5\right)$ |

**Table 21 –** Proposed regression coefficients at the NC limit state, if the chord rotation capacity under uniaxial bending is calculated by Eq. (25)

| Regression coefficient | Proposed expression |
|---|---|
| $C_0$ | $\exp(-5.29\nu - 2.77)$ |
| $C_f$ | $\left(-0.417\nu^2 + 0.425\,\nu - 0.036\right)h_w/b_f - 0.344\,\nu$ |
| $C_w$ | $\min(-0.293\,\nu + 0.027, -0.166)\,h_w/b_f - 0.69\,\nu - 0.296$ |
| $C_L$ | $-1.02\nu - 0.10$ |
| m | $\left(28\,\nu^2 - 12.5\,\nu + 3.93\right)\left(5\,h_w/b_f - 4\right)$ |

To provide a comprehensive assessment of the accuracy of the proposed formulation, the chord rotation capacities predicted for all the considered specimens by means of the proposed expressions have been compared in **Figs. 63 and 64** to those resulting from the FE models. Specifically, while **Fig. 63** refers to the chord rotation capacities corresponding to the SD limit state, **Fig. 64** refers to the chord rotation capacities at the NC limit state. In each figure, the results refer to all the considered cross-sections and angles of the displacement loading direction. Symbols with different colours and shapes have been used to indicate the axial load ratio of the specimen. The figures show that the prediction of the chord rotation capacities is more accurate when the regression coefficients are expressed as a function of the axial load ratio (**Figs. 63b** and **64b**), particularly in the case of high rotation capacities. However, even when the regression coefficients are defined regardless of the axial load ratio (**Figs. 63a** and **64a**), the maximum error in the predicted chord rotation capacity at the SD limit state only occasionally exceeds 20%. Larger errors are observed in the predicted chord rotation capacities at the NC limit state. Despite these discrepancies, the obtained coefficients of determination remain high, ranging from 0.94 (achieved when $\theta_{50\%}$ is predicted by Eq. (24)) to 0.97 (achieved when $\theta_{80\%}$ is predicted by Eq. (25)).

To statistically characterize the logarithms of the residuals, they have been calculated for both the SD and NC limit states, and their frequency distribution is illustrated using bar charts in **Figs. 65** and **66.**

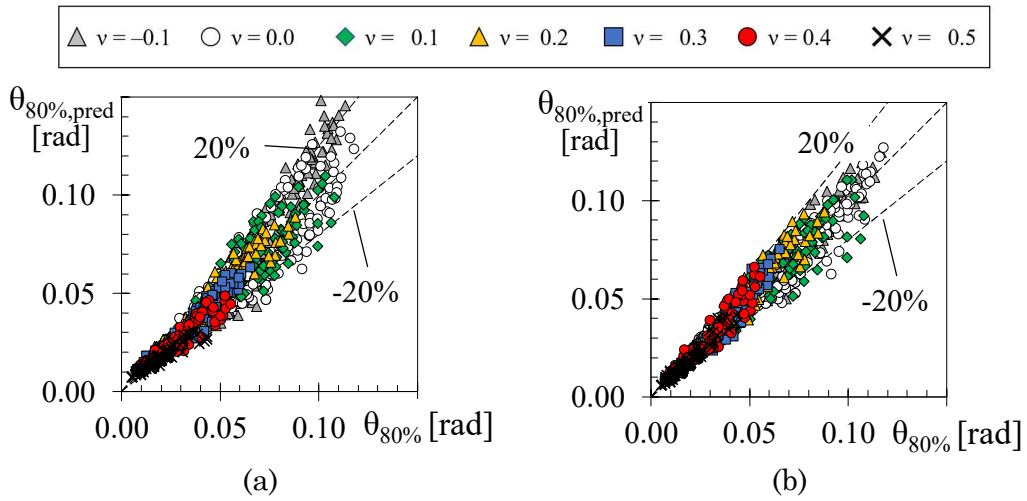


**Fig. 63** – Accuracy of the proposed equation in predicting the chord rotation capacity at the SD limit state: prediction by (a) Eq. (24) and (b) Eq. (25).

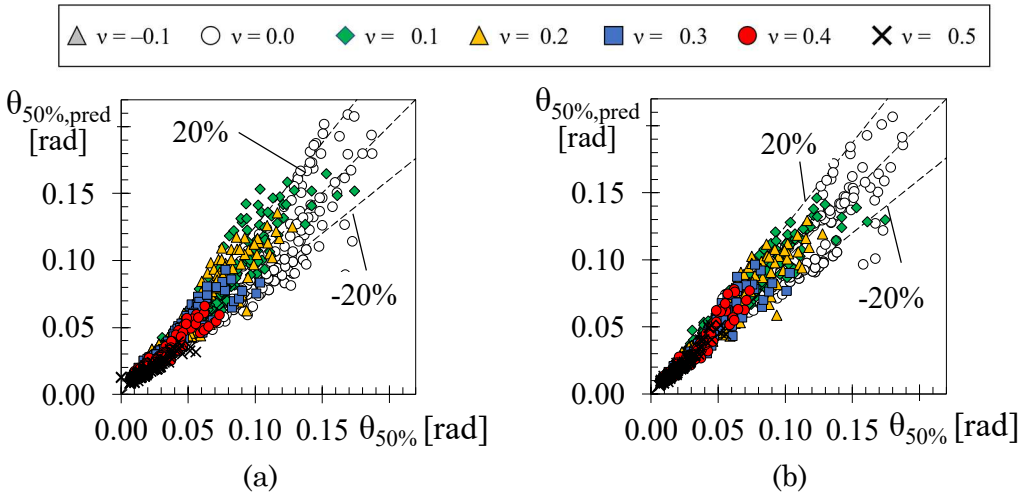


**Fig. 64** – Accuracy of the proposed equation in predicting the chord rotation capacity at the NC limit state: prediction by (a) Eq. (24) and (b) Eq. (25)

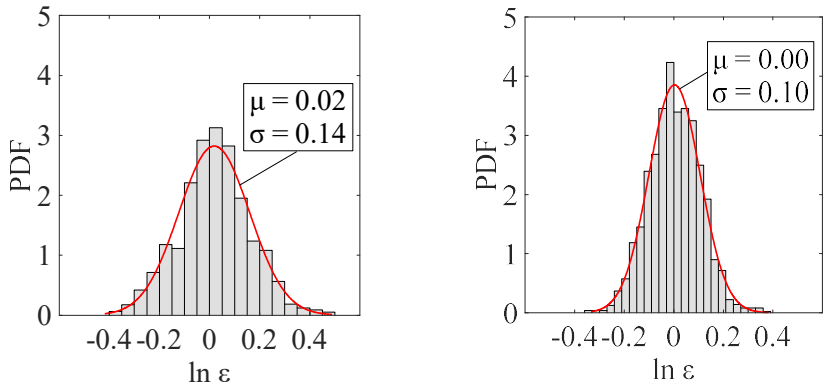


**Fig. 65** – Estimate of the logarithms of residuals in predicting the chord rotation capacity at the SD limit state: prediction by (a) Eq. (24) and (b) Eq. (25)

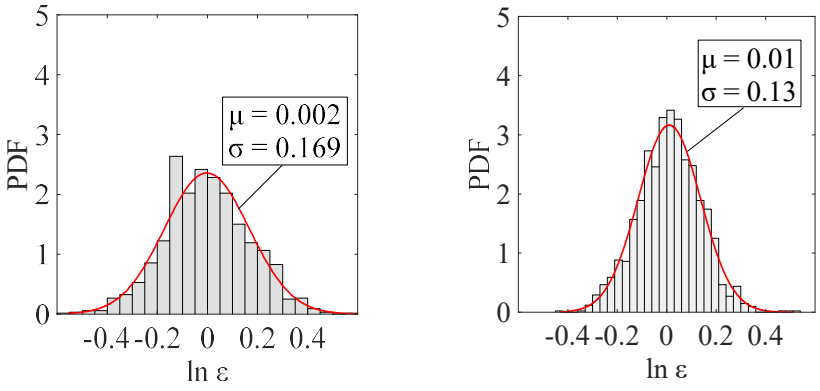


**Fig. 66** – Estimate of the logarithms of residuals in predicting the chord rotation capacity at the NC limit state: prediction by (a) Eq. (24) and (b) Eq. (25)

Inspection of the frequency distribution charts confirms that the logarithms of the residuals can be described by a normal distribution and that the mean value of the logarithms of the residuals is always close to 0.0. In the same figures, the normal distribution that best fits the data is

also reported, together with the mean and standard deviation of this normal distribution.

To more deeply investigate the influence of the angle of the displacement loading direction on the accuracy of the proposed equations, the frequency distribution of the logarithms of the residuals is shown in **Figs. 67 and 68** as a function of the assigned angle of the displacement loading direction. Specifically, **Figs. 67a and 68a** refer to residuals obtained when the chord rotation capacity under uniaxial bending is predicted by Eq. (24); **Figs. 67b and 68b**, instead, correspond to predictions obtained by Eq. (25). For each angle of the displacement loading direction, red dots also indicate the value of the logarithms of the residuals corresponding to the 50$^{th}$ percentile.

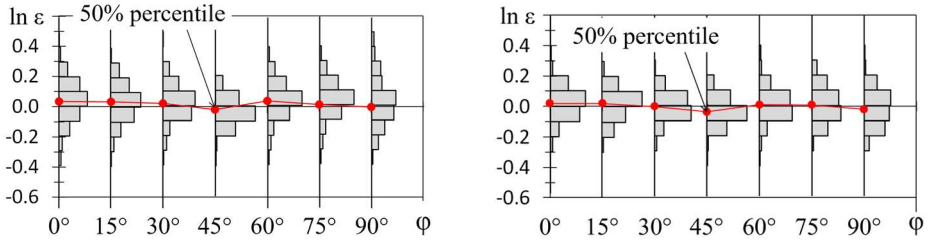


**Fig. 67** – Frequency distribution of the logarithms of the residuals at the SD limit state in the case of chord rotation capacity predicted by: (a) Eq. (24) and (b) Eq. (25).

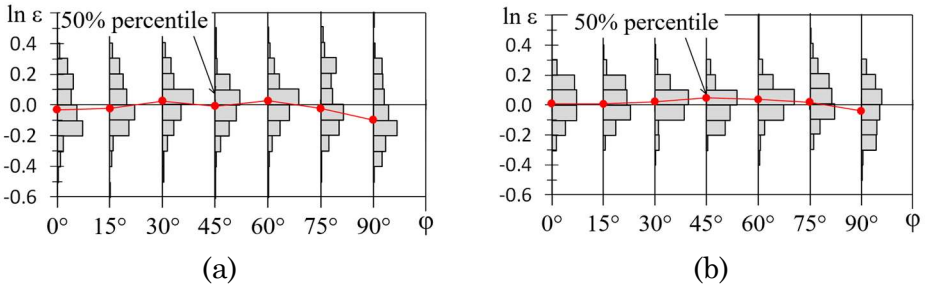


**Fig. 68** – Frequency distribution of the logarithms of the residuals at the NC limit state in the case of chord rotation capacity predicted by: (a) Eq. (24) and (b) Eq. (25).

Inspection of the frequency distribution charts suggests that: (1) the assumption that the logarithms of the residuals follow a normal distribution remains reasonable, regardless of the considered angle of the displacement loading direction; (2) the 50$^{th}$ percentile value is close to zero, particularly when the chord rotation capacity under uniaxial bending is predicted by Eq. (25).

## 6. Validation of the predictive equations with datasets different from those used for the calibration

To validate the accuracy of the proposed predictive equations against specimens different from those used in the calibration, two additional datasets are considered.

The first set comprises five cross-sections selected so as to cover a wide range of $b_f/t$ values. Very small cross-sections have been disregarded, as these sections do not find application in columns of moment resisting frames. Five cases were investigated for each cross-section. These cases were obtained assigning random values of the shear span length, axial load ratio and angle of displacement values (as reported in **Table 22**).

Furthermore, to validate the predictive equations also in the case of specimens with amplitude of imperfections smaller than that used in the parametric analyses, each of the considered specimens was investigated three times, considering an amplitude of the imperfection equal to either 0.1%, 0.35% and 0.64% of the cross-section width. This latter value corresponds to 80% of the fabrication tolerance used for European profiles.

**Figs. 69** and **70** present a comparison between the rotation capacity predicted by the proposed equations and that obtained from numerical models. Specifically, imperfection amplitudes equal to 0.1%, 0.35%, and 0.64% of the cross-section width are represented by white, grey, and black dots, respectively. The analysis of the figures, together with the coefficients of determination obtained for the different imperfection levels (**Table 23**), confirms that the prediction of rotation capacity maintains good accuracy within the considered range of imperfections. A slight reduction

in the coefficient of determination is observed for specimens with very low imperfection amplitudes.

**Table 22** – Features of the additional numerical cases considered for the validation of the proposed predictive equations.

| Section | | Case 1 | Case 2 | Case 3 | Case 4 | Case 5 |
|---|---|---|---|---|---|---|
| S250×250×10.0 | $L_v$ [mm] | 1500 | 2250 | 2250 | 2250 | 3000 |
| | v | 0.5 | 0.2 | 0.3 | 0.4 | 0.10 |
| | φ | 0° | 45° | 30° | 15° | 0° |
| S300×300×14.2 | $L_v$ [mm] | 1500 | 2250 | 2250 | 2250 | 3000 |
| | v | 0.4 | 0.1 | 0.2 | 0.3 | 0.00 |
| | φ | 15° | 0° | 45° | 30° | 15° |
| S300×200×10.0 | $L_v$ [mm] | 1500 | 2250 | 2250 | 2250 | 3000 |
| | v | 0.3 | 0.0 | 0.1 | 0.2 | 0.20 |
| | φ | 90° | 75° | 30° | 0° | 45° |
| S400×400×12.5 | $L_v$ [mm] | 1500 | 2250 | 2250 | 2250 | 3000 |
| | v | 0.4 | 0.1 | 0.2 | 0.3 | 0.0 |
| | φ | 45° | 30° | 15° | 0° | 45° |
| S200×200×9.0 | $L_v$ [mm] | 1500 | 2250 | 2250 | 2250 | 3000 |
| | v | 0.2 | 0.0 | 0.1 | 0.5 | 0.3 |
| | φ | 30° | 0° | 45° | 15° | 30° |

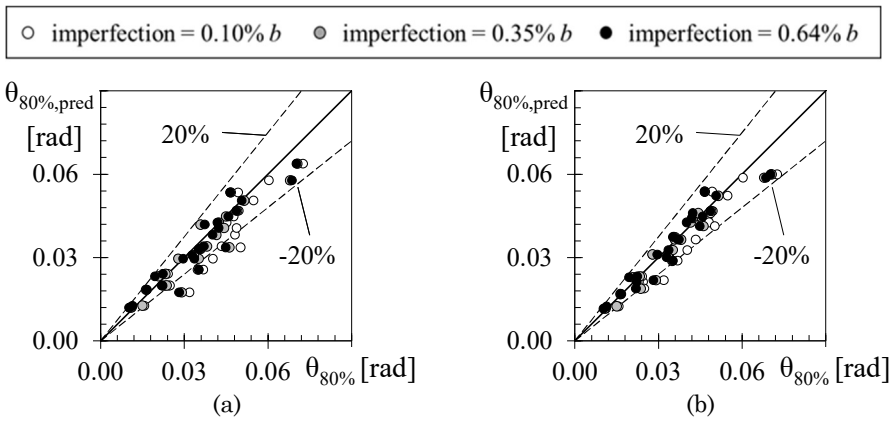


**Fig. 69** – Accuracy of the proposed equation in predicting the chord rotation capacity at SD limit state obtained by a second dataset of specimens: prediction by (a) Eq. (24) and (b) Eq. (25).

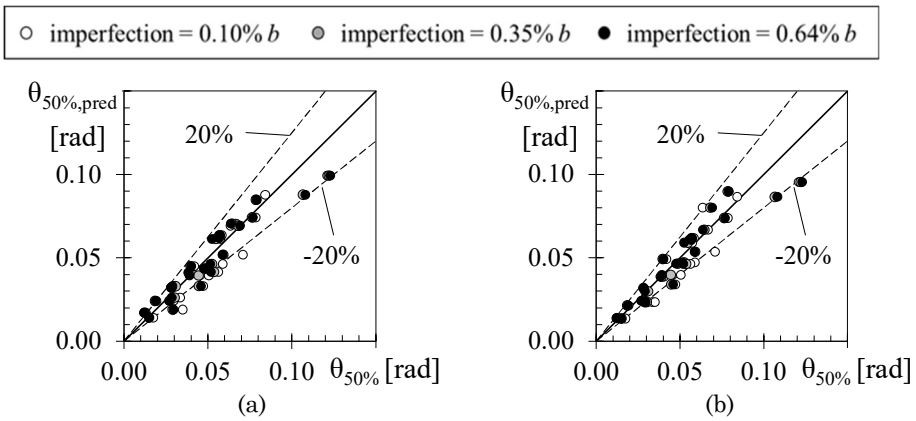


**Fig. 70** – Accuracy of the proposed equation in predicting the chord rotation capacity at NC limit state obtained by a second dataset of specimens: prediction by (a) Eq. (24) and (b) Eq. (25).

**Table 23** – Coefficients of determination for specimens with different amplitude imperfections

| Imperfection amplitude | $\theta_{80\%}$ by Eq (24) | $\theta_{80\%}$ by Eq (25) | $\theta_{50\%}$ by Eq (24) | $\theta_{50\%}$ by Eq (25) |
|---|---|---|---|---|
| 0.10% *b* | 0.77 | 0.88 | 0.85 | 0.84 |
| 0.35% *b* | 0.86 | 0.92 | 0.89 | 0.90 |
| 0.68% *b* | 0.89 | 0.93 | 0.89 | 0.90 |

The second additional set consists of specimens for which the cyclic response has been determined by laboratory tests available in the literature. In particular, tests conducted by Kurata et al. [29], Fadden and McCormick [31], Suzuki and Lignos [33], D'Aniello et al. [30], Ishida et al. [34], and Mukaide et al. [35] are considered. The selected specimens, listed in **Table 24**, differ in terms of cross-section dimensions, shear span length (ranging from 867 mm to 1875 mm), steel grade (STKR400, A500B, S355, BCR295), axial load ratio (from 0.0 to 0.40), and loading displacement angles. With regard to the latter aspect, most specimens were tested under uniaxial bending, whereas only a limited number – exclusively with square cross-sections – were investigated under displacement angles of 15°, 30°, or 45°. Unfortunately, no experimental tests are available in the literature to assess the response of rectangular sections under biaxial bending.

Following the methodology described in the paper, the rotation capacity corresponding to the first-cycle envelope of the cyclic response of the laboratory tests has been first determined and then compared with that predicted by the equations, as shown in **Figs. 71** and **72**. The Figures show that the proposed predictive equation is particularly adequate in predicting rotation capacity of specimens made of S355 and A500B and generally slightly underestimates the rotation capacity of specimens made of BCR295 steel grade. This result is expected to be related to the lower imperfections accepted for such specimens.

**Table 24** – Laboratory specimens considered for the validation of the proposed predictive equations.

| Reference | Specimen | Steel grade | $f_y$ (flat) [MPa] | $L_v$ [mm] | ν | φ |
|---|---|---|---|---|---|---|
| Kurata et al. [29] | 200×200×6 | STKR400 | 380 | 1265 | 0.10 | 0° |
| Kurata et al. [29] | 200×200×6 | STKR400 | 380 | 1265 | 0.30 | 0° |
| Kurata et al. [29] | 200×200×9 | STKR400 | 404 | 1265 | 0.10 | 0° |
| Kurata et al. [29] | 200×200×9 | STKR400 | 404 | 1265 | 0.30 | 0° |
| Kurata et al. [29] | 200×200×12 | STKR400 | 425 | 1265 | 0.30 | 0° |
| Fadden and McCormick [31] | 203×203×6.4 | A500B | 444 | 1537 | 0.00 | 0° |
| Fadden and McCormick [31] | 254×203×6.4 | A500B | 444 | 1537 | 0.00 | 0° |
| Fadden and McCormick [31] | 254×102×6.4 | A500B | 444 | 1537 | 0.00 | 0° |
| Suzuki and Lignos [33] | 254×254×9.5 | A500B | 418 | 1525 | 0.30 | 0° |
| Suzuki and Lignos [33] | 305×306×16 | A500B | 418 | 1825 | 0.30 | 0° |
| D'Aniello et al. [30] | 80×60×4 | S355 | 321 | 1875 | 0.00 | 0° |
| D'Aniello et al. [30] | 160×160×6.3 | S355 | 430 | 1875 | 0.00 | 0° |
| D'Aniello et al. [30] | 250×250×8 | S355 | 480 | 1875 | 0.00 | 0° |
| D'Aniello et al. [30] | 100×250×10 | S355 | 430 | 1875 | 0.00 | 0° |
| D'Aniello et al. [30] | 200×200×10 | S355 | 450 | 1875 | 0.00 | 0° |
| Ishida et al. [34] | 200×200×9 | BCR295 | 375 | 867 | 0.20 | 15° |
| Ishida et al. [34] | 200×200×9 | BCR295 | 375 | 867 | 0.40 | 15° |
| Ishida et al. [34] | 200×200×9 | BCR295 | 375 | 867 | 0.20 | 30° |
| Ishida et al. [34] | 200×200×9 | BCR295 | 375 | 867 | 0.40 | 30° |
| Ishida et al. [34] | 200×200×9 | BCR295 | 443 | 867 | 0.20 | 45° |
| Ishida et al. [34] | 200×200×9 | BCR295 | 443 | 867 | 0.40 | 45° |
| Mukaide et al. [35] | 300×300×9 | BCR295 | 362 | 1640 | 0.25 | 0° |
| Mukaide et al. [35] | 300×300×12 | BCR295 | 377 | 1640 | 0.00 | 0° |
| Mukaide et al. [35] | 300×300×12 | BCR295 | 377 | 1640 | 0.25 | 0° |
| Mukaide et al. [35] | 300×300×16 | BCR295 | 394 | 1640 | 0.25 | 0° |

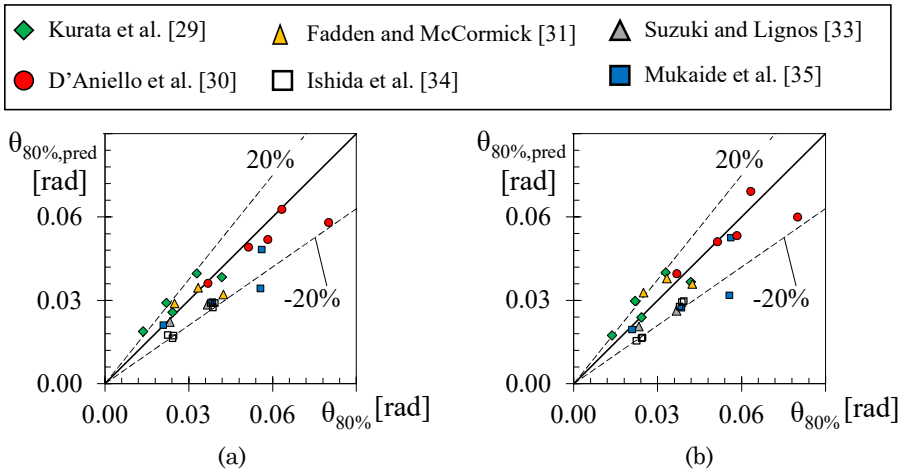


**Fig. 71** – Accuracy of the proposed equation in predicting the chord rotation capacity obtained by laboratory tests at the SD limit state: (a) Eq. (24) and (b) Eq. (25).

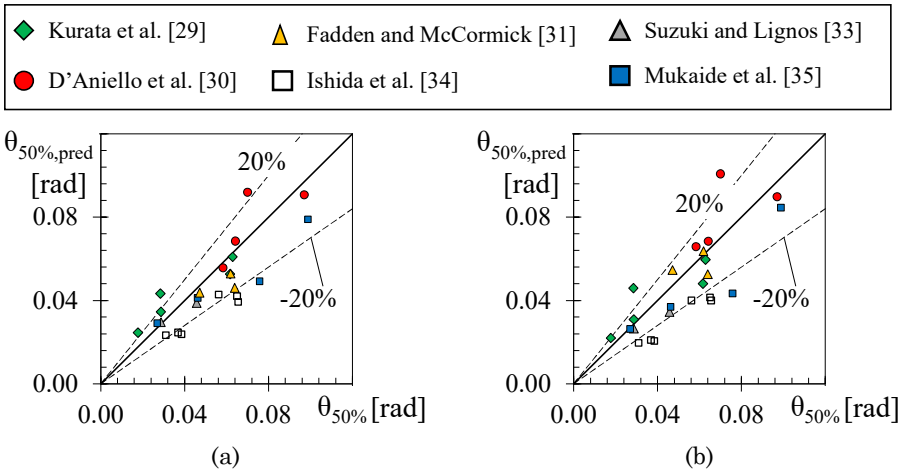


**Fig. 72** – Accuracy of the proposed equation in predicting the chord rotation capacity obtained by laboratory tests at the NC limit state: (a) Eq. (24) and (b) Eq. (25).

# Chapter 4

# SIMPLIFIED MODELLING OF THE CYCLIC RESPONSE OF HSS MEMBERS BY MEANS OF ENDING ZERO-LENGTH ROTATIONAL SPRINGS

In the present chapter, the results of the cyclic parametric analyses of columns under uniaxial bending with an axial load ratio up to $0.3N_{pl}$ presented in the previous chapter are used as a benchmark to calibrate a simplified numerical model. First, to simulate cantilever elements, the numerical model consists of a rigid element with a rotational spring at the base. The nonlinear response of the spring is simulated by the modified Ibarra-Krawinkler deterioration model (MIK) in terms of bending moment versus chord rotation. The considered cantilever elements differ because of the cross-section geometry, shear span ratio and axial load ratio. The response of such members has been obtained with reference to both monotonic and cyclic loading protocols and the values of the parameters of the MIK model have been separately calibrated to simulate the cyclic response and the first-cycle envelope curve. Analytical equations are provided for the parameters of the model as a function of the axial load ratio and geometric properties of the members; in addition, the residuals of the parameters of the Modified Ibarra-Krawinkler numerical model are modelled and estimated so that Monte Carlo analyses with uncertain cyclic response parameters may be performed.

Second, results of laboratory test results available in the literature and already discussed in Chapter 1 are used to validate the proposed equations with reference to structural elements and steel grades different from those considered in the phase of calibration.

Finally, the proposed equations for predicting the parameters of the MIK model are generalized so that they can be used to simulate the response of members modelled as elastic elements with rotational springs at both the ends or as elements with finite-length hinges.

## 1. The Modified Ibarra-Krawinkler deterioration model

The monotonic response offered by the Modified Ibarra-Krawinkler (**Fig. 73**) model is achieved by fixing values for three strength parameters and four deformation parameters. The strength parameters encompass the yield bending moment ($M_y$), the capping bending moment ($M_c$), and the residual bending moment ($M_r$). On the other hand, the deformation parameters include yielding rotation ($\theta_y$), the pre-capping plastic rotation ($\theta_p$), the post-capping plastic rotation ($\theta_{pc}$) and the ultimate rotation ($\theta_u$).

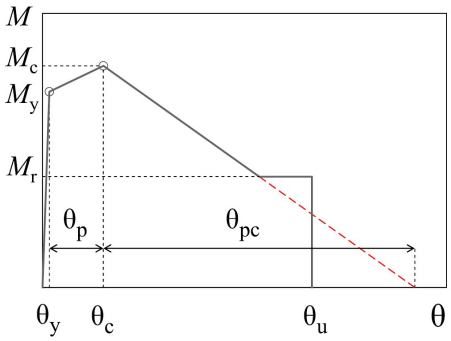


**Fig. 73** – Monotonic curve of the modified Ibarra-Krawinkler Model.

The pre-capping plastic rotation refers to the difference between the rotation associated with the capping bending moment and the rotation at yield, whereas the post-capping plastic rotation is defined as the difference between the rotation corresponding to a zero bending moment and the rotation corresponding to the capping bending moment. It should be noted that all the above-mentioned parameters must be determined based on the monotonic response of the specimens. Therefore, in addition to the cyclic analyses carried out in ABAQUS and discussed in Chapter

3, monotonic analyses were also performed on the same set of specimens, as they are required for the calibration procedure.

Once the monotonic curve is established, it is necessary to determine the rates Λ of cyclic deterioration in yield strength, post-capping strength, reloading stiffness, and unloading stiffness in order to model the cyclic response.

## 2. Identification of the target parameters derived by the monotonic response

As shown in **Fig. 74**, the considered members are characterized by different monotonic responses in terms of bending moment $M$ and chord rotation θ. In particular, elements with a null value of the axial force and with cross-sections characterized by low values of the ratios $b_f/t$ and $h_w/t$ show that, once the maximum bending moment has been reached, its value remains virtually constant for a wide range of plastic rotations. Conversely, in the case of elements with high values of the axial force and high values of the ratios $b_f/t$ and $h_w/t$, the strength degradation begins at chord rotations slightly larger than those corresponding to the achievement of the maximum bending moment.

To simulate these different responses properly, the bending moment at yield ($M_y$) is conventionally determined as the plastic resistance of the HSS cross-section reduced because of the axial load ($M_{pl,N}$), as shown in the following relation

$$M_y = M_{pl,N} = W_{pl} f_y - 2t\frac{y^2}{4} f_y \tag{28}$$

where $W_{pl}$ is the modulus of the plastic resistance of the cross-section, $f_y$ is the yield strength of steel of the flat parts and $y$ is the depth of the portion of the web that resists the applied axial force. It should be noted that, if applied to sections that can develop the full plastic resistance, Eq. (28) provides values of the bending moment at yield that are lower than the actual bending moments at yield because of the higher strength of steel of the corner parts at low strains. The same equation, instead, overestimates the bending moment at yield in sections that are not able to

develop the full plastic resistance because of the premature local buckling of the flat parts.

The chord rotation at yield is calculated by means of the following relation

$$\theta_y = \frac{M_{pl,N} L_V}{3EI} \tag{29}$$

where $L_v$ is the shear span, $E$ is the elastic modulus of steel and $I$ is the moment of inertia of the cross-section.

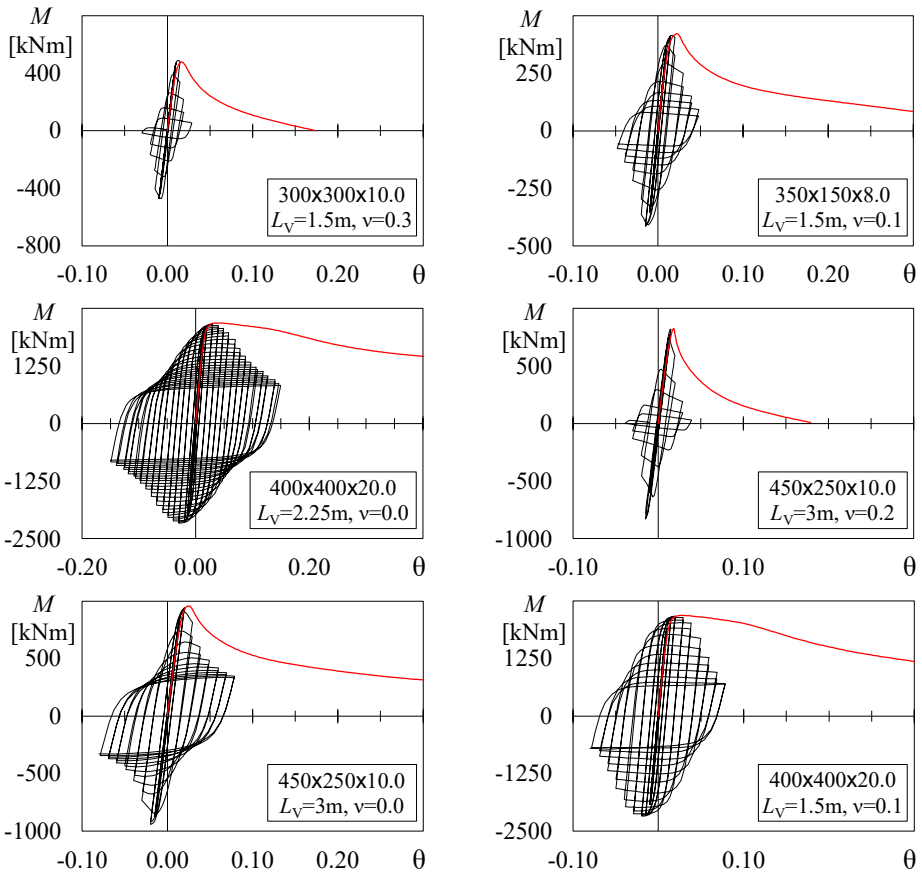


**Fig. 74** – Monotonic and cyclic responses of some specimens

The capping bending moment is calculated here as corresponding to the point of the descending branch of the monotonic curve that is characterized by a value of the bending moment equal to 98% of the maximum bending moment. The pre-capping plastic rotation is the difference between the rotation $\theta_m$ corresponding to the previously determined capping bending moment and the chord rotation at yield.

To calculate the rotation corresponding to a null bending moment, the following procedure is applied. First, the point of the target monotonic curve characterized by a chord rotation equal to $3\theta_m$ is identified and the corresponding bending moment is named $M_{3\theta}$. Second, the point of the target monotonic curve characterized by a bending moment equal to $M_2 = (M_c + M_{3\theta})/2$ is identified and the corresponding chord rotation is named $\theta_2$. Third, a straight line is drawn passing through points ($\theta_m$, $M_c$) and ($\theta_2$, $M_2$) and the chord rotation corresponding to a null bending moment ($\theta_{M0}$) is obtained by linear extrapolation. Fourth, the post-capping plastic rotation is calculated as $\theta_{M0} - \theta_m$. As an example, **Fig. 75** shows the degradation branch of the MIK model (dashed red line) and the corresponding monotonic curve for two of the considered cases. The figure highlights that the proposed procedure is suitable for capturing with sufficient accuracy the shape of the degradation branch of the monotonic curve in the case of either severe or low degradation rate. In particular, in the case of severe degradation rate the procedure is specifically intended to simulate the first part of the post peak curve. Indeed, in the case of severe degradation rate, an accurate estimate of the bending moment – chord rotation curve is not crucial at large values of the chord rotation as the level of damage corresponding to such chord rotations is such that the building is generally assumed to be collapsed. Such high degradation rates are usually achieved in columns subjected to high axial forces.

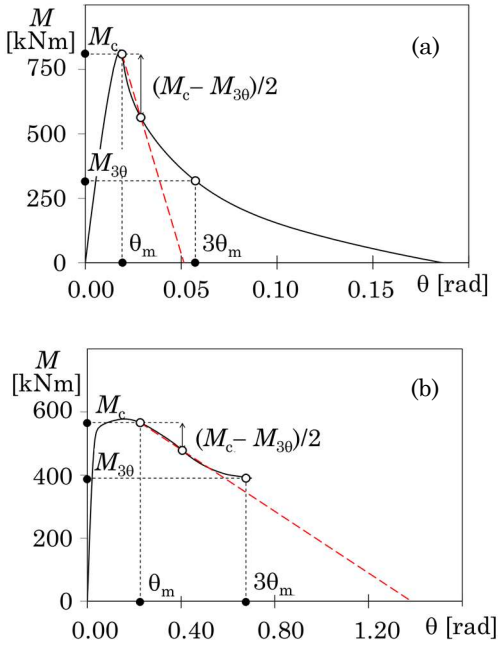


**Fig. 75** – Identification of the degradation branch of the monotonic curve: (a) cross-section S450x250x10.0 ($L_v$=3.0m, ν=0.2), (b) cross-section S300x150x14.2 ($L_v$=3.0m, ν=0.0)

## 3. Prediction of the parameters of the monotonic response

Once the target values of $M_c$, $\theta_p$, $\theta_{pc}$ have been determined, analytical equations are proposed to calculate the parameters of the MIK model as a function of the geometric and mechanical properties of the specimens discussed in the previous Chapther and their axial load ratio.

### 3.1. Methodology

The single parameter of the MIK model ($Y_{pred}$) is predicted by means of the most effective of the following two formulations

$$Y_{pred} = C_0 + \sum C_i X_i + \varepsilon \tag{30}$$

$$Y_{\text{pred}} = C_0 \cdot \prod X_{\text{i}}^{C_{\text{i}}} \cdot \varepsilon \tag{31}$$

In the above equations, $X_{\text{i}}$ are the predictors (geometric and load parameters) and $C_{\text{i}}$ are the regression coefficients. When Eq. (30) is used, the residuals ε, i.e. the errors between the target and predicted responses are assumed to be normally-distributed with a mean value equal to 0. Instead, when Eq. (31) is used, the regression is carried out on the log-transformed data, i.e.

$$\ln Y_{\text{pred}} = \ln C_0 + \sum C_{\text{i}} \ln X_{\text{i}} + \ln \varepsilon \tag{32}$$

In both cases, the least-squares method is used to determine the regression coefficients.

Of all the geometric and load parameters, those that are statistically significant to predict the strength and deformation parameters of the MIK model are first identified as potential predictors. In the case of parameters with similar significance, the ones that guarantee the fulfilment of the hypothesis of normally-distributed residuals are selected. Indeed, normally-distributed residuals allow the use of numerical models able to consider uncertainties in the cyclic response of members. The Lilliefors test [72] with a significance level of 5% is conducted on the residuals ε [or on ln ε if Eq. (31) is used] to confirm the hypothesis of normally-distributed residuals and the quantile-quantile plots are plotted. Further, the risk of collinearity between the values of the selected predictor variables is checked by means of the variance inflation factor, as suggested in [73].

To reach a compromise between accuracy and simplicity of the predictive equations, the above-mentioned procedure has been repeated several times, every time considering a different number of predictors. Based on this analysis, the most significant predictors for the parameters of the MIK model have revealed to be the slenderness of flanges and webs and the axial load ratio. It should be noted that also the ratios $h_{\text{W}}/b_{\text{f}}$, $L_{\text{v}}/b_{\text{f}}$ and $L_{\text{m}}/L_{\text{v}}$ are statistically significant. The introduction of just one of these predictors increases the coefficient of determination $R^2$ of the regression analysis, but no further improvement is recorded if all the three predictors are simultaneously considered because collinearity problems arise. Based on this, only the ratio $L_{\text{m}}/L_{\text{v}}$ has been added to the

previously selected predictors. The variance inflation factors corresponding to the selected predictor variables are equal to 3.45, 1.79, 2.91 and 1.06. As reported in the book by Chatterjee and Hadi [73], values of the variance inflation factor greater than 10 are often taken as a signal that the data have collinearity problems. Therefore, in this case, collinearity problems are not deemed to be present.

The predictive equations are derived in the following subsections where the quantile-quantile plots of residuals are also reported.

### 3.2. Capping bending moment

The capping bending moment is expressed as the bending moment at yield $M_y$ times the overstrength factor $s$.

$$M_c = s\,M_y \tag{33}$$

Target values of the overstrength factor $s$ for elements with a given value of the axial load ratio have been first obtained inverting Eq. (33). Then, the predicted overstrength factor $\underline{s}_{pred}$ has been expressed as a combination of the above-mentioned geometric parameters, i.e.

$$s_{pred} = C_{1,s}(\nu)\lambda_f + C_{2,s}(\nu)\lambda_w + C_{7,s}(\nu)\frac{L_m}{L_V} + C_{8,s}(\nu) + \varepsilon \tag{34}$$

The linear combination coefficients have been determined to minimize the sum of the squares of the differences between the values provided by the predictive equations and the target values provided by specimens with the same value of the axial load ratio. Finally, the obtained regression coefficients have been plotted as a function of the axial load ratio and have been expressed by means of simple relations.

The values of the combination coefficients that minimize the differences between target and predicted overstrength factors are shown by dots in **Fig. 76** as a function of the axial load ratio; in the same figure, a continuous line is used to represent the proposed values of the coefficients.

The coefficient of determination $R^2$ referring to the overstrength factor $s$ is equal to 0.966; the relative residuals $\varepsilon$ are normally distributed with mean equal to 0 and standard deviation equal to 0.018.

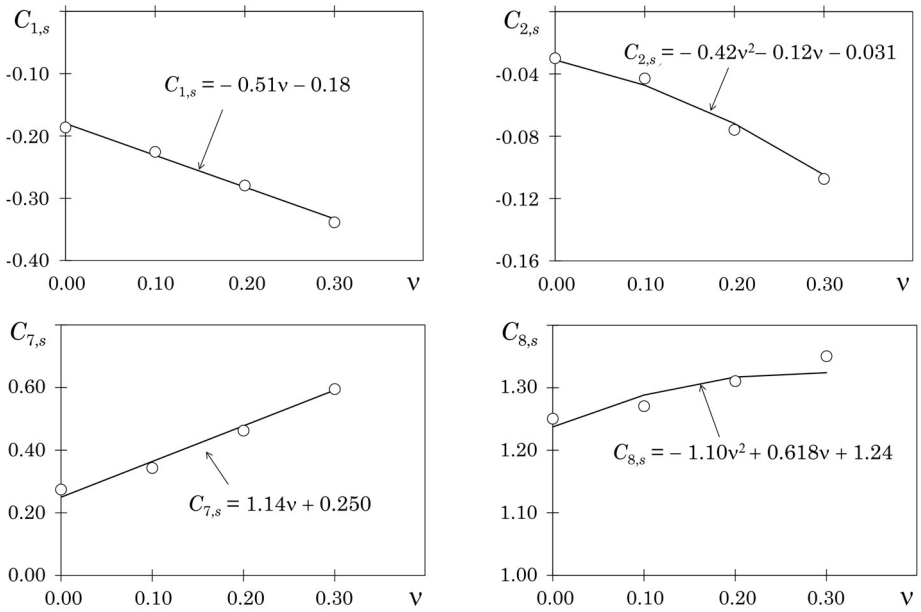


**Fig. 76** – Proposed coefficients for the evaluation of the overstrength factor

### 3.3. Pre-capping and post-capping plastic rotations

Based on the procedure previously illustrated, the following empirical equations are proposed

$$\theta_{p,pred} = 0.024 \cdot \lambda_f^{-0.687} \cdot \lambda_w^{-1.30} \cdot \left(\frac{L_m}{L_V}\right)^{-0.171} \cdot (1-\nu)^{2.314} \cdot \varepsilon \tag{35}$$

$$\theta_{pc,pred} = 0.406 \cdot \lambda_f^{-0.718} \cdot \lambda_w^{-1.60} \cdot \left(\frac{L_m}{L_V}\right)^{0.204} \cdot (1-\nu)^{4.29} \cdot \varepsilon \tag{36}$$

As a result of the regression analysis carried out on the log-transformed data, the coefficients of determination of the logarithms of $\theta_{p,pred}$ and $\theta_{pc,pred}$ are equal to 0.971 and 0.966, respectively; the logarithms of the residuals are normally distributed with mean value equal to 0 and standard deviation equal to 0.150 and 0.184, respectively.

### 3.4. Accuracy of the proposed equations

A comparison between target and predicted values of the overstrength factor *s* is shown in **Fig. 77a**, whereas target and predicted values of pre-capping and post-capping plastic rotations are compared in **Fig. 77b-c**, respectively. In all these figures, different symbols are used to distinguish between specimens characterized by a different value of the axial load ratio.

The difference between predicted and target values of pre-capping and post-capping plastic rotations (**Fig. 77b-c**) is generally larger than that obtained for the overstrength factor (this observation is particularly true for the post-capping plastic rotations). In particular, in the worst case, the difference between predicted and target values is slightly higher than 20%. In any case, visual inspection of the quantile-to-quantile plots (**Fig. 78**) confirms that the residuals are normally distributed.

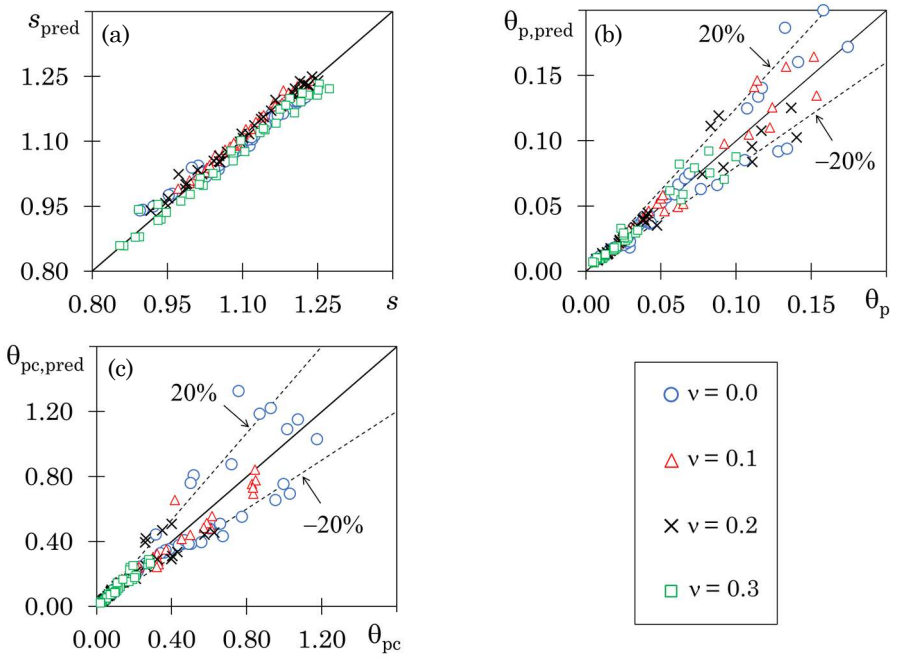


**Fig. 77** – Comparison between target and predicted values: (a) overstrength factor, (b) pre-capping plastic rotation, (c) post-capping plastic rotation

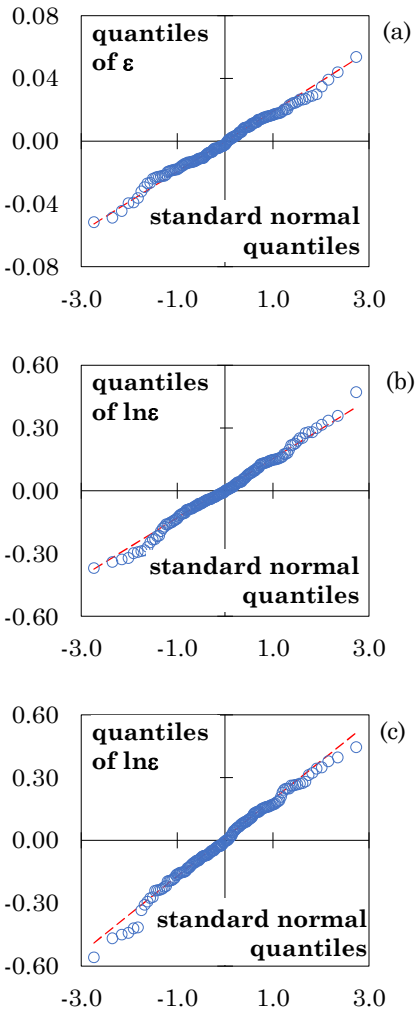


**Fig. 78** – Quantile-to-quantile plot: (a) overstrength factor *s*, (b) pre-capping plastic rotation $\theta_p$, (c) post-capping plastic rotation $\theta_{pc}$

## 4. Prediction of residual bending moment

The definition and determination of the target value of the residual bending moment is not trivial. In the past [61], due to the lack of a significant number of cyclic tests at large deformation amplitudes, a conventional

value of the normalized residual bending moment $r$, i.e. the ratio of the bending moment $M_r$ to the bending moment at yield $M_y$, was fixed equal to 0.4 for H-shaped beam cross-sections. The above value has been later reduced by a factor that, in the case of columns, is a function of the axial load ratio [62]. Although these conventional values do not correspond to a real residual strength, their practical use was justified as there is no need to simulate the cyclic response of members up to deformations leading to higher strength degradations.

In the present research study, instead, to determine the residual bending moment, the first-cycle envelope curve has been first determined by connecting points ($\theta$, $M$) corresponding to the peak chord rotation of each first-cycle of the loading protocol. Then, the flexural stiffness has been calculated as

$$K_{\mathrm{i}} = \frac{M_{\mathrm{i}} - M_{\mathrm{i\text{-}1}}}{\theta_{\mathrm{i}} - \theta_{\mathrm{i\text{-}1}}} \tag{37}$$

Hence, the residual bending moment $M_r$ has been fixed as that leading to a flexural stiffness equal to -2.5% of the initial flexural stiffness. In all the considered cases with axial load ratio equal to 0.3 and in some cases with axial load ratio equal to 0.2, see for example the column with cross-section 450x250x10 in **Fig. 74**, the degradation is abrupt and the residual bending moment becomes almost null. In such cases, a conventional value of the normalized residual bending moment equal to 0.05 has been considered.

Finally, the normalized residual bending moment $r$ has been determined and analytically predicted by means of the equation

$$r_{\mathrm{pred}} = \mathrm{e}^{C_{8,\mathrm{r}}(\nu)} \cdot \lambda_{\mathrm{f}}^{C_{1,\mathrm{r}}(\nu)} \cdot \lambda_{\mathrm{w}}^{C_{2,\mathrm{r}}(\nu)} \cdot \left(\frac{L_{\mathrm{m}}}{L_{\mathrm{V}}}\right)^{C_{7,\mathrm{r}}(\nu)} \geq 0.05 \tag{38}$$

where e is the Napier's constant. Coefficients $C_{1,\mathrm{r}}$, $C_{2,\mathrm{r}}$, $C_{7,\mathrm{r}}$ and $C_{8,\mathrm{r}}$ are first determined for assigned values of the axial load ratio ranging from 0 to 0.3; then, analytical equations are calibrated as shown in **Fig. 79**. A comparison between the values of the normalized residual bending moments $r$ that are predicted by means of the proposed equation and the target values is reported in **Fig. 80**.

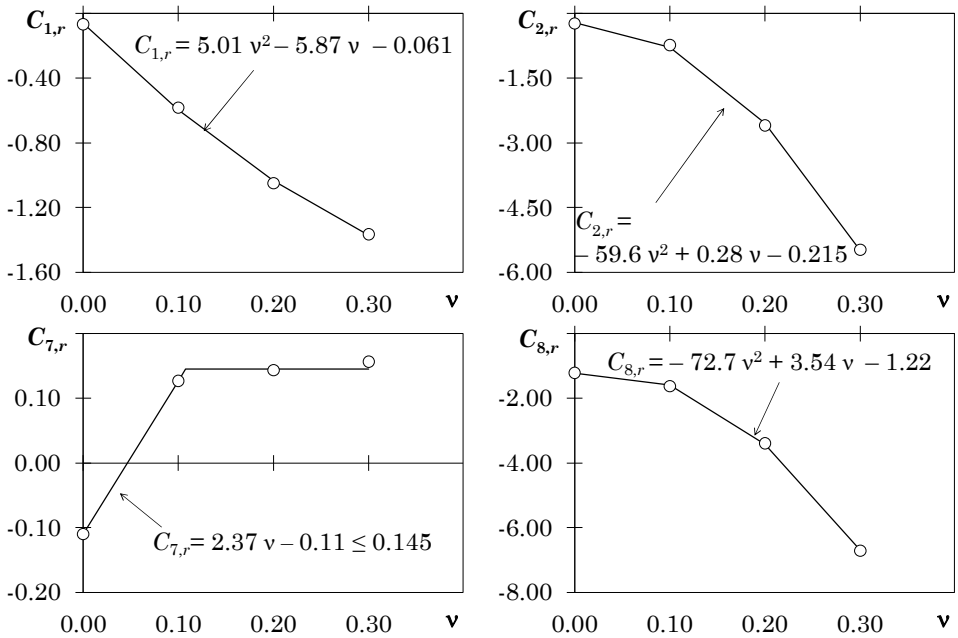


**Fig. 79** – Proposed coefficients for the evaluation of the normalized residual bending moment.

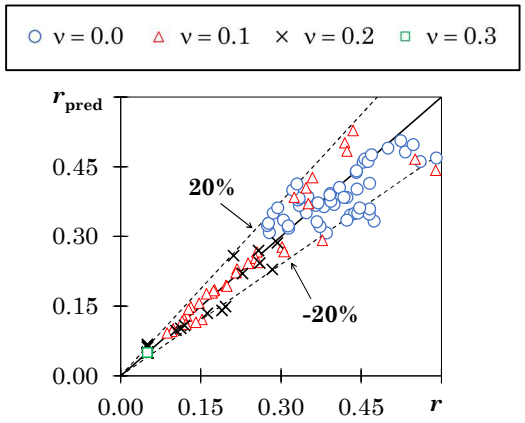


**Fig. 80** – Normalized residual bending moment: accuracy of the proposed equations.

It should be noted that, due to the introduction of a lower bound value of the residual bending moment, the logarithms of the residuals cannot fulfil the normal distribution and the heteroscedasticity assumptions. For this reason, only the mean value is reported here with reference to the normalized residual bending moments.

## 5. Prediction of the rate of degradation

Once the parameters defining the monotonic curve of the MIK model have been determined, the numerical model of all the considered specimens is built in OpenSees [74]. To this end, three nodes are defined. Nodes #1 and #2 are located at the base of the element whereas Node #3 is located at the tip of the element, i.e. at a distance $L_v$ from the base. The first node is fully restrained. The second node cannot move along the longitudinal axis of the member and is connected to node #1 by means of a horizontal spring that simulates the shear deformability of the element and by means of a rotational spring that simulates the flexural response of the element. This latter rotational spring is characterized by the MIK material model. Nodes #2 and #3 are connected by a rigid element. The tip of the beam (i.e. node #3) is subjected to the displacement protocol given in AISC 341 [75] for the qualification of beam-to-column connections.

To model the considered elements properly, two additional issues are considered:

- if the overstrength factor $s$ determined by Eq. (34) is smaller than 1.0, i.e. the cross-section is not able to develop the plastic flexural resistance, the bending moment at yield $M_{y,real}$ of the rotational spring should be smaller than the one given by Eq. (28). In such cases, the bending moment $M_{y,real}$ is set equal to the capping bending moment (see **Fig. 81a**).

$$M_{y,real} = sM_y \qquad \text{if } s < 1 \tag{39}$$

- if the overstrength factor $s$ determined by Eq. (34) is larger than 1.0, i.e. the cross-section is able to develop the plastic flexural resistance, the bending moment at yield determined by Eq. (28) underestimates the actual bending moment at yield because of the

higher strength of the corner parts at low strains (see **Fig. 81b**). In such cases, the bending moment $M_{\mathrm{y,real}}$ is determined considering the yield strength of steel in the flat parts and the ultimate strength in the corner parts.

$$M_{\mathrm{y,real}} = W_{\mathrm{pl}} f_y^{\mathrm{flat}} + W_{\mathrm{pl}}^{\mathrm{corner}} \left( f_u^{\mathrm{corner}} - f_y^{\mathrm{flat}} \right) - 2t \frac{y^2}{4} f_y^{\mathrm{flat}} \tag{40}$$

Because of the abovementioned adjustments on the bending moment at yield, the chord rotation at yield and the pre-capping chord rotation are determined by means of the following equations

$$\theta_{\mathrm{y,real}} = \frac{M_{\mathrm{y,real}} L_{\mathrm{V}}}{3EI} \tag{41}$$

$$\theta_{\mathrm{p,real}} = \theta_{\mathrm{p,pred}} + \theta_{\mathrm{y}} - \theta_{\mathrm{y,real}} \tag{42}$$

where $\theta_{\mathrm{p,pred}}$ and $\theta_{\mathrm{y}}$ are given by Eqs. (35) and (29), respectively. The equation above leads to $\theta_{\mathrm{p,real}} > \theta_{\mathrm{p,pred}}$ in the case of $s$ <1 (**Fig. 81a**), and to $\theta_{\mathrm{p,real}} < \theta_{\mathrm{p,pred}}$ in the case of $s$ >1 (**Fig. 81b**).

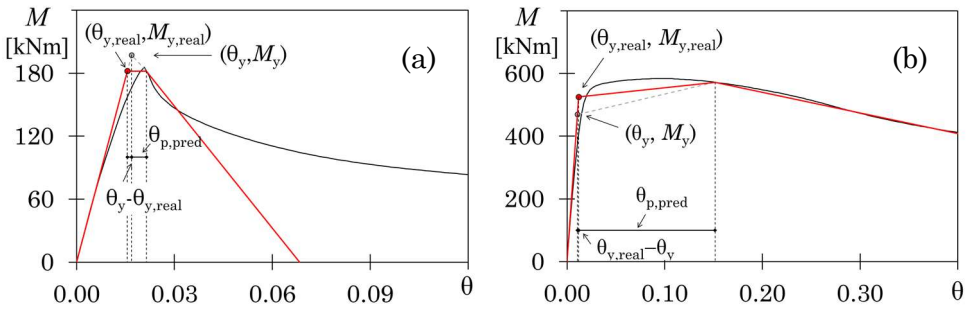


**Fig. 81** – Corrections to the bending moment at yield in the case of overstrength factors (a) lower than 1.0 ($\theta_{\mathrm{p,real}} > \theta_{\mathrm{p,pred}}$) ; (b) higher than 1.0 ($\theta_{\mathrm{p,real}} < \theta_{\mathrm{p,pred}}$).

Tentative values of the rates of cyclic degradation Λ are first assigned to the MIK model of the rotational spring. Specifically, the same rate of cyclic degradation Λ is assumed in regard to yield strength, post-capping strength, reloading and unloading stiffnesses. For each considered value of Λ, the cyclic response is determined and the cumulated dissipated

energy is computed at the end of the loading protocol by integration of the area subtended by the bending moment-chord rotation curve. Then, the energy evaluated from the response of the numerical model built in OpenSees is compared with the energy subtended by the cyclic response of the refined FE numerical test. The optimal value of $\Lambda$ is that leading to the minimum scatter between predicted and target dissipated energies.

Once the optimal value of $\Lambda$ has been determined for all the considered specimens, the following predictive equation is calibrated

$$\Lambda_{\text{pred}} = 0.974 \cdot \lambda_{\text{f}}^{-0.754} \cdot \lambda_{\text{w}}^{-1.54} \cdot \left(\frac{L_{\text{m}}}{L_{\text{V}}}\right)^{-0.0268} \cdot (1-\nu)^{6.66} \cdot \varepsilon \tag{43}$$

Once again, the proposed equation reveals to be fairly accurate (see the comparison between predicted and target values in **Fig. 82a**). In particular, the logarithms of the residuals are normally distributed (**Fig. 82b**) with mean value equal to 0 and standard deviation $\sigma_{\ln}$ equal to 0.225.

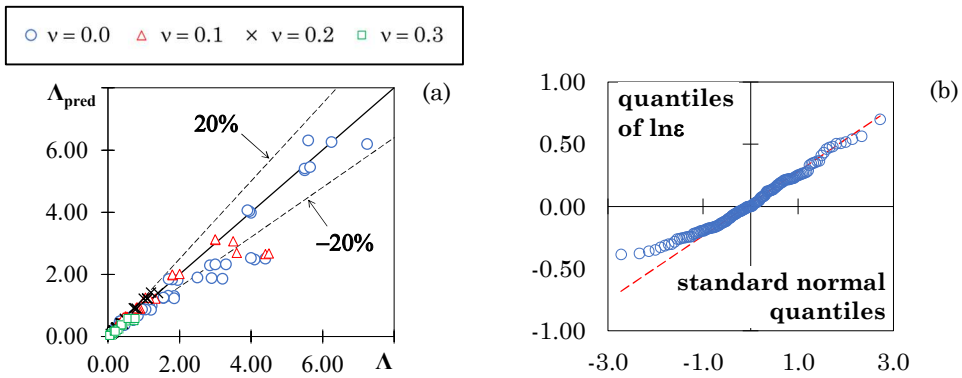


**Fig. 82** – Cyclic degradation parameters: (a) accuracy of the proposed equations, (b) quantile-to-quantile plot.

## 6. Effectiveness of the proposed predictive equations

To verify the accuracy of the proposed predictive equations, these equations have been used to determine the values of all the parameters of the

MIK model in all the considered specimens. Then, the predicted cyclic response has been compared with the target response, i.e. the response of the same specimen determined by FE models in Chapter 3. A visual comparison between predicted and target responses is shown in **Fig. 83**, whereas a comparison between predicted and cumulated dissipated energies at the achievement of a residual bending moment equal to 50% of the plastic flexural resistance is shown in **Fig. 84**.

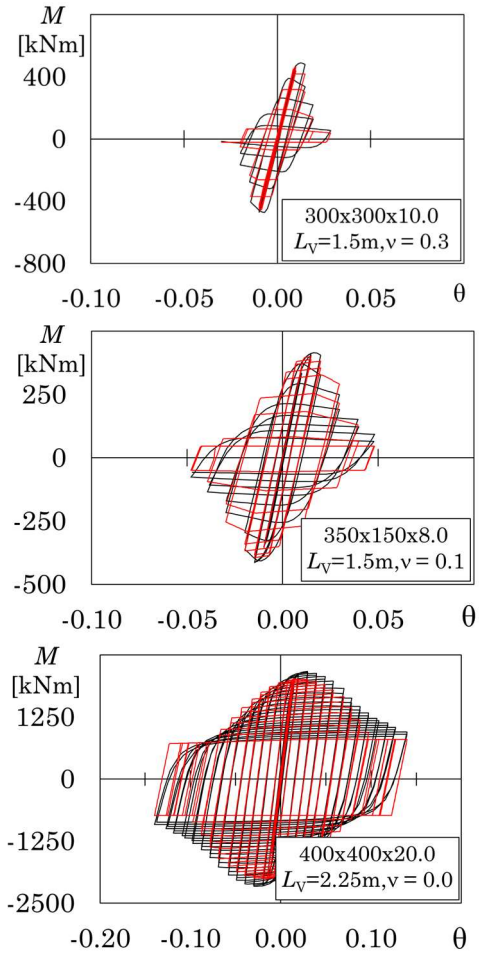


**Fig. 83** – Comparison between target (black line) and predicted (red line) cyclic responses.

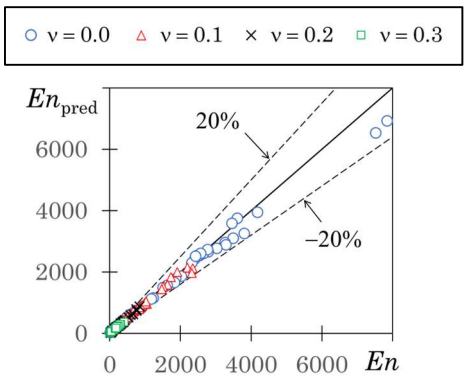


**Fig. 84** – Comparison between target and predicted cumulated energies (expressed in kNm).

The figures show that the equations proposed to determine the response parameters of the MIK model ensure high accuracy in the simulation of the cyclic response of structural members characterized by very different rates of degradation.

## 7. Predictive equations of the MIK model in the case of nonlinear static analysis

Even though nonlinear dynamic analysis is often used by researchers, practical engineers commonly use nonlinear static analysis to explore the inelastic response of structures. Unless a cyclic pushover analysis is carried out [76], the nonlinear static analysis is not able to account for the stiffness and strength degradations recorded during the cyclic response of members. To simulate this effect, the bending moment-chord rotation response of the ending parts of the members should be able to implicitly take into account the abovementioned degradation. For this reason, the parameters that have been specified in the MIK model to represent the monotonic response have been re-determined with reference to the first-cycle envelope curve. In particular, the ratio $s$ of the capping bending moment to the bending moment at yield $M_y$, the pre-capping and the post-capping plastic rotations have been re-determined and identified by

symbols $s^*$, $\theta_p^*$ and $\theta_{pc}^*$. Following a procedure similar to that described in sections 2 and 3, the predictive equations have been calibrated and the effectiveness of the proposed equations in predicting $s^*$, $\theta_p^*$ and $\theta_{pc}^*$ has been investigated, as shown in **Fig. 85**.

$$s^*_{\text{pred}} = C^*_{1,\text{s}}(\nu)\lambda_f + C^*_{2,\text{s}}(\nu)\lambda_w + C^*_{7,\text{s}}(\nu)\frac{L_m}{L_V} + C^*_{8,\text{s}}(\nu) + \varepsilon \qquad (44)$$

$$\theta^*_{\text{p,pred}} = 0.011 \cdot \lambda_{\text{f}}^{-0.389} \cdot \lambda_{\text{w}}^{-1.09} \cdot \left(\frac{L_{\text{m}}}{L_{\text{V}}}\right)^{-0.228} \cdot (1-\nu^2)^{11.34} \cdot \varepsilon \qquad (45)$$

$$\theta^*_{\text{pc,pred}} = 0.072 \cdot \lambda_{\text{f}}^{-0.077} \cdot \lambda_{\text{w}}^{-0.826} \cdot \left(\frac{L_{\text{m}}}{L_{\text{V}}}\right)^{0.005} \cdot (1-\nu)^{3.94} \cdot \varepsilon \qquad (46)$$

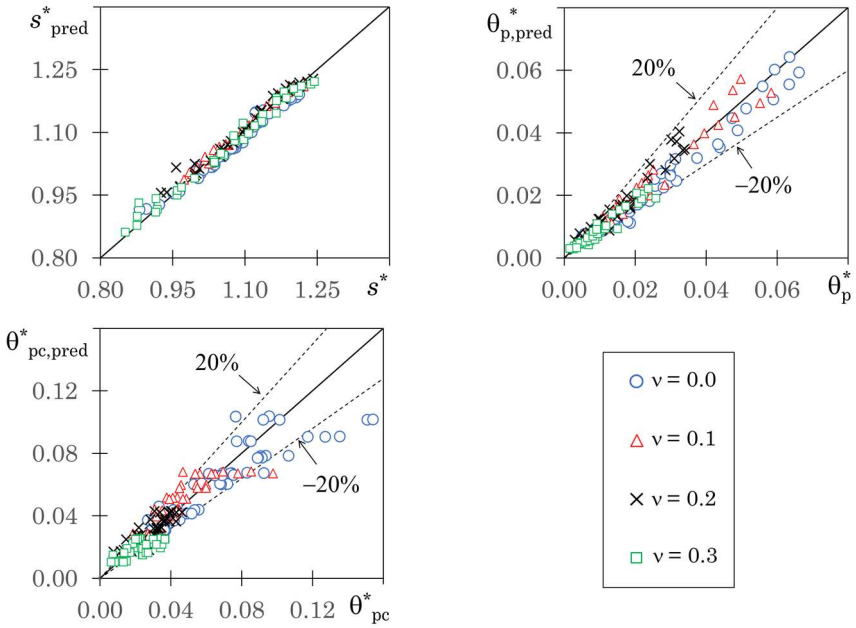


**Fig. 85** – Comparison between target and predicted parameters $s^*$, $\theta_p^*$ and $\theta_{pc}^*$

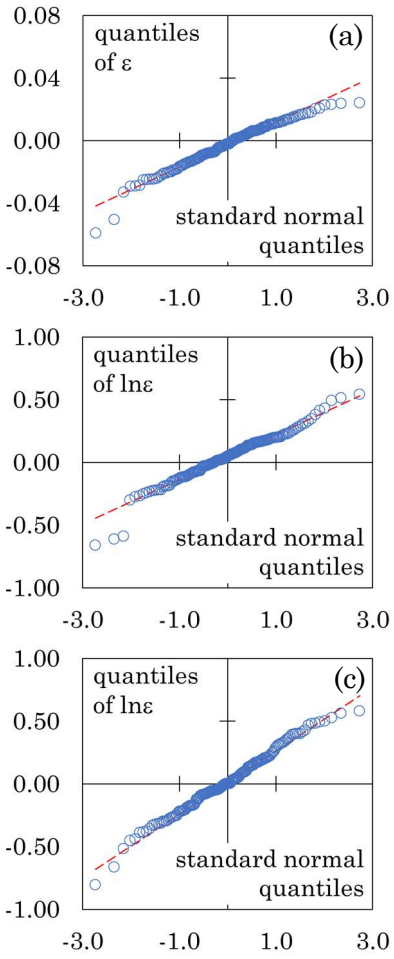


**Fig. 86** – Quantile-to-quantile plot: (a) overstrength factor $s^*$, (b) pre-capping plastic rotation $\theta_p^*$, (c) post-capping plastic rotation $\theta_{pc}^*$

**Table 25 –** Coefficients of the regression analysis to predict the overstrength factor $s^*$.

| | |
|---|---|
| $C_{1,s}^* = -0.263\,\nu - 0.189$ | $C_{2,s}^* = -1.156\nu^2 - 0.032$ |
| $C_{7,s}^* = 0.581\nu + 0.314$ | $C_{8,s}^* = 0.371\,\nu + 1.224$ |

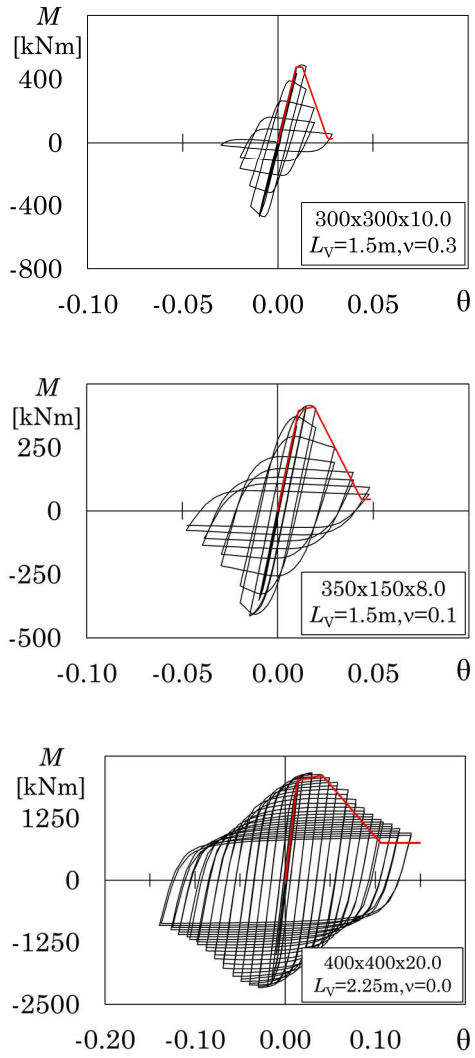


**Fig. 87** – Comparison between target cyclic response (black line) and predicted first envelope curve (red line)

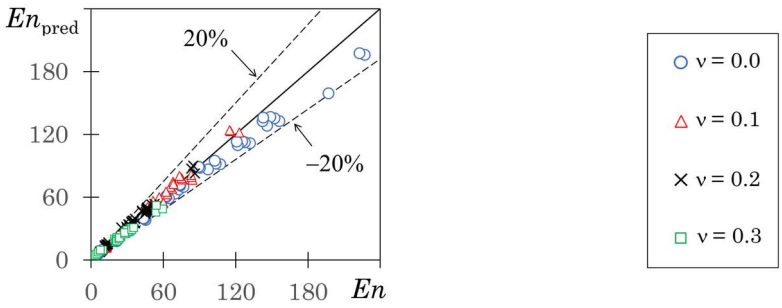


**Fig. 88** – Comparison between areas subtended by the target and predicted first envelope curves (kNm)

Coefficients to be used in Eq. (44) are provided in **Table 25**. The residuals in Eq. (44) are normally-distributed (**Fig. 86a**) with a standard deviation equal to 0.014. As a result of the regression analysis carried out on the log-transformed data, the coefficients of determination corresponding to the pre-capping and the post-capping plastic rotations are equal to 0.933 and 0.849, respectively; the logarithms of the residuals are normally distributed (**Fig. 86b-c**) with mean value equal to 0 and standard deviation $\sigma_{ln}$ equal to 0.189 and 0.250, respectively.

Referring to the same specimens investigated in **Fig. 83**, in **Fig. 87** the predicted first-cycle envelope curve (red line) is superimposed to the target cyclic response (black line). To generalize the accuracy of the prediction, the areas subtended by the target and predicted first-cycle envelope curves are also compared in **Fig. 88**. **Fig. 87** shows that the prediction is slightly conservative for systems with a lower rate of degradation.

## 8. Validation against results of laboratory tests

The equations proposed to predict the parameters of the MIK model have been calibrated based on the results of a wide set of numerical FE models. To prove the accuracy of the proposal also in the case of laboratory tests, which were not considered in the process of calibration, the predictive equations are used to replicate both the cyclic response and the first-cycle envelope curves of laboratory tests on square and rectangular hollow cold-formed sections (**Table 26**). All the considered specimens are

cantilever elements with an axial load ratio ranging from 0 to 0.3. Specimens tested in [30] are made of steel grade S355, i.e. the same steel grade assumed in the FE model, other specimens are made of different steel grades. **Table 26** also reports the yield strength of steel of the flat parts and, when available, the tensile strength determined on coupon tests extracted from the corner parts of the members. In cases in which no information is given about the material properties of the corner parts, based on results of tensile coupon tests on specimens extracted from flat and corner parts of other HSS profiles [7], the ultimate strength of steel of the corner parts has been conservatively assumed to be 1.2 times the yield strength of steel of the flat parts. The shear span $L_v$ (see **Table 26**) is such that the ratio $L_m/L_v$ is in the range from 0.05 to 0.19. The ratio $b_f/t$ is in the range from 10.67 to 30.33, whereas the ratio $h_w/t$ is in the range from 10.67 to 38.9. In particular, four specimens (i.e. 200x200x6, 254x203x6.4, 250x250x8 and 300x300x9) have ratio $b_f/t$ slightly larger than the maximum ratio considered in the phase of calibration whereas one specimen (200x200x12) has a ratio $h_w/t$ slightly smaller than the minimum value considered in the phase of calibration. With the sole exception of three specimens, for which collapse consistent loading protocols are considered, symmetric cyclic loading protocols are applied.

For each specimen, the parameters of the MIK model have been assigned using the provided predictive equations; then, the values of the same parameters corresponding to 16% and 84% percentiles have been calculated based on the defined standard deviations of the residuals. The comparison between the target cyclic response (reported by a black line) and the predicted cyclic response (red line) determined with parameters of the MIK model corresponding to the 50% percentile is shown in **Figs. 89-93** for the specimens subjected to symmetric loading protocols and in **Fig. 94** for the specimens subjected to collapse consistent loading protocols.

**Table 26** – Laboratory tests considered for the validation.

| Reference | Specimen | Steel grade | $f_y$ [MPa] flat | $f_u$ [MPa] corner | $L$ [mm] | Axial load ratio | Loading protocol |
|---|---|---|---|---|---|---|---|
| Kurata et al. [29] | 200x200x6 | STKR400 | 380 | Na | 1265 | 0.10 | Symmetric |
| Kurata et al. [29] | 200x200x6 | STKR400 | 380 | Na | 1265 | 0.30 | Symmetric |
| Kurata et al. [29] | 200x200x9 | STKR400 | 404 | Na | 1265 | 0.10 | Symmetric |
| Kurata et al. [29] | 200x200x9 | STKR400 | 404 | Na | 1265 | 0.30 | Symmetric |
| Kurata et al. [29] | 200x200x12 | STKR400 | 425 | Na | 1265 | 0.10 | Symmetric |
| Kurata et al. [29] | 200x200x12 | STKR400 | 425 | Na | 1265 | 0.30 | Symmetric |
| D'Aniello et al [30] | 160x80x4 | S355 | 321 | Na | 1875 | 0.00 | Symmetric |
| D'Aniello et al [30] | 160x160x6.3 | S355 | 430 | Na | 1875 | 0.00 | Symmetric |
| D'Aniello et al [30] | 250x250x8 | S355 | 480 | Na | 1875 | 0.00 | Symmetric |
| Fadden and McCormick [31] | 203x203x6.4 | A500B | 444 | 618 | 1537 | 0.00 | Symmetric |
| Fadden and McCormick [31] | 203x152x9.5 | A500B | 444 | 618 | 1537 | 0.00 | Symmetric |
| Fadden and McCormick [31] | 254x203x6.4 | A500B | 444 | 618 | 1537 | 0.00 | Symmetric |
| Mukaide et al [35] | 300x300x9 | BCR295 | 362 | 525 | 1640 | 0.25 | Symmetric |
| Mukaide et al [35] | 300x300x12 | BCR295 | 377 | 531 | 1640 | 0.00 | Symmetric |
| Mukaide et al [35] | 300x300x12 | BCR295 | 377 | 531 | 1640 | 0.25 | Symmetric |
| Mukaide et al [35] | 300x300x16 | BCR295 | 394 | 519 | 1640 | 0.25 | Symmetric |
| Suzuki and Lignos [33] | 254x254x9.5 | A500B | 418 | 593 | 1525 | 0.30 | Symmetric |
| Suzuki and Lignos [33] | 254x254x9.5 | A500B | 418 | 593 | 1525 | 0.30 | Near fault |
| Suzuki and Lignos [33] | 254x254x9.5 | A500B | 418 | 593 | 1525 | 0.30 | Long dur. |
| Suzuki and Lignos [33] | 305x306x16 | A500B | 418 | 593 | 1825 | 0.30 | Symmetric |
| Suzuki and Lignos [33] | 305x306x16 | A500B | 418 | 593 | 1825 | 0.30 | Near fault |

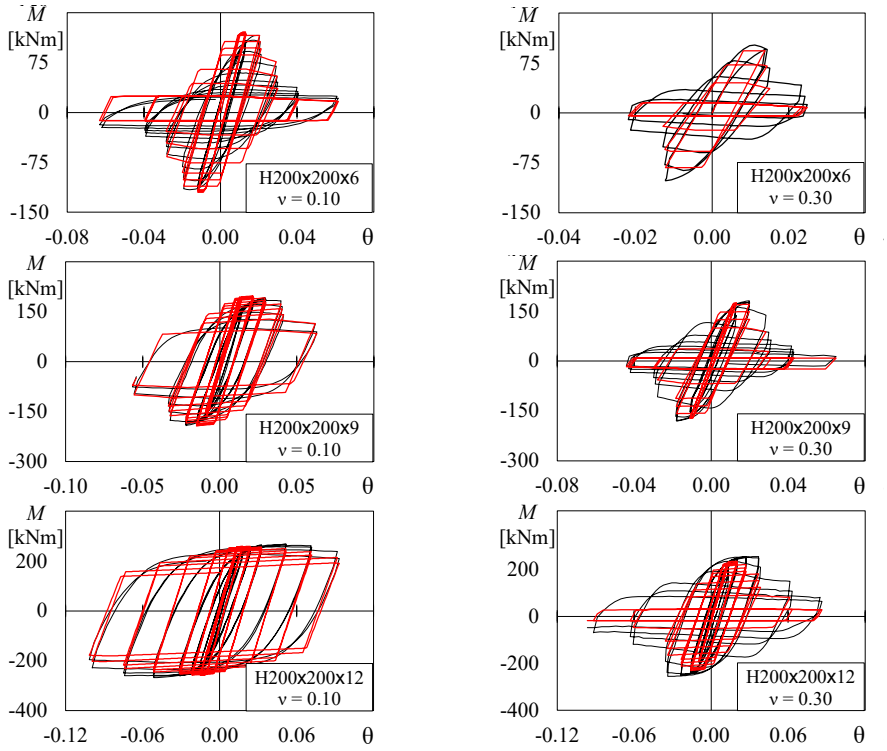


**Fig. 89** – Comparison between target cyclic response (black line) and predicted cyclic curve (red line) when model parameters correspond to 50% percentile: Kurata et al. [29].

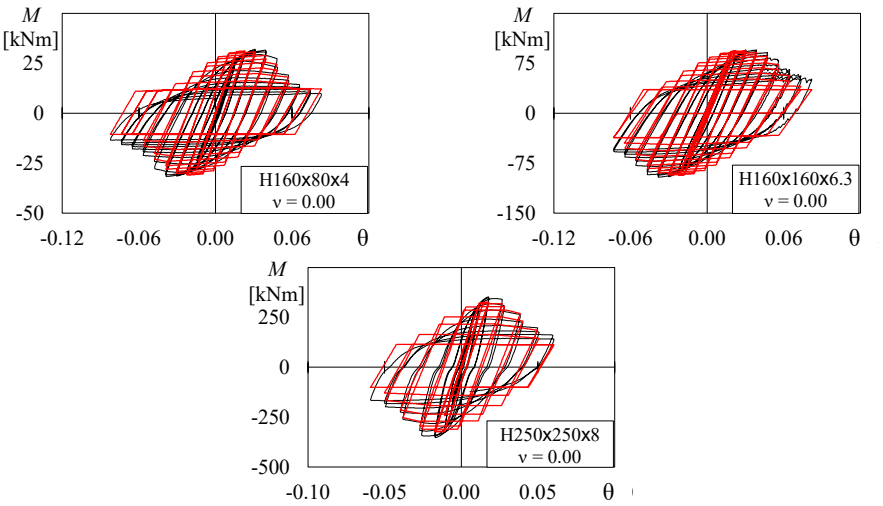


**Fig. 90** – Comparison between target cyclic response (black line) and predicted cyclic curve (red line) when model parameters correspond to 50% percentile: D'Aniello et al. [30].

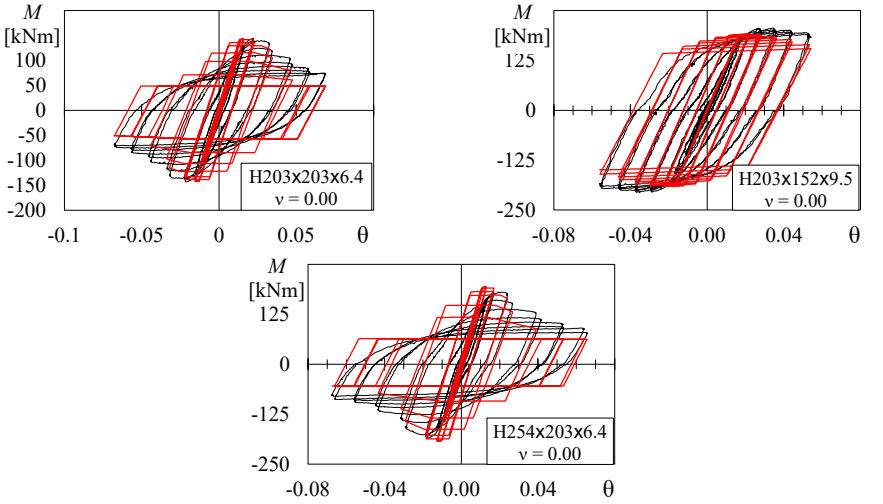


**Fig. 91** – Comparison between target cyclic response (black line) and predicted cyclic curve (red line) when model parameters correspond to 50% percentile: Fadden and McCormick [31].

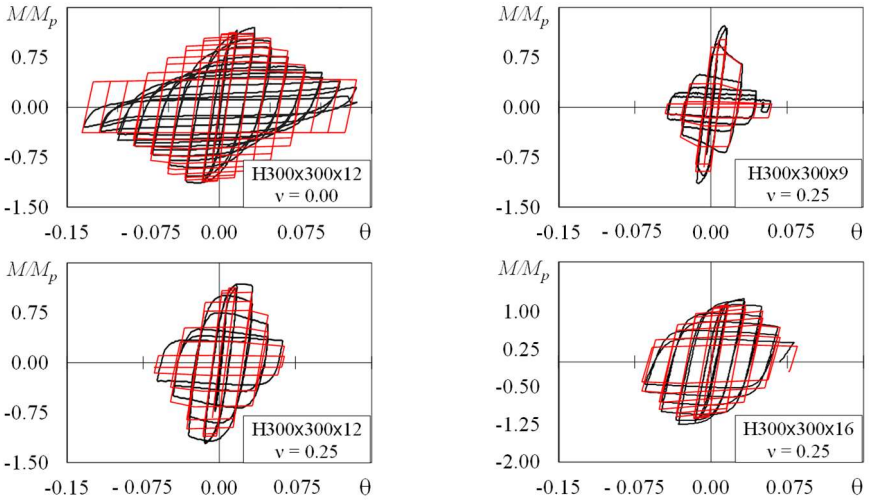


**Fig. 92** – Comparison between target cyclic response (black line) and predicted cyclic curve (red line) when model parameters correspond to 50% percentile: Mukaide et al. [35].

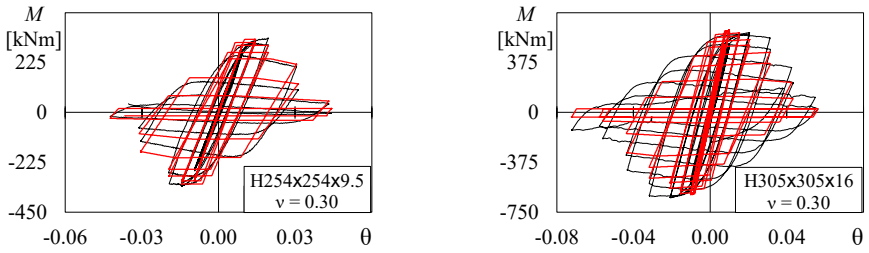


**Fig. 93** – Comparison between target cyclic response (black line) and predicted cyclic curve (red line) when model parameters correspond to 50% percentile: Suzuki and Lignos [33].

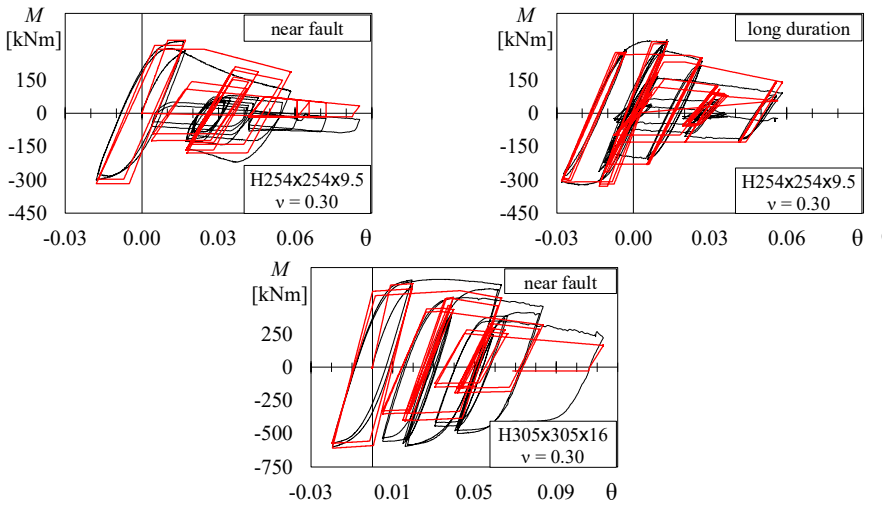


**Fig. 94** – Comparison between target cyclic response (black line) and predicted cyclic curve (red line) for specimens subjected to collapse consistent loading protocols (model parameters corresponding to 50% percentile).

Despite the uncertainty in the material properties of the corner parts of some specimens and the differences in the steel grades, the proposed equations lead to a satisfactory prediction of the shape of the cyclic response.

**Fig. 95** shows, for three of the considered specimens, the comparison between the target cyclic response (reported by a black line) and the predicted cyclic response (red line) determined with parameters of the MIK model corresponding to the 16% and 84% percentiles. Of these three specimens, one is selected to be representative of members with rectangular cross-section (160x80x4) and is subjected to a null axial load. The other two specimens are chosen to be representative of members with square cross-section (200x200x6 and 200x200x12) and exhibit the maximum and minimum rates of degradation of the parameters of the MIK model; the specimen with cross-section 200x200x6 is characterized by an axial load ratio equal to 0.3 whereas the specimen with cross-section 200x200x12 is characterized by an axial load ratio equal to 0.1.

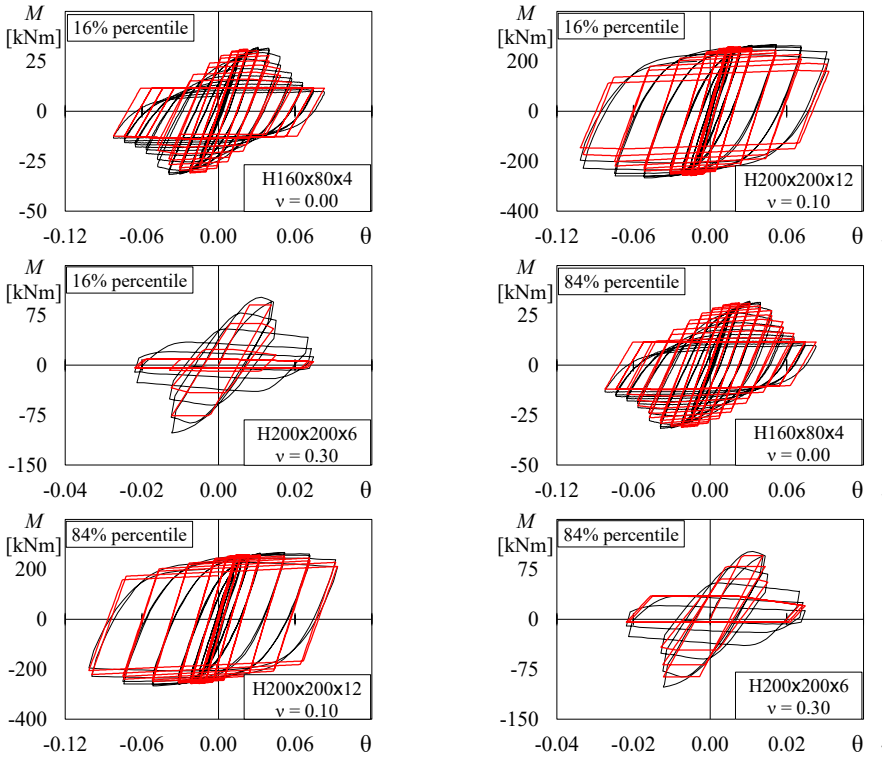


**Fig. 95** – Comparison between target cyclic response (black line) and predicted cyclic curve (red line) when model parameters correspond to 16% and 84% percentiles.

Finally, **Figs. 96-100** show the comparison between the target cyclic response (black line) and the predicted first cycle envelope curve. Specifically, the red solid line depicts the numerical response when the parameters of the model are equal to the median values, whereas the dashed lines represent the response when the parameters correspond to the 16% and 84% percentiles.

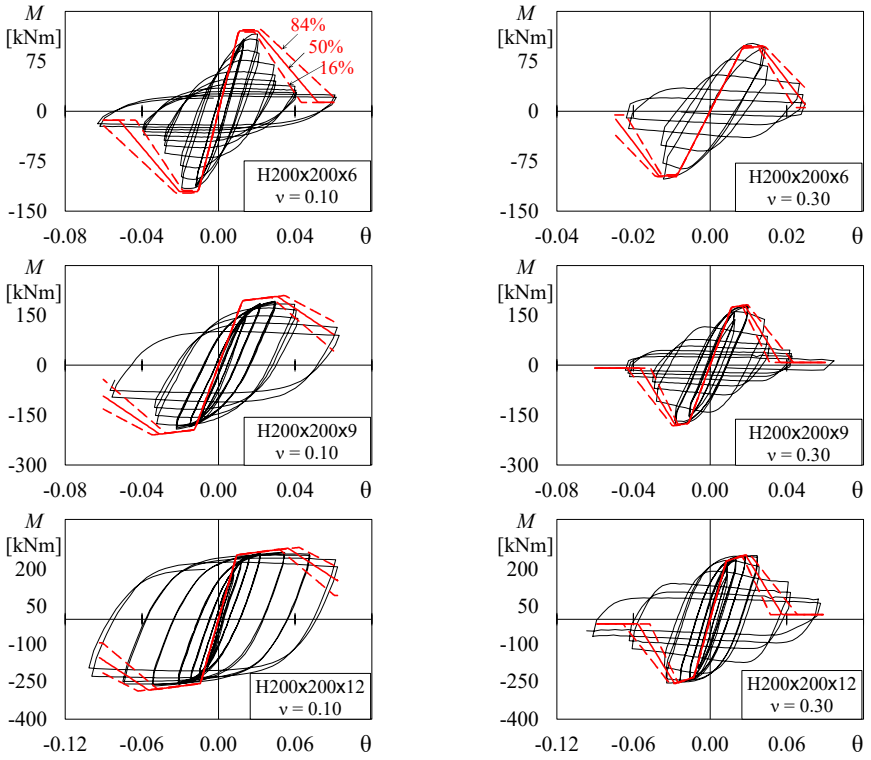


**Fig. 96** – Comparison between target cyclic response (black line) and predicted first cycle envelope curve (red line) when model parameters correspond to 84%, 50% and 16% percentiles: Kurata et al. [29].

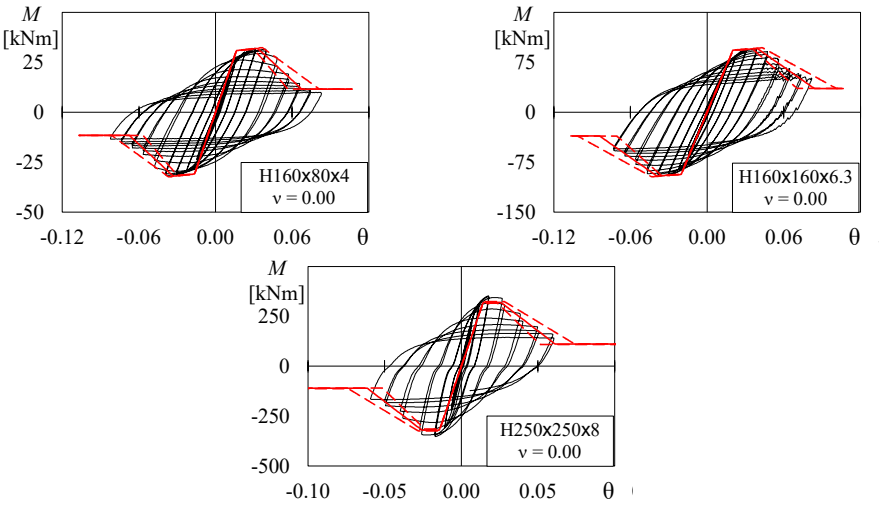


**Fig. 97** – Comparison between target cyclic response (black line) and predicted first cycle envelope curve (red line) when model parameters correspond to 84%, 50% and 16% percentiles: D'Aniello et al. [30].

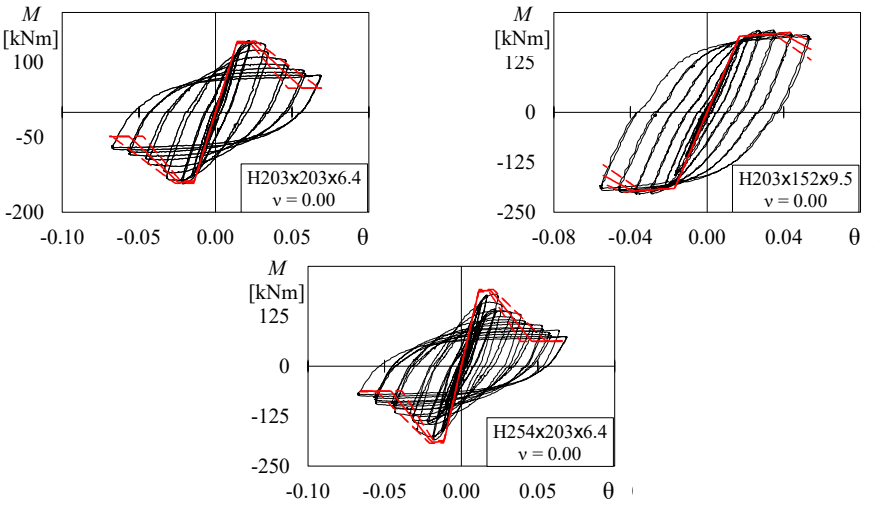


**Fig. 98** – Comparison between target cyclic response (black line) and predicted first cycle envelope curve (red line) when model parameters correspond to 84%, 50% and 16% percentiles: Fadden and McCormick [31].

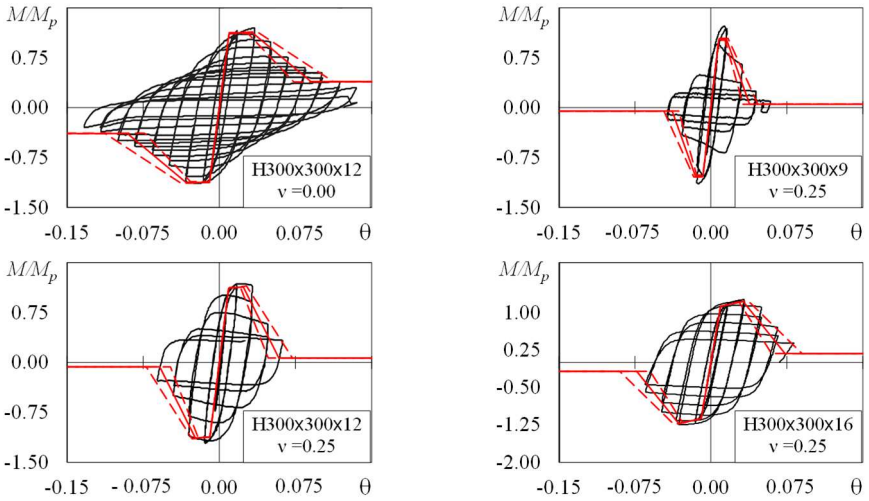


**Fig. 99** – Comparison between target cyclic response (black line) and predicted first cycle envelope curve (red line) when model parameters correspond to 84%, 50% and 16% percentiles: Mukaide et al. [35].

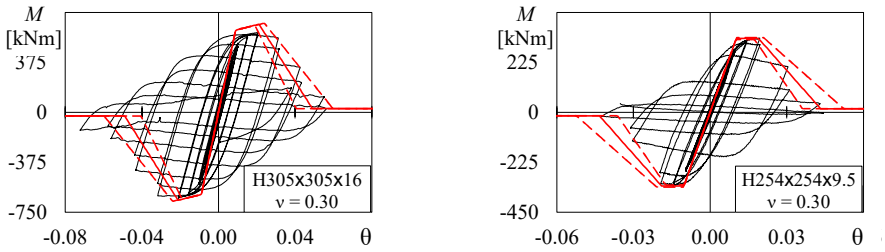


**Fig. 100** – Comparison between target cyclic response (black line) and predicted first cycle envelope curve (red line) when model parameters correspond to 84%, 50% and 16% percentiles: Suzuki and Lignos [33].

## 9. Application of the MIK model to other element models

The values of the parameters of the MIK model, obtained by means of the proposed equations, have to be modified if a numerical model different from that described in section 5 is used. In the following subsections, modifications to the values of the parameters of the MIK model determined by means of the proposed equations are derived for either elastic (not

rigid) elements with rotational springs at the ends or elements with finite length hinges.

### 9.1. Elements with finite length hinges

As stated in [77], if elements with finite length hinges are used, the bending moment-flexural curvature relation of the plastic hinge region and an equivalent moment of inertia ß $I$ of the cross-section of the interior (elastic) integration points have to be defined to replicate the bending moment-chord rotation response of the element.

The parameters of the bending moment-flexural curvature relation and the value of ß are defined here with specific regard to the *end point* integration rule, but a similar approach can be used in the case of other integration rules. In regard to the bending moment - flexural curvature relation, the parameters to be determined are the flexural stiffness ($K_{M\chi}$), the strain hardening ratio α', the pre-capping and the post capping flexural curvatures ($\chi_p$ and $\chi_{pc}$) and the ultimate flexural curvature ($\chi_u$).

For the element under investigation, the distances $z$ of the four integration points from the first end and the weights $w$ of the same points are

$$z = \left\{ 0; \quad L_{pl} + \frac{L_{int}}{2}\left(1 - \frac{1}{\sqrt{3}}\right); \quad L_{pl} + \frac{L_{int}}{2}\left(1 + \frac{1}{\sqrt{3}}\right); \quad L \right\} \tag{47}$$

$$w = \left\{ L_{pl}; \quad \frac{L_{int}}{2}; \quad \frac{L_{int}}{2}; \quad L_{pl} \right\} \tag{48}$$

where $L_{pl}$ is the length of the plastic hinge and $L_{int} = L - 2\,L_{pl}$ (**Fig. 101**).

If a cantilever element subjected to a force $F$ at the free end is modelled, the flexural curvatures $\chi$ at the four integration points are

$$\chi = \left\{ \frac{F \cdot L}{K_{M\chi}}; \quad \frac{F \cdot (L - z_2)}{\beta EI}; \quad \frac{F \cdot (L - z_3)}{\beta EI}; \quad 0 \right\} \tag{49}$$

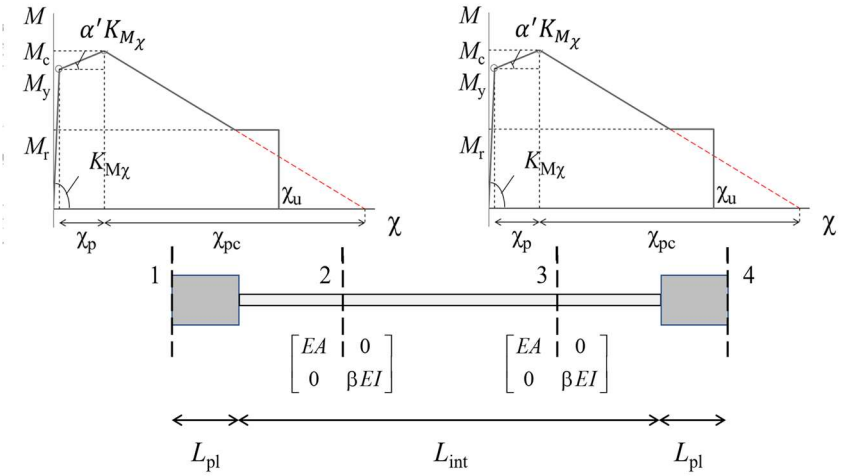


**Fig. 101** – Finite length hinge element in the case of end point integration rule.

Assuming that

$$K_{M\chi} = n\frac{3E\,\beta I}{L}L_{\mathrm{pl}} = n\,\beta\,K_{M\theta}L_{\mathrm{pl}}, \tag{50}$$

where $n$ is an arbitrary number larger than 1.0, the lateral displacement $u$ of the tip of the element is

$$u = \sum_{i=1}^{4}\chi_i w_i\left(L - z_i\right) = \frac{F\cdot L^2}{n\,\beta\,K_{M\theta}} + \frac{FL^3}{\beta 3EI}\left(1+\eta\right) \tag{51}$$

where

$$\eta = -2\frac{L_{\mathrm{pl}}^3}{L^3} + 3\frac{L_{\mathrm{pl}}^2}{L^2} - 3\frac{L_{\mathrm{pl}}}{L}. \tag{52}$$

To properly simulate the elastic response, the displacement $u$ has to be equal to the one provided by the proposed model discussed in section 5, i.e.

$$u = \frac{F\cdot L^2}{K_{M\theta}} = \frac{F\cdot L^3}{3EI} \tag{53}$$

The resulting value of ß is

$$\beta = \frac{n+1}{n} + \eta \tag{54}$$

Once yielding of the end section has occurred, the tip displacement $\Delta u$ provided by a force $\Delta F = (M_c - M_y) / L$ is

$$\Delta u = \frac{\Delta F \cdot L^3}{\alpha' n \ 3\beta EI} + \frac{\Delta F \ L^3}{3\beta EI}(1+\eta) \tag{55}$$

Equating the tip displacement $\Delta u$ to $\theta_p L$ leads to

$$\alpha' = \frac{\alpha}{n+1-\alpha n + n(1-\alpha)\eta} \tag{56}$$

where α is the strain hardening ratio of the MIK numerical model in terms of bending moment vs chord rotation.
The pre-capping flexural curvature is calculated as

$$\chi_p = \frac{M_c - M_y}{\alpha' n \beta K_{M\theta} L_{pl}} = \frac{\alpha}{\alpha' n \ \beta \ L_{pl}} \theta_p \tag{57}$$

The post capping flexural curvature is determined equating the tip displacement produced by $\Delta F = -M_c / L$ to $\theta_{pc} L$, i.e.

$$\chi_{pc} = \left[ \theta_{pc} + \frac{M_c L(1+\eta)}{3 \ E \ \beta I} \right] \frac{1}{L_{pl}} \tag{58}$$

Finally, the cyclic degradation parameter is evaluated as

$$\Lambda_\chi = \frac{\Lambda}{L_{pl}} \tag{59}$$

If an element with fixed end rotations is considered, following the procedure previously detailed and assuming that equal and opposite rotations arise at the two ends, the stiffness modification factor ß, the strain hardening ratio α' and the pre-capping flexural curvature are calculated by Eqs. (54), (56) and (57) assuming

$$\eta = -\frac{L_{pl}^3}{L_V^3} + 3\frac{L_{pl}^2}{L_V^2} - 3\frac{L_{pl}}{L_V} \ . \tag{60}$$

The post-capping curvature is calculated by Eq. (58), where the shear span $L_v$ is considered instead of $L$.

### 9.2. Elastic elements with zero-length moment-rotation springs

As already mentioned in the previous sub-section and stated in [77], in the case of an elastic element with rotational springs at the ends, the flexibility of the zero-length moment-rotation springs and that of the interior element are additive. Hence, following an approach similar to that described for elements with finite length hinges, the rotational stiffness of the spring $K_{M\theta} = 3EI/L_v$ should be amplified by a factor $n\beta$ whereas the moment of inertia of the elastic element should be amplified by a factor $\beta$ calculated by means of the following relation

$$\beta = \frac{n+1}{n} \tag{61}$$

Regarding the inelastic response, instead, the values of the strain hardening ratio should be modified as

$$\alpha' = \frac{\alpha}{n+1-\alpha n} \tag{62}$$

Note that $\beta$ and $\alpha'$ can be derived by Eqs. (54) and (56) assuming $\eta = 0$. The pre-capping and post-capping plastic rotations predicted by the proposed equations should be modified as follows

$$\theta_{p,mod} = \frac{\alpha\,\theta_p}{\alpha'\,n\,\beta} \tag{63}$$

$$\theta_{pc,mod} = \theta_{pc} + \frac{M_c L_V}{3E\,\beta I} \tag{64}$$

# Chapter 5
# A FIBRE BASED MODEL FOR BIAXIAL BENDING

Local buckling in the plastic range can be accurately reproduced through refined numerical models based on 3D solid elements. However, the high computational cost of such approaches makes them impractical for the seismic assessment of entire buildings. For this reason, and as already discussed in Chapter 4, simplified modelling strategies are typically adopted when the response of structural systems must be investigated with limited computational effort.

In this framework, the concentrated-plasticity model developed in the previous chapter represents an efficient tool for simulating the cyclic response of HSS members under uniaxial bending. Nevertheless, a key limitation of that approach is that it cannot realistically capture the interaction between axial force and biaxial bending, since the flexural resistance of the spring is defined as a single value and cannot inherently capture the interaction among different internal forces. Consequently, it is not suitable for simulating the response of members subjected to deviated bending.

This motivates the adoption of alternative strategies, such as fibre-based formulations, in which the cross-section is discretised into fibres and a material model is assigned to each fibre, allowing different constitutive rules to represent the steel response in tension and in compression.

Within this context, the study of steel bars undergoing lateral instability provides a useful reference for describing the local response of highly stressed fibres in cold-formed box sections. Consequently, investigating the monotonic and cyclic behaviour of bars represents a key

preliminary step towards the development of material models capable of reproducing realistically the response of hollow structural sections.

On this basis, as a preliminary step, the chapter presents a parametric study in which a set of representative square HSS cross-sections, commonly used in the European context, was analysed through monotonic and cyclic stub column simulations. The results of this parametric investigation provide an essential reference for calibrating a simplified fibre-based approach aimed at reproducing the initiation and evolution of local buckling phenomena.

As a second step, the chapter focuses on the SteelRebar uniaxial material model, originally formulated to simulate the cyclic response of reinforcing bars affected by lateral instability, and examines its applicability to fibres representing cold-formed box sections. After highlighting the limitations that arise when the original SteelRebar formulation is directly employed to reproduce the cyclic response of hollow sections, an improved stress–strain definition is introduced and the monotonic response of the SteelRebar material is accordingly redefined, with the ultimate goal of extending its application to fibre-based modelling of cold-formed HSS members subjected to uniaxial and biaxial bending.

## 1. Stub-Column tests

### 1.1. Selected HSS for the parametric analysis

The investigation included 9 square cold-formed HSS cross-sections. The selected cross-sections cover a wide range of $b_f/t$ ratios, as reported in **Table 27**. This geometric variability allows the influence of local slenderness on the mechanical response under cyclic loading protocols to be systematically assessed. In particular, **Table 27** shows that the local slenderness, evaluated with reference to the net flat-part width, ranges from a stocky configuration with a slenderness equal to 10 to a highly slender configuration with a slenderness equal to 35.

**Table 27** – Geometric properties of the investigated specimens

| Specimen | $r_e$ | $A$ | $b_f = h_w$ | $b_f / t$ | imp. |
|---|---|---|---|---|---|
| | mm | cm$^2$ | mm | - | mm |
| SHS_200x12.5 | 37.52 | 87.04 | 124.97 | 10.00 | 0.25 |
| SHS_350x16.0 | 48.01 | 202.77 | 253.98 | 15.87 | 0.51 |
| SHS_220x10.0 | 24.98 | 80.57 | 170.04 | 17.00 | 0.34 |
| SHS_350x14.2 | 42.60 | 182.08 | 264.80 | 18.65 | 0.53 |
| SHS_400x16.0 | 48.01 | 234.77 | 303.98 | 19.00 | 0.61 |
| SHS_400x14.2 | 42.60 | 210.48 | 314.80 | 22.17 | 0.63 |
| SHS_300x10.0 | 24.98 | 112.57 | 250.04 | 25.00 | 0.50 |
| SHS_350x10.0 | 24.98 | 132.57 | 300.04 | 30.00 | 0.60 |
| SHS_400x10.0 | 24.98 | 152.57 | 350.04 | 35.00 | 0.70 |

### 1.2. Loading protocols and global response of the sections

To investigate the influence of the loading history on the response of members, each FE model was subjected to five uniaxial compression protocols under strain-controlled loading: one monotonic and four cyclic histories. The cyclic protocols include: (i) an incremental-amplitude strain history up to a maximum strain of ±5% (C1); (ii) a constant-amplitude strain history with strain equal to ±5% (C2); (iii) a decreasing-amplitude strain history starting from a maximum strain of ±5% (C3); (iv) an asymmetric cyclic strain history with a maximum strain of ±9% (C4).

The choice of combining incremental- and constant-amplitude histories stems from the observation that constant-amplitude cyclic straining does not represent a realistic response during seismic events, as suggested by Lignos [61]. The protocols were applied in terms of displacements imposed along the longitudinal axis of the member. These displacements were computed as the product of the imposed strain and the expected plastic hinge length. The latter was assumed equal to 0.8 times the maximum cross-sectional dimension (0.8 $D$), thus adapting the protocol to the geometric characteristics of each section. **Fig. 102** shows the adopted loading histories in terms of strain, highlighting the differences among the considered protocols.

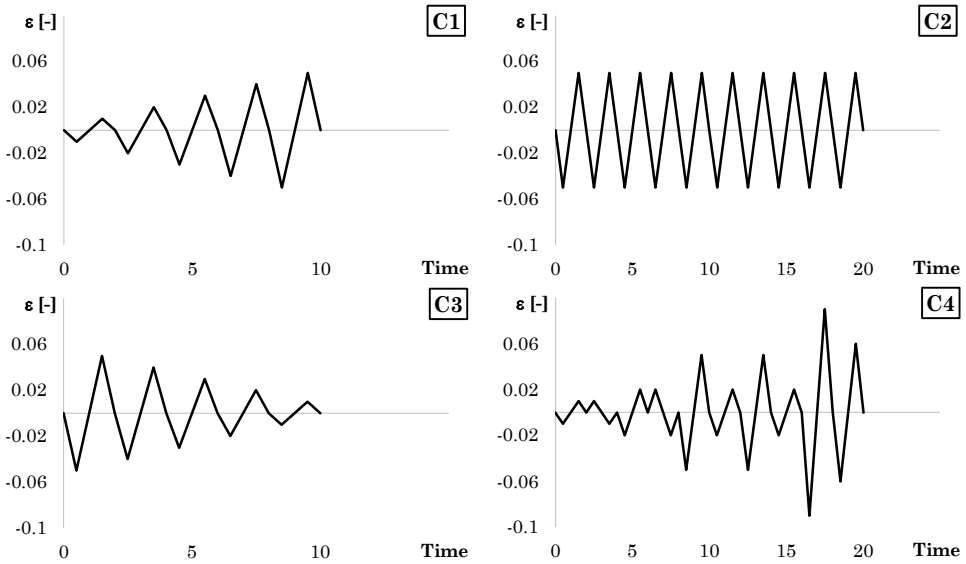


**Fig. 102** – Loading protocols investigated.

**Fig. 103** shows a comparison of the monotonic response between the stockiest specimen (SHS_200x12.5, $h_w/t$ = 10) and the slenderest specimen (SHS_400x10, $h_w/t$ = 35). The stockiest specimen exhibits a relatively flat post-yield response with slight strain hardening, whereas the slenderest specimen reaches a peak load followed by a rapid strength degradation, i.e., a pronounced post-peak softening.

As an example of the axial cyclic response, **Figs. 104**, **105** and **106** report three representative square HSS sections: the stockiest one (SHS_200x12.5, $h_w/t$ = 10), an intermediate-slenderness section (SHS_300x10, $h_w/t$ = 25), and the slenderest section (SHS_400x10, $h_w/t$ = 35). The hysteretic axial force–shortening curves clearly indicate that the structural response is strongly governed by the geometric properties of the cross-section.

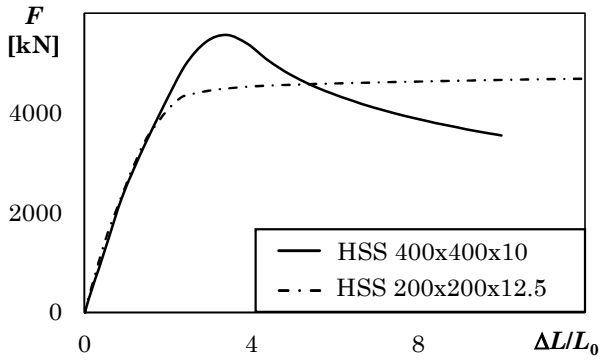


**Fig. 103** – Monotonic response of HSS 400x400x10 and HSS 200x200x12.5.

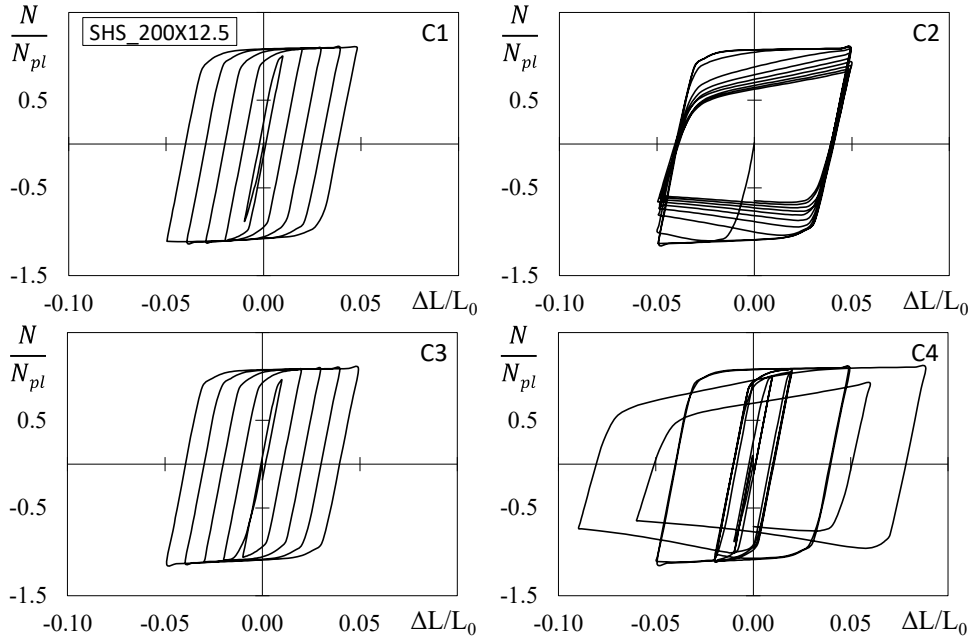


**Fig. 104** – Cyclic response SHS_200x12.5 for different loading protocols.

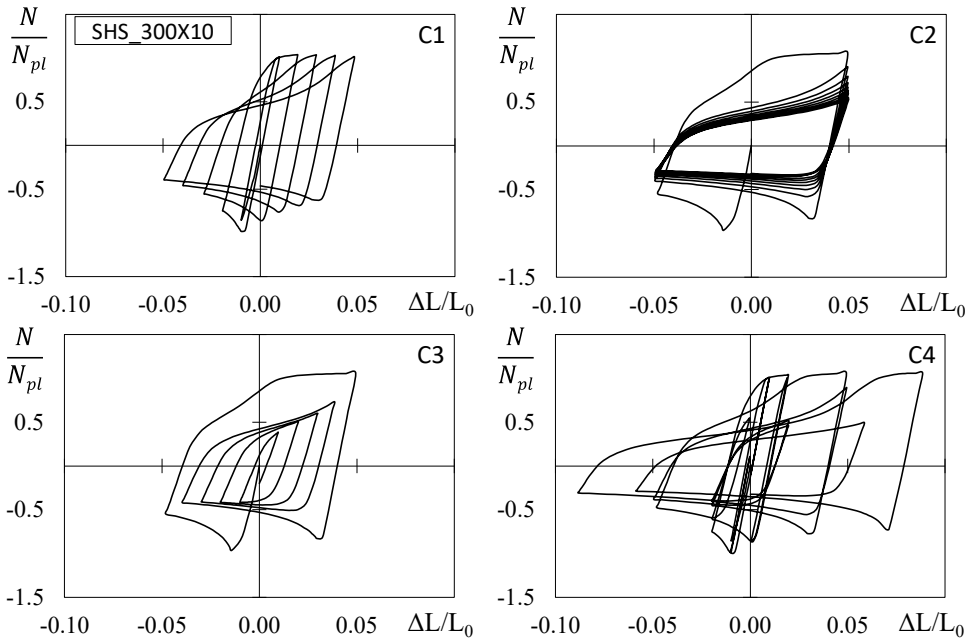


**Fig. 105** – Cyclic response of SHS_300x10 for different loading protocols.

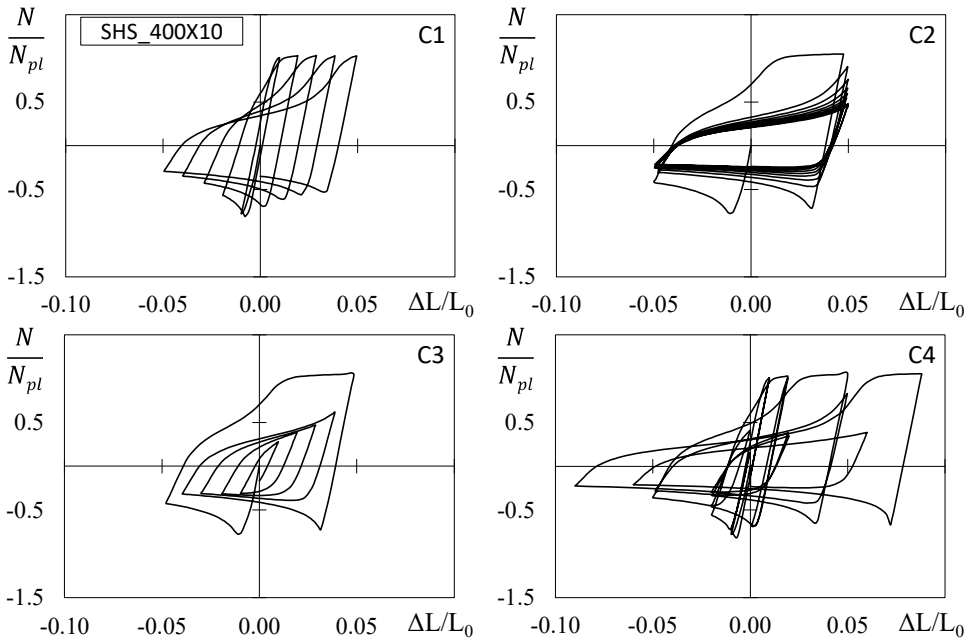


**Fig. 106** – Cyclic response of SHS_400x10 for different loading protocols.

The analysis of the cyclic response highlights a clear correlation between section slenderness and hysteretic behaviour. Specifically: (i) for protocol C1 (Incremental amplitude), stockier sections exhibit more stable hysteretic cycles and a reduced stiffness deterioration compared to more slender sections; (ii) for protocol C2 (constant amplitude), the progressive strength degradation becomes more pronounced as slenderness increases, due to the relaxation phenomenon implemented in the Abaqus constitutive material model; (iii) peak strength values are significantly affected by local slenderness, showing a decreasing trend with increasing $h/t$ ratio; (iv) more slender sections exhibit a more pronounced asymmetry in the response, which becomes especially evident under protocol C4, indicating a higher sensitivity to local instability phenomena.

### 1.3. Stress-strain response at different locations of flat and corner parts

The global response analysis carried out in the previous sub-section showed that the plate slenderness has a marked influence on the structural behaviour. To investigate the local behaviour of flat and corner parts, strips of the mesh at different positions in the flat parts and in the corner parts are isolated in the region where the plastic hinge develops. The region of interest, with length equal to $0.8\,D$, was isolated around the mid-height of the zone affected by instability. This choice is consistent with the fibre model that is to be calibrated, in which each fibre is intended to represent the average behaviour of the corresponding strip within the plastic zone. Once the region of interest was defined, stress–strain curves were extracted for the different mesh strips at selected positions along the cross-section.

In particular, strips were examined at mid-width, at one-quarter, at one-eighth, and at the edges of the flat parts, both in the vertical and in the horizontal direction, as well as all strips constituting the corner parts (**Fig. 107**). These latter parts are subdivided into four elements along their arc. Each strip has a length equal to the length of the plastic hinge, a height equal to the mesh size (20 mm), and a width equal to the wall thickness of the profile. The decision to study the local behaviour along fibres located in different positions reflects the way instability evolves:

fibres at the centre of the flat parts tend to buckle earlier than fibres located near the corner parts, because they are less restrained.

From the analysis of the buckling modes of the strips, it was observed that the strip at mid-width of the flat parts exhibits a purely flexural and perfectly symmetric deformed shape, whereas the strips in correspondence with the corner parts show a deformation with torsional components. These torsional effects arise from the compatibility of deformations between the orthogonal flat parts, which buckle with opposite curvatures.

To evaluate the monotonic stress–strain response of each strip, numerical data were extracted from Abaqus. In the XY data module, the normal stresses $\sigma_{33}$ at all integration points of each mesh element were extracted. For each strip, the mean value of $\sigma_{33}$ over all its elements was taken as the average axial stress. To evaluate the engineering strain, the nodes on the end surfaces of the mesh were isolated using the Unique nodal command, and the variable "Spatial displacement, U3" was selected, representing the axial shortening along the global z-axis. The mean displacement at each end was obtained as the average of the nodal displacements. The engineering strain was then calculated as the ratio between the difference in average end displacements and the initial length of the element. A stress–strain curve was thus obtained for each strip.

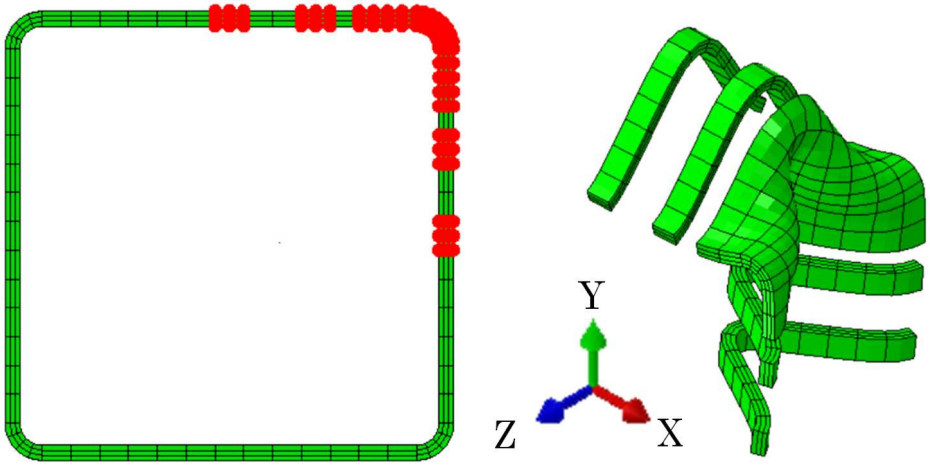


**Fig. 107** – Strips locations in the cross-section

**Fig. 108** shows the stress–strain relationships for the flat parts (**Fig. 108a**) and for the corner parts (**Fig. 108b**), for strips of some of the profiles examined. In particular, the responses are shown for a slender section (400×400×10, $b_f/t$ = 35), a section with intermediate slenderness (300×300×10, $b_f/t$ = 25) and a stocky section (200×200×12.5, $b_f/t$ = 10), highlighting how the local response is influenced by slenderness and how it differs between flat parts and corner parts.

In each plot, different dashed lines represent the results for fibres located near the corner parts (labelled L0O and L0V in the plots), at one-quarter of the flat-part width in the vertical and horizontal direction (L4O and L4V), at one-eighth (L8O and L8V), and at mid-width of the flat parts (L2O and L2V); the fibres in the corner parts are labelled R1, R2, R3, and R4. Since the four corner parts exhibit slightly different behaviours, an average curve is used to represent the response of the corner parts.

From these responses, it can be observed that: (i) for the stocky section, no instability phenomena are observed in the corner parts, while in the flat parts instability is limited to the mid-width strips, which buckle at relatively large strain levels; (ii) for the section with intermediate slenderness, instability mainly affects the central regions of the flat parts, whereas the regions close to the corner parts maintain a more stable behaviour; (iii) for the slender section, instability occurs at lower strain levels and progressively propagates from the central regions of the flat parts towards the corner parts.

These observations confirm that local slenderness has a significant influence on the structural behaviour and suggest the need to differentiate the material behaviour of the fibres within the cross-section in the fibre-based numerical model to be implemented in the OpenSees framework.

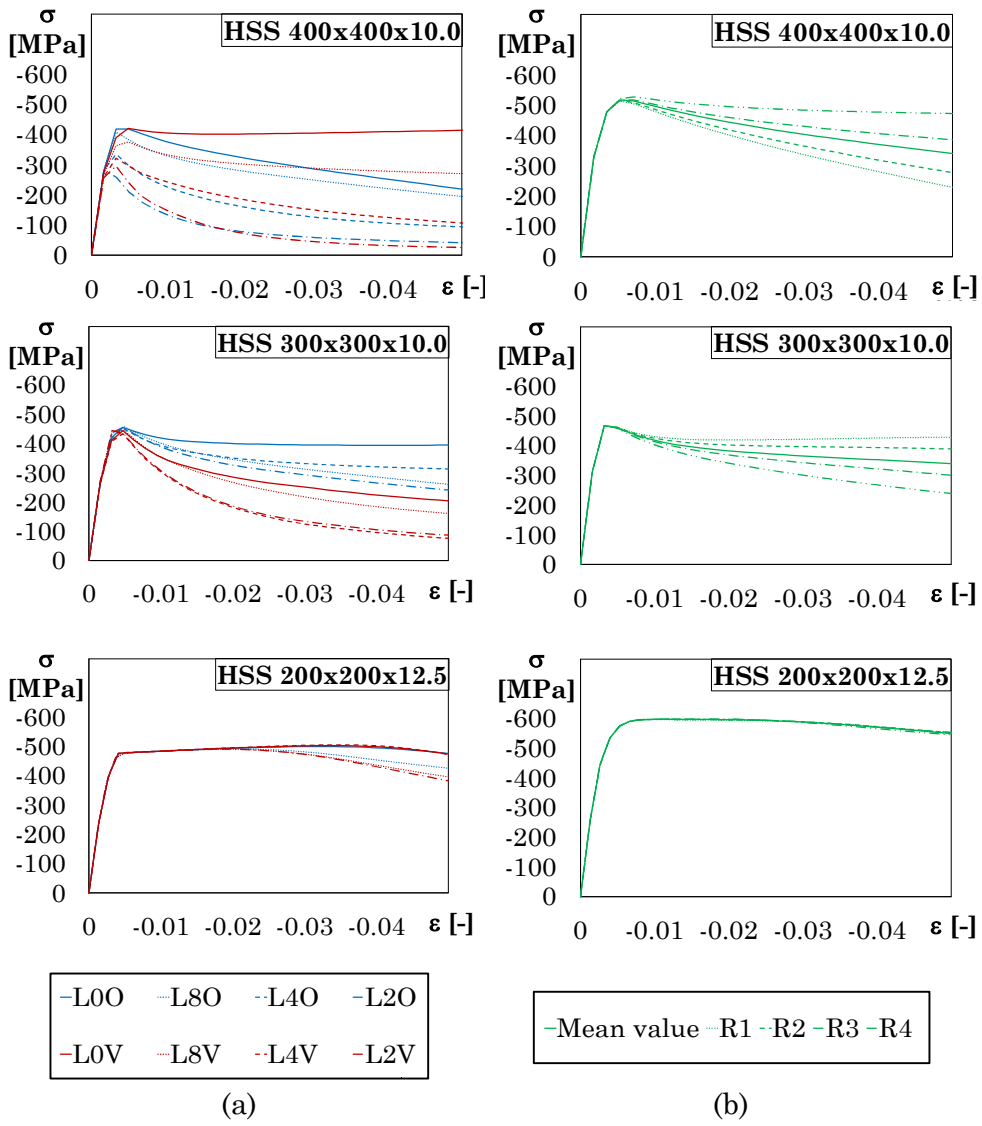


**Fig. 108** – Stress–strain curves along the strips for three sections with different local slenderness: (a) vertical and horizontal plates, (b) corner parts.

### 1.4. Modelling of HSS sections in OpenSees

The numerical modelling performed in OpenSees aims to reproduce the structural response observed in the nonlinear Abaqus simulations, and therefore to assess whether a simplified fibre model can capture the onset of local instability characterising stub column tests. To simulate the axial response of HSS members, the cross-section is discretised into fibres. Each fiber is idealised as an independent bar and is assigned a uniaxial material with properties selected to represent different instability conditions. In this framework, the properties of the uniaxial material model are assumed constant in the corner parts, whereas they vary along the flat parts according to a law that must be calibrated. This strategy enables the model to reflect the different behaviour of the various regions of the cross-section.

Fibres are located at the centroids of the mesh cells used to discretise the section, adopting a square target size of 5 mm. The section is thus subdivided into a discrete number of equal-size fibres, with the discretisation across the wall thickness depending on the profile thickness. In OpenSees, the discretisation is implemented through the patch command, which allows circular, rectangular and quadrilateral patches. Rectangular patches are used for the flat parts, requiring the coordinates of the patch vertices (with respect to a reference system) and the number of subdivisions in each direction. Circular patches are adopted for the corner parts, where the initial and final angles of the arc, the inner and outer radii, and the number of subdivisions along the radius and through the thickness must be specified.

To build the section, a set of dedicated procedures was implemented. A first procedure computes (i) the number of elements composing the cross-section mesh and (ii) the effective mesh size, so that an integer number of cells is obtained along each side of the section. This is performed considering the geometric properties of the cross-section (width, height, outer corner radius, wall thickness, area, moment of inertia and an initial trial mesh size) through which the effective dimensions of the flat parts, $b_f$ and $h_f$, are determined.

The same procedure also receives as input the mechanical parameters of the materials assigned to the flat parts and corner parts (elastic modulus,

yield stress, ultimate stress and ultimate strain), the characteristic slenderness values for flat and corner parts, and two exponential indices used to define the variation of slenderness along the flat parts. The member length is set equal to $3D$, consistently with code indications and to ensure coherence with the Abaqus simulations. Cyclic loading protocols, analogous to those used in the finite element models, are provided as input for the analyses. An example of a discretised section is shown in **Fig. 109**.

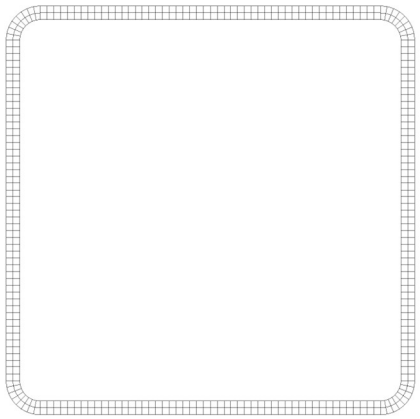

**Fig. 109** – Fibre discretization of the cross-section.

## 2. The SteelRebar uniaxial material model

To simulate the strength and stiffness degradation occurring in the cyclic response of HSS columns using a fibre-based model, a material model capable of reproducing local buckling phenomena is required. For this reason, the SteelRebar uniaxial material model, proposed by Panarelli et al. [78] and implemented in OpenSees, is adopted.

In its original development, the material model was proposed to replicate the response of steel bars characterised by a predefined $l/d$, where $l$ is the effective buckling length of the bar between the restraint points associated with global flexural instability and $d$ is the diameter of the cross-section.

The SteelRebar material model describes the normalised stress–strain response of a steel fibre through six path-dependent rules (R1–R6). Each rule is expressed by continuous curve segments, ensuring that reversals and reconnections occur without artificial stiffness jumps (as schematically shown in **Fig. 110**). Two envelope curves bound the response: specifically, rule R1 defines the compression envelope, while rule R2 defines the tension envelope. The tensile envelope R2 coincides with a Menegotto–Pinto/Steel02-type law [9]. The compressive envelope R1, instead, is constructed based on four characteristic points in the stress-strain plane that define the post-instability response of an axially compressed bar. For $l/d \geq 5$, the coordinates of these points follow the empirical formulation proposed by Akkaya et al. [79], depending primarily on slenderness ($l/d$) and on the strength ratio ($f_u/f_y$), and implicitly on imperfection sensitivity. For stockier bars ($l/d < 5$), the coordinates of the points are interpolated so that the envelope progressively recovers the reference steel material behaviour, and for $l/d = 1$ the compressive response coincides with the underlying Steel02 model. Under cyclic loading, R1 is also shifted along the strain axis when tensile plastic strains develop, to capture the asymmetric response after load reversals.

The remaining rules govern load reversals and reconnections: rules R3 and R4 model the transition from compression to tension and from tension to compression, with a curvature that depends on slenderness and cycle amplitude, while rules R5 and R6 are short "return" branches that reconnect an ongoing transition to the correct envelope (**Fig. 110**).

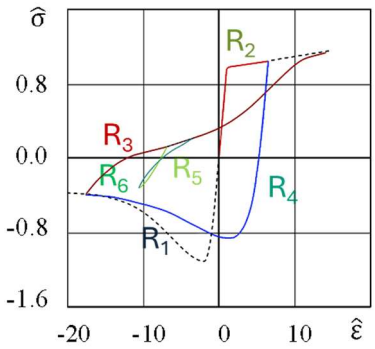


**Fig. 110** – Rules of the SteelRebar material model [78].

This rule-based architecture is attractive for fibre sections, where different effective $l/d$ values can be assigned to fibres located in different positions within flat portions and corners.

The SteelRebar material can be used either by assuming a constant $l/d$ throughout the loading protocol or by allowing $l/d$ to vary during the analysis. The first option, hereinafter referred to as "static material model", is suitable for simulating experimental tests on bare steel bars. The second one, hereinafter referred to as "dynamic material model", was conceived to represent bars embedded in concrete: as long as the concrete cover remains intact, bar instability is restrained and the effective slenderness is taken as $l/d = 1$; after the concrete spalling, the effective slenderness of the bar increases. To reduce the computational effort, Panarelli et al. [78] update the effective slenderness $l/d$ when unloading from tension as a function of the normalized minimum strain recorded within the loading protocol. In this way, $l/d$ increases from an initial to a final value according to a dedicated update law.

## 3. Issues in the application of the SteelRebar material model

A key limitation of the SteelRebar material model arises from the Akkaya-based characteristic points used in R1. In Akkaya's formulation, the stress $f_i$ associated with the $i$-th characteristic point is evaluated as

$$f_i = \alpha\ f_y \qquad f_{it} \geq f_i \geq 0.2 f_y \tag{65}$$

where $f_{it}$ is the stress evaluated on the tensile stress-strain curve at the strain $\varepsilon_i$ and the scaling factor $\alpha$ is defined through a piecewise relationship depending on whether the strain at the point, $\varepsilon_i$, exceeds the strain-hardening threshold $\varepsilon_{sh}$:

$$\alpha = \alpha_1 \alpha_2 \qquad \varepsilon_i > \varepsilon_{sh} \tag{66}$$

$$\alpha = 0.75 \alpha_1 \alpha_2 \qquad \varepsilon_i \leq \varepsilon_{sh} \tag{67}$$

where $\alpha_1$ and $\alpha_2$ are as follow:

$$\alpha_1 = 0.8 + 1.8\left(f_u / f_y\right)\left(d / l\right) \tag{68}$$

$$\alpha_2 = \left(1.1 - 0.016 r_b\right) \tag{69}$$

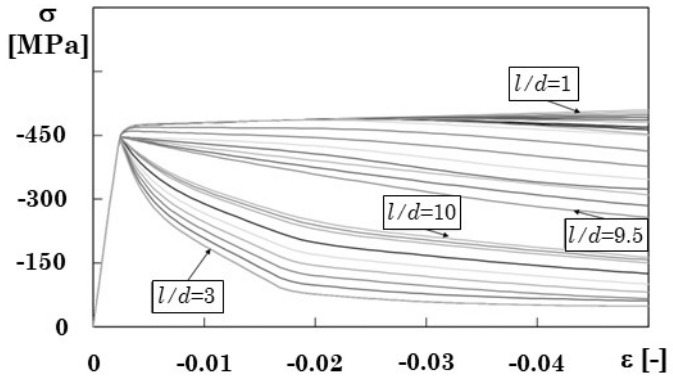


**Fig. 111** – Discontinuity of the SteelRebar material model with flat-plate properties.

The discontinuity in α at $\varepsilon_i = \varepsilon_{sh}$ propagates directly to $f_1$ through Eq. (65), and therefore to the coordinates of the Akkaya characteristic points defining the compressive envelope.

Therefore, the resulting R1 backbone is not strictly continuous with respect to $l/d$: small variations of $l/d$ in Eq. (68) can shift $\varepsilon_i$ across $\varepsilon_{sh}$, producing discrete changes in the point stress (and thus in the envelope shape), with abrupt variations in the monotonic stress–strain response. This becomes particularly critical when SteelRebar is employed with variable slenderness during the analysis or when different $l/d$ values are assigned fibre-by-fibre, since the sectional response may inherit these non-smooth transitions and adversely affect numerical robustness. In preliminary applications to HSS fibres, discontinuities were observed around $l/d \approx 8 – 8.5$ (corner-like properties) and $l/d \approx 9.5 – 10$ (flat-plate properties), with the irregular trend exemplified in **Fig. 111**. These issues motivate the need to revise the compression envelope rule (R1) before SteelRebar can be reliably used for the detailed modelling of cold-formed HSS members.

In addition, another critical aspect concerns the implementation of the model when assuming a variable *l*/*d* value within the cyclic response. Indeed, as already mentioned, the effective $l/d$ is updated only after unloading from tension as a function of the normalized minimum strain.

This implies that, in monotonic analyses or during the first cycle of cyclic analysis with a large first deformation excursion, the $l/d$ ratio is never updated, and any degradation associated with increasing slenderness is not captured.

## 4. Modification of the compression envelope rule (R1) in the SteelRebar material model

To solve the discontinuities in the SteelRebar material model, the monotonic compressive behaviour of SteelRebar was reformulated to obtain a continuous stress–strain law that varies smoothly with slenderness, hardening, and initial imperfection.

The new formulation was developed based on the results of an extensive parametric study on axially compressed circular bars discretised with fibre elements in OpenSees (reference model). The bars have a fixed total length, while the diameter is varied to cover a range of $l/d$ ratios consistent with the original calibration of the SteelRebar model.

### 4.1. Bar model with initial eccentricity

The simulations were performed in OpenSees (Open System for Earthquake Engineering Simulation) using a fibre-based discretisation of the cross-section. The model represents steel bars with a fixed length of 240 mm, while the diameter was varied to achieve the desired $l/d$. Specifically, the $l/d$ ratio was investigated over the range 1–30.

The bar is clamped at the base, whereas the top end is allowed to translate vertically, so that axial shortening can develop under the imposed loading. The member is discretised into 20 forceBeamColumn elements, with a circular fibre section subdivided into ten concentric rings and thirty-six radial sectors. The intermediate nodes are positioned to introduce an initial geometric imperfection equal to 1/1000 of the bar length. Element equilibrium is evaluated in the deformed configuration by means of a corotational formulation, which allows lateral instability to be activated under compressive loading. The steel material assigned to the fibres is the uniaxial Menegotto–Pinto model implemented in OpenSees as Steel02 [9]. **Fig. 112** illustrates the adopted bar model.

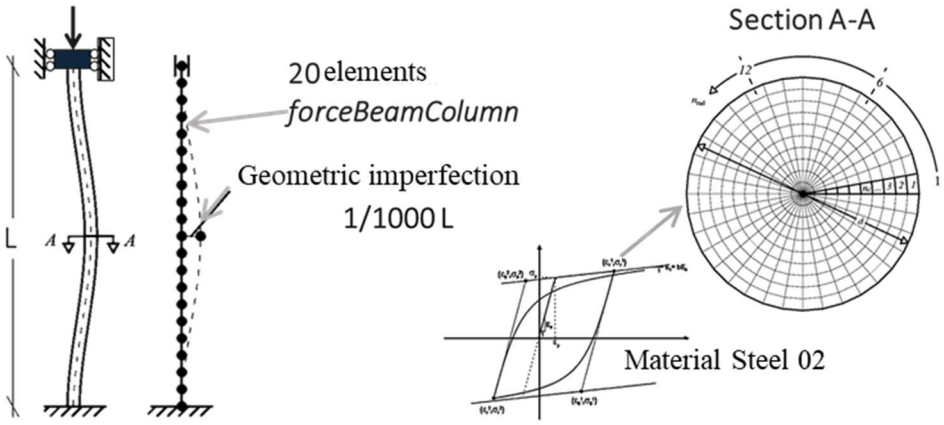


**Fig. 112** – Reference bar model.

In the present study, the Steel02 material is defined by assigning the yield strength $f_y$, the initial elastic modulus $E_s$ = 210000 MPa, the post-yield hardening ratio $b$, and the curvature parameters controlling the elastic-to-plastic transition ($R_0$, $cR_1$, $cR_2$). Specifically, $b$ is computed to match a linear post-yield slope consistent with the ultimate point of the stress–strain curve, using:

$$b = \frac{\left(f_u - f_y\right)E_s}{\left(\varepsilon_u - \varepsilon_y\right)} \tag{70}$$

Where $f_u$ is the ultimate stress, $\varepsilon_u$ is the ultimate strain (taken equal to 0.08), $\varepsilon_y$ is the yield strain defined as $\varepsilon_y = f_y/E_s$. The transition parameters were set to $R_0$ = 20.0, $cR_1$ = 0.925, and $cR_2$ = 0.150, as commonly recommended, while the optional isotropic hardening parameters ($a_1$–$a_4$) and the initial stress (sigInit) were not used.

### 4.2. Influence of imperfection and strain hardening

Before conducting the full parametric study, a set of preliminary trial analyses was carried out to verify whether the response of the bar depends solely on the $l/d$, or whether it is also influenced by the absolute bar length and the amplitude of the initial geometric imperfection. In this

context, the following parameters were varied: (i) three different values of $l/d$, respectively equal to 5, 10, and 15; (ii) two different yield strengths with values of 300 MPa and 500 MPa; (iii) four different hardening ratios, considering a ratio of the hardening modulus $E_h$ to the Young Modulus $E_s$ equal to 0.5%, 1.0%, 1.5%, and 4%.

Each specimen was tested with: (i) two different bar lengths, 12 cm and 24 cm, and for both lengths the diameter of the bar is that necessary to achieve the prefixed $l/d$ ratio; (ii) three different levels of imperfections, respectively 1/100, 1/1000, and 1/10000 of the bar length.

An increasing axial shortening $\delta l$ was imposed at the tip of the bar, and the corresponding axial force $F$ required to achieve the applied shortening was monitored. To compare all cases on a common basis, the results were expressed in terms of normalized stress and strain. For each bar, the axial stress was calculated as

$$\sigma = \frac{F}{A} \tag{71}$$

where $A$ is the cross-section area, while the axial strain was obtained as

$$\varepsilon = \frac{\delta l}{l} \tag{72}$$

where $l$ is the bar length. Stress and strain were then normalized by the corresponding yield values $\sigma_y$ and $\varepsilon_y$

As a representative example, **Fig. 113** shows the comparison between the responses obtained for bar lengths of 12 cm (grey line) and 24 cm (black dashed line), with $f_y$ = 300 MPa and $E_h/E_s$ = 0.5%. The figure clearly demonstrates that, once the $l/d$ is fixed, the normalised response is independent of the absolute bar length and is governed solely by the $l/d$ ratio.

Using the same parameter set, **Fig. 114** compares the responses obtained with initial imperfections equal to 1/100 $L$ (grey line), 1/1000 $L$ (black dashed line), and 1/10000 $L$ (black continuous line). The results show that the curves corresponding to imperfections of 1/100 $L$ and 1/1000 $L$ are practically coincident, whereas a smaller imperfection of 1/10000 $L$ may fail to correctly trigger the instability of the bar. The continuous black curve in **Fig. 114** refers to the case with $l/d$ = 10; the curves for the other $l/d$ are perfectly superposed to those obtained with an

imperfection of 1/1000 $L$. Based on these observations, an initial imperfection equal to 1/1000 $L$ was adopted in the subsequent analyses.

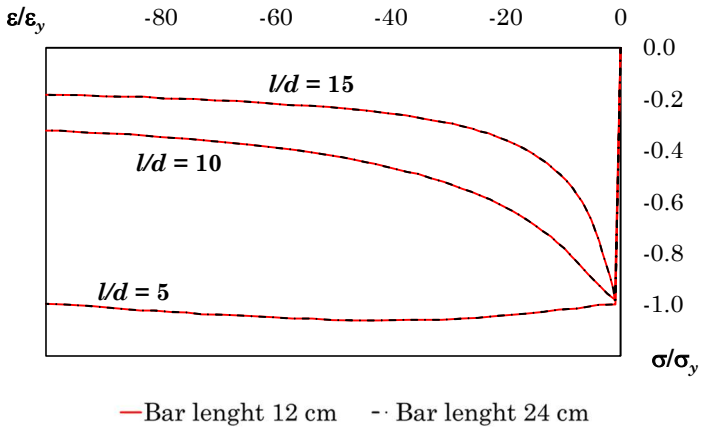


**Fig. 113** – Bar length influence: case study with $f_y$ = 300 MPa, $E_h/E_s$ = 0.5% and imperfection equal to 1/1000 $L$

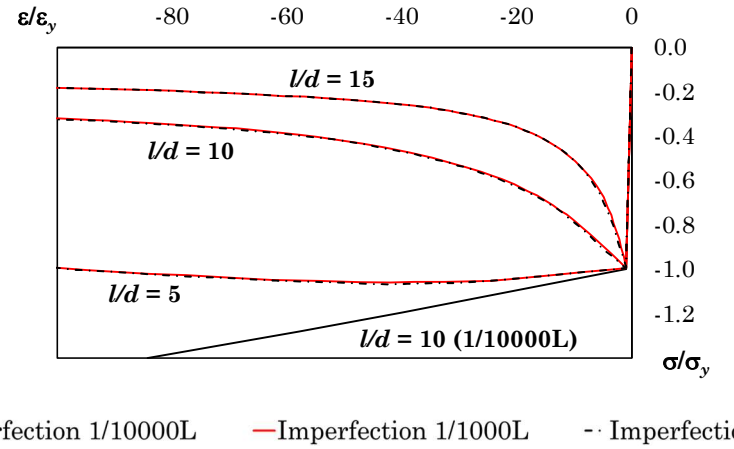


**Fig. 114** – Geometrical imperfections influence: case study with $f_y$ = 300 MPa and $E_h/E_s$ = 0.5%

Finally, **Fig. 115** shows normalised stress-strain curves obtained for two different hardening ratios, namely $E_h/E_s$ = 1.5% (dashed line) and $E_h/E_s$ = 4.0% (solid line). The figure highlights that the influence of strain hardening on the stress-strain response increases as the bar slenderness decreases. In particular, for bars with $l/d$ = 5, a significant dependence on the hardening ratio is observed, whereas this influence becomes less pronounced for $l/d$ = 10 and $l/d$ = 15.

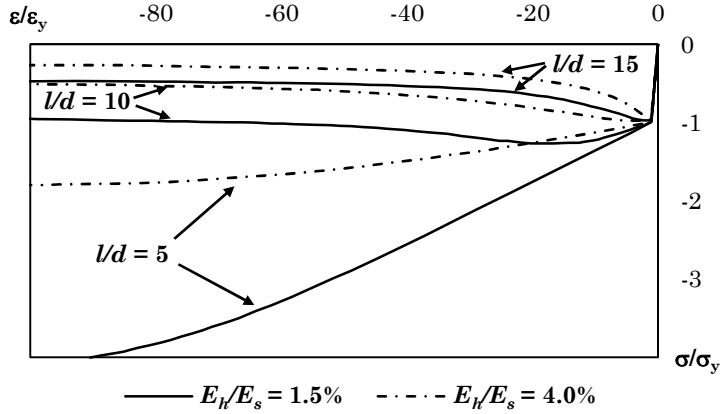


**Fig. 115** – Normalized stress-strain curves: case study with $f_y$ = 300 MPa, $E_h/E_s$ = 1.5% and $E_h/E_s$ = 4.0%.

### 4.3. Parametric analysis

To investigate the influence of the $l/d$ on the mechanical response of steel bars in compression, a parametric study was carried out in OpenSees. On the basis of the observations made in the previous section on the role of initial geometric imperfections and strain hardening, the following ranges of mechanical parameters were considered: (i) yield strength $f_y$ varying between 300 and 600 MPa; (ii) hardening ratio $b = E_h/E_s$ expressed as a percentage, taking values between 0.1% and 4.5%; and (iii) the ratio $l/d$ in the range from 1 to 30.

For each combination of $f_y$ and $E_h/E_s$, monotonic compression tests were simulated on bars with constant total length and variable diameter, chosen so as to obtain the desired values of the $l/d$.

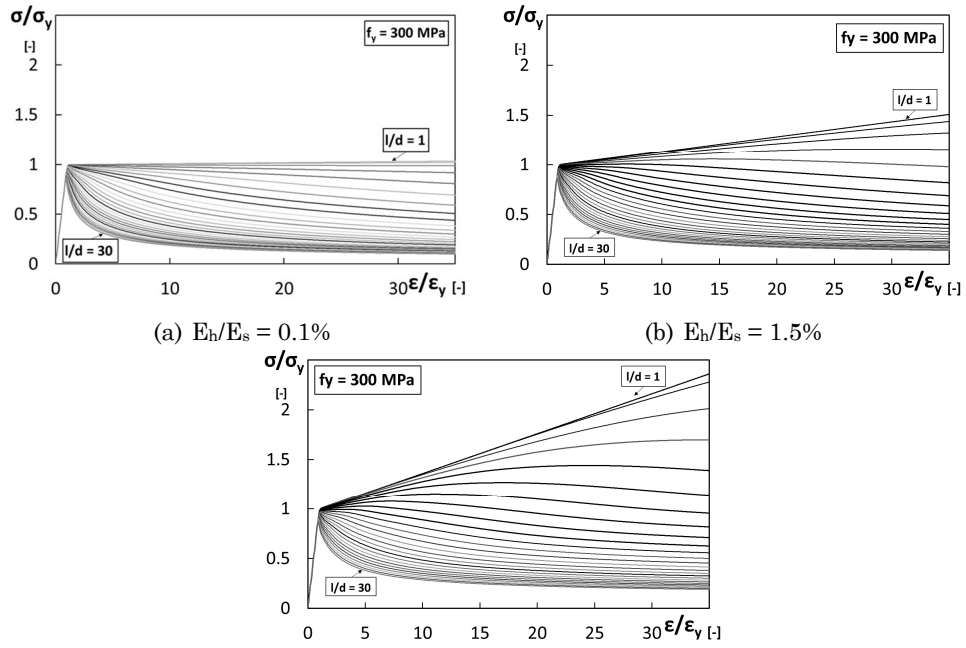


(a) $E_h/E_s$ = 0.1% (b) $E_h/E_s$ = 1.5%

(c) $E_h/E_s$ = 4 %

**Fig. 116** – Normalized stress-strain curves for different values of the $l/d$: Case study $E_h/E_s$ equal to (a) 0.1%, (b) 1.5%, (c) 4.0%.

**Fig. 116** shows, as an example, the normalized stress-strain curves obtained for different values of the $l/d$, for three representative hardening ratios: (i) low, with $E_h/E_s$ = 0.1%; medium, with $E_h/E_s$ = 1.5%; high, with $E_h/E_s$ = 4%.

To characterize these normalized curves, three target normalized strain levels were selected: (i) $\varepsilon/\varepsilon_y = 7$; (ii) $\varepsilon/\varepsilon_y = 15$; (iii) $\varepsilon/\varepsilon_y = 30$. For each target strain, the corresponding normalized stress values were extracted from the parametric analyses for all considered values of $l/d$. In this way, for each target strain level, a set of points $\sigma/\sigma_y$ as a function of $l/d$ was obtained.

**Fig. 117** shows the evolution of normalized stress with slenderness for the three target normalized strain values. The results show that, for a fixed $l/d$, the normalized stress exhibits a scatter that depends on the yield strength and on the hardening ratio; this scatter is more pronounced within specific slenderness ranges, which in turn depend on the

chosen target strain. In particular, it can be seen that: (i) for the target strain $\varepsilon/\varepsilon_y = 7$ and $\varepsilon/\varepsilon_y = 15$, the largest variation is observed for $5 \leq l/d \leq 15$; (ii) for the target strain $\varepsilon/\varepsilon_y = 30$, the widest variability occurs for $1 \leq l/d \leq 10$.

In general, an increase in the hardening ratio leads to an increase in normalized stress, with a steeper trend at higher target strain levels.

Following the approach adopted in some existing models in the literature [79], where instability parameters for bars are expressed as functions of yield strength and hardening, a modified $l/d$ was introduced in this study to remove the explicit dependence on the yield strength. The modified $l/d$ is defined as:

$$\left(\frac{l}{d}\right)_{\text{mod}} = \frac{l}{d}\sqrt{\frac{f_y}{100}} \tag{73}$$

where $f_y$ is expressed in MPa.

Moreover, as observed in **Fig. 117**, the scatter of the curves is influenced by the strain hardening. Therefore, in order to make the curves more comparable, each plot was filtered by selecting, among the available data, only those corresponding to a fixed hardening ratio.

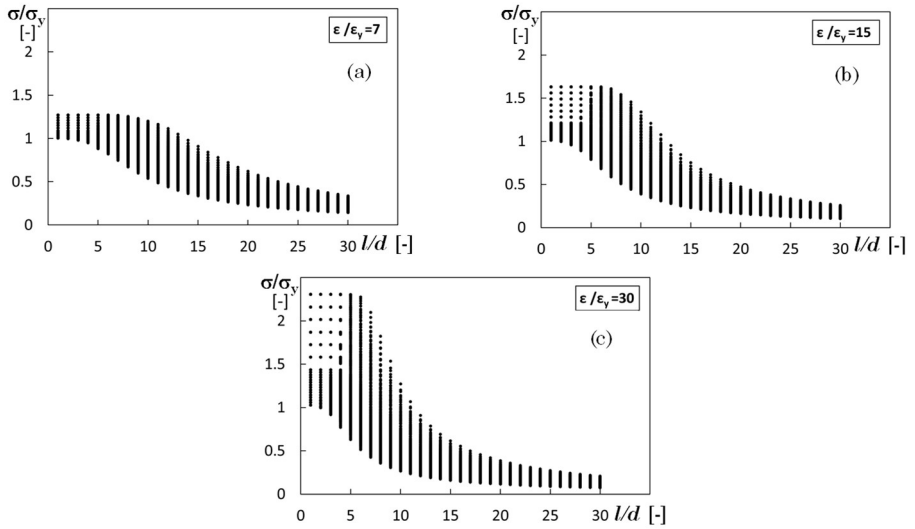


**Fig. 117** – Evolution of normalized stress with slenderness for the three target strain values equal to (a) 7, (b) 15, (c) 30.

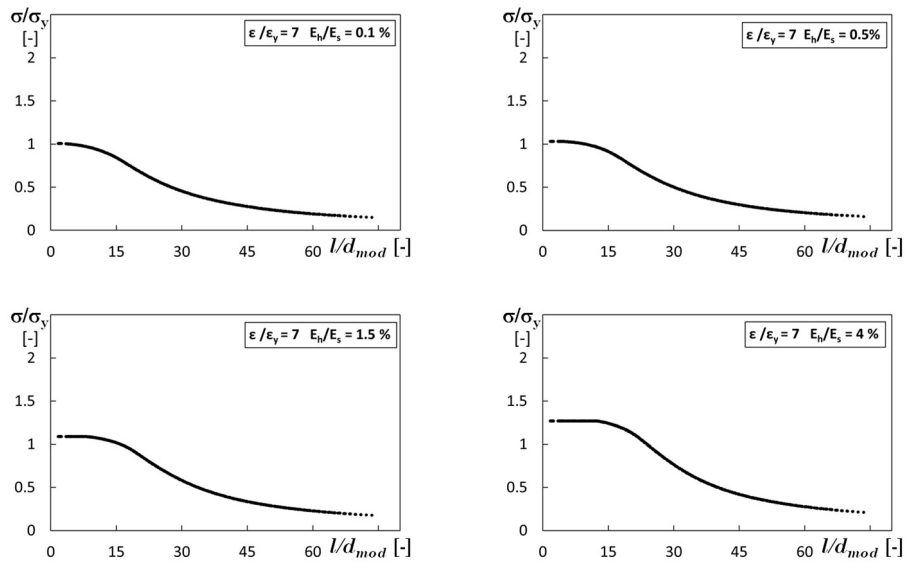


**Fig. 118** – Normalized stresses versus $l/d_{mod}$ for different hardening values: case $\varepsilon/\varepsilon_y = 7$.

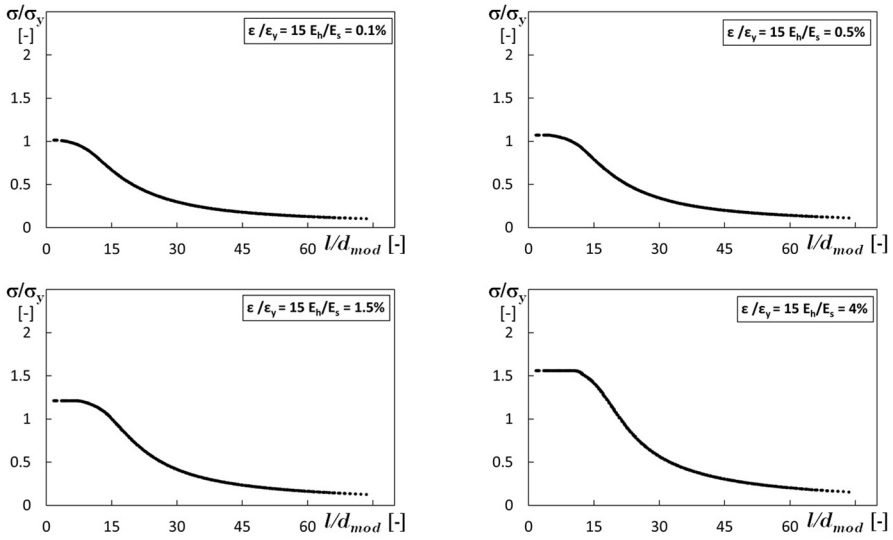


**Fig. 119** – Normalized stresses versus $l/d_{mod}$ for different hardening values: case $\varepsilon/\varepsilon_y = 15$.

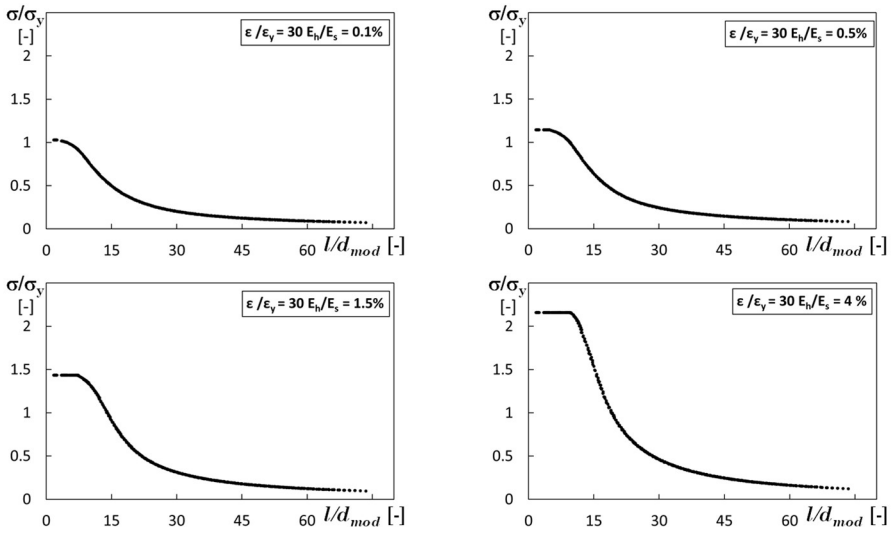


**Fig. 120** – Normalized stresses versus $l/d_{mod}$ for different hardening values: case $\varepsilon/\varepsilon_y = 30$.

This approach yields a more uniform representation of the trend of normalized stress as a function of the modified $l/d$, as shown in **Figs.118, 119** and **120**.

This modified $l/d$ is used in the formulation of the new monotonic compressive law for the SteelRebar material.

### 4.4. Calibration of the proposed equations

The curves depicted in **Figs. 118, 119** and **120**, that show the normalized stress as a function of the modified $l/d$, have a shape that closely resembles the classical buckling curves of columns with imperfections. For this reason, it was considered appropriate to describe these trends using formulations analogous to those adopted in the Italian code (Norme tecniche per le costruzioni 2018 [80]) and the European code (Eurocode 3 [67]) to predict the buckling resistance of members.

The general expression proposed for the normalized stress $\sigma_n$ is:

$$\sigma_n = \min\left(\frac{1}{\eta + \sqrt{\left|\eta^2 - \bar{\lambda}^2\right|}}; \beta\right) \tag{74}$$

where η and the normalized slenderness $\bar{\lambda}$ are defined as:

$$\eta = \gamma\left[1 + \alpha\left(\bar{\lambda} - \delta\right) + \bar{\lambda}^2\right] \tag{75}$$

$$\bar{\lambda} = \frac{(l/d)_{\text{mod}}}{30} \tag{76}$$

The parameters α, β, γ, and δ are coefficients introduced to reproduce curves with a trend similar to those obtained from the parametric study (**Figs. 118-120**). The above parameters are determined by means of a least-squares procedure, minimizing the sum of the squared differences between the normalized stresses predicted by the equation and those obtained from the numerical analyses. Specifically, the optimal values of α, β, γ, and δ are identified for each considered hardening ratio and normalised target strain $\varepsilon/\varepsilon_y$.

By plotting the normalized stress $\sigma_n$ computed from Eq. (74) as a function of the normalized slenderness, it was verified that the proposed expression approximates with good accuracy the curves derived from the parametric study, as illustrated in **Figs. 121**, **122** and **123** for the three target strain levels $\varepsilon/\varepsilon_y$ = 7, 15 and 30. In these figures, the normalized stress $\sigma_n$ is computed from Eq. (74) using the values of α, β, γ and δ obtained from the regression analysis.

The calibrated coefficients α, β, γ, and δ were then plotted as functions of the hardening ratio $E_h/E_s$ in **Figs. 124**, **125** and **126** for the three target normalized strains $\varepsilon/\varepsilon_y$ = 7, 15 and 30, respectively. The figures show that coefficients β, γ can be expressed as a function of the hardening ratio by linear relationships, while α and δ can be represented by piecewise functions consisting of a constant branch and a linear branch. These relationships were obtained through regression analyses and are reported, for each target strain, in Eqs. (77)-(88).

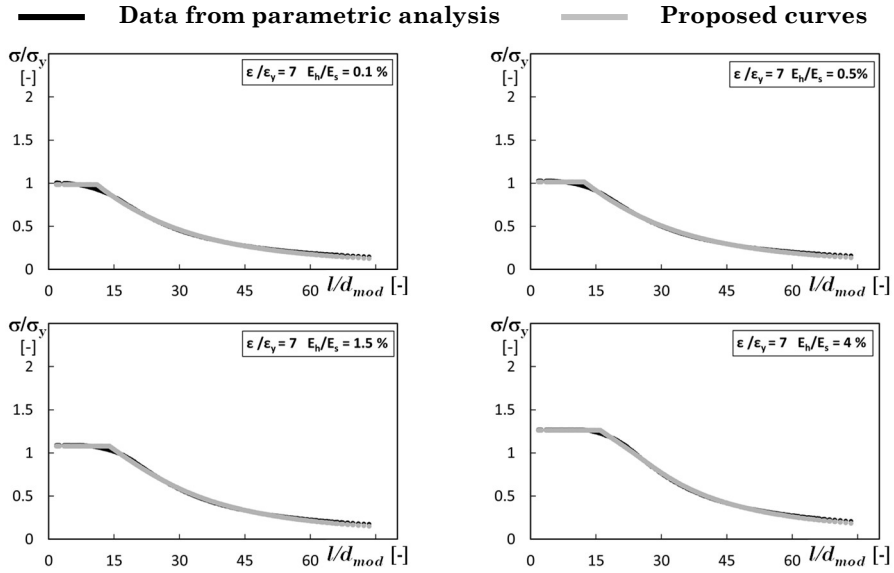


**Fig. 121** – Comparison between normalized stresses determined by the parametric analysis and those predicted by the proposed equations for different $E_h/E_s$ ratios: case $\varepsilon/\varepsilon_y = 7$.

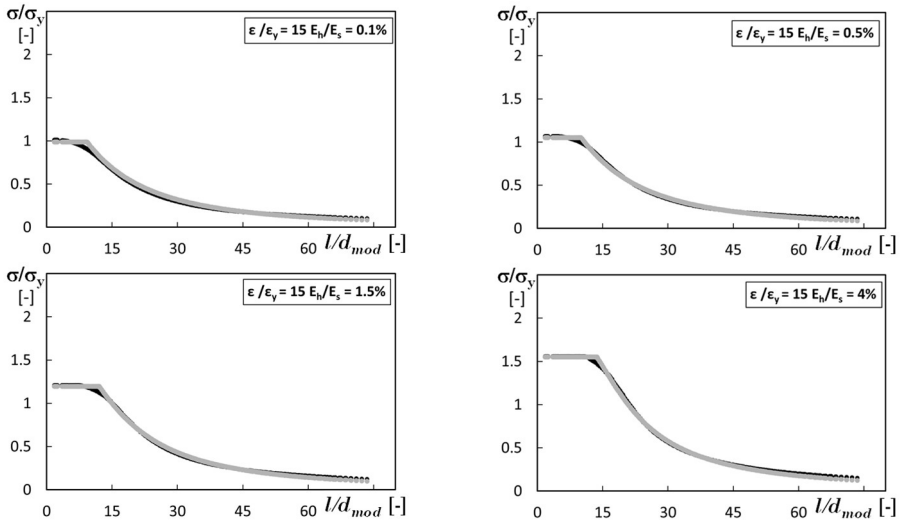


**Fig. 122** – Comparison between normalized stresses determined by the parametric analysis and those predicted by the proposed equations for different $E_h/E_s$ ratios: case $\varepsilon/\varepsilon_y = 15$.

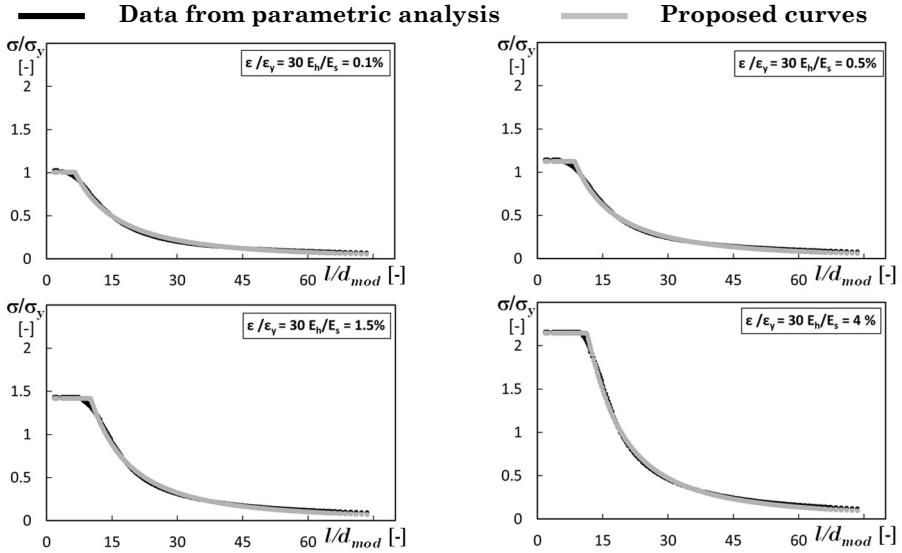


**Fig. 123** – Comparison between normalized stresses determined by the parametric analysis and those predicted by the proposed equations for different $E_h/E_s$ ratios: case $\varepsilon/\varepsilon_y = 30$.

For $\varepsilon/\varepsilon_y = 7$:

$$\beta = 0.063\left(E_h/E_s\right) + 0.9839 \tag{77}$$

$$\gamma = -0.0291\left(E_h/E_s\right) + 0.4075 \tag{78}$$

$$\alpha = 0.2038\left(E_h/E_s\right) + 1.0436 \geq 1.45 \tag{79}$$

$$\delta = -0.02081\left(E_h/E_s\right) + 0.2368 \leq 0.2 \tag{80}$$

For $\varepsilon/\varepsilon_y = 15$:

$$\beta = 0.1434\left(E_h/E_s\right) + 0.9813 \tag{81}$$

$$\gamma = -0.0376\left(E_h/E_s\right) + 0.6487 \tag{82}$$

$$\alpha = -0.1989\left(E_h/E_s\right) + 1.280 \geq 1.00 \tag{83}$$

$$\delta = 0.1369\left(E_h/E_s\right) + 0.4894 \leq 0.7 \tag{84}$$

For $\varepsilon/\varepsilon_y = 30$:

$$\beta = 0.2938\left({}^{E_h}/_{E_s}\right) + 0.9785 \tag{85}$$

$$\gamma = -0.0645\left({}^{E_h}/_{E_s}\right) + 0.9443 \tag{86}$$

$$\alpha = -0.3117\left({}^{E_h}/_{E_s}\right) + 1.38 \geq 0.75 \tag{87}$$

$$\delta = 0.2933\left({}^{E_h}/_{E_s}\right) + 0.5739 \leq 1.15 \tag{88}$$

The values of the coefficients computed by the above equations are superimposed on those obtained by regression analysis in **Figs. 124**, **125** and **126** for the target normalized strain cases 7, 15 and 30.

To assess the effectiveness of the proposed formulation, the variation laws for the coefficients α, β, γ, and δ were used to compute the normalized stress $\sigma_n$ at the selected target strain levels, for the full range of $l/d$ and hardening values considered in the parametric study. For each target strain and hardening ratio, the stress-strain curves obtained from the analytical equations were compared with those derived directly from parametric analyses.

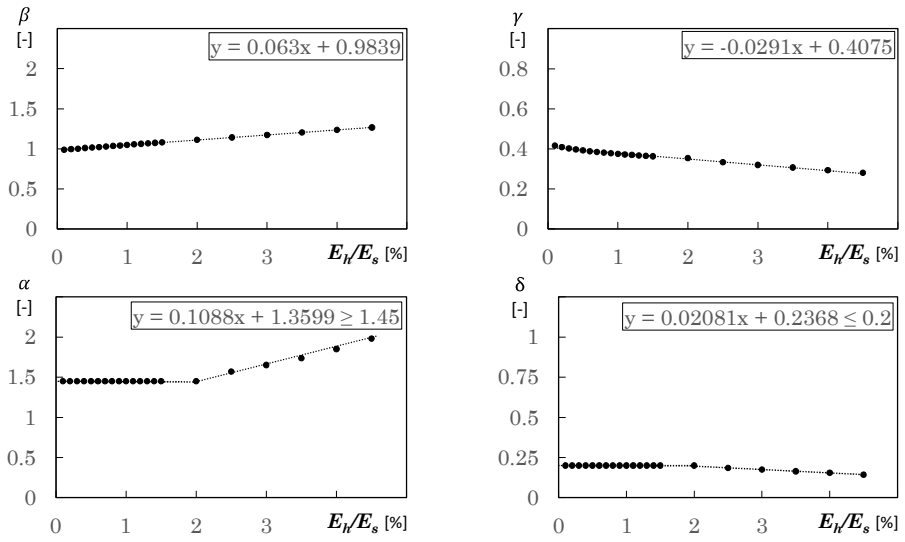


**Fig. 124** – Influence of the hardening ratio on coefficients α, β, γ, and δ: target strain case 7.

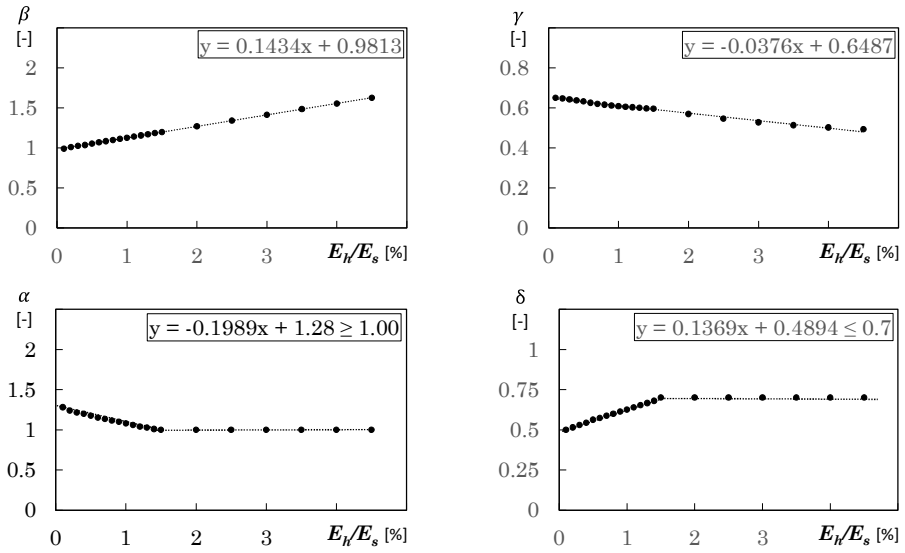


**Fig. 125** – Influence of the hardening ratio on coefficients α, β, γ, and δ: target strain case 15.

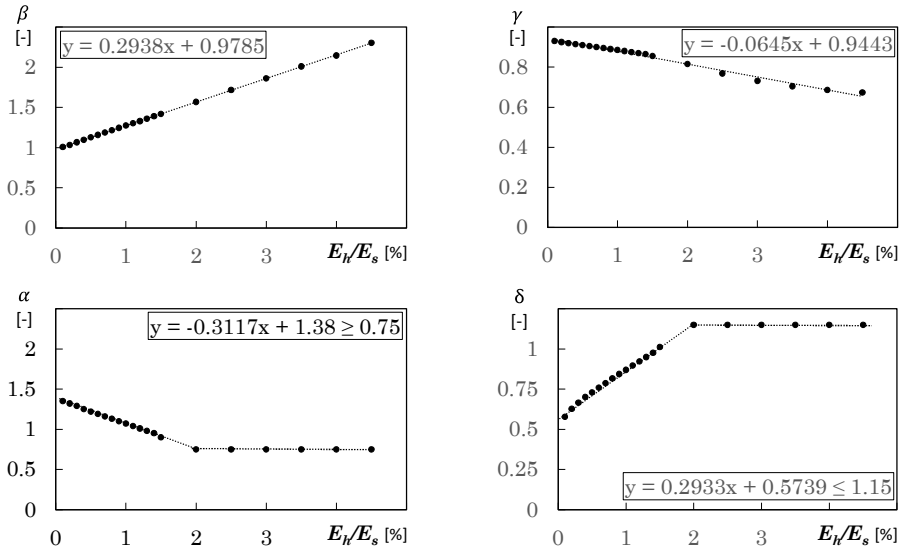


**Fig. 126** – Influence of the hardening ratio on coefficients α, β, γ, and δ: target strain case 30.

**Figs. 127-128** report this comparison, showing the stress-strain relationships. In each plot, results corresponding to different $l/d$ are reported: the continuous lines represent the curves obtained from the parametric analysis, while the points indicate the values predicted by the proposed equations, for different hardening ratios. It can be seen that the points closely follow the numerical curves over the entire investigated domain, demonstrating that the formulation is able to accurately reproduce the monotonic compressive behaviour captured by the parametric study.

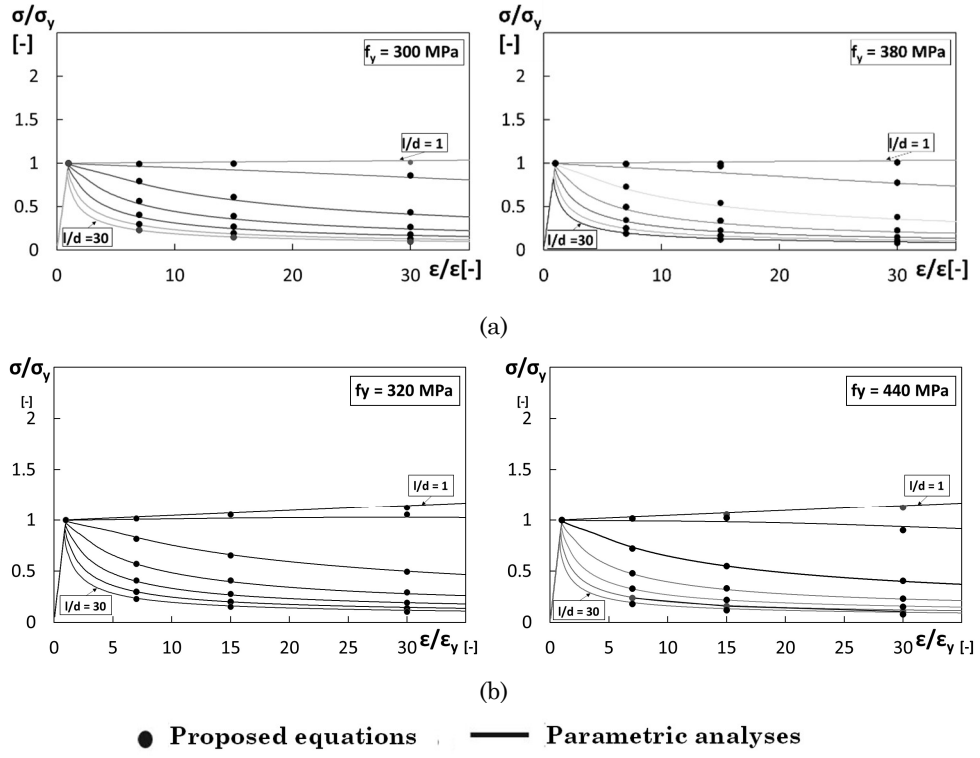


**Fig. 127** – Accuracy of the proposed equations for the cases with: (a) $E_h/E_s$ = 0.1%, (b) $E_h/E_s$ = 0.5%.

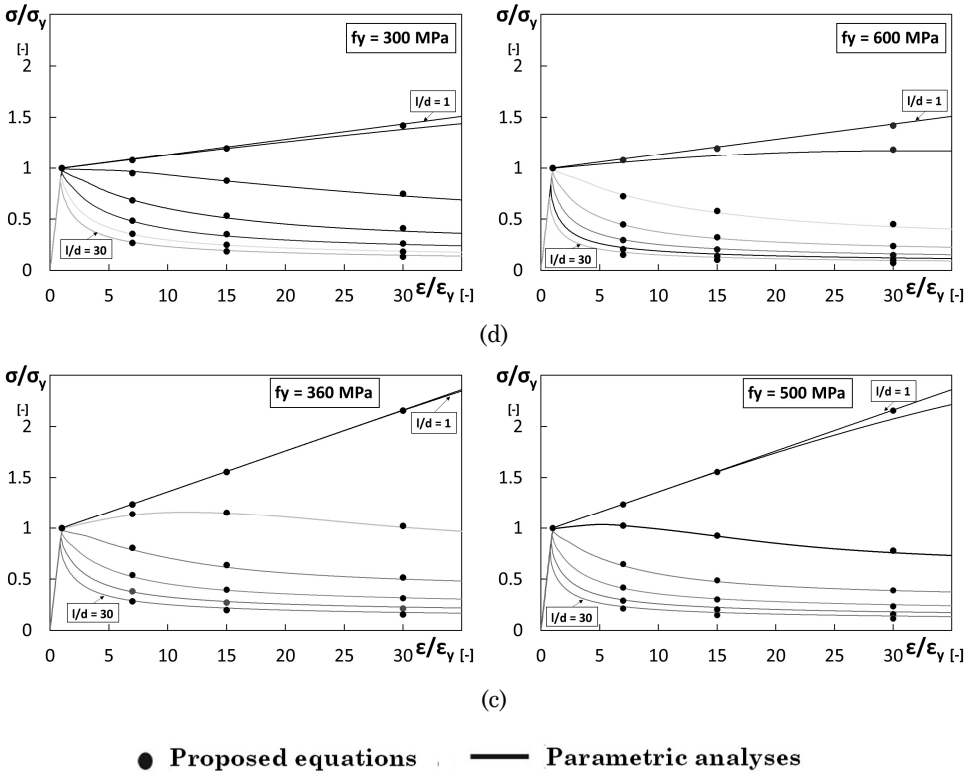


**Fig. 128** – Accuracy of the proposed equations for the cases with:
(a) $E_h/E_s$ = 0.1%, (b) $E_h/E_s$ = 0.5%, (c) $E_h/E_s$ = 1.5%, (d) $E_h/E_s$ = 4.0%.

The proposed equations, based on a buckling-type formulation and calibrated against the numerical database, reproduce with good accuracy the normalized compressive response over the investigated range of modified $l/d$ and hardening ratios. In addition, they overcome the discontinuity issue associated with the Akkaya's characteristic points. Therefore, the monotonic compression envelope of the SteelRebar material has been modified by replacing the Akkaya's points with those characterised by normalized strain levels equal to 7, 15, 30 and normalized stress provided by the proposed equations.

### 4.5. Additional modifications to the SteelRebar material

As mentioned in Section 2 of this Chapter, the SteelRebar material can be used either by assuming a constant $l/d$ throughout the loading protocol or by allowing $l/d$ to vary during the analysis.

In the original SteelRebar formulation, the $l/d$ of the rebar is updated when unloading from tension as a function of the normalized minimum strain. Furthermore, the variation of $l/d$ is assumed to be a linear function of the normalized minimum strain reached in compression, between an initial threshold $\varepsilon_{lim,ini}$ and a final threshold $\varepsilon_{lim,fin}$. These features present two shortcomings. First, in the case of a monotonic compressive loading, no updating of $l/d$ occurs because there is not unloading from tension. Second, the assumption of a linear variation of the $l/d$ has not been experimentally verified.

To make the model more flexible, the evolution law for the variable $l/d$ was therefore modified by introducing an exponent $\eta$ in the original equation, controlling the rate at which $l/d$ increases with compressive strain. The modified expression is given in the following equation:

$$\frac{l}{d} = \left(\frac{l}{d}\right)_{ini} + \left(\frac{|\varepsilon_{min}| - \varepsilon_{lim,ini}}{\varepsilon_{lim,fin} - \varepsilon_{lim,ini}}\right)^{\psi} \left[\left(\frac{l}{d}\right)_{fin} - \left(\frac{l}{d}\right)_{ini}\right] \geq \left(\frac{l}{d}\right)_{ini} \tag{89}$$

Low values of $\psi$ lead to a rapid increase in the $l/d$ even at relatively small compressive strains, whereas higher values of $\psi$ produce a slower evolution of $l/d$, delaying the onset of high $l/d$.
Furthermore, Eq. (89) is evaluated at every step of the loading protocol rather than only at strain reversal from tension.

## 5. Advantages of the modified Steel rebar material over the original formulation

Both the rule R1 proposed in section 4 and the new evolution equation for the $l/d$ were implemented in OpenSees within the SteelRebar material.

Additional numerical analyses were carried out to assess whether the modified formulation is able to eliminate the discontinuities previously observed in the compressive response of bars modelled with the original SteelRebar law when varying the $l/d$.

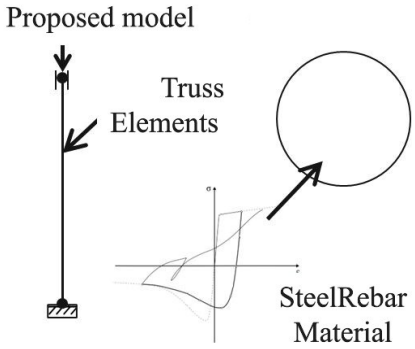


**Fig. 129** – Proposed model

The numerical model used for this verification consists of a single element, without geometric imperfections, with cross-sectional area equal to that of the bar and without fibre discretization (**Fig. 129**). The SteelRebar material is assigned directly to the element area. Monotonic compression tests were performed using mechanical properties representative of the flat parts and the corner parts of the HSS cross-section. The adopted parameters are reported in **Table 28**.

The result of these analyses, expressed in terms of normalized strain and normalized stress, confirm the effectiveness of the implemented laws and the modified $l/d$ evolution rule. The discontinuities previously observed in the bar response are removed, as shown in **Fig. 130**, which reports the monotonic stress-strain curves for different $l/d$ for corners and plates under the assumption of constant $l/d$.

**Table 28** – Material properties of bars representing flat parts and corner parts.

| Material | $E$ [MPa] | $f_y$ [MPa] | $f_u$ [MPa] | $\varepsilon_y$ [-] | $E_h/E_s$ [-] |
|---|---|---|---|---|---|
| Flat parts | 200000 | 475.0 | 560.0 | 0.0024 | 0.36% |
| Corner parts | 200000 | 600.0 | 610.0 | 0.003 | 0.075% |

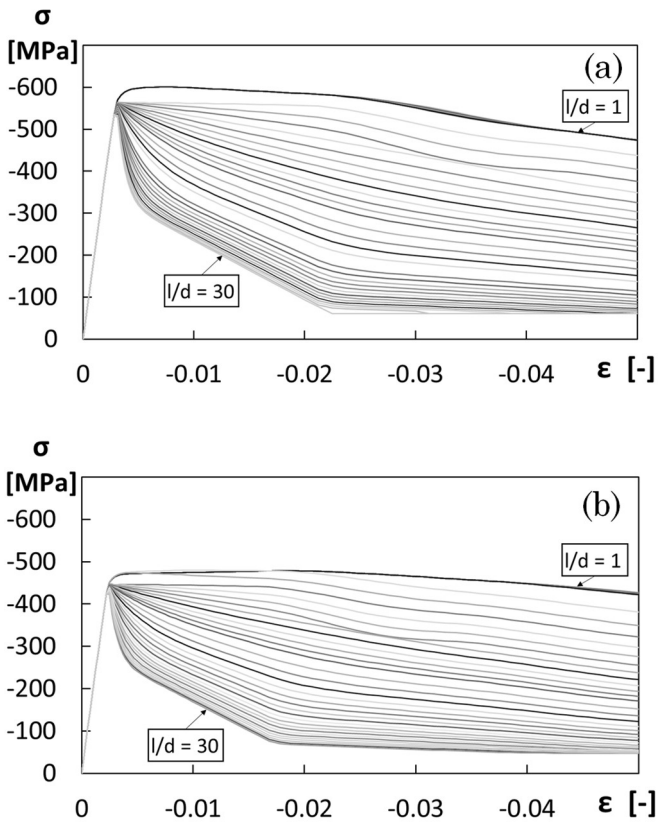


**Fig. 130 –** Stress–strain relationship for different bar $l/d$ values provided by the modified Steel Rebar Material: (a) corner parts, (b) flat parts.

## 6. Validation against cyclic tests on reinforcing bars

A validation of the implemented laws was carried out by comparing the numerical response of the bar model using the modified SteelRebar material with experimental results from the literature. Two experimental campaigns were considered: the tests by Monti and Nuti (1996) [81] and those by Prota et al. (2009) [82]. In total, 24 specimens were analysed: 12 tested by Monti and Nuti, with $l/d$ between 5 and 11, and 12 tested by

Prota et al., with $l/d$ between 5 and 20. In all cases, the bars tested by the researchers were reproduced numerically so as to match the reported geometry, mechanical properties and boundary conditions. The displacement applied at the bar tip followed the same displacement histories adopted in the laboratory tests and was imposed in the direction parallel to the bar longitudinal axis. A brief description of the experimental programmes is given below, followed by the comparison between numerical and experimental responses.

### 6.1. Cyclic tests by Monti and Nuti

Monti and Nuti [81] investigated the effects of local instability on the monotonic and cyclic behaviour of reinforcing bars in reinforced concrete members. The steel used for the bars was an Italian grade FeB44k, with a nominal yield strength of 440 MPa. The bars were tested in a fixed–fixed configuration, in order to reproduce the restraint provided by transverse reinforcement on longitudinal bars in RC elements. The bar length was chosen to obtain the desired $l/d$.

**Table 29** – Material properties of specimens tested by Monti and Nuti [81].

| Specimen | $f_y$ [MPa] | $f_u$ [MPa] | $E_s$ [MPa] | $E_h/E_s$ [-] | $l/d$ [-] |
|---|---|---|---|---|---|
| A1 | 470.0 | 620.0 | 200000 | 0.020 | 5 |
| A2 | 470.0 | 608.0 | 200000 | 0.018 | 5 |
| A3 | 430.0 | 692.0 | 180000 | 0.039 | 5 |
| A4 | 450.0 | 815.0 | 160000 | 0.062 | 5 |
| C1 | 470.0 | 605.0 | 200000 | 0.018 | 11 |
| C2 | 470.0 | 632.0 | 200000 | 0.022 | 11 |
| C3 | 430.0 | 515.0 | 180000 | 0.013 | 11 |
| C4 | 470.0 | 615.0 | 160000 | 0.025 | 11 |
| C5 | 450.0 | 534.0 | 160000 | 0.014 | 11 |
| A3_0 | 470.0 | 766.0 | 200000 | 0.039 | 5 |
| B3_0 | 470.0 | 804.0 | 200000 | 0.045 | 8 |
| C3_0 | 470.0 | 819.0 | 200000 | 0.047 | 11 |

Three values of $l/d$ were considered, $l/d$ = 5, 8, 11, using bars with diameters $d$ = 16, 20 and 24 mm. The tests were carried out under displacement control and identified by the labels An, Bn and Cn, where A, B and C denote, respectively, (i) tests with $l/d$ = 5, (ii) tests with $l/d$ = 8, and (iii) tests with $l/d$ = 11. The index $n$ specifies the loading protocol, namely (i) $n$ = 1, 2 for random protocols, (ii) $n$ = 3 for a protocol symmetric with respect to ε = 0, and (iii) $n$ = 4, 5 for non-symmetric protocols. The mechanical properties here used to replicate Monti and Nuti's experimental tests are reported in **Table 29** with the considered ratio $E_h/E_s$.

### 6.2. Cyclic tests by Prota and Cosenza

Prota and Cosenza [82] carried out an extensive experimental programme on the cyclic behaviour of smooth steel bars used as reinforcement in existing RC structures. The study also addressed the comparison between the cyclic response of smooth bars and that of ribbed bars with improved bond. Although modern RC structures typically use only ribbed bars, many existing structures are still reinforced with smooth bars. Since these structures were often designed before the introduction of seismic provisions, they may experience instability, cover spalling and concentrated damage in dissipative regions during earthquakes, especially where transverse reinforcement is inadequately spaced.

The test programme included bars with diameters $d$ = 8, 12, 14 and 16 mm and different lengths, covering a $l/d$ range $5 \le l/d \le 100$. The tests were conducted under displacement control with a top-end strain rate corresponding to a displacement rate of 0.05 mm/s. The specimens were labelled *Sn*, $R1_n$ e $R2_n$, where the leading letter identifies the bar type and the index $n$ is the progressive test number. In particular, (i) *S* denotes smooth bars, (ii) *R1* denotes ribbed bars that satisfy the requirements of Italian and European codes [D.M. 14/01/2008; Eurocode 2/2004 – Part 1-1], which limit the overstrength to the range 1.15-1.35 and require the ratio between nominal and actual yield strength to be less than 1.25, and (iii) R2 denotes ribbed bars with mechanical properties outside the limits adopted for R1 bars. The average mechanical properties here used for each bar category with the considered ratio $E_h/E_s$ are given in **Table 30.**

**Table 30** – Material properties of specimens tested by Prota and Cosenza [82].

| Specimen | $f_y$ [MPa] | $f_u$ [MPa] | $E_s$ [MPa] | $E_h/E_s$ [-] | $l/d$ [-] |
|---|---|---|---|---|---|
| S01 | 340 | 440 | 200000 | 0.0130 | 5 |
| S02 | 340 | 440 | 200000 | 0.0120 | 10 |
| S03 | 340 | 440 | 200000 | 0.0020 | 15 |
| S04 | 340 | 440 | 200000 | 0.0020 | 20 |
| R11 | 540 | 640 | 200000 | 0.0004 | 5 |
| R12 | 540 | 640 | 200000 | 0.0040 | 10 |
| R13 | 540 | 640 | 200000 | 0.0400 | 15 |
| R14 | 540 | 640 | 200000 | 0.0390 | 20 |
| R21 | 534 | 850 | 200000 | 0.0290 | 5 |
| R22 | 534 | 850 | 200000 | 0.0420 | 10 |
| R23 | 534 | 850 | 200000 | 0.0001 | 15 |
| R24 | 534 | 850 | 200000 | 0.0001 | 20 |

### 6.3. Comparison between numerical and laboratory cyclic response

The cyclic response of the bars tested by Monti and Nuti and by Prota and Cosenza was determined in OpenSees using the modified Steel Rebar Material and the mechanical properties reported in **Tables 29 and 30**. The accuracy of the material model was assessed by comparing the experimentally obtained displacement-controlled cyclic responses with those reproduced numerically. The comparison of the hysteresis loops, shown for some of the considered bars in **Figs. 131** and **132**, confirms the good agreement between the predicted and experimental data, both for the primary cycles and for the secondary cycles.

To further demonstrate the accuracy of the modified SteelRebar Material model, including the cases not shown in **Figs. 131** and **132**, errors in predicting the cyclic response, as well as the coefficient of determination $R^2$ were computed (**Table 31 and 32**). In the same tables, the $R^2$ values obtained using the original SteelRebar material, as formulated by Panarelli et al. [78], are also reported.

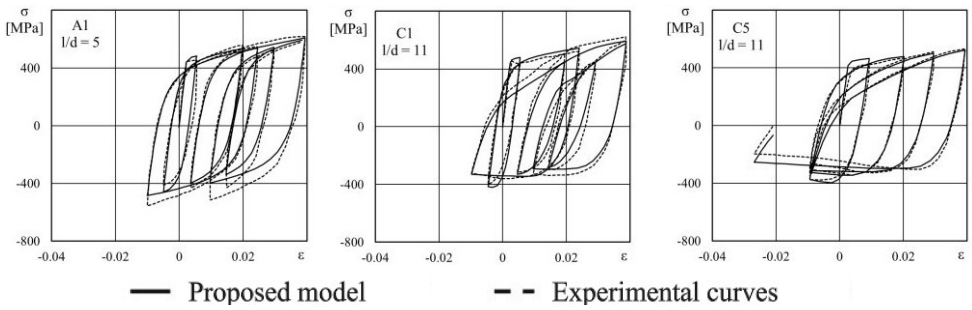


**Fig. 131** – Accuracy of the modified Steel Rebar model in predicting the results of the laboratory tests carried out by Monti and Nuti [81].

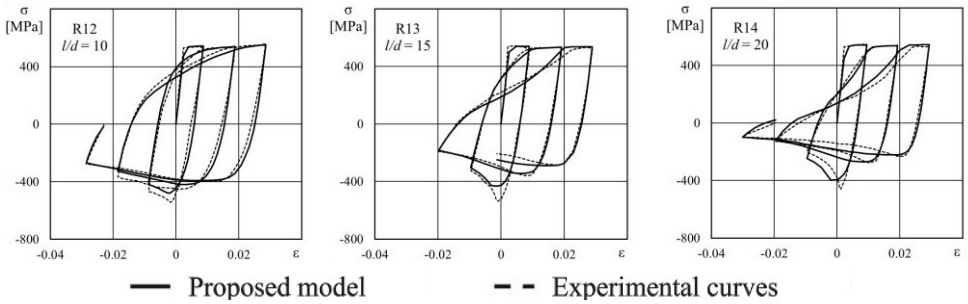


**Fig. 132** – Accuracy of the modified Steel Rebar model in predicting the results of the laboratory tests carried out by Prota et al [82].

To further demonstrate the accuracy of the modified SteelRebar Material model, including the cases not shown in **Figs. 131** and **132**, errors in predicting the cyclic response, as well as the coefficient of determination $R^2$ were computed (**Table 31 and 32**). In the same tables, the $R^2$ values obtained using the original SteelRebar material, as formulated by Panarelli et al. [78], are also reported.

The comparison between the $R^2$ values obtained using the original and the modified SteelRebar numerical models shows that the new formulation preserves the high accuracy of the original SteelRebar model in reproducing experimental responses for cases with fixed $l/d$, while, as discussed previously, it also eliminates the discontinuities observed when modelling bars with variable $l/d$.

**Table 31** – Coefficient of determination for Monti and Nuti [81] tests: comparison between original and modified SteelRebar models.

| Monti and Nuti specimens | $R^2$ original SteelRebar | $R^2$ modified SteelRebar |
|---|---|---|
| A1 | 0.96 | 0.97 |
| A2 | 0.98 | 0.98 |
| A3 | 0.97 | 0.97 |
| A4 | 0.94 | 0.94 |
| C1 | 0.96 | 0.97 |
| C2 | 0.97 | 0.97 |
| C3 | 0.96 | 0.95 |
| C4 | 0.98 | 0.98 |
| C5 | 0.98 | 0.98 |
| A3_0 | 0.98 | 0.98 |
| B3 | 0.96 | 0.96 |
| C3_0 | 0.89 | 0.90 |

**Table 32** – Coefficient of determination for Prota et al. [82] test: comparison between original and modified SteelRebar models.

| Prota et al. specimens | $R^2$ original SteelRebar | $R^2$ modified SteelRebar |
|---|---|---|
| S01 | 0.96 | 0.96 |
| S02 | 0.83 | 0.84 |
| S03 | 0.96 | 0.96 |
| S04 | 0.97 | 0.97 |
| R11 | 0.94 | 0.93 |
| R12 | 0.98 | 0.98 |
| R13 | 0.99 | 0.99 |
| R14 | 0.97 | 0.99 |
| R21 | 0.97 | 0.98 |
| R22 | 0.97 | 0.97 |
| R23 | 0.99 | 0.99 |
| R24 | 0.98 | 0.98 |

## 7. Use of the SteelRebar material model in HSS cross-sections

The formulation of the SteeRebar material model, in its original development, was calibrated against a refined numerical "reference rebar model" and subsequently validated on independent datasets; in the present work, the same constitutive structure is exploited, with specific attention to the definition of the compressive backbone and its implications when SteelRebar is used in fibre-based models to reproduce the different response of strips in HSS box sections. In particular, each fibre of the cross-section is assumed to behave independently of the adjacent fibres, with $l/d$ varied according to the fibre position within the cross-section. The purpose is to represent the initiation and development of local instabilities at different locations along the section, as this is particularly relevant for these members.

To this end, a four-steps procedure, detailed in the following subsections, is adopted.

First, for the fibres located at the mid-width of the flat part, at one quarter, at one eighth, or near the corners, an appropriate $l/d$ ratio is defined based on the comparison between the monotonic stress-strain response predicted by the modified SteelRebar material and the target response obtained from the stress-strain curves of the strips isolated in the ABAQUS models subjected to stub column tests.

Second, quadratic trend lines are defined to assign a $l/d$ ratio also to those fibres for which the target stress-strain curves of the strips were not extracted from the ABAQUS models.

Third, stub column tests under the cyclic loading protocols described in Section 1 are carried using the proposed fibre-based modelling in OpenSees. In this stage of the procedure, a variable $l/d$ radio is employed within the loading protocol. The comparison with the results of cyclic stab column tests performed in ABAQUS is used to select the value of the parameter controlling the rate of variation of the $l/d$ radio with the minimum compression strain, in order to achieve to the best estimate of the cyclic response.

Fourth, analytical equations are formulated to assign the $l/d$ ratio as a function of the cross-section's geometric properties and the position of the fibre within the section.

### 7.1. Selection of appropriate *l/d* ratio for fibres located in a specific position

The definition of the appropriate $l/d$ ratio for fibres located in a specific position, required in the first step of the procedure, is carried out through linear interpolation. The procedure is applied to all the fibres in the flat parts and corner parts for which the target stress-strain responses of the strips isolated in the ABAQUS are available.

Specifically, the stress–strain curves computed by the modified SteelRebar model for different $l/d$, ranging from $l/d$ = 1 to 30, are plotted together with the target stress-strain response. The procedure involves selecting target strain levels between 1% and 5% and, for each level, identifying within the set of curves corresponding to different l/d ratios the two curves whose stresses lie immediately above and below the stress of the strip under consideration. Interpolation between these two curves yields the $l/d$ that best represents the fibre in question.

**Fig. 133** illustrates the assignment procedure by comparing the fibres modelled in OpenSees with the corresponding flat parts modelled in Abaqus. As an example, the $l/d$ obtained for the mid-width strip of the horizontal and vertical flat parts (L2O and L2V) of the 300×300×10 section, at a strain level of 3%, is equal to 17.83 for the horizontal flat part and 16.96 for the vertical flat part.

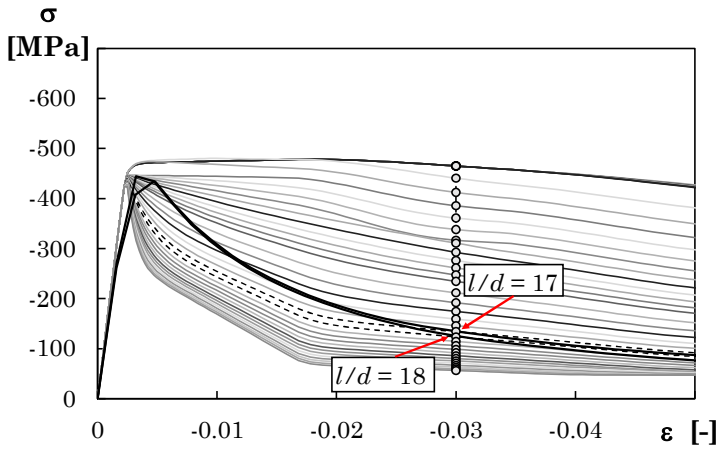


**Fig. 133** – Example of $l/d$ evaluation for the mid-width strips of the 300×300×10 section.

### 7.2. Variability of the *l/d* ratio within the cross-section

The approach described in the previous subsection is applied to all fibres in the flat parts and corner parts, resulting in a position-dependent variation of $l/d$ along the cross-section. The outcomes show that $l/d$ varies along the cross-section rather than remaining constant. In general, fibres located in the central region of the flat parts exhibit larger $l/d$ values, being farther from restraint and therefore more prone to local instability. Conversely, fibres in the corner parts are associated with smaller $l/d$ values, consistent with the limited contribution of these regions to instability. For this reason, a constant $l/d$ is adopted for the corner parts, computed as a weighted average of the responses of the strips composing the corners.

The information obtained from this procedure is then incorporated into the fibre model to improve the section discretisation by explicitly including the variation of the $l/d$ ratio. For the flat parts, the position-dependent $l/d$ is described through a quadratic law calibrated to replicate the values obtained for the fibres located at the mid-width of the flat part, at one quarter, at one eighth, and near the corners, whereas a single constant value is used for the corner parts. **Fig. 134** reports the trend lines obtained for the analysed sections. In these plots, (i) the ordinate is the $l/d$ ratio value of the horizontal and vertical flat parts obtained by linear interpolation at different fibre locations, and (ii) the abscissa is the fibre position normalised with respect to the net length of the flat part (0 identifies fibres close to the corner parts, and 0.5 identifies fibres at mid-width). These curves indicate that the trend evolves from nearly linear to markedly nonlinear as the slenderness ($b_f/t$) of the flat parts increases.

In all cases, the $l/d$ ratio variation law to be assigned to the fibres is expressed as a second-degree polynomial function. The coefficients of this function capture the evolution of $l/d$ along the flat parts, while the constant term represents the $l/d$ value assigned to the corner parts. The $l/d$ values resulting from the calibrated functions are then assigned to the fibres of the cross-section modelled in OpenSees.

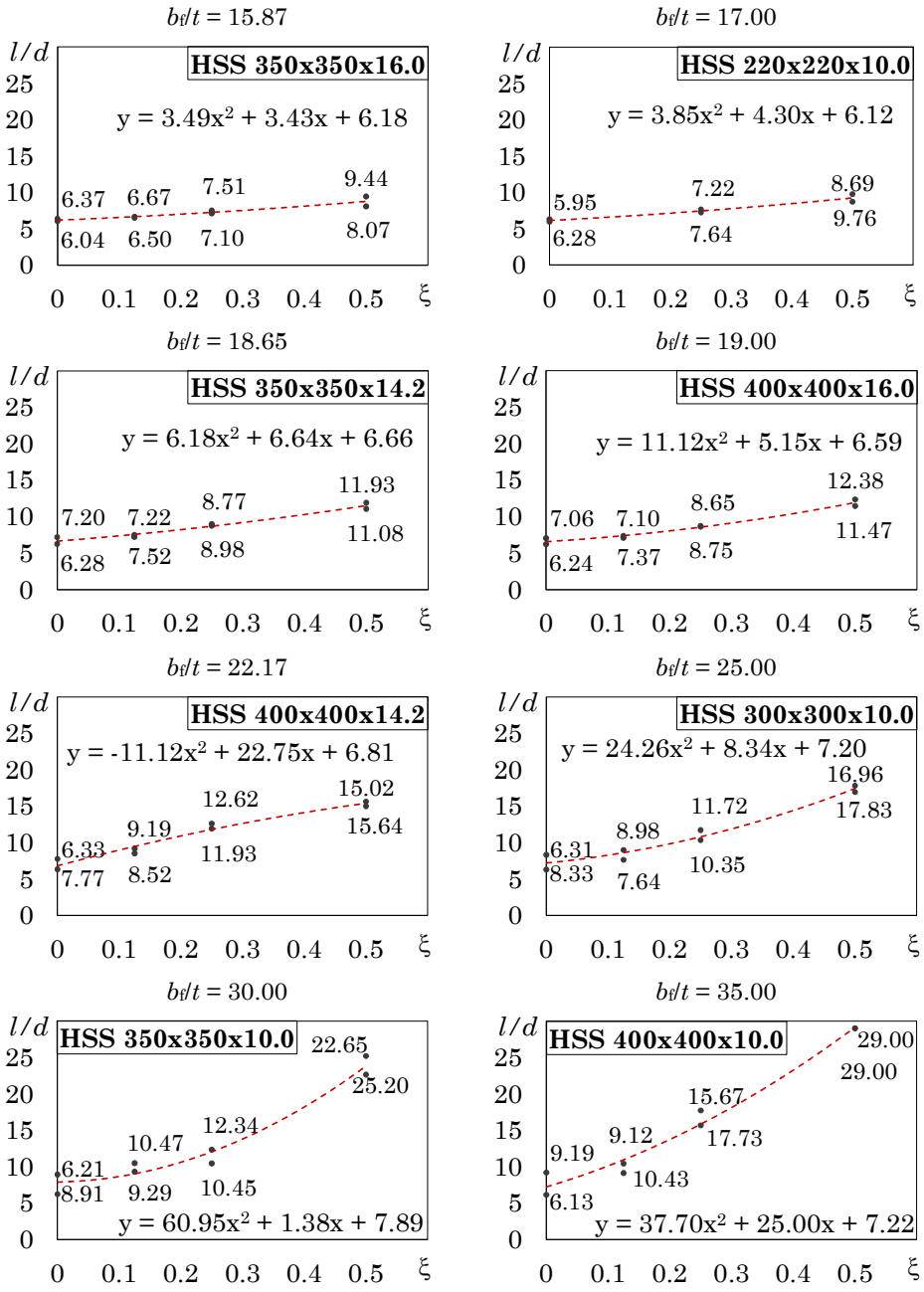


**Fig. 134** – Trend lines as a function of cross-section slenderness.

### 7.3. Dynamic variation of the *l/d* ratio

To investigate the behaviour of HSS members affected by local instability, the quadratic laws previously derived were implemented in the OpenSees fibre model and the results were compared with the response of the FEM model. This comparison was first carried out by adopting both the static and the dynamic versions of the SteelRebar material. In this preliminary phase, the dynamic formulation was used with $\psi = 1$, as prescribed in the original SteelRebar definition, with the objective of identifying which approach provides a closer approximation of the cyclic response obtained from the finite element simulations.

In addition, to evaluate the influence of the loading history on stub column behaviour, each profile was analysed under four cyclic loading protocols, consistent with those used in the Abaqus models. The outcome of this preliminary comparison, discussed in the following section, shows that the accuracy of the static and dynamic approaches in predicting the cyclic response depends on both the section slenderness and the applied loading protocol.

To propose a single modelling strategy for cyclic response prediction, the cyclic behaviour of the sections was then evaluated by adopting a variable $l/d$ and by assigning to the exponent $\psi$ in Eq. (89) values ranging from 0.10 to 1. A visual comparison between the cyclic responses obtained in Abaqus and those computed in OpenSees for different $\psi$ values indicated that the agreement improves as $\psi$ decreases.

Beyond qualitative observations, a mean error index was introduced to quantify the differences, to verify whether the accuracy depends on the section slenderness, and to identify, as a function of slenderness, the $\psi$ value that minimises the discrepancy. For each cycle, the point characterised by the maximum shortening strain was identified for both the Abaqus response and the OpenSees fibre response. The error at those points, expressed as a percentage, was computed as

$$Err_{\%} = \frac{F_{Op} - F_{Ab}}{F_{Ab}} \tag{90}$$

where $F_{Op}$ and $F_{Ab}$ are the forces obtained from the fibre model and from the FEM model, respectively.

The mean error was then evaluated as

$$Err_{medio} = \frac{Err_{\%}}{n^{\circ}_{err}} \tag{91}$$

where $n^{\circ}_{\mathrm{err}}$is the number of load reversals considered in the analysis.

Based on the mean error estimation, the exponent providing the smallest error was found to be $\psi = 0.10$, which therefore represents the most effective value for reproducing the cyclic response of the FEM model. For this reason, the subsequent comparisons between the cyclic responses of the fibre model and those of the finite element model refer to $\psi = 0.10$.

### 7.4. Accuracy of the OpenSees model in simulating stub column tests

The comparison between the results obtained with the fibre model and those derived from finite element modelling plays a key role in validating the simplified approach, as it allows the accuracy and predictive capability under cyclic loading to be assessed. The following figures present the investigate the behaviour of HSS members affected by local instability, the quadratic laws previously derived were implemented in the OpenSees fibre model and the results were compared with the response of the FEM model. This comparison was first carried out by adopting both the static and the dynamic versions of the SteelRebar material, with the objective of identifying which approach provides a closer approximation of the cyclic response obtained from the finite element simulations. In this preliminary phase, the dynamic formulation was used with $\psi = 1$, $\varepsilon_I = 3.6‰$, $\varepsilon_f = 25‰$ and $l/d_i = 1$.

In addition, to evaluate the influence of the loading history on stub column behaviour, each profile was analysed under four cyclic loading protocols, consistent with those used in the Abaqus models. The outcome of this preliminary comparison, discussed in the following section, shows that the accuracy of the static and dynamic approaches in predicting the cyclic response depends on both the section slenderness and the applied loading protocol.

The following figures present the comparison for three representative sections: a stocky section (350×350×16), a slender section (400×400×10), and an intermediate-slenderness section (350×350×14.2).

Each section is analysed under cyclic conditions using the four loading protocols.

For each case, the following comparisons are provided: (i) FEM results versus fibre-model results obtained with the original SteelRebar formulation, considering both static and dynamic configurations, prior to the modifications introduced to overcome the discontinuities observed in bars modelled with SteelRebar (**Figs. 135**, **136** and **137**); (ii) FEM results versus the numerical bar model obtained by introducing the equations proposed in the section 4, again considering both static and dynamic configurations with $\psi = 1$ (**Figs. 138**, **139** and **140**).

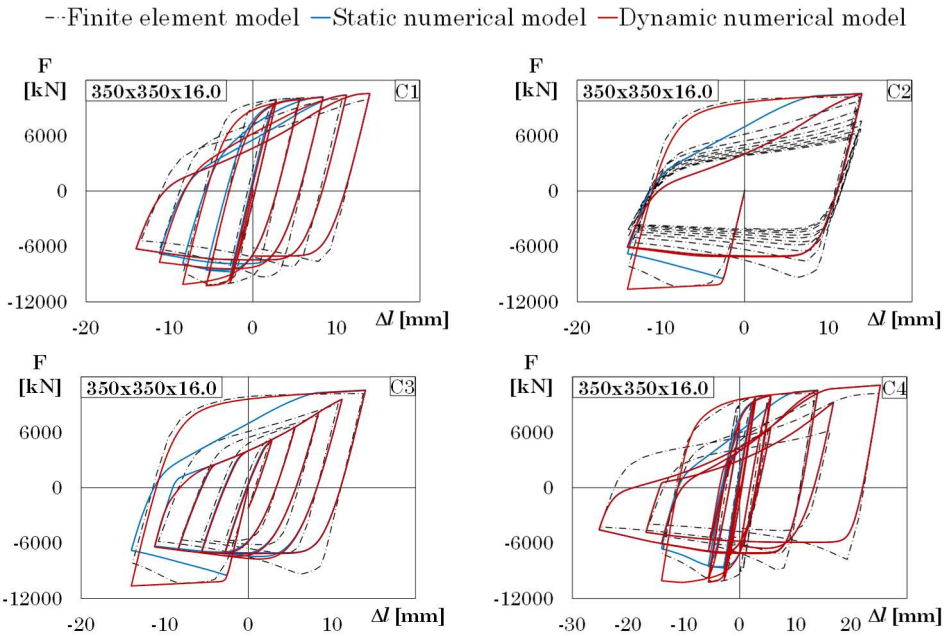


**Fig. 135** – Comparison between the cyclic responses of the FEM model and the fibre-based model for the 350×350×16 section: original SteelRebar model.

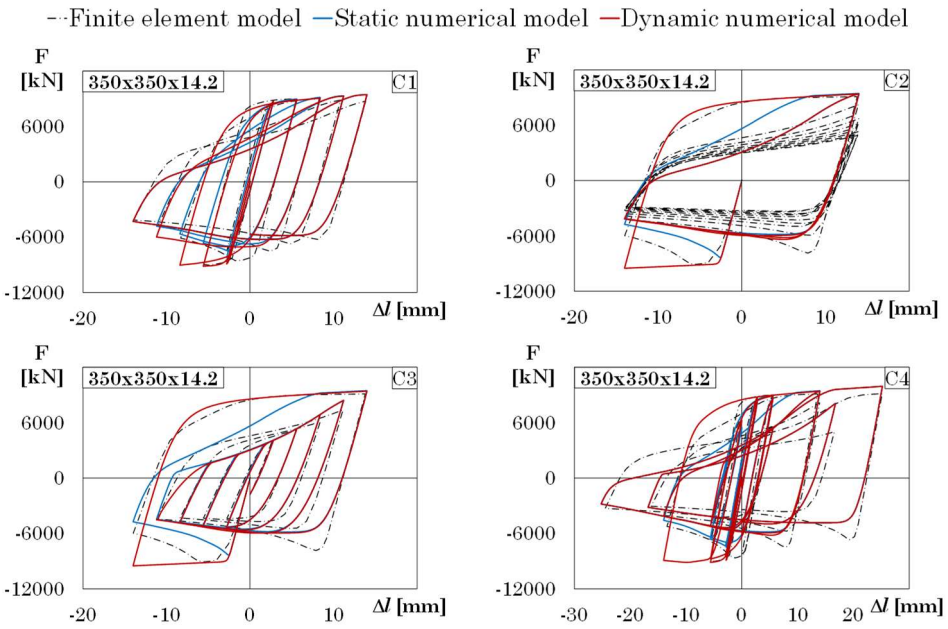


**Fig. 136** – Comparison between the cyclic responses of the FEM model and the fibre-based model for the 350×350×14.2 section: original SteelRebar model.

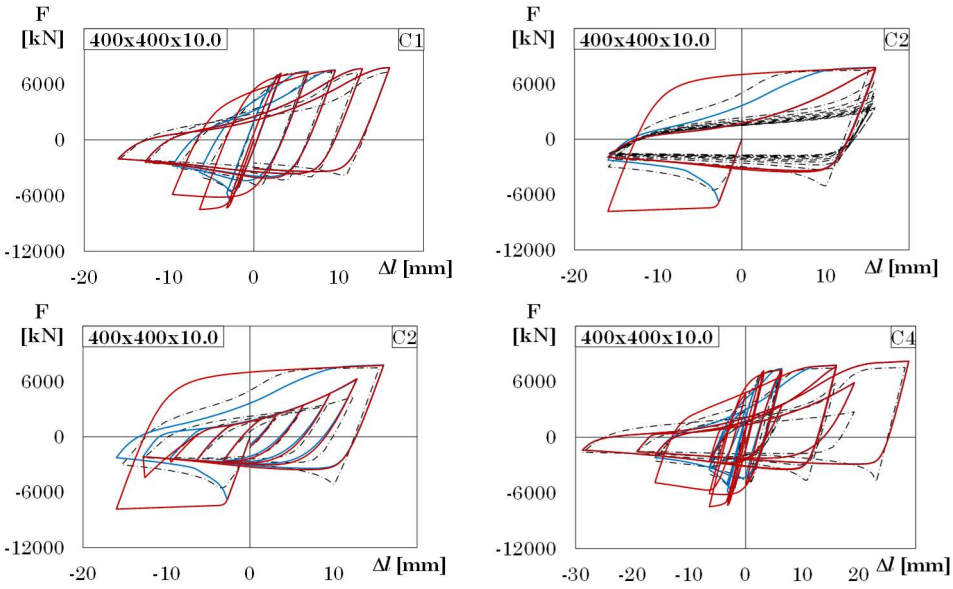


**Fig. 137** – Comparison between the cyclic responses of the FEM model and the fibre-based model for the 400×400×10.0 section: original SteelRebar model.

The plots refer to $l/d$ values calibrated to reproduce the stress obtained in Abaqus at a strain level equal to 3%. The response is presented in terms of force–displacement curves. FEM results are reported with dashed lines, whereas fibre-model results are shown with continuous lines for the static model and with dashed-dotted lines for the dynamic model.

The fibre model is able to reproduce the cyclic response with good accuracy, showing satisfactory agreement with the FEM simulations.

For the slender section, the static model reproduces the evolution of the FEM response with good accuracy. Conversely, the dynamic model with $\psi = 1$, particularly in the initial cycles, deviates from the finite element response. This discrepancy is reduced in the modified numerical model after introducing the proposed equations, confirming the effectiveness of the proposed formulation.

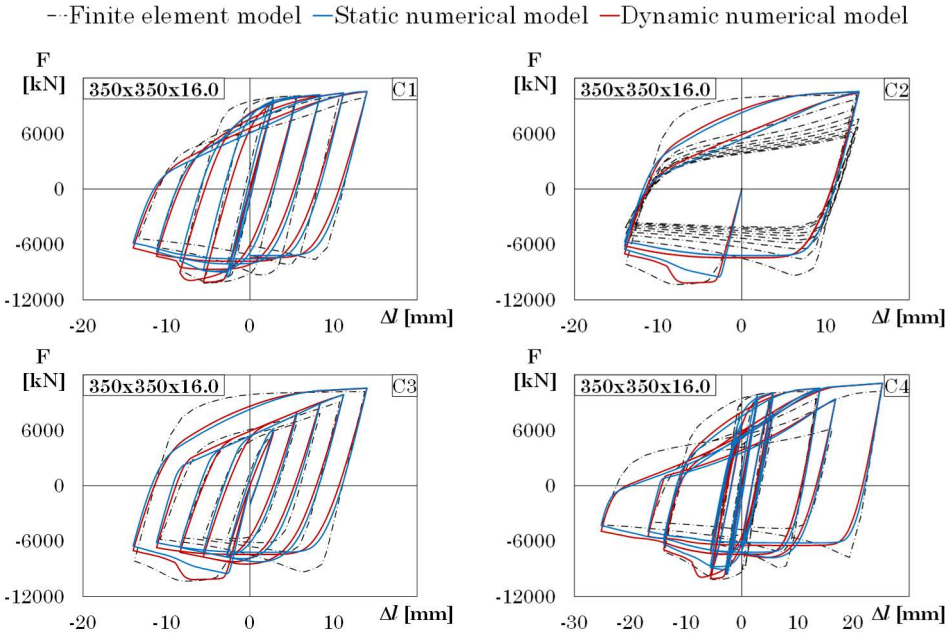


**Fig. 138** – Comparison between the cyclic responses of the FEM model and the fibre-based model for the 350×350×16 section: modified SteelRebar model.

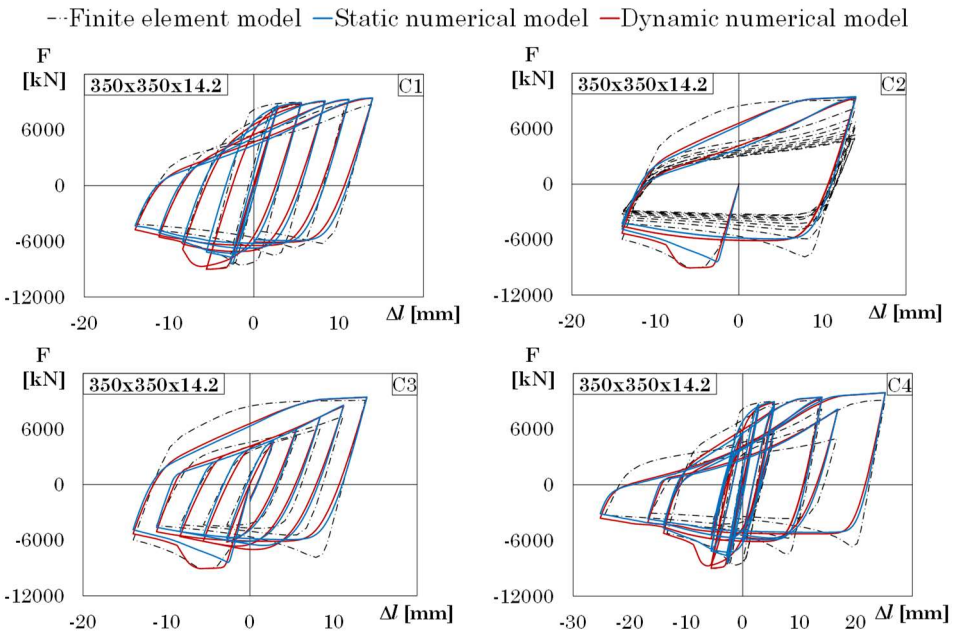


**Fig. 139** – Comparison between the cyclic responses of the FEM model and the fibre-based model for the 350×350×14.2 section: modified SteelRebar model.

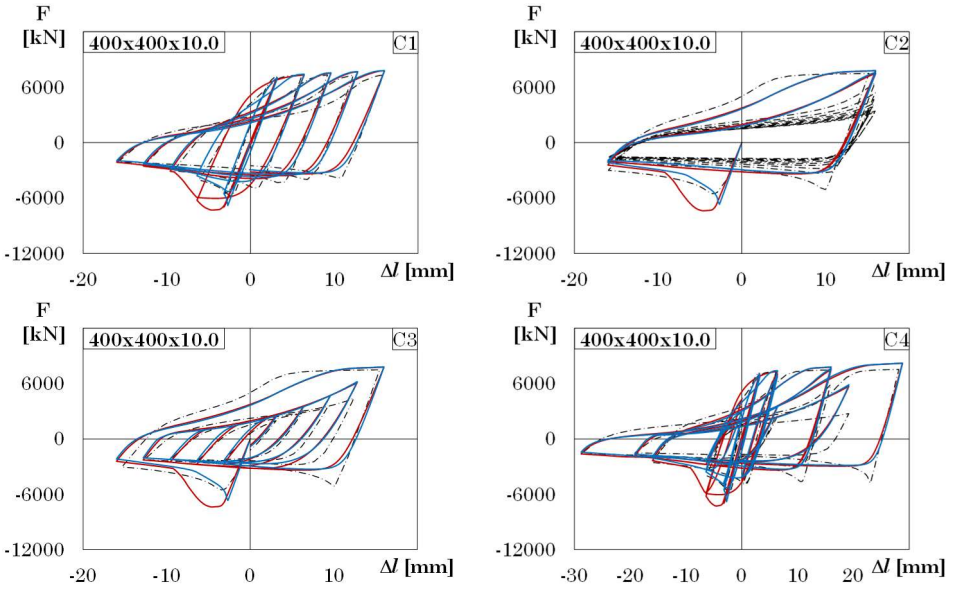


**Fig. 140** – Comparison between the cyclic responses of the FEM model and the fibre-based model for the 400×400×10.0 section: modified SteelRebar model.

For the intermediate-slenderness section, the accuracy differs from cycle to cycle. In the initial cycles the dynamic model provides a better approximation, whereas at larger cycles the static model appears more consistent with the Abaqus response. The accuracy generally improves when the modified SteelRebar model is used.

For the stocky section, the dynamic model provides a more accurate estimate than the static model. However, the difference between the two approaches becomes negligible as the section becomes less slender, since instability effects no longer significantly influence the response.

In the dynamic model with $\psi = 1$, a curved trend can be observed in the initial cycles. This behaviour is attributed to the rate of transition from one $l/d$ value to the next, which is gradual as $\psi$ approaches unity.

To propose a single modelling strategy for cyclic response prediction, the cyclic behaviour of the sections was then evaluated by adopting a variable slenderness ratio $l/d$ and by assigning to the exponent $\psi$ in Eq. (89) values ranging from 0.10 to 1. A visual comparison between the cyclic responses obtained in Abaqus and those computed in OpenSees for different $\psi$ values indicated that the agreement improves as $\psi$ decreases.

Beyond qualitative observations, a mean error index was introduced to quantify the differences, to assess whether the accuracy depends on the section slenderness, and to identify, the $\psi$ value that minimises the discrepancy between the cyclic response obtained from numerical models built in ABAQUS and OpenSees. For each cycle, the point characterised by the maximum shortening strain was identified for both the Abaqus response and the OpenSees fibre response. The error at those points, expressed as a percentage, was computed as

$$Err_{\%} = \frac{F_{Op} - F_{Ab}}{F_{Ab}} \tag{92}$$

where $F_{Op}$ and $F_{Ab}$ are the forces obtained from the fibre model and from the FEM model, respectively.

The average error was then evaluated as

$$Err_{av} = \frac{Err_{\%}}{n^{\circ}_{err}} \tag{93}$$

where $n^{\circ}_{\mathrm{err}}$is the number of load reversals considered in the analysis.

Based on the average error estimation, the exponent providing the smallest error was found to be $\psi = 0.10$, which therefore represents the most effective value for reproducing the cyclic response of the FEM model. For this reason, the subsequent comparisons between the cyclic responses of the fibre model and those of the finite element model refer to $\psi = 0.10$.

**Figs. 141**, **142** and **143** show the comparison between the cyclic responses obtained with the proposed fibre model using $\psi = 0.10$ and those derived from finite element modelling, for the same cross-sections investigated in the previous figures. The figures show that adopting an exponent $\psi = 0.10$ in the dynamic model further reduces the differences between the cyclic response obtained by FE and fibre models. Furthermore, the lower value of $\psi$ results in a more abrupt transition between different $l/d$ values, thus eliminating the curved trend observed in the initial cycles predicted by the dynamic model with $\psi = 1$.

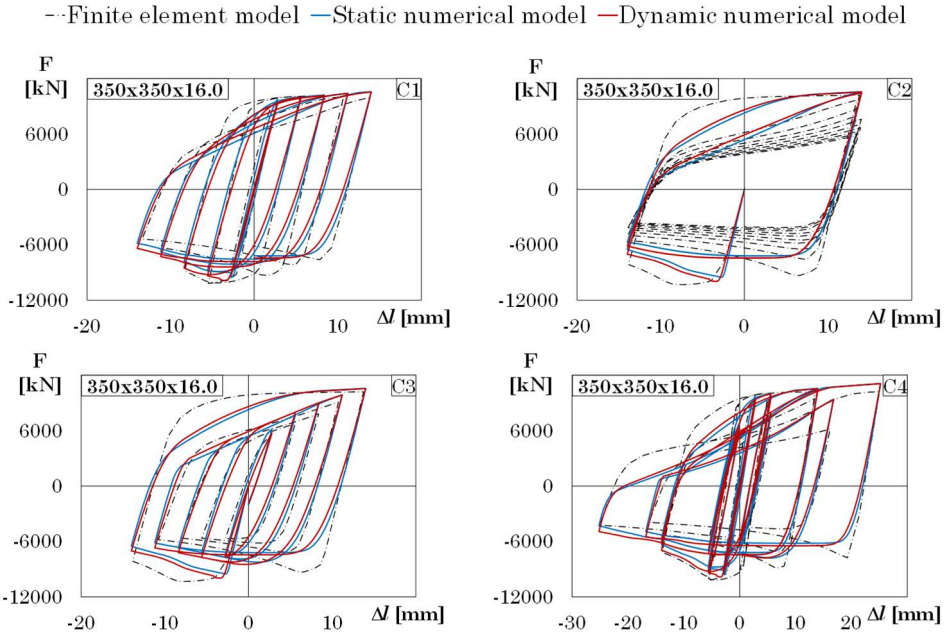


**Fig. 141** – Comparison between the cyclic responses of the FEM model and the fibre-based model for the 350×350×16 section: modified SteelRebar, $\psi = 0.10$.

Independently of the slenderness of the flat parts forming the cross-section, additional trends can be observed with respect to the loading protocol: (i) for protocols with increasing deformation amplitude (protocol C1), the fibre model accurately follows the response evolution and captures the instability phenomenon; (ii) for protocols characterised by cycles at constant deformation amplitude (protocol C2), the fibre model is not suitable for reproducing the relaxation effects observed in the finite element simulations; (iii) for protocols with a first cycle at high deformation followed by cycles at lower deformation (protocol C3), the transition curve from compression to tension exhibits a tensile response lower than that obtained in Abaqus; and (iv) for asymmetric loading protocols (protocol C4), the fibre model effectively reproduces the cycle asymmetry, although, as the number of cycles increases, a reduction of the peak stress amplitude is observed and attributed to local instability.

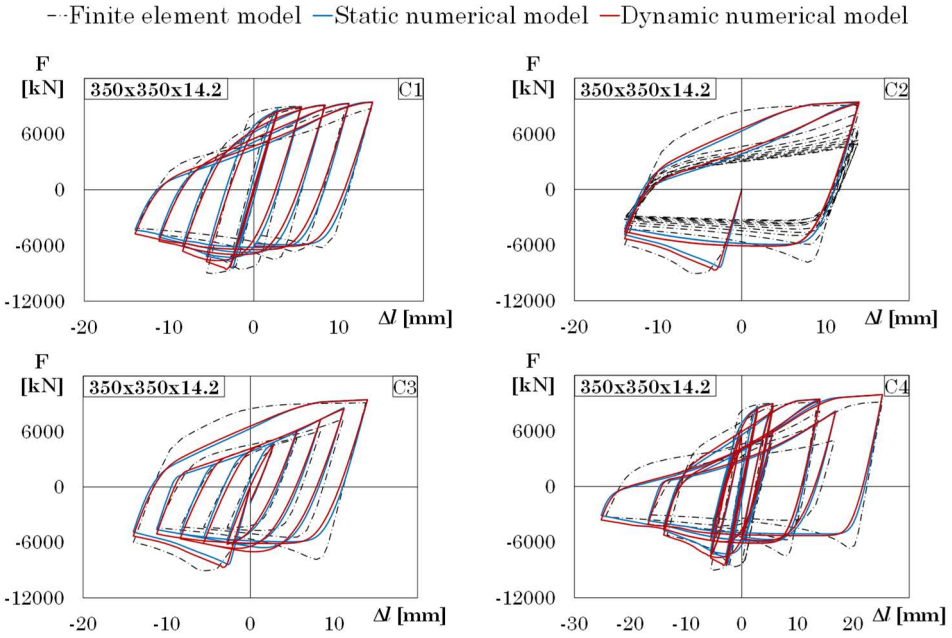


**Fig. 142** – Comparison between the cyclic responses of the FEM model and the fibre-based model for the 350×350×14.2 section: modified SteelRebar, $\psi = 0.10$.

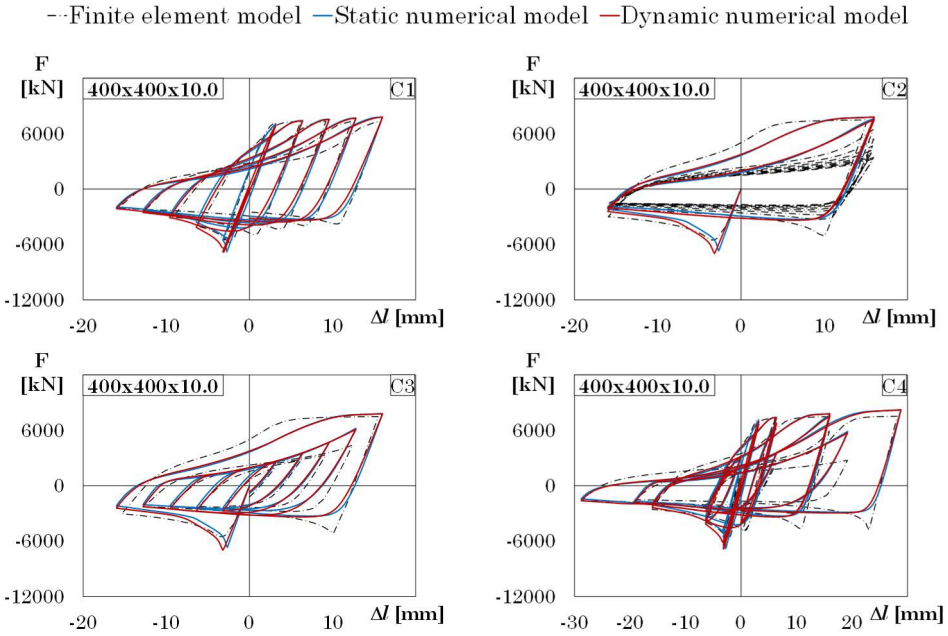


**Fig. 143** – Comparison between the cyclic responses of the FEM model and the fibre-based model for the 400×400×10.0 section: modified SteelRebar, ψ = 0.10.

### 7.5. Proposal of an equation to evaluate the variability of *l/d* along the cross-section

To make the proposed fibre-based approach generally applicable to any HSS cross-section, it was necessary to introduce a practical rule to assign the slenderness ratio $l/d$ to the fibres in the flat portions.

In the calibration phase, the $l/d$ distribution at a given location along the plate was obtained by building a dedicated Abaqus FE model and extracting the stress–strain response of a set of longitudinal strips, which is clearly not feasible for routine applications or for sections outside the investigated set. For this reason, a predictive equation was developed to provide the value of $l/d$ to be assigned to each flat-plate fibre directly as a function of $D_n/t$, where $D_n$ is the clear flat width (side length excluding corner parts) and $t$ is the thickness.

The proposed equation is as follows

$$\left(\frac{l}{d}\right)_{fin,i} = a\left(\frac{x_i}{D_n}\right)^2 + b\frac{x_i}{D_n} + c \qquad \text{for } 0 \le \frac{x_i}{D_n} \le 0.5 \tag{94}$$

where $(l/d)_{\text{fin,i}}$ is the l/d ratio of the fibre located at a distance $x_i$ from the end of the corner part achieved at the final threshold of the normalized minimum strain reached in compression, $\varepsilon_{\text{lim,fin}}$. In the proposed equation, $\frac{x_i}{D_n} = 0$ at the flat-corner junction and $\frac{x_i}{D_n} = 0.5$ at the plate mid-width.

Due to cross-section symmetry, the $l/d$ distribution is assumed to be symmetric as well. The coefficients $a$, $b$ and $c$ are defined as functions of $D_n/t$ and are as follow

$$a = 0.0674\left(\frac{D_n}{t}\right)^2 - 1.25\frac{D_n}{t} + 1.09 \tag{95}$$

$$b = 0.0055\left(\frac{D_n}{t}\right)^2 + 0.467\frac{D_n}{t} - 6.71 \tag{96}$$

$$c = -0.0057\left(\frac{D_n}{t}\right)^2 + 0.402\frac{D_n}{t} + 0.437 \tag{97}$$

**Fig. 144** compares the $l/d$ values predicted by equations (95)-(97), i.e. $(l/d)_{\text{p}}$ with those derived from the Abaqus strips $(l/d)_{\text{t}}$ for the nine stub-column sections and for four different positions of the fibres: $x_i/D_n$=0, 1/8, 0.25 and 0. The figure shows an excellent agreement between target and predicted $l/d$.

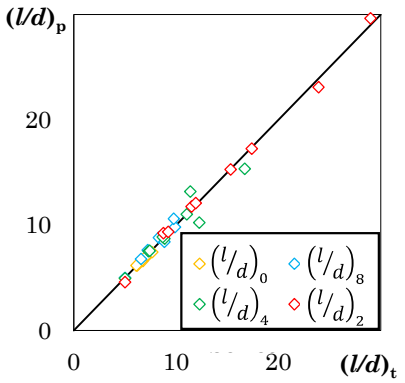


**Fig. 144** – Comparison between target and predicted values of $l/d$ along the flat plate of the cross-section

**Fig. 145** shows the response of 400x400x14.2 that reports the major variation in l/d among all the specimen because of the equation. The figure shows how the curves are nearly superimposed, demonstrating the accuracy of the equation.

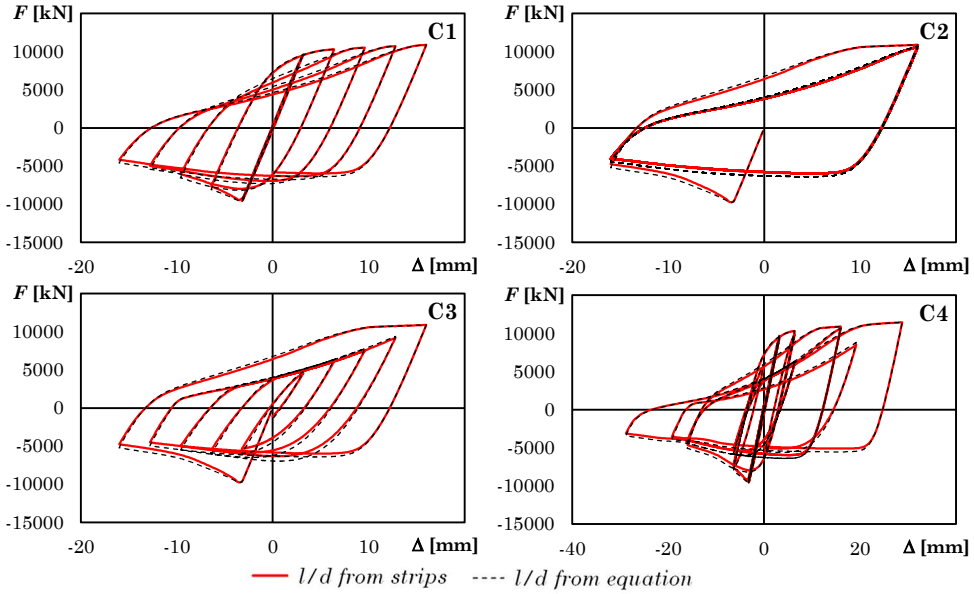


**Fig. 145** – Comparison of cyclic responses for the 400×400×14.2 section using l/d values derived from FEM extracted strips and from the calibrated equation.

## 8. Accuracy of the OpenSees model in simulating uniaxial bending tests

To assess the ability of the proposed simplified fibre-based modelling strategy to reproduce the cyclic response of cold-formed HSS members under bending tests, two configurations of simulations were performed: (i) cantilever members under uniaxial bending tests and (ii) biaxial bending.

For the comparison, selected cases from the parametric finite element analyses presented in Chapter 3 were used for the comparison and

are reported in **Table 33**. All the specimens considered have been tested with an axial load ratio from $0.0N_{pl}$ to $0.5\ N_{pl}$.

**Table 33** – Geometric properties of the investigated sections.

| Specimen | $b_f$ [mm] | t [mm] | $r_e$ [mm] | $b_f/t$ [-] | Lv [mm] | | |
|---|---|---|---|---|---|---|---|
| 350x350x16.0 | 253.98 | 16.0 | 48.01 | 15.87 | 1500 | 2250 | 3000 |
| 350x350x14.2 | 264.80 | 14.2 | 42.60 | 18.65 | 1500 | 2250 | 3000 |
| 400x400x16.0 | 303.98 | 16.0 | 48.01 | 19.00 | 1500 | 2250 | 3000 |
| 400x400x14.2 | 314.80 | 14.2 | 42.60 | 22.17 | 1500 | 2250 | 3000 |
| 300x300x10.0 | 250.04 | 10.0 | 24.98 | 25.00 | 1500 | 2250 | 3000 |

### 8.1. Simulation of tests under axial load and uniaxial bending

The proposed fibre-based model used for the stub-column tests was adapted to simulate the flexural response.

Cantilever members were represented by a single force-based beam-column element with finite-length plastic hinges equal to 0.8 times the section depth. The midpoint numerical integration scheme was employed as discussed in Scott and Fenves [83]. The fiber-discretised section, defined consistently with the stub column simulations, was assigned to the first integration point, whereas elastic sections were assigned to the remaining integration points. The $l/d$ assigned to the fibres are assigned based on equation (94).

In the figures that follow, the Abaqus responses are reported with continuous black lines, whereas the OpenSees responses are shown with continuous red lines. The results are reported in terms of bending moment versus chord rotation. For consistency, the cyclic curves are cut at the step where the Abaqus finite element model reaches $\theta_{50\%}$, i.e., the chord rotation corresponding to a residual moment equal to 50% of the maximum bending moment.

**Figs. 146-148** show the cyclic responses for the stockiest section (350×350×16) for all the shear length and with four different values of the axial load ratio. **Figs. 149-151** and **Figs. 152-154** show the same comparison respectively for an intermediate-slenderness section

(400×400×16.0), and the slenderest section (300×300×10). Since the aim of the comparison is to assess the accuracy of the OpenSees model in reproducing the FEM response, rather than to compare the cyclic responses of different cross-sections, the figures are presented using different x-axis scales, in order to improve the readability of the cases characterised by higher axial load levels.

The SHS 300×300×10 specimen with a shear length of 3.00 m showed in **Fig. 154** was analysed only up to an axial load ratio of 0.4, since its pronounced slenderness and brittle response led to numerical instabilities at higher axial load levels.

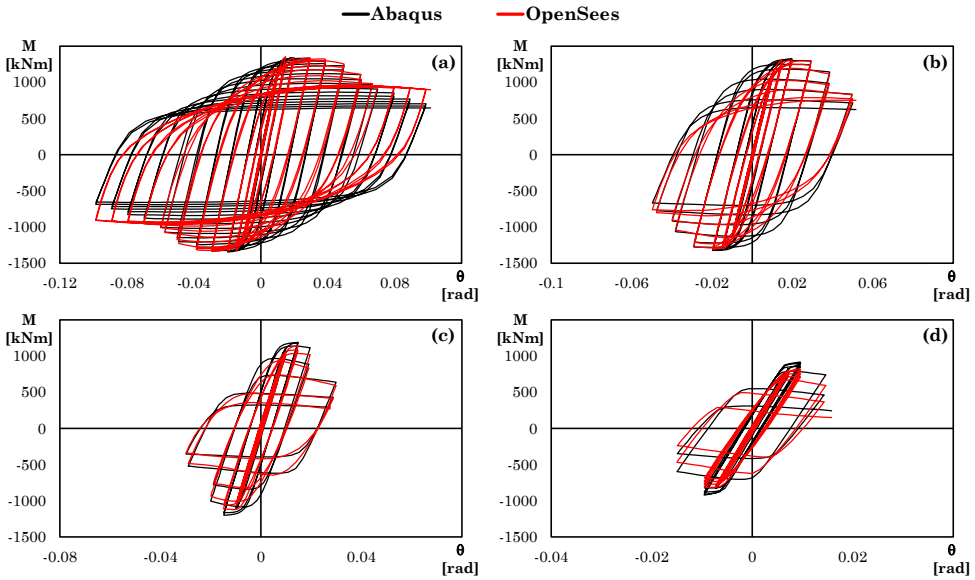


**Fig. 146** – Comparison between the cyclic responses of the FEM and the OpenSees model for the 350×350×16.0 section ($L_v$ = 1.50 m) and axial load ratio equal to: (a) 0.0; (b) 0.1; (c) 0.3; (d) 0.5.

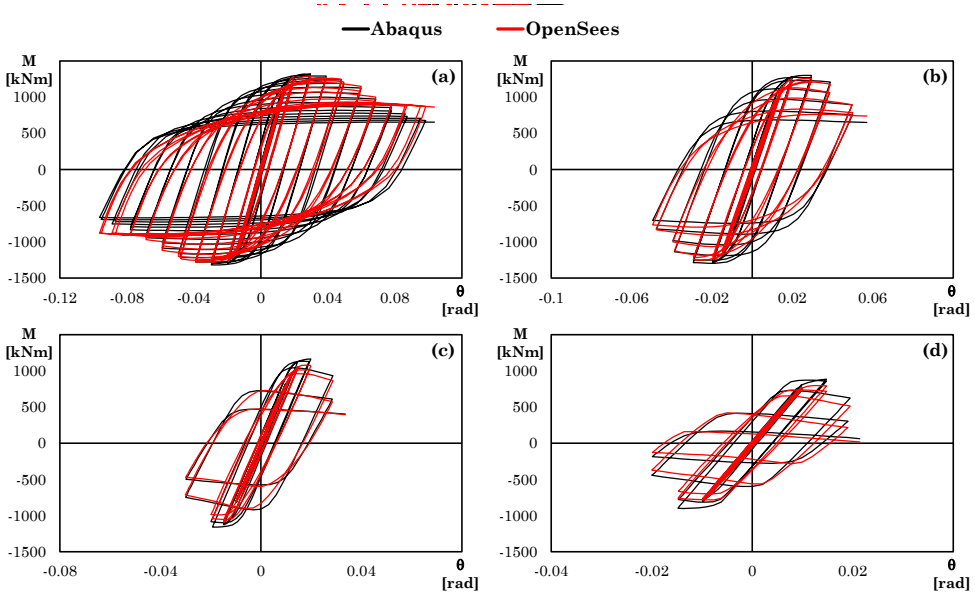


**Fig. 147** – Comparison between the cyclic responses of the FEM and the OpenSees model for the 350×350×16.0 section ($L_v$ = 2.25 m) and axial load ratio equal to: (a) 0.0ν; (b) 0.1ν; (c) 0.3ν; (d) 0.5ν.

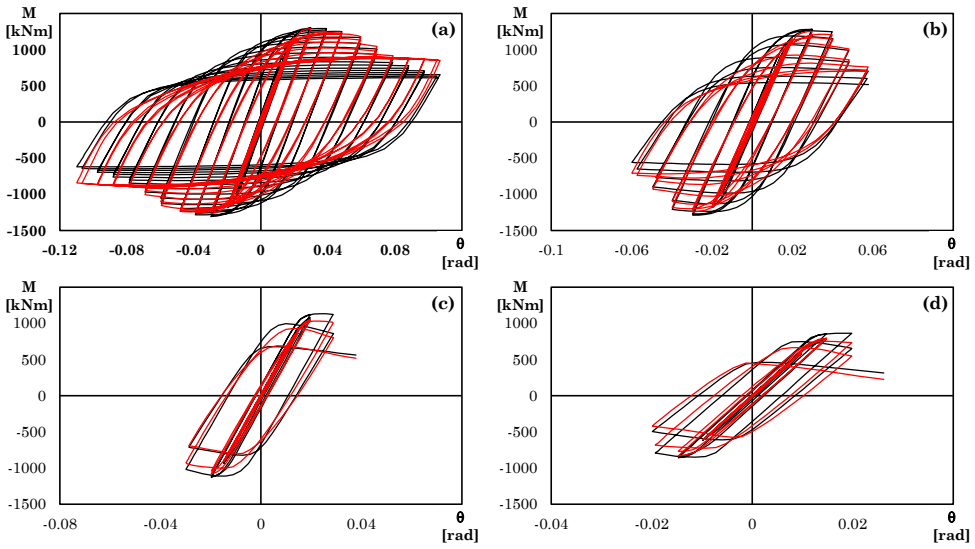


**Fig. 148** – Comparison between the cyclic responses of the FEM and the OpenSees model for the 350×350×16.0 section ($L_v$ = 3.00 m) and axial load ratio equal to: (a) 0.0; (b) 0.1; (c) 0.3; (d) 0.5.

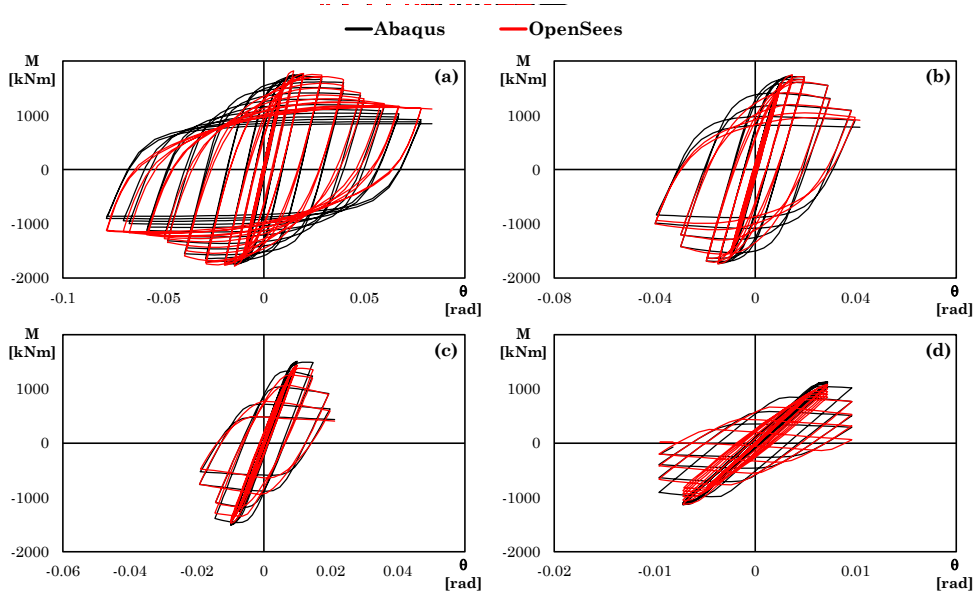


**Fig. 149** – Comparison between the cyclic responses of the FEM and the OpenSees model for the 400×400×16.0 section ($L_v$ = 1.50 m) and axial load ratio equal to: (a) 0.0; (b) 0.1; (c) 0.3; (d) 0.5.

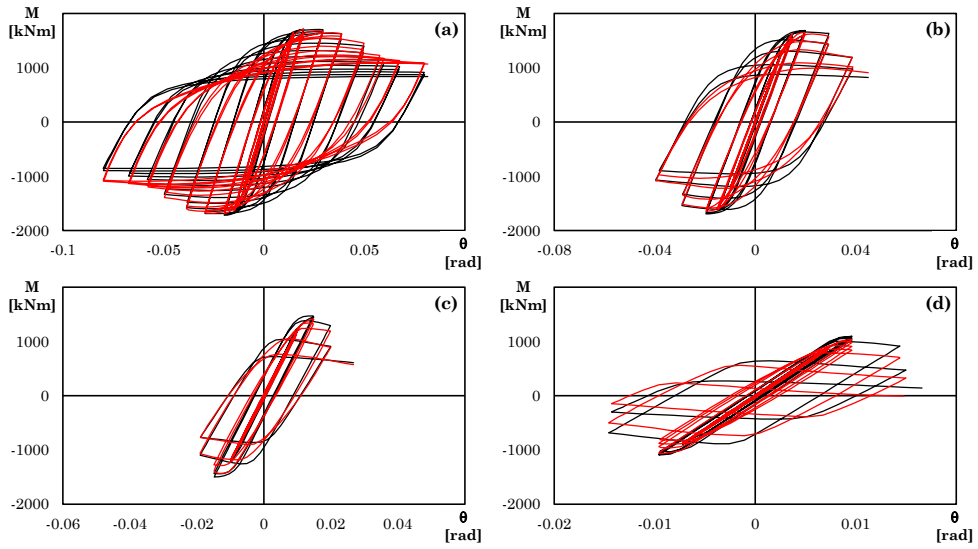


**Fig. 150** – Comparison between the cyclic responses of the FEM and the OpenSees model for the 400×400×16.0 section ($L_v$ = 2.25 m) and axial load ratio equal to: (a) 0.0; (b) 0.1; (c) 0.3; (d) 0.5.

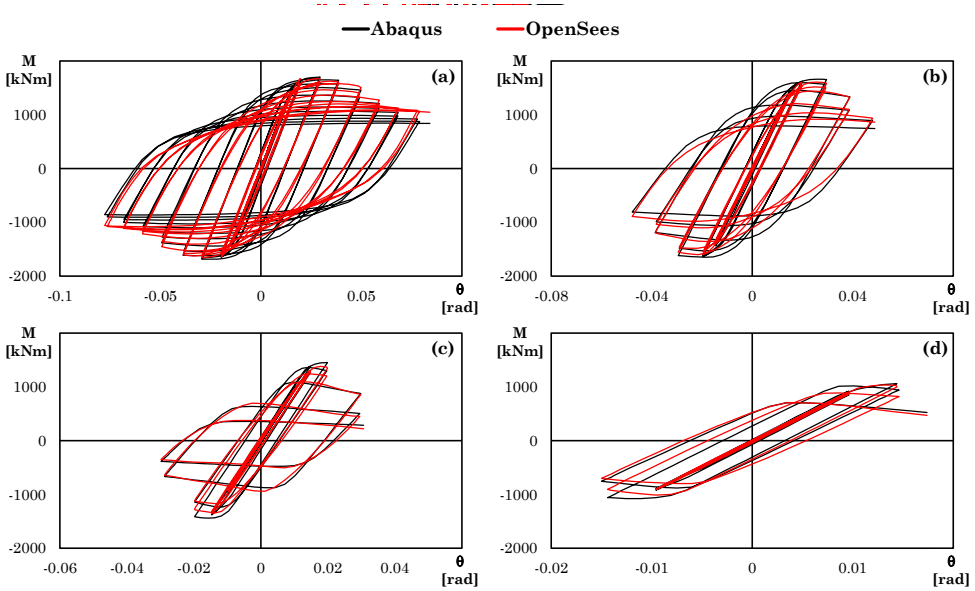


**Fig. 151** – Comparison between the cyclic responses of the FEM and the OpenSees model for the 400×400×16.0 section ($L_v$ = 3.00 m) and axial load ratio equal to: (a) 0.0; (b) 0.1; (c) 0.3; (d) 0.5.

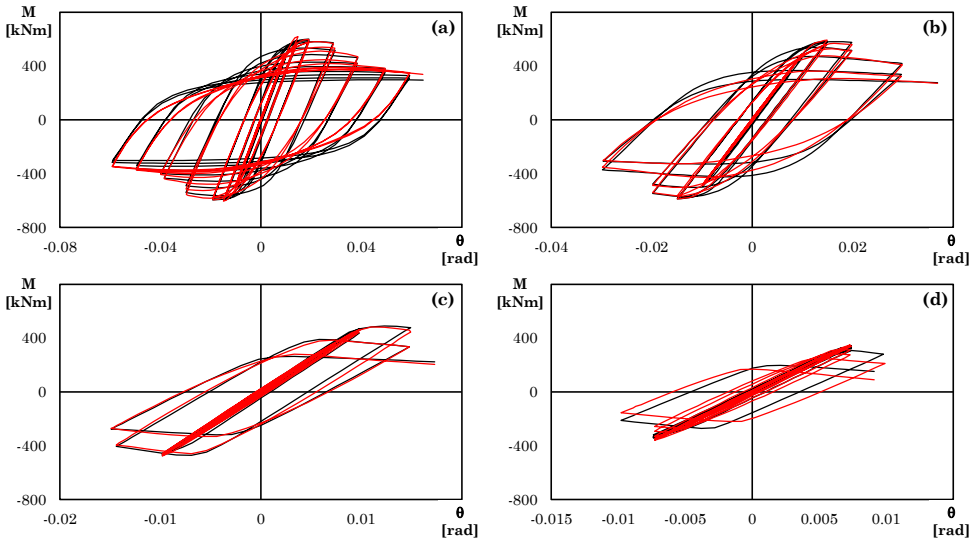


**Fig. 152** – Comparison between the cyclic responses of the FEM and the OpenSees model for the 300×300×10.0 section ($L_v$ = 1.50 m) and axial load ratio equal to: (a) 0.0; (b) 0.1; (c) 0.3; (d) 0.5.

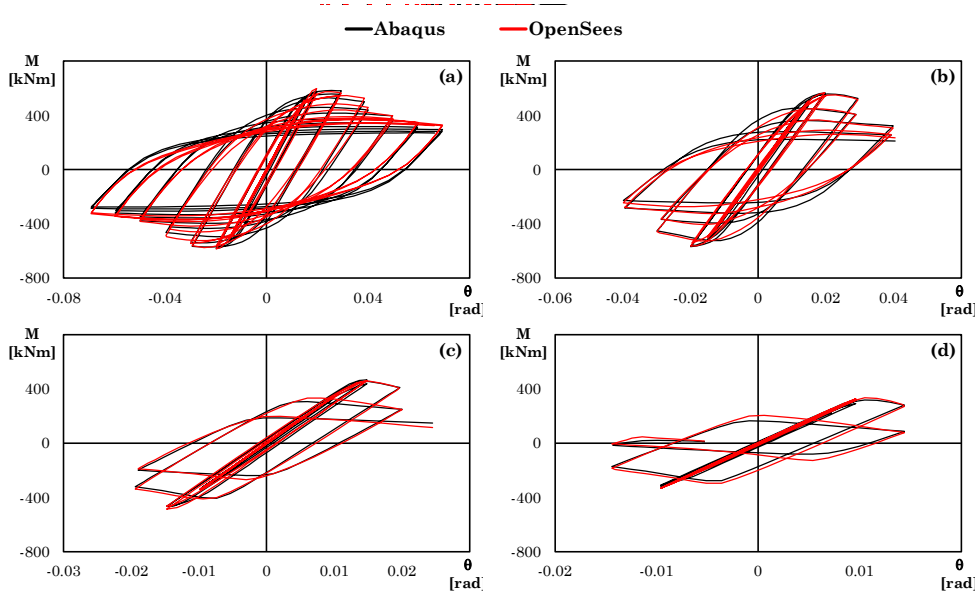


**Fig. 153** – Comparison between the cyclic responses of the FEM and the OpenSees model for the 300×300×10.0 section ($L_v$ = 2.25 m) and axial load ratio equal to: (a) 0.0; (b) 0.1; (c) 0.3; (d) 0.5.

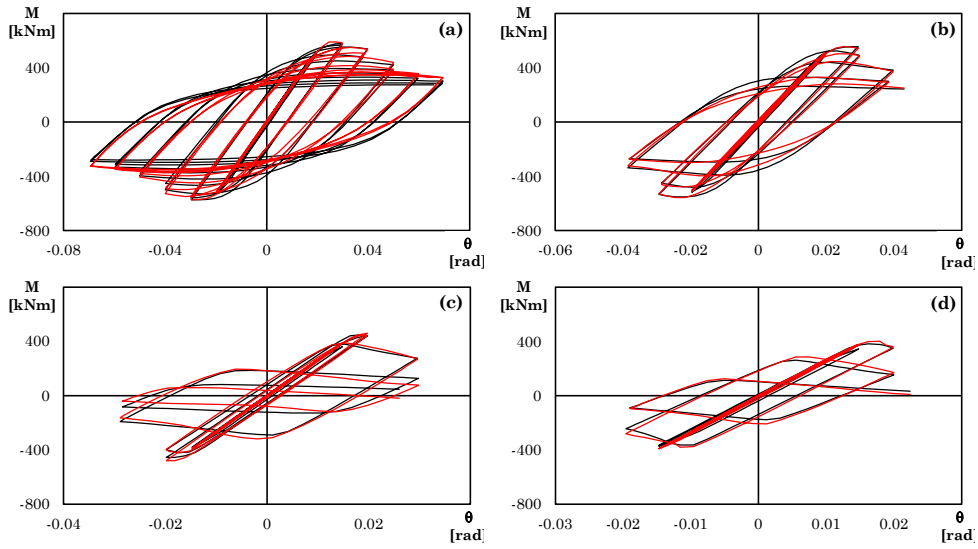


**Fig. 154** – Comparison between the cyclic responses of the FEM and the OpenSees model for the 300×300×10.0 section ($L_v$ = 3.00 m) and axial load ratio equal to: (a) 0.0; (b) 0.1; (c) 0.3; (d) 0.5.

The comparisons presented in the figures highlight the overall high accuracy of the proposed model, with a better performance for members subjected to axial load. This trend is reasonably expected, since the modified SteelRebar formulation and its $l/d$ assignment strategy were calibrated starting from stub-column simulations, where the response is inherently governed by compressive behaviour under relevant normal force. Conversely, the cases without axial load tend to slightly overestimate the bending moments at large deformation demands.

To evaluate the accuracy of the Opensees model for all the considered specimens, the bending moment predicted using the Opensees model at a given rotation demand is normalized to the maximum bending moment $M_{max,OS}$. The normalized curve is used to evaluate the envelope curve corresponding to the first cycle and the chord rotations $\theta_{80\%,OS}$ and $\theta_{50\%OS}$ at the achievement of a residual normalized bending moment equal to 0.80 and 0.50. The sub-script "OS" is added to underline that both the residual bending moment and the maximum bending moment are determined using the Opensees model. The values of the chord rotations $\theta_{80\%,OS}$ and $\theta_{50\%OS}$ are compared in **Figs. 155 and 156** to the corresponding values derived starting from the cyclic response predicted by the Abaqus model ($\theta_{80\%,Abaqus}$ and $\theta_{50\%Abaqus}$).

**Fig. 155**, shows that, when considering $\theta_{80\%}$, which is representative of the Significant Damage (SD) limit state, the agreement between the predictions provided by the two numerical models is excellent. However, at larger rotations, the discrepancy becomes more pronounced. **Fig. 156**, compares the $\theta_{50\%}$ values (with the Near Collapse, NC, limit state), and shows that the deviation increases for sections without axial load and for the stockiest sections with $\nu = 0.1$. In these cases, the OpenSees model tends to predict less severe degradation.

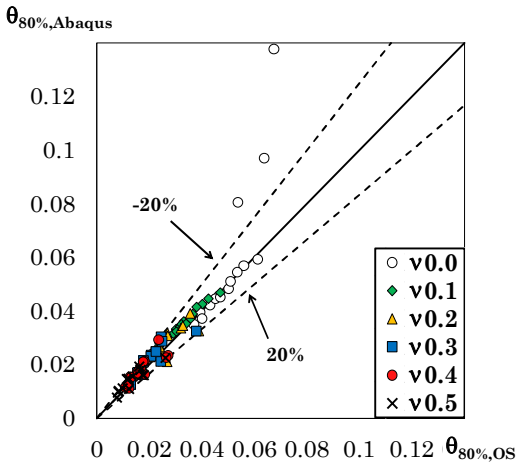


**Fig. 155** – Comparison of the chord rotation $\theta_{80\%}$ (Significant Damage limit state) predicted by the Abaqus and OpenSees models for all investigated specimens.

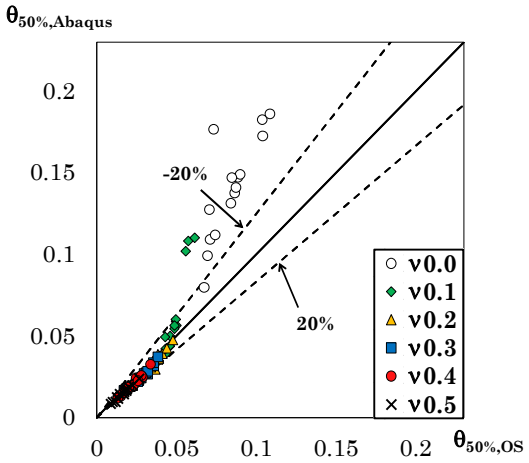


**Fig. 156** – Comparison of the chord rotation $\theta_{50\%}$ (Near Collapse limit state) predicted by the Abaqus and OpenSees models for all investigated specimens.

## 9. Accuracy of the model for the biaxial bending tests

The OpenSees model developed in this work adopts a fibre-based formulation in which each fibre is assigned the modified SteelRebar material. Since the section response is obtained by integrating the uniaxial stress–strain laws over the fibre discretization, the model naturally captures the axial force–biaxial bending interaction without additional phenomenological coupling assumptions. As a result, the proposed model is suitable not only for purely axial or uniaxial bending conditions, but also for simulating combined axial load and biaxial bending, as typically experienced by steel columns under seismic actions where flexure about both principal axes develops simultaneously.

### 9.1. Modifications to the model to apply the biaxial bending moment

To enable the simulation of biaxial bending, the original 2D OpenSees model was extended to a 3D formulation. The forceBeamColumn elements were assigned a linear geometric transformation using the geomTransf Linear command. The components of the vector required in a three-dimensional model to define the mapping between the element local system and the global reference frame are assigned so that the loading protocol is still applied at the same control node and along the same global axes, while the local element axes (and thus the section orientation) are rotated by an angle φ. In other words, the same global displacements imposed in specimens subjected to uniaxial bending generate the desired combination of bending about the two principal local axes.

### 9.2. Simulation of tests under axial load and biaxial bending

In the figures that follow a comparison of the responses of columns under biaxial bending between the two models is reported. The Abaqus responses are reported with continuous black lines, whereas the OpenSees responses are shown with continuous red lines.

As in section 8.1, the results are reported in terms of resulting bending moment (determined as discussed in Section 2 of Chapter 3) versus

chord rotation, and the cyclic curves are cut at the step where the Abaqus finite element model reaches $\theta_{50\%}$.

**Figs. 157-159** show the cyclic responses for the stockiest section 350×350×16 with a shear length of 2.25m and for the angle of displacements 15°, 30° and 45°. For each angle, the cyclic response corresponding to four different values of the axial load ratio are presented. **Figs. 160-162** and **Figs. 163-165** show the same comparison respectively for an intermediate-slenderness section (400×400×16.0), and the slenderest section (300×300×10). Also in this case, the aim of the comparison is to assess the accuracy of the OpenSees model in reproducing the FEM response. Therefore, the figures are reported using different x-axis scales, in order to improve the readability of the cases characterised by higher axial load levels.

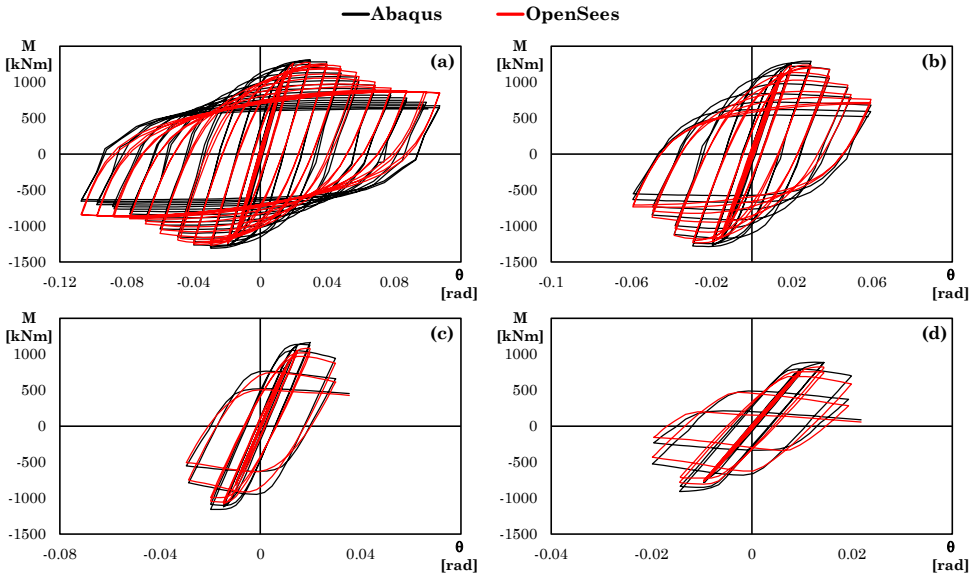


**Fig. 157** – Comparison between the cyclic responses of the FEM and the OpenSees model for the 350×350×16.0 section with $L_v$ = 2.25 m, φ=15° and ν equal to (a) 0.0; (b) 0.1; (c) 0.3; (d) 0.5.

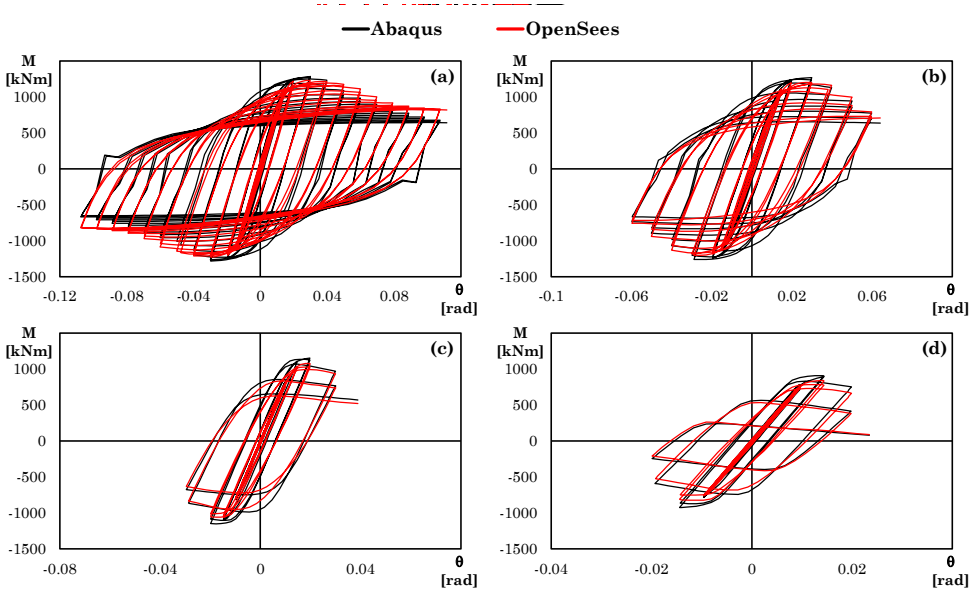


**Fig. 158** – Comparison of the cyclic responses of the FEM and the OpenSees model for the 350×350×16.0 section with $L_v$ = 2.25 m, φ=30° and ν equal to (a) 0.0; (b) 0.1; (c) 0.3; (d) 0.5.

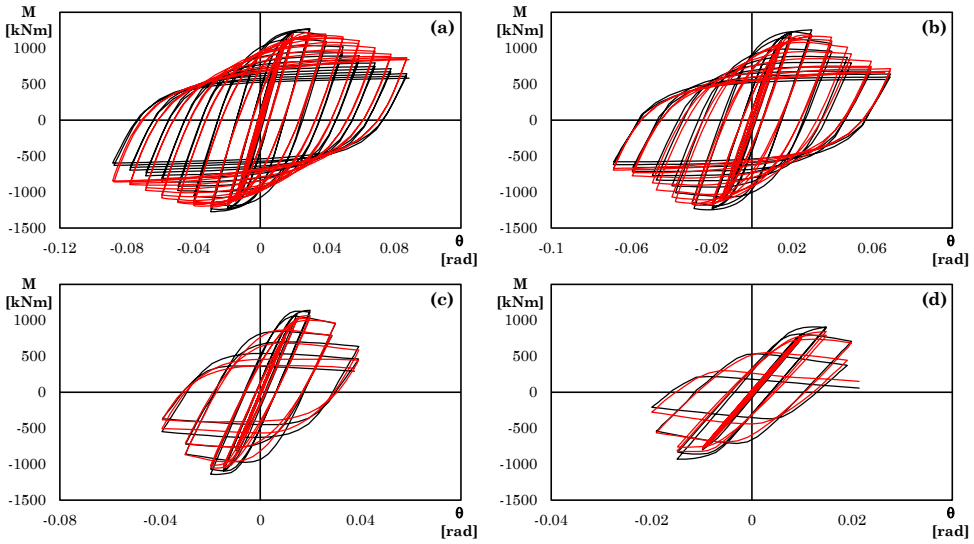


**Fig. 159** – Comparison of the cyclic responses of the FEM and the OpenSees model for the 350×350×16.0 section with $L_v$ = 2.25 m, φ=45° and ν equal to (a) 0.0; (b) 0.1; (c) 0.3; (d) 0.5.

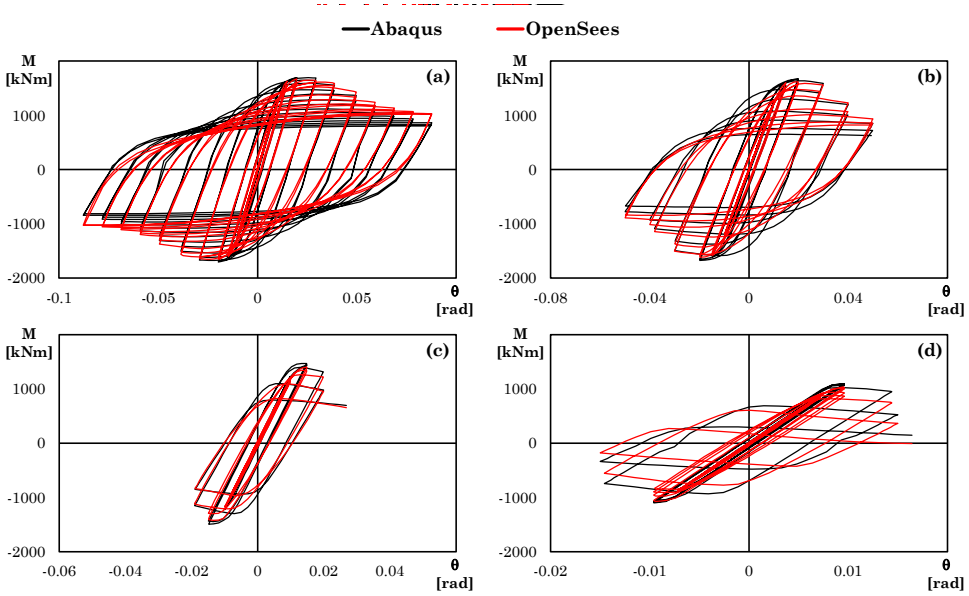


**Fig. 160** – Comparison of the cyclic responses of the FEM and the OpenSees model for the 400×400×16.0 section with $L_v$ = 2.25 m, φ=15° and ν equal to (a) 0.0; (b) 0.1; (c) 0.3; (d) 0.5.

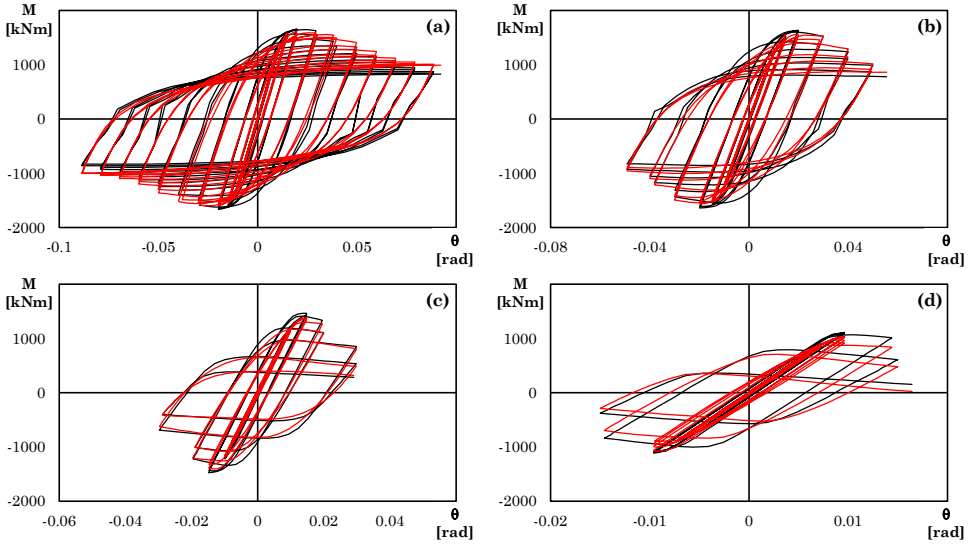


**Fig. 161** – Comparison of the cyclic responses of the FEM and the OpenSees model for the 400×400×16.0 section with $L_v$ = 2.25 m, φ=30° and ν equal to (a) 0.0; (b) 0.1; (c) 0.3; (d) 0.5.

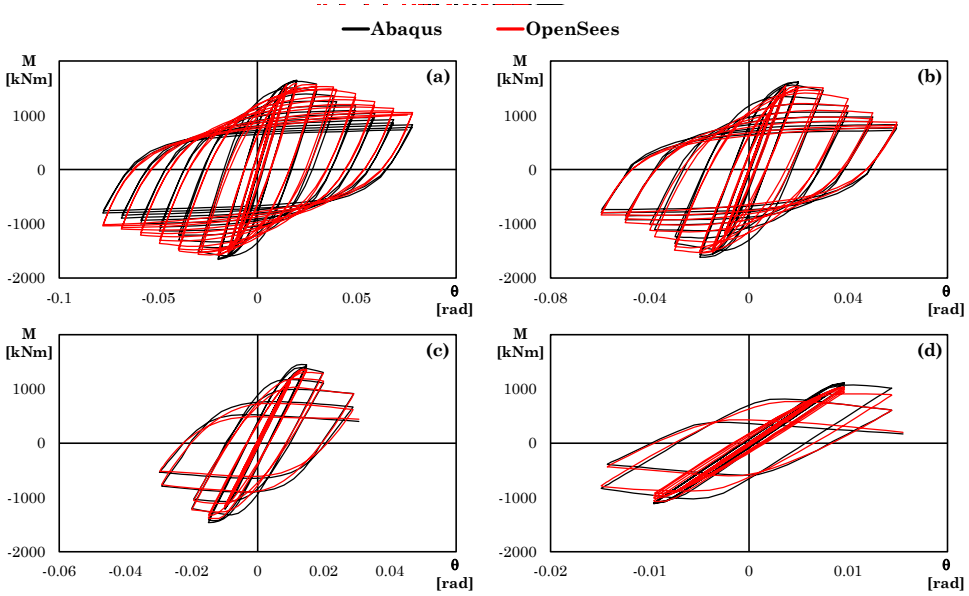


**Fig. 162** – Comparison of the cyclic responses of the FEM and the OpenSees model for the 400×400×16.0 section with with $L_v$ = 2.25 m, φ=45° and ν equal to (a) 0.0; (b) 0.1; (c) 0.3; (d) 0.5.

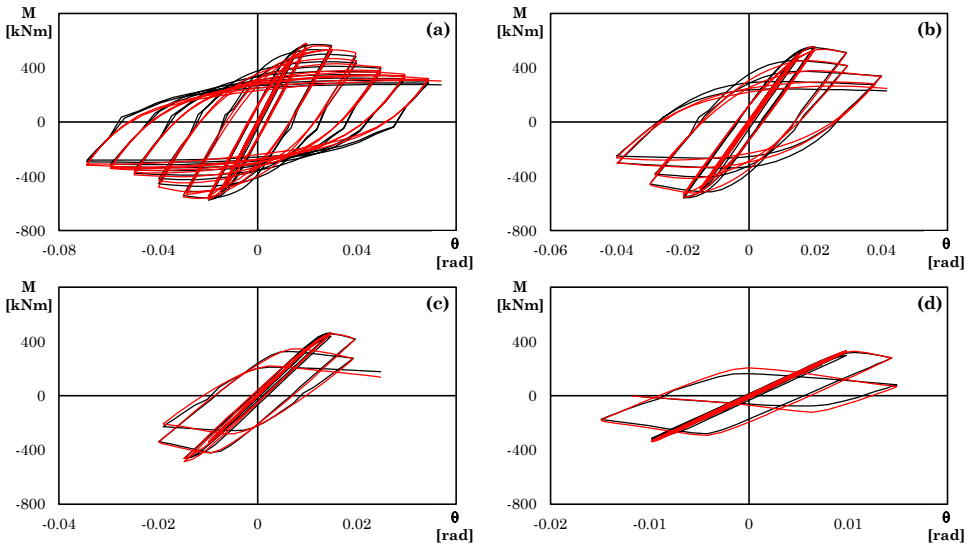


**Fig. 163** – Comparison of the cyclic responses of the FEM and the OpenSees model for the 300×300×10.0 section with $L_v$ = 2.25 m, φ=15° and ν equal to (a) 0.0; (b) 0.1; (c) 0.3; (d) 0.5.

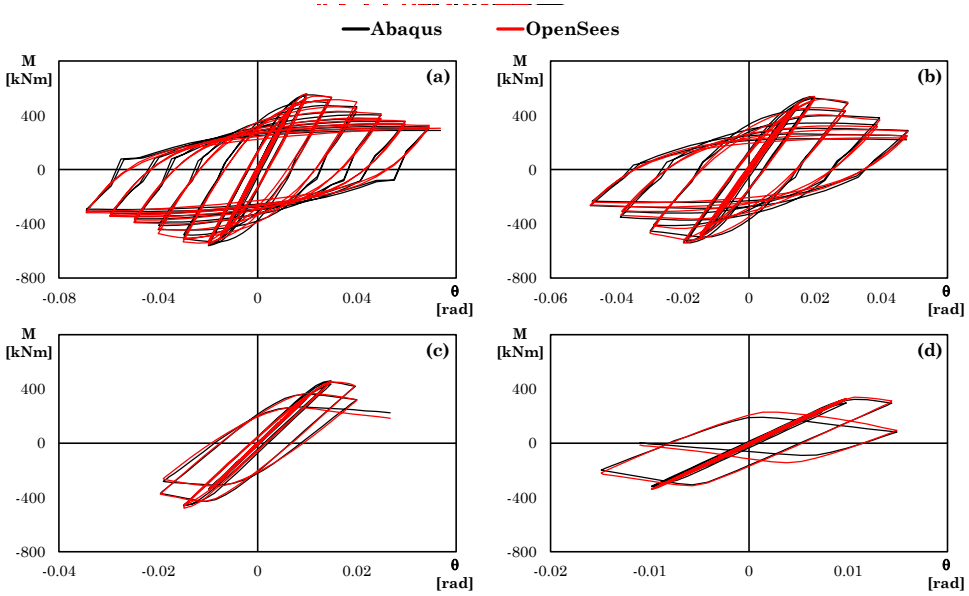


**Fig. 164** – Comparison of the cyclic responses of the FEM and the OpenSees model for the 300×300×10.0 section with $L_v$ = 2.25 m, φ=30° and ν equal to (a) 0.0; (b) 0.1; (c) 0.3; (d) 0.5.

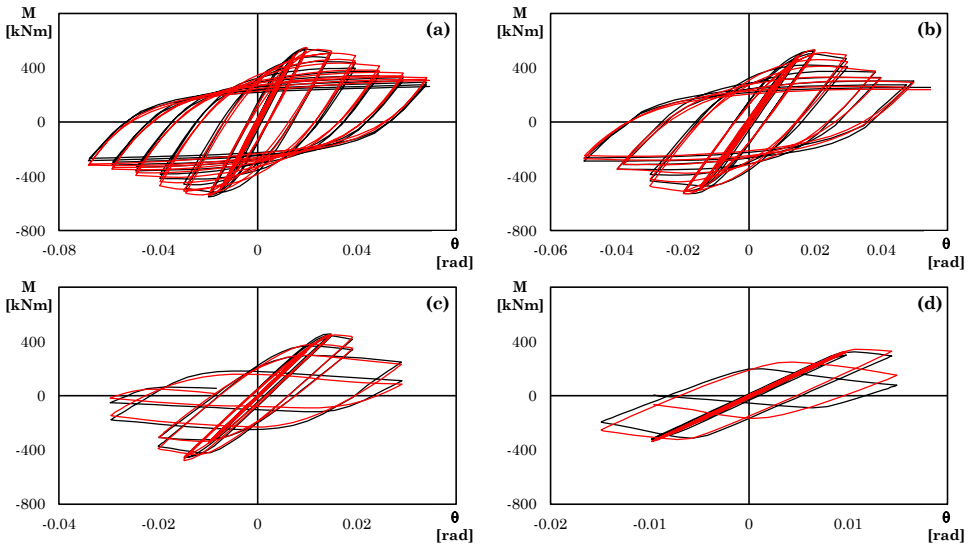


**Fig. 165** – Comparison of the cyclic responses of the FEM and the OpenSees model for the 300×300×10.0 section with $L_v$ = 2.25 m, φ=45° and ν equal to (a) 0.0; (b) 0.1; (c) 0.3; (d) 0.5.

The comparisons presented in the figures highlight that even in the case of biaxial bending the model has a high accuracy. Similarly to what was achieved for the specimens subjected to uniaxial bending, the model shows a better performance for members subjected to axial load than those without an axial load. In these latter cases, the model tends to slightly overestimate the bending moments at large deformation demands.

This is confirmed by **Fig. 166**, which shows excellent correspondence between the values of $\theta_{80\%}$ predicted by the OpenSees model ($\theta_{80\%OS}$) and those predicted using Abaqus simulations ($\theta_{80\%,Abaqus}$) for $\nu > 0$. However, as already observed for members under uniaxial bending, the discrepancy between the values predicted by the two models becomes more pronounced at larger rotations. **Fig. 167**, reporting the comparison of values of $\theta_{50\%}$ predicted using the two numerical models, shows that the deviation increases for sections without axial load and for the stockiest sections at $\nu = 0.1$, where the OpenSees model tends to predict less severe degradation.

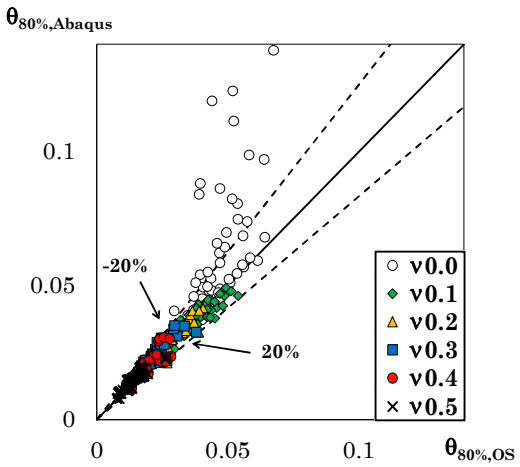


**Fig. 166** – Comparison of the chord rotation $\theta_{80\%}$ (SD limit state) predicted by the Abaqus and OpenSees models for all investigated specimens.

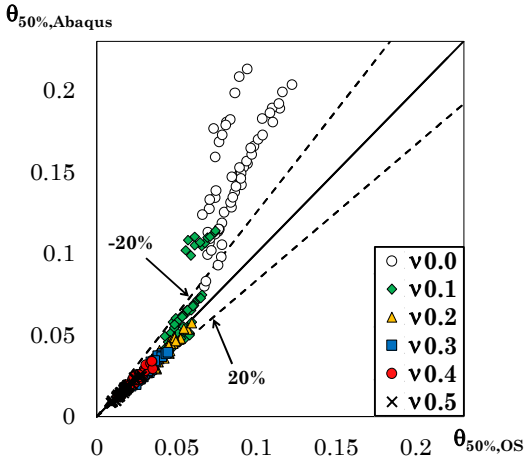


**Fig. 167** – Comparison of the chord rotation $\theta_{50\%}$ (NC limit state) predicted by the Abaqus and OpenSees models for all investigated specimens.

The cyclic responses shown in the previous figures, for both the Abaqus and OpenSees models, indicate that for stocky sections under zero axial load, the residual bending moment tends to stabilize at large chord rotations. Consequently, substantial differences in the predicted $\theta_{50\%}$ may not be meaningful if the residual bending moment at which the OpenSees response tends to flatten is only slightly higher than that toward which the Abaqus response converges. To better investigates on this issue, the residual bending moment predicted by the OpenSees model was extracted at the chord rotation corresponding to $\theta_{50\%}$ of the Abaqus FE model ($\theta_{50\%,Abaqus}$). This residual bending moment provided by the Opensees model was then normalised by the peak bending moment, and plotted in **Fig. 168** for all cases with $\nu = 0.0$ and $\nu = 0.1$. A normalised residual bending moment value equal to 0.5 would indicate that the Opensees model accurately predicts the residual strength at $\theta_{50\%}$, whereas deviations from 0.5 reflect differences in the simulation of post-peak degradation. **Fig. 168a** confirms a marked overestimation of the normalised residual bending moment by the OpenSees model for $\nu = 0.0$. The largest discrepancy is observed for the 350×350×16.0 section with $L_v = 2.25$ m and $\varphi = 45°$, for which the normalised residual bending moment reaches 0.717. 18 specimens exhibit normalised residual bending moments greater than 0.65.

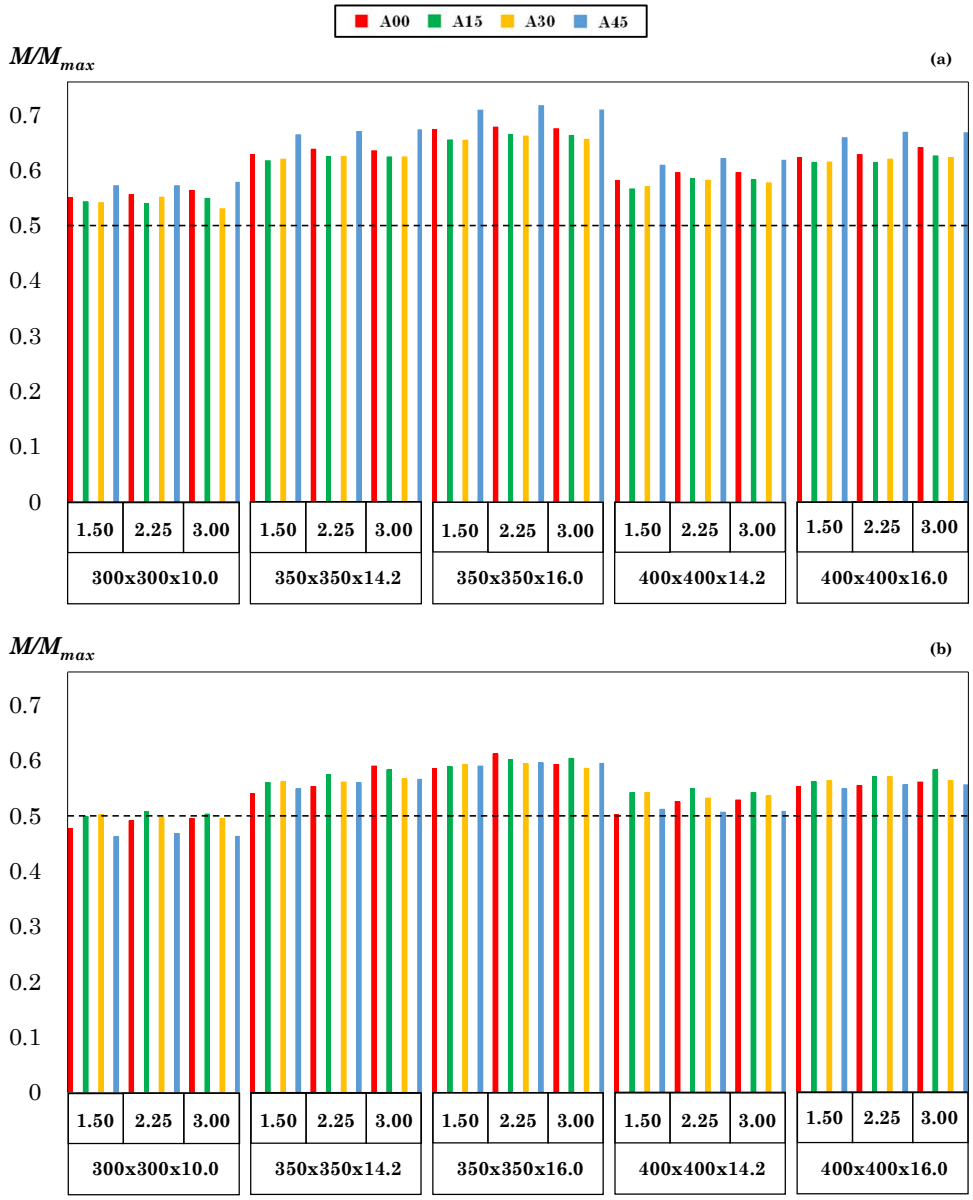


**Fig. 168** – OpenSees normalised bending moment when $\theta_{50\%}$ is achieved on Abaqus model: (a) specimens with $\nu = 0.0$; (b) specimens with $\nu = 0.1$.

**Fig. 168b** shows a milder overestimation for ν = 0.1, mainly for the stockiest sections; in this case, the maximum deviation occurs for the 350×350×16.0 section with $L_v$ = 2.25 m and φ = 0°, for which the normalised residual bending moment reaches 0.612.

**Fig. 169** extends the same comparison to all specimens as a function of the axial load ratio. The median value of the normalised residual bending moment decreases as ν increases: it is 0.60 for ν = 0.0, 0.55 for ν = 0.1, approximately 0.50 for ν = 0.2 and ν = 0.3, and 0.45 for ν = 0.4. For ν = 0.5, the results show a wider scatter and a shift towards lower values, with most normalised residual bending moments falling in the 0.3–0.4 range.

Although the cases with ν = 0.5 also exhibit normalised residual bending moments noticeably different from 0.5, this is mainly attributable to the rapid loss of resistance that may occur in these profiles at relatively small chord rotations. So, this type of comparison becomes less informative for assessing accuracy at high axial loads. **Fig. 170** shows the comparison of the responses of specimen 400x400x14.2 as an example of the worst case with ν = 0.5 that reports a normalized residual bending moment $M/Mmax$ = 0.219.

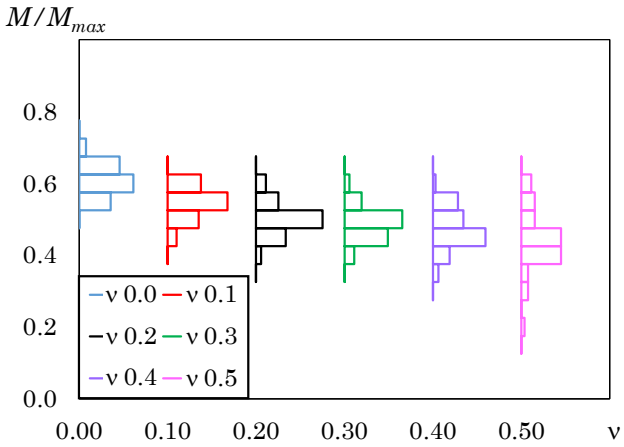


**Fig. 169** – OpenSees normalised bending moment when $\theta_{50\%}$ is achieved on Abaqus model for all specimens.

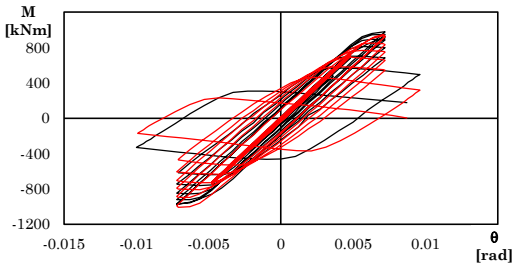


**Fig. 170** – Comparison between the cyclic responses of the FEM model and the OpenSees model for the 400×400×14.2 section with $L_v$ = 1.50 m, ν = 0.5 and an angle of displacement of 30°.

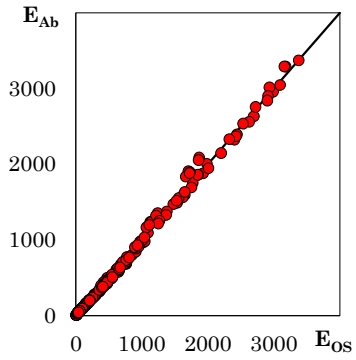


**Fig. 171** – Comparison of the energy dissipation prediction by the Abaqus and OpenSees models for all investigated specimens.

A final check on the OpenSees predictive capability is performed in terms of energy dissipation, computed as the area enclosed by the hysteretic loops, as reported in **Fig. 171**. Despite the aforementioned tendency to overestimate the bending moments at large deformation demands for ν = 0.0 (and for ν = 0.1 in the stockiest sections), the overall dissipated energies are captured with excellent accuracy.

# Conclusions

This thesis investigated the cyclic response and chord-rotation capacity of cold-formed Hollow Structural Section (HSS) members used as beam–column components under combined axial load and bending moments. Specific attention was given to biaxial bending demands representative of three-dimensional moment-resisting frames. The work combined refined finite element (FE) modelling, large-scale parametric simulations, and the development and calibration of simplified numerical tools suitable for design-oriented applications and structural-system analyses.

A refined FE modelling strategy was first used and validated against experimental evidence available in the literature for members under the combined effects of axial loads and biaxial bending. The validation demonstrated that the adopted FE framework can reproduce the response of cold-formed HSS columns with good accuracy in terms of (i) bending moment versus chord rotation and (ii) axial shortening. In addition, the analyses confirmed that including geometric imperfections consistently with the Eurocode 3 philosophy leads to a conservative estimate of chord-rotation capacity, highlighting the role of imperfection sensitivity in governing local buckling initiation and post-peak degradation.

The validated modelling assumptions were then used to carry out an extensive parametric study, consisting of 1272 analyses on cantilever members selected to cover variations in cross-section geometry and size, axial load ratio, shear length, and loading direction angle. The FE database enabled the development of predictive equations for the chord-rotation capacity under symmetric cyclic biaxial bending at both the Significant Damage (SD) and Near Collapse (NC) limit states. The proposed

expressions account for the key geometric and mechanical parameters controlling instability and degradation (i.e., the web and flange slenderness of the cross-sections, the axial load ratio, the ratio of the half-wavelength of the buckled flange to the shear length, the depth-to-width ratio, and the angle of the displacement loading direction), and were calibrated through regression analyses on log-transformed data.

The derived equations were shown to provide accurate estimates of the chord rotation capacity across the full investigated range of loading directions. Moreover, the logarithmic of residuals resulting from the regression analysis were found to be approximately normally distributed with mean close to zero; this is an important property for probabilistic applications (e.g., Monte Carlo simulations for seismic performance assessment).

To support efficient nonlinear analyses at the structural level, a simplified concentrated-plasticity strategy was proposed by calibrating the parameters of the modified Ibarra–Krawinkler (MIK) deterioration model for cantilever members made of cold-formed HSS sections. Predictive equations were provided for strength, deformation, and degradation-rate parameters as a function of the geometric and mechanical quantities governing local buckling. The proposed formulation (i) estimates median parameter values, (ii) yields residuals compatible with normal and lognormal assumptions, (iii) explicitly incorporates cold-forming effects (different strength of flat and corner parts), and (iv) reproduces cyclic response accurately over cases with low-to-high degradation rates, with dissipated energy generally predicted within about 20% error. Based on the calibration domain, the equations are recommended primarily for axial load ratios not exceeding 0.3 and within the reported geometric limits of the database.

To overcome the intrinsic limitations of single-spring models in capturing axial force–biaxial bending interaction, a fiber-based OpenSees strategy was developed using a material model with different behaviour in tension and compression. Specifically, the SteelRebar uniaxial material model is used. In its original development, this material model was proposed to replicate the response of steel rebars characterised by a predefined $l/d$, where $l$ is the buckling length of the bar and $d$ is the diameter

of the cross-section. The original SteelRebar compression rule, based on Akkaya characteristic points, was found to introduce non-smooth trends and discontinuities; therefore, the monotonic compressive backbone of the SteelRebar material model was reformulated through a buckling-type, continuously varying law calibrated on a dedicated numerical database.

To account for local buckling phenomena, in the proposed fiber model, the material behaviour of the fibres within the cross-section is differentiated based on the position of the fiber. In particular, fibres located in the central region of the flat parts are assimilated to steel rebars characterized by $l/d$ ratios larger than those of rebars associated to fibres located near the corner parts. A closed-form relationship was proposed to assign $l/d$ to flat-plate fibres as a function of the local slenderness of the flat parts of the cross-section and of the fiber position.

The comparison of the cyclic responses predicted by the FE and the fiber based models of members under uniaxial and biaxial bending showed an overall good agreement, particularly for cases with non-zero axial load. The proposed fiber-based model is able to adequately simulate the strength degradation, although some overestimation of the resisting bending moments at large rotations was observed for members subjected to low axial load ratios. Nonetheless, the dissipated energy was captured with satisfactory accuracy.

From an engineering perspective, the simplified models developed in Chapters 4 and 5 should be regarded as complementary tools. The concentrated-plasticity model based on the MIK spring is primarily suited to members under uniaxial bending, as it represents the inelastic response through a moment–rotation law concentrated at the base section. The fibre-based model, instead, is intended for cases in which axial load–biaxial bending interaction must be explicitly captured through a cross-section discretised into fibres with position-dependent constitutive properties. Both models are suitable for engineering applications, but they differ in scope and modelling detail. Accordingly, the model in Chapter 4 may be regarded as the preferred tool for efficient design-oriented analyses under uniaxial bending, whereas the model in Chapter 5 provides a more

versatile framework when biaxial response and N–My–Mz interaction need to be captured explicitly.

Overall, the thesis provides: (i) FE-based predictive equations for chord-rotation capacity domains under axial load and biaxial bending; (ii) a computationally efficient spring-based numerical model for uniaxial bending applications; and (iii) a fiber-based model developed in the OpenSees framework capable of representing N–My–Mz interaction and local-instability-driven degradation through a refined uniaxial material formulation. These developments support performance-based assessment and can inform future improvements of code-oriented acceptance criteria for cold-formed HSS columns under realistic seismic demands.

Future work related to the proposed fiber-based model should primarily address (a) reducing the residual overestimation at very low axial load ratios at large rotations, (b) improving the representation of behaviours observed in FE under specific cyclic protocols (e.g., relaxation effects under constant-amplitude histories), and (c) extending/validating the simplified models against additional experimental datasets and loading histories to further strengthen their generality for design and assessment applications.

## References


[1] Mirambell E., Real E., On the calculation of deflections in structural stainless-steel beams: an experimental and numerical investigation. Journal of Constructional Steel Research 54(1):109–33, 2000.

[2] Somodi B., Kovesdi B., Residual stress measurements on cold-formed HSS hollow section columns. *Journal of Constructional Steel Research* 128:706–720, 2017.

[3] Pics from "http://www.distritube.fr/wp-content/uploads/2014/11/distritube-tubes-construction-1.pdf"

[4] Pics from "http://www.dica.unict.it/users/prossi/Files/Files%20Progetto/Lezione%2032%20%20Strutture%20%28Strutture%20Acciaio%201%29.pdf"

[5] Pics from "https://www.abelard.org/france/motorway-aires10.php"

[6] Ramberg W., Osgood W.R., Description of stress-strain curves by three parameters. Technical Note No. 902, National Advisory Committee for Aeronautics, Washington, D.C., USA, 1943.

[7] Poursadrollah A., D'Aniello M., Landolfo R., Experimental and numerical tests of cold-formed square and rectangular hollow columns. Engineering Structures 273: 115095, 2022.

[8] Gardner L., Yun X., Description of stress-strain curves for cold-formed steels. Construction and Building Materials. 189: 527-538, 2018.

[9] Filippou F.C., Popov E.P., Bertero V.V., Effects of Bond Deterioration on Hysteretic Behavior of Reinforced Concrete Joints. Report EERC 83-19, Earthquake Engineering Research Center, University of California, Berkeley, 1983.

[10] Afshan S., Rossi B., Gardner L., Strength enhancements in cold-formed structural sections – Part I: Material testing. Journal of Constructional Steel Research 83:177–188, 2013.

[11] Gardner L., Saari N., Wang F., Comparative experimental study of hot-rolled and cold-formed rectangular hollow sections. Thin-Walled Structures 48(7):495–507, 2010.

[12] Kesti J., Local and Distortional Buckling of Perforated Steel Wall Studs. Ph.D. thesis, Helsinki University of Technology, Finland, 2000.

[13] Kaitila O., Web Crippling of Cold-Formed Thin-Walled Steel Cassettes. Ph.D. thesis, Helsinki University of Technology, Finland, 2004.

[14] Kettler M., Elastic-Plastic Cross-Sectional Resistance of Semi-Compact H- and Hollow Sections. Ph.D. thesis, Graz University of Technology, Austria, 2008.

[15] Kyvelou P., Gardner L., Nethercot D.A., Composite action between cold-formed steel beams and wood-based floorboards. International Journal of Structural Stability and Dynamics 15(8):1540029–1540046, 2015.

[16] Kyvelou P., Gardner L., Nethercot D.A., Testing and analysis of composite cold-formed steel and wood-based flooring systems. Journal of Structural Engineering (ASCE) 143(11):04017146, 2017.

[17] Li H.T., Young B., Material properties of cold-formed high strength steel at elevated temperatures. Thin-Walled Structures 115:289–299, 2017.

[18] Li H.T., Young B., Tests of cold-formed high strength steel tubular sections undergoing web crippling. Engineering Structures 141:571–583, 2017.

[19] Ma J.L., Behaviour and Design of Cold-Formed High Strength Steel Tubular Members. Ph.D. thesis, University of Hong Kong, Hong Kong, China, 2016.

[20] Ma J.L., Chan T.M., Young B., Material properties and residual stresses of cold-formed high strength steel hollow sections. Journal of Constructional Steel Research 109:152–165, 2015.

[21] McCann F., Gardner L., Kirk S., Elevated temperature material properties of cold-formed steel hollow sections. Thin-Walled Structures 90:84–94, 2015.
[22] Nseir J., Development of a new design method for the cross-section capacity of steel hollow sections. Ph.D. thesis, University of Liège, Liège, Belgium, 2015.
[23] Schillo N., Theofanous M., Gardner L., Feldmann M., Material properties and local buckling behaviour of high strength steel hollow sections. Proceedings of the 7th European Conference on Steel and Composite Structures, Napoli, Italy, 2014.
[24] Salmi P., Kouhi J., Puthli R., Herion S., Fleischer O., Espiga F., Croce P., Bayo E., Goni R., Björk T., Ilvonen R., Design rules for cold-formed structural hollow sections. EUR 21973, European Commission, 2006.
[25] Tran A.T., Veljkovic M., Rebelo C., da Silva L.S., Resistance of cold-formed high strength steel circular and polygonal sections – Part 1: Experimental investigations. Journal of Constructional Steel Research 120:245–257, 2016.
[26] Ballio G., Mazzolani F., Bernuzzi C., Landolfo R., Strutture di acciaio-teoria e progetto. Ulrico Hoepli, 2020.
[27] CEN, EN 10219-2:2019 Cold formed welded steel structural hollow sections – Part 2: Tolerances, dimensions and sectional properties. European Committee for Standardization (CEN), Brussels, Belgium, 2019.
[28] Toffolon A., Generalised slenderness-based resistance method for the strength prediction of hollow sections. Universitat der Bundeswehr München, 2021.
[29] Kurata M., Nakashima M., Suita K., Test on large cyclic deformation of steel tube columns having fixed column bases. Journal of Structural and Construction Engineering. AIJ 598: 149-154, 2005.
[30] D'Aniello M., Landolfo R., Piluso V., Rizzano G., Ultimate behavior of steel beams under non-uniform bending. Journal of Constructional Steel Research 78: 144-158, 2012.
[31] Fadden M., McCormick J., Cyclic quasi-static testing of hollow structural section beam members. Journal of Structural Engineering 138 (5): 561-570, 2012.

[32] Bai Y., Kurata M., Nakashima M., Modelling post-local buckling behavior of beam-columns with hollow steel section. Proceedings of the 8th International Conference on Behavior of Steel Structures in Seismic Areas, 2015.
[33] Suzuki Y., Lignos D.G., Experimental evaluation of steel columns under seismic hazard-consistent collapse loading protocols. Journal of Structural Engineering ASCE 147 (4) 0402102, 2021.
[34] Ishida T., Yamada S., Shimada Y. Bi-axial Bending Behavior of RHS-columns Including Post-buckling and Deterioration Range. Proceedings of the 15th World Conference on Earthquake Engineering, Lisbon, 2012.
[35] Mukaide S., Oku N., Matsuo K., Tada M., Loading test in the range of large deformation for RHS columns with different manufacturing process. Steel Construction Engineering 23 (90): 51-64, 2016.
[36] Yamada M., Tsuji B., Tokuda K., Elasto – Plastics Deformation and Fracture Behavior of Steel Box Columns Subjected to Double Curvature Bending Under Constant Axial Load. In Proceedings of AIJ, 1982.
[37] Tsujioka S., Igarashi K., Sugiyama S., Experimental Investigation of Inelastic Behavior of Cold - Formed Rectangular Hollow Structural Sections. In Proceedings of AIJ, 1986.
[38] Kadono A., Sasaki M., Okamoto K., et al., Experimental Study on the Effect of Yield Ratio on the Bending Strength Increasing Ratio and Ductility of Steel Structures Members. Journal of Structural Construction Engineering 40B, no. 3: 673-682, 1994.
[39] Tremblay R., Inelastic seismic response of steel bracing members. Journal of Constructional Steel Research 58, pp 665-701, 2002.
[40] Goggins J.M., Broderick B.M., Elghazouli A.Y., Lucas A.S., Behaviour of tubular steel members under cyclic axial loading. Journal of Constructional Steel Research, 58, pp 121-131, 2006.
[41] Han S.W., Kim W.T., Foutch D.A., Seismic behavior of HSS bracing members according to width and thickness ratio under symmetric cyclic loading. Journal of Structural Engineering 133, pp 264-273, 2007.

[42] CEN. EN 1998-1, EuroCode 8: Design of Structures for Earthquake Resistance – Part 1: General Rules. Seismic Actions and Rules for Buildings, European Committee for Standardization, Bruxelles, 2004.
[43] Cerqueira E., Eshaghi C, Peres R., Castro M., Preliminary assessment of biaxial bending effects on the rotation capacity of steel tubular members. STESSA 2024, LNCE 519: 138-149, 20024.
[44] Bosco M., D'Aniello M., Landolfo R., Pannitteri C., Rossi PP., Overstrength and deformation capacity of steel members with cold-formed hollow cross-section. Journal of Constructional Steel Research 191, 107187, 2022.
[45] Fadden M., McCormick J., Finite element model of the cyclic bending behavior of hollow structural sections. Journal of Structural Steel Research 94: 64-75, 2014.
[46] Bosco M., Tirca L., Numerical Simulation of Steel I-Shaped Beam Using Fibre-Based Damage Accumulation Model. Journal of Constructional Steel Research 133:241–255, 2017.
[47] Coffin L., A study of the effect of cyclic thermal stress on a ductile metal. Journal of Fluids Engineering 76:931–950, 1954.
[48] Manson S., Fatigue: a complex subject – some simple approximations. Experimental Mechanics 5(7):193–226, 1965.
[49] Engelhardt M.D., Sabol T.A., Testing of welded steel moment connections in response to the Northridge Earthquake. Progress Report to the AISC Advisory Subcommittee on Special Moment Resisting Frame Research, 1994.
[50] Kim T., Whittaker A.S., Gilani A.S.J., Bertero V.V., Takhirov S.H., Cover-Plate and Flange-Plate Reinforced Steel Moment Resisting Connections. PEER Report 2000/07, Pacific Earthquake Engineering Research Center, University of California, Berkeley, 2000.
[51] Tsai K.C., Popov E.P., Steel Beam-Column Joints in Seismic Moment Resisting Frames. Report No. UCB/EERC-88/19, Earthquake Engineering Research Center, Berkeley, 1988.
[52] Uang C.M., Latham C., Cyclic Test of Full Scale MNH-SMRFTH Dual Strong Axis Moment Connections. Report No. TR-95/01, University of California, San Diego, USA, 1995.

[53] Newell J., Uang C.-M., Cyclic behavior of steel wide-flange columns subjected to large drift. Journal of Structural Engineering 134(8):1334–1342, 2008.
[54] Elkady A., Lignos D.G., Full-scale testing of deep wide-flange steel columns under multiaxis cyclic loading: loading sequence, boundary effects, and lateral stability bracing force demands. Journal of Structural Engineering 144(2):04017189, 2018.
[55] Wang M., Shi Y., Wang Y., Equivalent constitutive model of steel with cumulative degradation and damage. Journal of Constructional Steel Research 79:101–114, 2012.
[56] Suzuki Y., Lignos D.G., Fibre-based hysteretic model for simulating strength and stiffness deterioration of steel hollow structural section columns under cyclic loading, Earthquake Engineering & Structural Dynamics 49 (15): 1702–1720, 2020.
[57] Ibarra L.F., Medina R.A., Krawinkler H., Hysteretic models that incorporate strength and stiffness deterioration. Earthquake Engineering & Structural Dynamics 34(12):1489–1511, 2005.
[58] Lignos D.G., Krawinkler H., Sidesway collapse of deteriorating structural systems under seismic excitations. Rep. No. TB 172, The John A. Blume Earthquake Engineering Center, Stanford University, Stanford, CA, 2009.
[59] Tartaglia R., D'Aniello M., Landolfo R., Seismic performance of Eurocode-compliant ductile steel MRF. Earthquake Engineering & Structural Dynamics 51:2527–2552, 2022.
[60] Vaez S.R.H., Samani A.A., Mobinipour S.A., Dehghani E., Effect of uncertainties in design variables on the hysteresis response of 2D steel moment-resisting frames. Practice Periodical on Structural Design and Construction (ASCE) 27(4):04022044, 2022.
[61] Lignos D.G., Krawinkler H., Deterioration modelling of steel components in support of collapse prediction of steel moment frames under earthquake loading. Journal of Structural Engineering 137:1291–1302, 2011.
[62] Lignos D.G., Hartloper A.R., Elkady A., Deierlein G.G., Hamburger R., Proposed updates to the ASCE 41 nonlinear modelling parameters for wide-flange steel columns in support of performance-based

seismic engineering. Journal of Structural Engineering 145(9):04019083, 2019.

[63] Lignos D.G., Krawinkler H., A steel database for component deterioration of tubular hollow square steel columns under varying axial load for collapse assessment of steel structures under earthquakes. Joint Conference Proceedings of the 7th International Conference on Urban Earthquake Engineering and the 5th International Conference on Earthquake Engineering, Tokyo, Japan, 2010.

[64] Sediek O.A., Wu T.-Y., McCormick J., El-Tawil S., Collapse behavior of hollow structural section columns under combined axial and lateral loading, Journal of Structural Engineering 146 (6): 0402009, 2020.

[65] Suzuki Y., Earthquake-induced collapse of steel moment resisting frames with conventional and high-performance steel columns. Ph.D. dissertation, McGill University, 2019.

[66] Kurata M., Nakashima M., Suita K., Effect of column base behaviour on the seismic response of steel moment frames. Journal of Earthquake Engineering 9(2):415–438, 2005.

[67] CEN. EN 1993-1-5, Eurocode 3: Design of steel Structures – Part 1–5: Plated Structural Elements, European Committee for Standardization, Bruxelles, 2006.

[68] CEN, EN 1993-1-1:2022 Eurocode 3: Design of steel structures – Part 1-1: General rules and rules for buildings (Second generation). European Committee for Standardization (CEN), Brussels, Belgium, 2022.

[69] UNI EN 10219. Cold formed welded structural hollow sections of non-alloy and fine grain steels. Part 2. Tolerances, dimensions and sectional properties.

[70] Del Zoppo M., Di Ludovico M., Prota A. Deformation capacity of non-conforming r.c. columns under compressive axial load and biaxial bending. Engineering Structures 124: 480-493, 2016.

[71] Jarque CM, Bera AK. A test for normality of observations and regression residuals. Int Stat Rev 1987;55:163–72.

[72] Lilliefors H. W. On the Kolmogorov-Smirnov test for normality with mean and variance unknown. Journal of the American Statistical Association 1967; 62 (318): 399–402.
[73] Chatterjee S, Hadi A. S. Regression analysis by example, John Wiley & Sons. Print ISBN:9780471746966 |Online ISBN:9780470055465 |DOI:10.1002/0470055464.
[74] Mazzoni S., McKenna F., Scott M.H., Fenves G.L., et al., OpenSees Command Language Manual. Pacific Earthquake Engineering Research Center, University of California, Berkeley, 2007.
[75] AISC, ANSI/AISC 341-16 Seismic Provisions for Structural Steel Buildings. American Institute of Steel Construction, Chicago, 2016.
[76] Barbagallo F., Bosco M., Ghersi A., Marino E.M., Rossi P.P., Seismic assessment of steel MRFs by cyclic pushover analysis. Open Construction & Building Technology Journal 13(1):12–26, 2019.
[77] Ribeiro F.L.A., Barbosa R.A., Scott M.H., Neves L.C., Deterioration modeling of steel moment resisting frames using finite-length plastic hinge force-based beam-column elements. Journal of Structural Engineering 141(2):04014112, 2015.
[78] Bosco M., Floridia A., Panarelli D., Rossi P.P., A new uniaxial material model for the simulation of lateral buckling of steel rebars. Engineering Structures 323:119293, 2025.
[79] Akkaya Y., Guner S., Vecchio F.J., Constitutive model for inelastic buckling behavior of reinforcing bars. ACI Structural Journal 116(2):195–204, 2019.
[80] Ministero delle Infrastrutture e dei Trasporti, Decreto 17 gennaio 2018: Aggiornamento delle «Norme tecniche per le costruzioni» (GU Serie Generale n.42 del 20-02-2018, Suppl. Ordinario n. 8). Gazzetta Ufficiale della Repubblica Italiana, Roma, Italy, 2018.
[81] Monti G., Nuti C., Nonlinear cyclic behavior of reinforcing bars including buckling. Journal of Structural Engineering 118(12):3268–3284, 1992.
[82] Prota A., De Cicco F., Cosenza E., Cyclic behavior of smooth steel reinforcing bars: Experimental analysis and modeling issues. Journal of Earthquake Engineering 13:500–519, 2009.

[83] Scott M.H., Fenves G.L., Plastic Hinge Integration Methods for Force-Based Beam-Column Elements. Journal of Structural Engineering 132(2):244–252, 2006.